TRANSVERSE-ENERGY PRODUCTION AND FLUCTUATIONS OVER CENTRALITY AND ACCEPTANCE IN RELATIVISTIC HEAVY-ION AND NUCLEON-NUCLEON COLLISIONS: QUARK VERSUS NUCLEON INTERACTIONS AND A SEARCH FOR THE QUARK-GLUON PLASMA

BY

RAUL L. ARMENDÁRIZ, B.S., M.S.

A Dissertation submitted to the Graduate School

in partial fulfillment of the requirements

for the degree

Doctor of Philosophy

Major Subject: Physics

New Mexico State University

Las Cruces New Mexico

May 2007

“Transverse-energy production and fluctuations over centrality and acceptance in relativistic heavy-ion and nucleon-nucleon collisions: quark versus nucleon interactions and a search for the quark-gluon plasma,” a dissertation prepared by Raul L. Armendáriz in partial fulfillment of the requirements for the degree, Doctor of Philosophy, has been approved and accepted by the following:

Linda Lacey
Dean of the Graduate School

Stephen F. Pate
Chair of the Examining Committee

Date

Committee in charge:

Dr. Stephen F. Pate, Chair

Dr. Mary Ballyk

Dr. Alexander Bazilevsky

Dr. Matthias Burkardt

Dr. Gary Kyle

Dr. Jeffrey T. Mitchell

Dr. Michael J. Tannenbaum

DEDICATION

I dedicate this work to my family: my grandmother Marie who opened our eyes to the beauty of higher education; to my parents John and Barbara who always encouraged us to excel; to my siblings Mark, Cynthia, Shawn, Andre, Robert, and Sergio, who have always stood by me through the real struggles of life; and to my two beautiful sons Bernardo Mark II, and John Edward to whom I dedicate my entire self.

ACKNOWLEDGMENTS

Thank you to my NMSU Advisor Dr. Stephen Pate for research guidance, understanding, funding, and for creating opportunities at the Brookhaven National Laboratory (BNL). Thank you to my Mentor Dr. Mike Tannenbaum (BNL) for proposing my project, teaching me how to conduct research in experimental nuclear physics, for sharing from his pioneering discoveries, pushing me to excel, and for taking the time and interest to teach me how to be a physicist — it was a pleasure to work with such an accomplished individual. Thanks to Dr. Jeffrey Mitchell (BNL) for teaching me the analysis of fluctuations in energy production, the daily hands-on instruction with C++, the ROOT histogramming software, and for showing me example code, without his help this work would not have been possible. Thanks to Dr. Alexander Bazilevsky (BNL) for teaching me how the EMC detector works, methodology on the PHENIX energy measurement, and the important lesson on being a careful scientist. Thanks to Dr. Chris Pinkenburg and Dr. Sergey Belikov (BNL) for help with computational algorithms and solving background problems. Thanks to Dr. Gary Kyle and Dr. Vassili Papavassiliou for years of nuclear physics instruction, and to Dr. Matthias Burkardt and Dr. Mary Ballyk (NMSU) for serving on my dissertation committee. Thank you to Dr. Laurie Churchill (NMSU-AGEP) and Dr. Bob Belle (SREB) for fellowship support. Without them I could not have made this contribution to science, nor accomplished my goal of becoming a productive physicist.

VITA

1990-1994	B.S., Physics, Loyola University of Chicago, Chicago, Illinois
1994-1996	M.S., Physics, University of Texas at El Paso, El Paso, Texas – *research area: gravitational-wave astrophysics,* *conducted at the Jet Propulsion Laboratory, NASA*
1997-1999	Electrical Engineer, F.P.M. Analytics Inc., Buffalo Grove, Illinois – *area: hardware systems design*
1999-2001	Electrical Engineer, Very Large Array, National Radio Astronomy Observatory, Socorro, New Mexico – *area: radio frequency and small antennae systems design*
2001-2007	Ph.D., Physics, New Mexico State University, Las Cruces, New Mexico – *research area: experimental nuclear physics,* *conducted on PHENIX-RHIC at Brookhaven National Laboratory*
2006-2008	Postdoctoral Fellow and Research Associate, Observational Astrophysics Brookhaven National Laboratory, Upton New York, and Harvard University, Cambridge, Massachusetts – *area: cosmology, dark matter in galaxy clusters*

PROFESSIONAL AND HONORARY SOCIETIES

American Astronomical Society

National Society of Hispanic Physicists

PUBLICATIONS OR PAPERS PRESENTED FOR PUBLICATION

(primary authorship †, extensive contribution ⋆)

1. (†) *Transverse energy production and fluctuations in 62.4 GeV Au+Au and 200 GeV Au+Au relativistic heavy-ion collisions: quark versus nucleon interactions and a search for QGP.* Raul Armendariz for the PHENIX Collaboration. Prepared for Conference of the National Societies of Black, and Hispanic Physicists, Boston, MA, Feb. 2007. Submitted for publication by American Institute of Physics conference proceedings series (2007).

2. (†) *Evolution of event-by-event E_T fluctuations over collision centrality in RHIC interactions.* Raul Armendariz for the PHENIX Collaboration. 3pp. Prepared for Particles and Nuclei International Conference, (PANIC) Nov. 2005. Published by American Institute of Physics, AIP conference proceedings 842 (2006), Archive: nucl-ex/0701018.

3. *Azimuthal angle correlations for rapidity separated hadron pairs in d+Au Collisions at $\sqrt{s_{NN}}$ = 200 GeV.* PHENIX Collaboration (S.S. Adler et al.). March 2006. 6pp. Submitted to Physical Review Letters. e-Print Archive: nucl-ex/0603017

4. *Nuclear effects on hadron production in d+Au and $p+p$ collisions at $\sqrt{s_{NN}}$ = 200 GeV.* PHENIX Collaboration (S.S. Adler et al.). March 2006. 13pp. e-Print Archive: nucl-ex/0603010

5. *Improved measurement of double helicity asymmetry in inclusive midrapidity π^0 production for polarized $p+p$ collisions at $\sqrt{s_{NN}}$ = 200 GeV.* PHENIX Collaboration (S.S. Adler et al.). Feb 2006. 4pp. e-Print Archive: hep-ex/0602004

6. *Jet structure from dihadron correlations in d+Au collisions at $\sqrt{s_{NN}}$ = 200 GeV.* PHENIX Collaboration (S.S. Adler et al.). Oct 2005. 30pp. Published in Physical Review C 73 054903, 2006 e-Print Archive: nucl-ex/0510021

7. *J/psi production and nuclear effects for d+Au and p+p collisions at $\sqrt{s_{NN}}$ = 200 GeV* PHENIX Collaboration (S.S. Adler et al.). Jul 2005. 6pp. Published in Physical Review Letters 96 012304, 2006 e-Print Archive: nucl-ex/0507032

8. *Nuclear modification factors for hadrons at forward and backward rapidities in deuteron-gold collisions at $\sqrt{s_{NN}}$ = 200 GeV.* PHENIX Collaboration (S.S. Adler et al.). Nov 2004. 6pp. Physical Review Letters 94 082302, 2005 e-Print Archive: nucl-ex/0411054

9. *Saturation of azimuthal anisotropy in Au+Au collisions at* $\sqrt{s_{NN}} = 62$ *GeV to 200 GeV.* PHENIX Collaboration (S.S. Adler et al.). Nov 2004. 7pp. Physical Review Letters 94 232302, 2005 e-Print Archive: nucl-ex/0411040

10. *Formation of dense partonic matter in relativistic nucleus-nucleus collisions at RHIC: Experimental evaluation by the PHENIX collaboration.* PHENIX Collaboration (K. Adcox et al.). Oct 2004. 127pp. Nuclear Physics A 757 184-283, 2005 e-Print Archive: nucl-ex/0410003

11. *Jet structure of baryon excess in Au+Au collisions at* $\sqrt{s_{NN}} = 200$ *GeV.* PHENIX Collaboration (S.S. Adler et al.). Aug 2004. 6pp. Physical Review C 71 051902, 2005 e-Print Archive: nucl-ex/0408007

12. *Double helicity asymmetry in inclusive mid-rapidity* π^0 *production for polarized* $p+p$ *collisions at* $\sqrt{s_{NN}} = 200$ *GeV.* PHENIX Collaboration (S.S. Adler et al.). Apr 2004. 6pp. Physical Review Letters 93 202002, 2004 e-Print Archive: hep-ex/0404027

13. *PHENIX muon arms.* PHENIX Collaboration (H. Akikawa et al.). 2003. 19pp. Nuclear Instruments and Methods A 499 537-548, 2003

14. *PHENIX detector overview.* PHENIX Collaboration (K. Adcox et al.). 2003. 16pp. Nuclear Instruments and Methods A 499 469-479, 2003

15. *Absence of suppression in particle production at large transverse momentum in* $\sqrt{s_{NN}} = 200$ *GeV. d+Au collisions.* PHENIX Collaboration (S.S. Adler et al.). Jun 2003. 6pp. Physical Review Letters 91 072303, 2003 e-Print Archive: nucl-ex/0306021

16. ($\star$) *Optical alignment system for the PHENIX muon tracking chambers.* J. Murata[1], A. Al-Jamel[2], R. Armendariz[2], and others. ((1) RIKEN BNL Center, (2) New Mexico State University) . Dec 2002. 14pp. Nuclear Instruments and Methods A 500 309-317, 2003 e-Print Archive: nucl-ex/0212027

FIELD OF STUDY

Experimental Particle and Nuclear Physics

ABSTRACT

TRANSVERSE-ENERGY PRODUCTION AND FLUCTUATIONS OVER CENTRALITY AND ACCEPTANCE IN RELATIVISTIC HEAVY-ION AND NUCLEON-NUCLEON COLLISIONS: QUARK VERSUS NUCLEON INTERACTIONS AND A SEARCH FOR THE QUARK-GLUON PLASMA

BY

RAUL L. ARMENDÁRIZ, B.S., M.S.

Doctor of Philosophy

New Mexico State University

Las Cruces, New Mexico, 2007

Dr. Stephen Pate, Chair

Measuring energy produced in relativistic heavy-ion collisions is a way to investigate if a model of quark participants, or nucleon participants better describes the internal dynamics of the collision. The energy produced is proportional to the energy density in the interaction region; changes in fluctuations of energy production could be a signature for a phase transition between ordinary hadronic matter to a liberated quark-gluon plasma phase, QGP, thought to have existed

one millionth of a second after the Big Bang creation of the Universe and before protons and neutrons had formed.

Three experimental nuclear physics data-analyses were conducted using the sum energy of all particles produced in the direction transverse to the beam, E_T, when nuclei collide in a 2.4 mile long circular atom smasher. The nuclei are accelerated in opposite directions at 99.995% the speed of light, and center-of-mass energies available for new particle production of $\sqrt{s_{NN}} = 62.4$ GeV, and 200 GeV per colliding nucleon pair were studied. The E_T was recorded by the lead-scintillator electromagnetic calorimeter detectors of the Pioneering High Energy Interactions Experiment (PHENIX), at the Relativistic heavy Ion Collider (RHIC), of Brookhaven National Laboratory (BNL).

The collision systems studied were 200 GeV protons with protons ($p + p$), deuterons with Au ions (d+Au), and 62.4 GeV and 200 GeV gold ions with gold ions (Au+Au). The first analysis, *mean E_T in collision centrality*, explores whether a model of nucleon participants, or quark participants, better describes energy production with collision impact. The second analysis, *E_T fluctuations in collision centrality*, looks for non-random fluctuations in E_T distributions when the density of colliding partons becomes high. The third analysis, *E_T fluctuations in geometric acceptance*, examines fluctuations as a function of detector fiducial volume in a search for correlated energy distribution in space (*correlations*), known to occur in phenomena such as elliptic flow and particle jets.

The Au+Au results are as follows. In both 62.4 GeV and 200 GeV interactions mean E_T production per participant nucleon rises steadily, and per participant quark remains constant to within the identified errors. In both 62.4 GeV and 200 GeV collisions energy densities estimated for QGP formation were measured: at 200 GeV these levels of 1 GeV/fm^3 to 3 GeV/fm^3 were measured respectively in the 60-65%, and 25-30% centrality classes of data (corresponding to modeled interactions of 30 and 150 participant nucleons). In neither 62.4 GeV nor 200 GeV interactions are changes in fluctuations over collision impact observed above the 40% systematic errors introduced by the centrality definitions. Fluctuations in acceptance for the 200 GeV 0-5% most central class of collisions, corresponding to 350 participant nucleons, exhibit a 115% rise in a 6-fold increase of the transverse angle; from this a correlation-length of 3.1° is calculated. Correlations due to π^0 particle showers, reaction plane rotation, and elliptic flow should be considered before drawing any further conclusions.

CONTENTS

LIST OF TABLES

LIST OF FIGURES

1 INTRODUCTION: QUARKS, NUCLEONS, ENERGY PRODUCTION AND QGP

Experimental data obtained in high energy collider experiments can be accounted for by the Standard Model of Particles and Interactions [36]. The model states that all matter is built from six types of quarks and six types of leptons, together with their antiparticles, and that there are four fundamental types of interactions mediated by boson fields. The four fundamental forces are

1. The Strong Force, which is responsible for binding quarks within nucleons and nucleons within atomic nuclei, and is mediated by fields carried by gluons. The theory of quantum chromodynamics, QCD, is the field theory of the Strong color interaction between quarks.

2. The Electromagnetic Force, which is responsible for binding electrons within nuclei and electric current, and is mediated by the photon.

3. The Weak Force is responsible for beta-decay, and is mediated by the fields carried by the $W^{\pm}$ and Z^0 bosons.

4. The Gravitational Force, which acts between all types of matter, and is mediated by the yet undetected graviton.

The atomic nucleus is made of protons and neutrons where each contain three quarks held together by gluons. Big Bang cosmology theory states that only in the first microsecond after the creation of the universe, when the universe was hot and dense enough, the quarks, which are now bound together by the gluons, were free from one another and moved about independently. This is referred to as the quark-gluon plasma phase of matter, QGP, as opposed to the current hadronic-matter phase of the universe. Figure 1 on page 145 shows the Big Bang model of the universe: after about the first one millionth of one second after the creation of the universe the quarks and gluons bonded into protons and into neutrons. QGP energy-densities are obtainable in accelerator "atom-smasher" experiments. The RHIC accelerator was built to search for a matter phase-transition signature from ordinary hadronic matter to the QGP phase. It is expected that this phase transition may occur in high energy heavy-ion collisions when the density of colliding quarks becomes high enough, but not in $p+p$ collisions where the available quarks are limited. Figure 2 on page 146 is an illustration for the phase transition for water. Similarly Figure 3 on page 146 illustrates the hadronic-matter to QGP-matter phase transition diagram which depicts many interesting things; in the Figure the QGP region is indicated at an energy density of a few GeV per cubic femtometer (fm), where 1 fm = 10^{-15} meters; the region at relatively low density and low temperature is the "normal nucleus" region where quarks are still confined in their respective protons and neutrons. The regions corresponding to collider energies are also indicated. Note the overlapping nucleons at high densities depicting the interaction length scale of less than 1 fm where quarks from colliding nucleons may interact.

The main contributer to multiplicity production in $p+p$ collisions may be either the nucleon-nucleon interaction or the internal partonic interaction and this depends on the collision energy. Heavy-ion collisions are not as well understood as $p+p$ collisions. Figure 4 on page 147 is a BNL-RHIC Au+Au simulated collision at $\sqrt{s_{NN}} = 200$ GeV per nucleon pair in the Ultra-relativistic quantum molecular dynamics (UrQMD) model: the hadrons, shown in red, are relativistically flattened (transverse to the collision axis) before the collision shown at t = -19.89 fm/c; after the collision mesons are produced, shown in yellow, and excited baryons, shown in blue. Had there been any free quarks produced upon collision we would not expect to still see them at 29.61 fm/c which is a long enough time for all particles to have escaped the original collision; also shown is much later at 54.61 fm/c. Figure 5 on page 148 shows a computer simulation of a CERN-SPS Pb+Pb nuclei collision at 160 GeV per nucleon (GeV/A) also in the UrQMD model, where the hadrons are in white - shown is immediately after the collision at t = 1.6 fm/c - notice the quarks in red, blue, and green, are stretched along the collision axis. The hadrons which remain after the collisions did not participate in the event and as such are termed "spectators" in a spectator-participant collision model.

There are three physics goals of this thesis. The first goal is to explore if the dominant mechanism of energy production occurring in high energy density collisions is the nucleon-nucleon or the quark-quark interaction; this is done via the mean E_T analysis. The second goal is to look for changes in fluctuations of energy production with collision energy density as a possible signature of a QGP phase transition. The third goal examines changes in fluctuations of energy production with an increase in the geometrical acceptance of the detector; changes to such spatial correlations as particle jets and elliptic flow could also be a signature of a QGP phase transition.

2 ACCELERATOR AND DETECTOR APPARATUS, AND TRANSVERSE ENERGY MEASUREMENT

2.1 RHIC particle beam and new particle production

The RHIC particle and heavy-ion accelerator complex is shown in Figure 6 on page 150, Figure 7 on page 151, and Figure 8 on page 151. RHIC accelerates and then collides two beams of particles circulating in opposite directions along a 2.4 mile ring. The beams move at relativistically high speed such that their collisions result in a region of very high energy density. The acceleration process for nuclei is different than that for protons. For gold ions, the Tandem Van de Graaff accelerates them, stripping off their electrons; a booster then injects them into the Alternating Gradient Synchrotron, AGS, which accelerates them to $\sim$ 10 GeV/nucleon; finally, RHIC accelerates them to 100 GeV/nucleon. For protons, a proton source generates them and a linear accelerator begins their acceleration; the booster injects them into the AGS which accelerates them to 28 GeV/proton; lastly, RHIC accelerates them to 100 GeV/proton [25]. Photographs of the accelerator facilities are in Figure 9 on page 152 and Figure 10 on page 152.

In each beam the colliding particles (p, d, or Au) are in discrete bunches that circulate around the ring at 99.995% the speed of light; the number of collision events per second, or event rate is $R = \sigma L$, where σ is the interaction cross-section and L is the particle luminosity of the beams in units $\frac{1}{\text{cm}^2\text{s}}$. The Luminosity is given by [36]

$$L = \frac{fnN_1N_2}{A}, \tag{1}$$

where N_1 and N_2 are the number of particles in each bunch, n is the number of bunches around the ring, A is the cross-sectional area of the beams (assuming completely overlapped), and f is the revolution frequency. In the collision of any two nucleons the center-of-momentum energy is represented by $\sqrt{s_{NN}}$ (where the usage of two N's implies two nucleons). RHIC was designed for Au+Au collisions of $\sqrt{s_{NN}} = 200$ GeV and $L = 10^{26}\frac{1}{\mathrm{cm^2 s}}$, and $p+p$ collisions of $\sqrt{s_{NN}} = 500$ GeV and $L = 10^{31}\frac{1}{\mathrm{cm^2 s}}$. Using $\sigma_{\mathrm{Au+Au}} = 6.8$ barns the Au+Au event rate is

$$\begin{aligned} R &= L\sigma_{\mathrm{Au+Au}} = 10^{26}\frac{1}{\mathrm{cm^2 s}} \times 6.8\mathrm{b} \times 10^{-24}\frac{\mathrm{cm^2}}{\mathrm{b}} \\ &= 680 \ \mathrm{Au+Au\ collisions\ per\ second} \end{aligned} \tag{2}$$

When the p, d, and/or Au collide, if the strong force is overcome they break apart and their constituent partons are momentarily freed from one another. The strong force quickly recombines quarks – but not necessarily the same quarks – creating new particles. Consider two colliding nucleons moving in opposite directions, one in each beam, the nucleons have mass M, energy E_1 and E_2, momentum p_1 and p_2. In a head-on collision their combined energy available to create new particles, or energy in their center-of-momentum system is given by [36]

$$\sqrt{s_{NN}} = \sqrt{2(E_1E_2 + p_1p_2) + 2M^2} \sim 2\sqrt{E_1E_2}. \tag{3}$$

Some of the energy becomes the kinetic energy of the newly created particles. If

$E_1 = E_2$ then the center of momentum is at rest in the laboratory frame and almost all the energy is available for new-particle creation.

Figure 11 on page 153 shows computer simulations of Au+Au nuclei collisions at impact $b = 5$ fm, but for the different energies of (top left) 1.5 GeV/u, (top right) 10.6 GeV/u, (bottom left) 200 GeV/u, and (bottom right) 5 TeV/u, in the Ultra-relativistic quantum molecular dynamics (UrQMD) Cascade model. QGP is expected in collisions of very high temperatures $T \sim 170$ MeV, requiring high collision energy densities of ∼1 to 3 $\frac{\text{GeV}}{\text{fm}^3}$ [38]. The primary goal in RHIC collisions is to smash apart nucleons in heavy nuclei to investigate this hadronic-matter to QGP-matter phase transition [12]. The four large experiments on RHIC, each with specific goals and located at different locations on the ring have the acronyms PHENIX, STAR, BRAHMS, and PHOBOS. PHENIX detectors were used in this doctoral dissertation. Figure 12 on page 154 shows particle tracks created in a real Au+Au collision reconstructed by PHENIX, particles which have components of energy and momentum transverse to the beam direction (E_T and p_T), and which provide information on the collision dynamics.

2.2 PHENIX subsystems and measuring transverse energy

The PHENIX collaboration involves many people from many countries. Figure 13 on page 155 is a group picture. The PHENIX experimental assembly consists of 4 arms placed in the North, South, East, and West directions relative to the beam interaction region and is shown in Figure 14 on page 156.

PHENIX uses specific detectors to identify when a collision has occurred, referred to as "triggering the event." Triggering detectors are placed along, near, or far away from the beam line and in the North and South arms, and the location depends on what type of event trigger is desired. There is a large central magnet system used to steer the trajectories of charged particles created in the interactions. PHENIX also has Muon Arm detectors (not used in this thesis). There are detectors oriented transverse to the beam line in East and West "Central Arms," for lepton, photon, and hadron detection. The triggering detectors used in this analysis were the two Zero Degree Calorimeters (ZDC), and two Beam-Beam Counters (BBC), and are used in the "minimum bias triggering." The Beam-Beam Counters are an assembly of Cerenkov photomultiplier tubes. They are located along the beam line (in the "forward" and "backward" beam directions) and each BBC has a hole cut out of it allowing the beam to pass through it as shown in Figure 15 on page 157. They cover an acceptance $3 < |\eta| < 3.9$ and $\Delta\phi = 360^0$, and are placed at $\pm$ 144.5 cm from the origin of the targeted interaction region. The BBC's provide a measure of the charge deposited by particles emitted into their acceptance. The Zero Degree Calorimeters measure the energy of neutrons. The ZDC's are placed directly in the beam path, but much further out from the targeted interaction region then the BBC location; steering magnets situated near the ZDC's steer charged particles such as the non-interacting ions around the ZDC's leaving them open primarily for unbounded neutrons. Most of the neutrons incident into the ZDC acceptance were neutrons not involved in the collision and a model is used to estimate the actual number of spectator neutrons. The BBC's and ZDC's provide charge, energy, and timing information of produced particles (albeit into their acceptances) which are used to estimate: (1) the collision event location, referred to as "Zvertex," along the beam path relative to the geometric origin of the magnet system and detectors, (2) the time the interaction occurred relative to the nominal time targeted by the beam-control system, and (3) the nucleus-nucleus collision impact, or "event centrality," estimated by assuming a monotonic relation between particle production and impact parameter.

The triggering detectors play a crucial part in gathering the data for the centrality-based analysis presented here. Both the BBC's by themselves, and the ZDC's by themselves, reconstruct the time they believe the event to have occurred; this time measurement is relative to the beam clock nominal zero-time which is when the beam control algorithm planned for the two opposing bunches to be in an ideal collision orientation. The formula used to reconstruct event time, referred to as "$bbct0$" for BBC's and "$zdct0$" for ZDC's, is similar for the two systems and is given by

$$Event\ time \equiv bbct0 = \frac{(T_{south} + T_{north}) - 2L/c}{2} \tag{4}$$

where T_{south} and T_{north} are the time of arrival for multiplicity on the event to the individual arms relative to the beam clock, L is the separation distance between the BBC's of 144.5 cm, and c is the speed of light. From the event time a Zvertex position is reconstructed as

$$Zvertex = \frac{T_{south} - T_{north}}{2} \times c \tag{5}$$

The 2 Central Arms consist of several subsystems and those used in this analysis are the 6 equally-sized Lead Scintillator Electromagnetic Calorimeter sectors (PbSc EMC), the 5 Pad Chamber multiplicity detectors (PC1, PC2, .., PC5), and 2 Drift Chamber tracking detectors (DC). The detectors used to measure E_T were the 6 PbSc EMC sectors. Figure 16 on page 158 shows the assembly of one PbSc EMC sector and the mounting of the sector onto the EMC arm. Figure 17 on page 159 shows the EMC relative to other central Arm subsystems, and Figure 18 on page 160 shows the coordinate system used in the E_T measurements. Figure 19 on page 161 shows an individual calorimeter module where each module contains 4 PbSc towers; 6×6 modules form a "supermodule" of 144 PbSc towers, and each of the 6 EMC sectors contains 2592 PbSc towers. The PbSc detectors use a total sampling method via a tower assembly design of alternating lead and scintillator tiles sandwiched together along the particle trajectory – the sandwiching provides a more linear response to incident particle energy. The lead is an absorber material. The incident hadrons react via the strong force with lead nuclei converting the hadron energy into a shower of several charged and neutral hadrons (hadronic shower), and electrons and photons (electromagnetic shower). The shower energy undergoes further transformation in the scintillator material which is a plastic of organic p-bis-benzene scintillator molecules and fluorescent p-terphenyl molecules used as an additive. The PbSc EMC was primarily designed to measure the energy, position, and timing of incident electrons and photons, but was used in this analysis to measure the entire energy (within its geometric acceptance) created in nucleus-nucleus interactions. The produced energy is predominantly charged and neutral pions.

2.2.1 Shower production in PbSc Calorimeters

In a Au+Au collision about 80% of the energy produced is initially in the form of pions and goes through the following transformations inside the calorimeter [36], [12].

1. **Hadron shower is proportional to lead nuclear absorption length**

   High energy incident pions called "parent" pions undergo nuclear interactions via the strong force with lead nuclei and lead nucleons. The probability that an incident pion will interact with a lead nucleus is given by the total cross section, σ_T, which includes terms for the different interactions of inelastic absorption, σ_{abs}, elastic scattering off the whole nucleus, σ_{el}, and quasi-elastic scattering off individual nucleons, σ_q, thus $\sigma_T = \sigma_{abs} + \sigma_{el} + \sigma_q$. The incident pion excites the lead nucleus and when it returns to the ground state it emits two lower kinetic energy charged or neutral pions, a process which grows creating a hadronic shower

$$\pi_{\mathrm{incident}} + n \to n + \pi + \pi. \tag{6}$$

Dividing Avogadro's number (N_o) by the atomic weight of lead (A) gives the number of lead atoms per gram. Using the density of lead $\rho = 11.35\ \frac{\mathrm{g}}{\mathrm{cm}^3}$, $N_o \rho A^{-1}$ is the number of lead atoms per cm^3 of lead. Thus $N_o \rho \sigma_T A^{-1}$ is the number of lead atoms the incident pion interacts with per cm of depth, and related to this are the *interaction length* $L_{Int\ (\mathrm{cm})}$, and the amount of actual material the particle traverses between interactions L_{Int} (over which distance its intensity drops by $1/e$) [12]

$$L_{Int\ (\mathrm{cm})} = \frac{A}{N_o \rho \sigma_T} = 10.2\ \mathrm{cm} \tag{7}$$

$$L_{Int} = \frac{A}{N_o \sigma_T} = 116.2\ \mathrm{g/cm}^2, \tag{8}$$

where the difference between the expressions is the density. The part of the total cross section corresponding to inelastic absorption, σ_{abs}, determines the material's *absorption length* $\lambda_{abs\ (\mathrm{cm})}$ - the distance over which the growth of the pion shower scales; over this distance the amount of material actually traversed, λ_{abs}, is obtained using the density

$$\lambda_{abs\ (\mathrm{cm})} = \frac{A}{N_o \rho \sigma_{abs}} = 17\ \mathrm{cm} \tag{9}$$

$$\lambda_{abs} = \frac{A}{N_o \sigma_{abs}} = 194\ \mathrm{g/cm}^2. \tag{10}$$

2. **Electromagnetic shower is proportional to lead radiation length**

   A neutral pion decays to two photons $\pi^0 \to 2\gamma$, and the photons interact with charge in the volume producing electron-positron pairs $\gamma \to e^+ + e^-$. The electrons and positrons are decelerated in the electric field of lead nuclei causing them to radiate photons via bremsstrahlung $e^- \to \gamma + e^-$. These photons can pair-produce again repeating the process and creating a shower of electrons and photons — an electromagnetic shower. Thus each electron of initial energy E increases the size of the electromagnetic shower but loses an amount of energy in its radiation loss dE. The rate of energy loss due to radiation of the incident charge is

   $$\frac{dE}{dx}_{radiation} = -\frac{E}{X_0}, \tag{11}$$

   where X_0 is the *radiation length* of lead. Using m as the electron mass and Z as the atomic number for lead [36], [22]

   $$X_0^{-1} = 4Z^2\alpha^3\,[N_o/A]\,\left[(hc)/(2\pi mc^2)\right]^2\,\left[\ln(183/Z^{1/3})\right] \tag{12}$$

   $$X_{0\ (\mathrm{cm})} = 0.53\ \mathrm{cm} \tag{13}$$

   $$X_0^{-1} = 6\ \mathrm{cm}^2/\mathrm{g} \tag{14}$$

3. **Some incident energy is lost in ionization of the lead**

   A certain amount of energy is lost by ionizing the lead and corrected for in the energy measurement. Charged pions and electrons from the showers ionize lead atoms by knocking loose their electrons which in turn further ionize the lead. The Bethe-Bloch formula gives the average rate of energy lost to ionization by the charged particles which traverse a depth x [36]

$$\frac{dE}{dx}_{ionization} = \frac{4\pi N_o z^2 \alpha^2}{mv^2} \frac{Z}{A} \left[\ln \left[\frac{2mv^2}{I(1-\beta^2)} \right] - \beta^2 \right] \tag{15}$$

where z, and v, are the charge (in electron units) and velocity of the particle, $\beta = v/c$ is the relativistic term, and I is an average ionization potential of the lead ($\sim 10Z$ eV). Ideally a calorimeter is to have a lead absorber thick enough to create a good shower so the energy can be detected in the scintillator, but not too thick in which case the shower would die out before it reaches the scintillator material. Table 1 on page 129 lists general properties of lead, and the PHENIX PbSc calorimeter performance [14].

4. **Specifics of scintillator material**

The shower enters the scintillator plastic where charged hadrons and leptons interact electromagnetically with the organic p-bis-benzene molecules, exciting those atoms to higher vibrational and rotational states. When the atoms return to their ground state they radiate ultraviolet photons (scintillate), which excite the p-terphenyl dye molecules which then emit a blue light (wavelength shifting). A metal case around each PbSc module contains the blue light by internal reflection and the light eventually propagates down a fiber optic line running longitudinally along the module central axis. The light is guided into a photomultiplier tube at the back of each module where it is converted to a current via the photoelectric affect, amplified, and the signal energy recorded. The signal energy is proportional to the incident energy of the parent pion.

A single incident pion hitting the EMC typically produces a concentrated cluster of charge spread over an area approximately 15 cm by 15 cm, or 3×3 PbSc towers large. A cluster finding algorithm records the incident particle energy and coordinates. There are six PbSc sectors and each sector is 72 towers wide and 36 towers high. Towers are 5.535 cm $\times$ 5.535 cm square and each contains 66 sampling cells of alternating lead and scintillator tiles.

2.2.2 PHENIX measurement of raw $E_{T\ \mathrm{(EMC)}}$ and total E_T

The geometry of the experimental setup is as follows. In the PHENIX coordinate system the beam is along the Z-axis, and collision vertices's are measured with respect to $Z = 0$. The origin ($X = 0$, $Y = 0$, $Z = 0$) is the center of the PHENIX structural magnet system and also the center of the EMC geometry. The EMC covers half a circular circumference about Z with radius 5.1m, and points on its surface are indicated by polar angle θ and azimuthal angle ϕ. $\theta = 0°$ is along the beam line $+Z$ (North direction), and $\phi = 0°$ is along $+X$ (West direction). The Z-coordinate of the EMC, Z_{EMC}, is synonymous with the beam line. Each of the six PbSc sectors is 2m high and 4m wide, and the sectors are stacked along ϕ

with 4 in the West Arm (labeled W0, W1, W2, and W3), and 2 in the East Arm (labeled E2 and E3). Each PbSc sector has an angular aperture $\Delta\phi = 22.5°$ and $\Delta\theta = 45°$. The six sectors together cover $\Delta\phi = 135°$ and $\Delta\theta = 45°$ (expanding approximately over $67.5° < \theta < 112.5°$).

A convenient way to look at the polar angular measurement of a particle coming out of a reaction is in terms of the related rapidity variable y. The rapidity is defined in terms of the particle's energy E, transverse and longitudinal components of momentum p_T and p_L, and transverse mass m_T

$$y = \ln\left(\frac{E + p_L}{m_T}\right), \tag{16}$$

where $\cosh(y) = E/m_T$, $\sinh(y) = p_L/m_T$, $m_T = \sqrt{m^2 + p_T^2}$, and $E = \sqrt{p_L^2 + m_T^2}$ [40]. The rapidity dimension is convenient because it is additive in the relativistic case [42] - the shape of the multiplicity distribution is unchanged, or relativistically invariant, between lab and collider frames. It is additionally convenient as a pair of secondary particles can be identified as having decayed from the same primary particle if they are close in rapidity. In the limit $m << E$ an approximation to the rapidity is the pseudorapidity η, an angular density

$$\eta = -\ln[\tan(\theta/2)]. \tag{17}$$

and in this limit $\cosh(\eta) = \csc(\theta)$, $\sinh(\eta) = \cot(\theta)$ (discussed further in Chapter 4.2, and [40]). The EMC aperture is centered at zero pseudorapidity (or mid-rapidity) covering a range $-0.382 < \eta < +0.382$ [15].

For Au+Au interactions the energy measured in the PbSc sectors is known via Monte Carlo studies to be comprised of $\sim 40\%$ charged pions, $\sim 40\%$ photons from π^0 and other decays, and $\sim 20\%$ from decay muons, kaons, protons, and other particles [3]. E_T on an event is a multi-particle variable consisting of the energy of i particles

$$E_T = \Sigma_i E_i \sin(\theta_i), \tag{18}$$

where E_i is the energy of the i^{th} particle and θ_i is the polar angle of the i^{th} particle measured relative to the beam axis. By convention E_i is the kinetic energy for nucleons and total energy for all other other particles [3]. In terms of the pseudorapidity

$$\frac{dE_T(\eta)}{d\eta} = \sin\theta(\eta)\frac{dE(\eta)}{d\eta}. \tag{19}$$

E_T is very useful in a search for the QGP phase transition as it is a measure of collision energy density [3]

$$\epsilon = \frac{dE_T}{dy}\frac{1}{\tau_0 \pi R^2}, \tag{20}$$

where $\tau_0 \sim 1$ fm ($c \equiv 1$) is typically accepted as the formation time of the initial medium; πR^2 is the effective overlap area of the two colliding nuclei and is estimated using a geometrical model of the structure of the nucleus [38]. This is discussed further in Chapter 4.2. E_T on the event was measured using the reconstructed particle showers, or EMC "clusters" available in PHENIX nano-DST data files where the cluster energy variable labeled "e" was used (note that this is slightly different than the shower energy variable "ecore" used in the π^0 reconstruction as discussed in Chapter 3.6). Each event E_T is defined as the sum of that event's clusters' E_T. A 30 MeV energy per cluster was used as the minimum-energy requirement threshold. The definition of a cluster begins with the requirement that adjacent PbSc towers each have an energy greater than 10 MeV, and reconstruction of clusters was done prior to this thesis. $\langle E_T \rangle$ analysis measures an absolute value of energy produced on the event in the EMC acceptance.

The following corrections to the measured or "raw" transverse energy $E_{T\ (\mathrm{EMC})}$ are applied to obtain the total transverse energy on the event in a given reference acceptance, which is referred to as "corrected hadronic E_T."

(I) The first correction term discussed here is a scale factor referred to as the "k-factor," or k-correction, and it is determined by simulating the following three known detector effects of the EMC measurement:

1. Imperfect Calorimeter Hadronic Response: the EMC was designed for electromagnetic particle detection thus its depth is shallower than a typical hadronic calorimeter and energetic charged pions pass through the calorimeter only depositing the minimum ionization potential energy (MIP); due to this affect the amount of measured $E_{T\ (\mathrm{EMC})}$ on the Au+Au event is only

75% of the produced E_T, thus [3]

$$E_T = \frac{1}{[0.75]} \times E_{T\ \text{(EMC)}} \tag{21}$$

2. Energy Inflow: the inflow results from the energy of undesired incident particles from two sources, those which (1) decayed from parent particles having original trajectory outside the fiducial EMC aperture, and (2) from particles which reflected off the PHENIX iron magnet poles and hit the EMC surface. On a Au+Au event 24% of the measured $E_{T\ \text{(EMC)}}$ is unwanted inflow, thus [3]

$$E_T = [1 - 0.24] \times E_{T\ \text{(EMC)}} \tag{22}$$

3. Energy Losses: there are three types of energy loss, (1) desired particles with original trajectories inside the EMC fiducial aperture but which have decay by-products which leave the fiducial aperture and miss the EMC surface, (2) losses from sector edge systematics (i.e. voltage gains, and shower energy spreading outside of the sector), and (3) missed energy from the imperfect choice of a minimum cluster energy threshold (the minimum is specified at 30 MeV per cluster, a level below which contains spurious PbSc electronic noise energy). Due to these affects, on a Au+Au event 22% of the produced E_T is lost, thus [3], [4]

$$E_T = \frac{1}{[1 - 0.22]} \times E_{T\ \text{(EMC)}} \tag{23}$$

The k-factor correction is a product of these three affects, and was previously determined in Au+Au to be independent of collision centrality, and to have the same value for Au+Au collisions at 19.6 GeV, 62.4 GeV, and 200 GeV. In summary, the components of the correction were obtained via Monte Carlo techniques [3], [4], with values Hadronic response = 75%, Energy inflow = 24%, Energy losses = 22%, thus the correction is

$$k - \text{factor } \textit{correction } (\text{Au} + \text{Au}) = \frac{[1 - \text{inflow}(0.24)]}{[\text{response}(0.75)] \times [1 - \text{losses}(0.22)]} = 1.3 \tag{24}$$

$k-$factors should be determined specifically for the $p+p$ and d+Au collision systems, however for the $\langle E_T \rangle$ measurements conducted in this thesis the value of $k = 1.3$ was borrowed from Au+Au. This raises questions as to the validity of the final result of $\langle E_T \rangle$. Since the $k-$factor was shown to be independent of centrality one might justify its use in $p+p$ arguing that the $p+p$ interaction is similar to a "2 participant-nucleon" Au+Au interaction. If the $k-$factor is in fact different in $p+p$ and in d+Au than in Au+Au, then determination of which of its components is the most different is important, and in this regard the following assumptions are made. It is reasonable to assume that the hadronic response would not change between Au+Au, $p+p$, and d+Au as the response is associated with the depth of the calorimeter and the types of incident particles produced. Due to the much lower multiplicity environments in $p+p$ and d+Au it is unlikely that the percent of energy inflow and/or outflow would be any larger than are seen in Au+Au, and in fact it is not unreasonable to expect that both terms would be smaller. Thus three extreme cases are considered, (1) no inflow and no outflow, (2) no inflow and maximum outflow (maximum meaning levels like in Au+Au), and (3) no outflow and maximum inflow (maximum meaning levels like in Au+Au), and under these assumptions the $k-$factor would be:

$$k - \text{factor (no inflow, no outflow)} = \frac{1}{[\text{response}(0.75)]} = 1.33 \tag{25}$$

$$k - \text{factor (no inflow, max outflow)} = \frac{1}{[\text{response}(0.75)] \times [1 - \text{losses}(0.22)]} = 1.71 \tag{26}$$

$$k - \text{factor (max inflow, no outflow)} = \frac{[1 - \text{inflow}(0.24)]}{[\text{response}(0.75)]} = 1.01 \tag{27}$$

The extreme and likely over estimated error on k is thus

$$\frac{1.71 - 1.3}{1.3} = +31\% \tag{28}$$

$$\frac{1.01 - 1.3}{1.3} = -22\% \tag{29}$$

$$k - \text{factor } \textit{correction} \text{ } (p + p \text{ and } d + Au, \text{ extreme case}) = 1.3^{+31\%}_{-22\%} \tag{30}$$

The analysis performed in this thesis used the $k-$factor = 1.3, and added the smaller error of (1.33-1.3)/1.33 = $\sim$ 3% in quadrature to the other known errors on the $p+p$ and d+Au measurements

$$k - \text{factor } \textit{correction} \text{ (actually used for } p + p \text{ and } d + \text{Au}) = 1.3 \pm 3\% \tag{31}$$

(II) The second correction term discussed is that for faulty PbSc towers, which were identified, removed, and corrected for via the method described in Chapter 3.5 (faulty towers are also removed in the fluctuations analyses). Basically the total number of PbSc towers "missing" from each sector is the sum of dead towers plus removed hot towers; since there are 2592 towers in each sector the tower correction per sector, and for the $n-$sector measurement where n = 1, 2, ..., 6 of the sectors used, are respectively

$$\textit{tower correction}_{\ 1\ sector} = \frac{2592}{2592 - (\text{missing towers in sector})} \tag{32}$$

$$\textit{tower correction}_{\ n\ sectors} = \frac{n \times 2592}{(n \times 2592) - (\text{missing towers in n sectors})} \tag{33}$$

(III) The π^0 mass peak was used to correct the measured energy on every cluster to an absolute energy scale; this was performed by PHENIX experts prior to this thesis (see for example [6]). The π^0 mass peak was measured in this thesis as a cross-check for the final results, and this is discussed in Chapter 3.6.

(IV) A geometric acceptance correction, or reference "scale correction," is applied: as previously mentioned each PbSc sector has dimensions $\Delta\theta = 45°$ (or equivalently $\Delta\eta = 0.764$), and $\Delta\phi = 22.5°$, and typically the 6 sectors were used covering a total area of $\Delta\eta = 0.764$ and $\Delta\phi = 135°$. To scale correct an $n-$sector $\langle E_T \rangle$ measurement to the reference acceptance of 1 unit $\Delta\eta$ and 360° $\Delta\phi$ the correction factor is

$$\textit{acceptance scale correction} = \frac{1}{0.764} \times \frac{360°}{(n \times 22.5)} \tag{34}$$

Thus for Au+Au the final result for $\frac{dE_T}{d\eta}|_{\eta=0}$ involves the corrections

$$\frac{dE_T}{d\eta}|_{\eta=0} \text{ Au} + \text{Au} = E_{T\ (\text{EMC})} \times (k) \times (towers) \times (\pi^0) \times (acceptance) \tag{35}$$

(V) A fraction of the minbias event triggers resulted in zero $E_{T\ (\text{EMC})}$ in the calorimeter and are included in the $\langle E_T \rangle$ analyses. The number of such events were measured at about 0.5% in 62.4 GeV Au+Au (where a 2 particles per BBC requirement was imposed on top of the minbias definition), 2% in 200 GeV Au+Au minbias (where 2 particles per BBC is part of that minbias definition), 6% in d+Au minbias, and $\sim$ 19% in $p+p$ minbias. In $p+p$ and d+Au interactions these "EMC zeros" were initially discarded from the $p+p$ and d+Au $E_{T\ (\text{EMC})}$ event selection and were re-included only in the mean E_T analyses (but not the fluctuations analyses) via the correction factors of

$$\begin{aligned} EMC\ zeros\ correction\ for\ p+p &= 0.813 \qquad (36) \\ EMC\ zeros\ correction\ for\ d+\text{Au} &= 0.94 \qquad (37) \end{aligned}$$

(VI) For $p+p$ there is an estimation (determined prior to this thesis by PHENIX experts) on the number of inelastic collisions which go undetected due to the limited acceptance BBC. This "trigger bias" correction ($\sigma_{\text{BBC}}/\sigma_{p+p}$) is further adjusted in accordance to what the bias is at the central arm calorimeter (ϵ_{EMC}) used in the E_T analysis

$$trigger\ bias\ correction\ at\ EMC = \frac{\sigma_{\text{BBC}}/\sigma_{p+p}}{\epsilon_{\text{EMC}}} = \frac{21.8\ \text{mb}/41\ \text{mb}}{0.75} = 0.52/0.75 = 0.69 \tag{38}$$

Thus for $p+p$ and d+Au respectively

$$\frac{dE_T}{d\eta}|_{\eta=0}\, p{+}p = E_{T\ (\mathrm{EMC})} \times (k) \times (towers) \times (\pi^0) \times (acceptance) \times 0.813 \times 0.69 \quad (39)$$

$$\frac{dE_T}{d\eta}|_{\eta=0}\ d + \mathrm{Au} = E_{T\ (\mathrm{EMC})} \times (k) \times (towers) \times (\pi^0) \times (acceptance) \times 0.94. \quad (40)$$

3 DATA ANALYSIS

3.1 Data selection and initial cuts above the minimum bias triggers

The PHENIX data used for $p + p$ and d+Au was from the third RHIC Run (year 2003), and for Au+Au was from the fourth RHIC Run (year 2004). In all the analyses presented here, for all species, the data used was minimum bias (minbias), which means that a least amount of constraints were met to identify an interaction. The data was selected from the reduced size or nano-data summary tape files ("nano-dst") located in the BNL-RCF computer system data-disks. The data files were selected from an official list of PHENIX data categorized by the Photon Working Group (PWG). All data analyzed was recorded with the PHENIX magnetic field on. Prior PHENIX E_T analyses were done with magnetic field off, and the field-on data was chosen in this thesis to facilitate a comparable charged particle track analysis if needed at a later date. The hadronic k-correction factors applied to the mean E_T measurements had been obtained prior to this thesis with field-off data, however they were demonstrated at that time to be independent of the magnetic field status. E_T was summed on each event using the energy of reconstructed particle showers, referred to as clusters, as opposed to manually summing the energy recorded within each PbSc tower (prior to this thesis the clusters were reconstructed from the PbSc tower energy by PHENIX EMC experts). A minimum energy requirement for a valid cluster of 30 MeV was used to avoid including PbSc electronic noise in the total energy measurement. The elimination of unwanted events was done via the following sequence of "cuts" to the data.

Cuts for Au+Au:

The 6 PbSc sectors were utilized. A 20 cm Zvertex determined by the BBC's. Requirement of at least two particles having been recorded in each BBC (referred to as two "hits"). Events which resulted in zero particles into the EMC were kept in the sample but contribute negligibly ($\sim 0.5 - 2\%$) and are limited to the most peripheral centrality classes of data. Faulty PbSc towers were removed, and are referred to as hot towers when they add spurious energy into the event, and dead towers when they are disabled and record no energy on the event. This was done by designing for each PbSc sector a bad-tower location map.

Cuts for 200 GeV Au+Au:

Data files called Stripe-2 were used with the PHENIX PLAY version of data analysis library routines (preceding the benchmark library version called pro.71). The current version of the PHENIX automated data correction algorithm (the "Master Re-calibrator") was used, which among other things, removes events which were triggered during test-only ion bunch crossings. Additionally the Master Re-calibrator applies an energy correction factor to each cluster, sector by sector; this correction was estimated previous to this thesis by measuring π^0 mass peaks, and which scales linearly with an increase in transverse momentum of the clusters.

Shuffling the events into collision centrality bins was done with a method which used both the BBC's and both the ZDC's together, referred to as "centrality-by-clock." The nano-dst data is provided by PHENIX in time incremented files, or "run numbers." A quality assurance examination (QA) was performed in this thesis to remove data files containing atypical average event information such as average event E_T, average cluster transverse energy e_T, average Zvertex, and average BBC charge; a total of 15 variable were checked in the QA. Unwanted events referred to as background were identified and removed – specifically events which had an interaction time beyond the detectable range of the BBC were removed, and pile-up of two Au+Au interactions in the same beam bunch crossing was removed from the 0-50% centrality class.

Cuts for 62.4 GeV Au+Au:

Data files referred to as pro.58 were used with the PLAY version of PHENIX data analysis library routines (preceding the benchmark library version called pro.71). Clusters in these files already had a sector by sector correction to cluster energy. The shuffling the events into collision centrality bins was done with a method which only uses the two BBC detectors referred to as the centrality-by-BBC described in [32] (to be more accurate the PHENIX "PercentileRecalReco" version of the method was used). Background events due to a faulty Pad Chamber electronic reset were removed.

Cuts for $p+p$ and d+Au:

Only 5 PbSc sectors were utilized as sector "West 3" was discarded entirely due to an excessive number of faulty PbSc towers. A 30 cm Zvertex was used and a requirement of at least one particle in each BBC. For d+Au distributions minbias events which resulted in zero energy into the EMC were discarded entirely, but their affect was added back into the mean E_T measurement. $p+p$ distributions were measured both with and without the minbias events which resulted in zero energy into the EMC, and likewise these "EMC zeroes" were included into the mean E_T measurement. To remove faulty PbSc towers the previously designed PHENIX location maps (called "deadmap" and "warnmap") were used; these maps were not successful in removing all hot towers and thus left a minor spurious energy contribution to E_T.

Statistics analyzed:

After all cuts 42,939,350 200 GeV Au+Au events, 22,401,880 62.4 GeV Au+Au events, 15,179,580 $p+p$ events, and 10,812,790 d+Au events were analyzed in the mean E_T, fluctuations in centrality, and fluctuations in acceptance analyses.

3.2 Distributing events into collision centrality classes represented by a modeled number of collision participants

Before dividing up the events into centrality classes the BBC charge on each event and/or ZDC energy on each event were increased, or "corrected" using known information on systematic affects which occurred during the data taking. This is to account for variations in detector voltage gains, and affects which occur in the different collision systems. Placement of the BBC detectors relative to the interaction region is non-ideal for the 62.4 GeV beam energy, and this results in an uncorrelated response in BBC versus the EMC and Drift Chambers, an affect which is centrality dependent and Zvertex dependent; to correct this the BBC charge on 62.4 GeV events were adjusted by a scale factor proportional to the number of created particles (referred to as "multiplicity") detected by the Pad Chamber 1 [32]; this is discussed further in Chapter 3.3. For 200 GeV Au+Au data the measured BBC charge and ZDC energy on each event was first adjusted due to identified detector problems which occurred in time sequential runs. Both of these adjustments were performed by the PHENIX centrality software modules employed.

Categorizing the data into event centralities is a procedure which shuffles the events into classes of equal numbers of events. This can be achieved by different methods. A minbias event-by-event distribution including all centrality classes and all incident particles is referred to as an "inclusive" distribution. The inclusive BBC charge distribution is shown in Figure 20 on page 163 and is used to define collision centrality classes by PHENIX with the RHIC Run 4 62.4 GeV data in the centrality-by-BBC-charge method. The centrality-by-BBC procedure slices the BBC charge inclusive distribution into bins containing equal numbers of events, where each bin is defined by the range of BBC charge required to fill it. This is done by assigning the most central events to have the highest BBC charge. Since grazing, or large impact parameter events (which result in low BBC charge) are more common than head on collisions the peripheral event classes cover a smaller range in BBC charge.

The 200 GeV Au+Au scatter plot of ZDC energy vs. event BBC charge shown in the left plot of Figure 21 on page 164 is used to define collision centrality classes for PHENIX Run 4 200 GeV Au+Au analyses in the centrality-By-Clock method. This scatter plot is the simultaneous responses in both the BBC's and the ZDC's, and is sliced into bins of equal numbers of events. This procedure is done by assigning the most central events to have the highest BBC charge simultaneous with the lowest ZDC energy. On an event the non-interacting or "spectator" part of the beam impacts the ZDC's, otherwise upon no collision the charged ion beams are guided around the ZDC's. The scatter plot is double valued in ZDC as the number of spectator neutrons is small in central events (when more of the neutrons interact) as well as in peripheral events (when more of the neutrons remained bound in the ion which is guided around the ZDC's).

To represent each centrality class of triggered interactions with a physical variable that is related to the energy produced in that class a geometrical model of nuclear interactions is used. The mean number of nucleons which participate in the collisions of different centrality classes is estimated in a 3 step process. Firstly a geometrical description of the nucleus like the Woods-Saxon density distribution is used, and various further assumptions in a “Glauber model” such as each projectile nucleon travels along a straight path through the target nucleus [27]; this step estimates the number of nucleons which are available for interaction as a function of the Au+Au impact parameter. Secondly the Wounded Nucleon Model (WNM) is used to estimate from the collision geometry the number of first struck or “participant” nucleons with which the multiplicity production scales in the model; this step together with the first step provides a relationship between the number of participant nucleons and impact parameter [16]. Thirdly a model for the relative probabilities of Au+Au interactions as a function of impact parameter is used; this step provides a relationship between impact parameter (and thus number of participant nucleons) and centrality percentages of events. Thus using together the geometrical model, participant nucleon model, and the model for probability of interaction with impact parameter provides a method to estimate the mean number of nucleons which “participate” $\langle N_p \rangle$ for any modeled centrality class 0-5%, 5-10%, ... of interactions. $\langle N_p \rangle$ is then associated with the average number of particles (or energy) produced in each centrality class of recorded events 0-5%, 5-10%, ... in the real data. The procedure to estimate participant nucleons is discussed further in Chapter 4.1, and the procedure which is used to bin events in centrality is given in Chapter 5.1. Figure 22 on page 164 shows the typical errors on the N_p determination. The results of a Monte Carlo simulation of Au+Au collisions using the 3-step model assumptions, and from simulating the BBC and

ZDC responses is shown in the BBC-ZDC centrality clock in the right plot of Figure 21 on page 164.

For an assumed impact parameter one can model $\langle N_p \rangle$, and how many of these experience multiple (2nd, 3rd, ..) collisions where the total number of binary collisions is represented by N_{coll}. If one assumes quarks interact with one another a quark-quark cross section is used as a model parameter rather than a nucleon-nucleon cross section and a determination of "quark participants," N_q, with impact parameter is obtained. N_p, N_{coll}, and N_q represent collision geometries and are not directly measurable quantities but determined only by modeling and simulation [27]. In this thesis labels used interchangeably are $N_p \equiv N_{\text{nuc-part}}$, $N_q \equiv N_{\text{quark-part}}$, and $N_{coll} \equiv N_{\text{binary collisions}}$.

The Au+Au data was divided into 5% wide centrality bins and the average energy produced, and magnitude of fluctuations about the average were examined over increasing centrality. It is worth noting here that after all background was removed the integrity of the centrality cuts remained relatively high; this can be observed in the distribution of events in centrality which remained effectively flat for both 62.4 GeV and 200 GeV Au+Au in Figure 23 on page 165 and Figure 24 on page 165. This is because the background occurs at low enough levels of 10^{-3}, and in the case of 200 GeV Au+Au data is distributed across all centrality classes. Thus it was not necessary to redefine the BBC nor ZDC centrality cut ranges after background removal.

3.3 62.4 GeV Au+Au background at 10^{-3}, identification and removal

This section discuses how the largest background component in the 62.4 GeV Au+Au data was identified and removed by discarding all events which occurred in the RHIC beam's bunch crossing region numbered 57 through 71 [7]. The background was present in the data at a rate of about 1 event in 800, specific to the peripheral centrality region, and is due to be due to events having an incorrect multiplicity in the PHENIX Pad Chambers. The cause was a scheduled Pad Chamber hardware reset, occurring once every 101 beam revolutions, affecting data which found its way into the collision centrality prescription.

The Centrality-by-BBC PercentileRecalReco version of the collision centrality prescription (see Chapter 3.2) described in [32] was used, and this utilizes an adjusted, or corrected beam-beam counters (BBC) charge sum. As the top plot in Figure 25 on page 166 shows the one dimensional inclusive BBC charge distribution does not appear unusual, however when E_T is plotted versus BBC charge a background problem and corrupted centrality is apparent in the peripheral bins, and this is seen in the bottom plot. The background shows up as gross distortions appearing 3 orders of magnitude down in the peripheral event semi-inclusive E_T distribution upper tails; the more central semi-inclusive distributions do not have this problem as the top plots in Figure 26 on page 167 show. The effect this has on the E_T fluctuations analysis is illustrated in the lower plots of Figure 26 on page 167.

3.3.1 Isolating the problem

To locate the source of the background approximately 45 million min-bias events were analyzed (approximately $\frac{2}{3}$ of the available data). The centrality prescription makes use of the Pad Chamber 1 (PC1) multiplicity represented by the nano-dst variable $npc1$, as a secondary centrality estimator to apply an offline adjustment, or "correction" to event BBC charge to make the BBC response appear more linear in centrality [32].

Events were selected and examined from above the diagnostic cut line shown in Figure 27 on page 168. Scatter plots were made of event multiplicity, energy, and charge as measured in one detector plotted against that measured in another detector. These bad events consistently have one hit in PC1 (as Figure 28 on page 169 shows), zero hits in PC2, (represented by $npc2 = 0$) and either one or two hits in PC3 ($npc3 = 0,\ 1$); and bad events are always present in any plot including either the adjusted-BBC charge or PC multiplicity, but not present in plots which do not include either.

3.3.2 Events with wrong pad chamber multiplicity corrupt centrality

The top plot in Figure 29 on page 170 shows that the number of BBC hits versus the raw BBC charge does not contain the background, but the(bottom plot shows the number of BBC hits versus the $npc1$-adjusted BBC charge does contain the background; this illustrates the source of the background is not the BBC but rather the pad chamber. The formulas in the centrality prescription which use the number of Pad Chamber 1 hits to apply the adjustment to the measured BBC charge are given below, where CN and CS are the North BBC and South BBC correction factors respectively, p_0, p_1, p_2, p_3, p_4, and k_{30} are constants [32]. One can see by the equations that an incorrect value of $npc1$ ruins the centrality determination on the event, and for these bad PC events ($npc1$ always equal to 1) results in classifying real central events as peripheral. Figure 30 on page 171 shows this result;

$$k = p_0 + (p_1 + p_2[npc1] + p_3[npc1]^2)(1 - e^{\frac{-npc1}{p_4}}) \tag{41}$$

$$CN = \frac{k}{k_{30}} e^{-k \times Zvertex} \tag{42}$$

$$CS = \frac{k}{k_{30}} e^{k \times Zvertex} \tag{43}$$

$$corrected\ BBC\ charge\ sum = \tag{44}$$

$$CN \times (measured\ north\ BBC\ charge) + (measured\ south\ BBC\ charge) \times CS.$$

The number of Drift Chamber (DC) tracks for the bad events was found to be correlated to what the EMC, BBC, and ZDC observed on the events, but not to the number of PC hits recorded (always being 0, 1, or 2). The fact that the bad events have a number of tracks which can be very large confirms that they have incorrect PC information. Next a bunch crossing histogram was filled for all events having the incorrect arrangement of 1 hit in PC1 with more than 20 DC tracks, and as Figure 31 on page 172 illustrates all these bad events appear within bunch crossing numbers 57 through 71. The bad events being limited to a specific bunch crossing region indicates the pad chamber fault occurs systematically over a specific portion of the RHIC beam revolution. The removal of beam test bunches was done prior, and after which only crossings numbered 57, 59, 62, 65, 67, 69, and 71 remained as affected out of the total of 55 non-test (or "physics") bunch crossings.

The Run-operations "GTM file" software algorithm specifies that during RHIC Run 4 a hardware reset of the PHENIX Pad Chambers front end module electronics performed to bleed off charge from the integrator occurred at a regular frequency of once in every 101 beam revolutions, and for a duration over bunch crossings 20 to 39. The PC Timing Control algorithm asserted a signal to block event triggers from being issued to the Pad Chamber over bunch crossings 20 through 59 during each beam revolution containing the reset; note that bunch crossing number 59 is close to number 57, the location where the bad PC data begins to appear — the first strong indication that the hardware reset is the cause of the bad data. Since bunch crossing number 72 is where the bad PC events no longer appear in the data sample, this apparently marks where the after-affects of the PC reset subside and the Pad Chamber is restored to a proper operation mode. In assuming the distribution of min-bias triggers is roughly equal over physics bunch crossings, an expected rate for these bad PC events to appear in the min-bias data would be $\frac{1}{800}$, or

$$expect \sim \frac{1\ reset}{per\ 101\ revolutions} \times \frac{7\ affected\ bunches}{55\ total\ bunches} \approx \frac{1\ corrupted\ event}{800\ minbias\ events}. \tag{45}$$

Using the PC hit signature of the bad data [$npc1 = 1$, $npc2 = 0$, ($npc3 = 1$ or $npc3 = 2$)], bad PC events were identified and removed at a rate of about $\frac{1}{750}$

$$identified\ as\ bad\ PC\ events \sim \frac{1\ event}{750\ minbias\ events}. \tag{46}$$

This confirmed that the PC hardware reset is the cause of the background problem. Based on this information it was judged that the signal blocking 40 bunch crossings is not long enough, and events recorded over those bunch crossings exposed during revolutions containing the reset have bad Pad Chamber information. As Figure 32 on page 173 shows there are not many events in the data, neither good nor bad, having zero hits to PC1, this is also the case in PC3; and all bad events have zero hits to PC2, thus a very likely explanation for the bad PC event signature of [$npc1 = 1$, $npc2 = 0$, ($npc3 = 1$ or $npc3 = 2$)] is the presence of one hot pad chamber cell in each of PC1 and PC3, and an additionally warm cell (i.e. sometimes hot) in PC3.

3.3.3 Cuts designed to remove the bad pad chamber data

Three different ways were evaluated to remove the background and each cut found to work reasonably well. The first cut method is to throw out bunch crossing region 57-71. This was the method used in the 62.4 GeV data analyses presented in this thesis. The second cut method is to throw out events having the signature [$npc1 = 1$, $npc2 = 0$, $npc3 = 1$ or $npc3 = 2$, $ndc > 2$], where ndc is the number of reconstructed tracks in the DC. The third cut method is, in a set of events having a number of DC tracks greater than 5 throw out the subset having [$npc1 = 1$, $npc2 = 0$, $npc3 = 1$ or $npc3 = 2$]; but for those events having 5 or less DC tracks together with [$npc1 = 1$, $npc2 = 0$, $npc3 = 1$ or $npc3 = 2$] loop over their tracks and throw out only those events where all their tracks have bad quality. The last two cut methods are more involved. Full details are given in [7].

3.4 200 GeV Au+Au background identification procedure

There are two dominant sources of background in the 200 GeV Au+Au data set and which are shown relative to one another in Figure 33 on page 173. The first (shown in blue) are late events for which the BBC's could not reconstruct a valid interaction time relative to the nominal RHIC beam bunch crossing time, but that had remained part of the minbias through the ZDC selection criteria. These events have a value of charge in one BBC arm relatively lower than that measured in multiple other detectors, and were found to contaminate centrality where the BBC is the principal measure. It is unclear what the source of this background is, however it has some characteristics like background due to two interactions in sequential bunch crossings which are mistakenly recorded as single events; yet this might not be the cause as the trigger detectors (BBC and ZDC) are designed to be much faster – with pico second resolution – than the 100 nano second time interval which elapses between sequential beam bunches. Little “satellite” bunches which are part of and closer to the actual beam bunch is another possibility. The background is in all but the most central semi-inclusive distributions and also in the trigger detectors. The second source of background (shown in red in Figure 33 on page 173) is pile-up of two interactions in a single bunch crossings which are mistakenly recorded as a single event. As in the case of the 62.4 GeV Au+Au background identifying the source and designing a cut was a considerable task, limited in its presentation here. Figure 34 on page 174, Figure 35 on page 174, Figure 36 on page 174, and Figure 37 on page 175 show $E_{T\ (\mathrm{EMC})}$ distributions in the different centrality classes both before (left) and after (right) the background cuts were applied.

To figure out the cause of the background and design cuts to remove it various physical variables of the minbias events were examined and compared. Specifically the PbSc EMC, the BBC, and the ZDC event information were used to make three different scatter plots: $E_{T\ (\mathrm{EMC})}$ vs. BBC charge, ZDC energy vs. BBC charge, and $E_{T\ (\mathrm{EMC})}$ vs. ZDC energy. Note that each one of the three scatter plots involves only two detectors, and not the third detector; this provides a way to check if the background appears in all 3 detectors simultaneously, to isolate its location and explore how it gets into the analysis results.

The plots in Figure 38 on page 176 are filled with 66 million events. They are ZDC energy vs. BBC charge before and after background removed, and Figure 39 on page 177 is a close up view after the background cuts. This scatter plot is used for centrality determination and thus it is apparent how displaced events corrupt centrality. Figure 40 on page 178 shows ZDC energy vs. $E_{T\ (\mathrm{EMC})}$, and Figure 41 on page 179 shows $E_{T\ (\mathrm{EMC})}$ vs. BBC charge, both before and after background removed – these plots were also used to determine the sources of background.

3.4.1 Events at 10^{-4} with no valid BBC trigger timing displaced in centrality

The first type of background identified appears at 10^{-4} in the minbias semi-inclusive distributions and are events which have a relatively low BBC charge in one arm. This happens in very late triggered events occurring beyond the 21 nsec BBC timing dynamic range, but which are accepted as minbias via the ZDC which has a larger timing dynamic range. Removing these events is easily done by limiting the selection from the minbias to keep only those events with a valid Zvertex as determined by the BBC; this works because in order for the BBC to have determined a Zvertex the event has to have a valid BBC timing.

Figure 42 on page 180 is the BBC charge (left plot) and ZDC energy (right plot) each plotted against their corresponding event trigger times, and included are all events before any background was removed. The BBC's can determine event trigger times at a limited ± 10.5 nsec relative to the RHIC beam clock nominal zero time, but the ZDC's have a larger timing dynamic range shown here out to ± 12 nsec. In Figure 43 on page 181 the left plot is also the ZDC energy vs. ZDC event trigger time but this time filled only with background events which were hand selected from the uncorrelated region within the green circle of the E_T vs. BBC charge scatter plot seen in Figure 41 on page 179. The ZDC shows this background to have the characteristic timing signature of about $|10|$ nsec (the reason this plot shows the background only at negative ZDC times is because to simplify the analysis a cut isolating only one ZDC arm was used). The right plot in Figure 43 on page 181 is the event trigger time as determined by the BBC for all events, and the underflow at -99 nsec is the default time this background is assigned. It is clear that this specific background has trigger times near and outside the BBC dynamic timing range. The left plot in Figure 44 on page 181 shows event BBC charge in the North arm vs. the South BBC arm. The background events are uncorrelated and located far from the central lobe.

3.4.2 Pile up double-events at $10^{-4} - 10^{-5}$: two events in same bunch crossing

The second type of background was identified as pile-up, meaning 2 Au+Au collisions occurring in the same bunch crossing but recorded by the BBC, ZDC, and EMC as a single collision. These were found to occur at a rate of about 1 event in $10^{-4} - 10^{-5}$ of the minbias semi-inclusive distributions. The first indicator that pile-up background was present was observing a class of events in the centrality-by-clock ZDC-BBC space having a distance from the clock origin approximately double the distance single interactions do, this can be seen in the middle plot of Figure 38 on page 176; the pile up is removed by throwing out events above the geometrical cut line in the figure. The placement of the cut line was chosen to maximize the background removal. This effectively removes the pile-up in the mid-central to most central collisions but fails to remove it in the peripheral region where it blends back into the single interaction part of that distribution.

Figure 45 on page 182 shows the number of events as a function of run-number sequence: the left plot was filled with all minbias events before the background was cut, and the right plot is filled only with background events hand selected from above the pile-up cut line drawn in ZDC-BBC space; both distributions are essentially flat. The run-numbers in used in this Figure were then placed in order of increasing beam luminosity, as seen in Figure 46 on page 182: the left plot is again the number of minbias events with no background cut, and the right plot is filled only with events selected from above the pile-up cut line drawn in ZDC-BBC space – this shows that the background grows faster with luminosity than does the minbias, a characteristic feature of pile-up, and a second indicator that the background is pile up. Figure 47 on page 183 is the ratio of pile-up events to minbias events as a function of (right plot) run-number sequence, and (left plot) luminosity. The background occurs at a rate of 1 event in 10^{-4} and the following calculation predicts that this should be its frequency of occurrence, and is a third indicator that the background is pile-up. The single Au+Au interaction rate $R_{\text{Au+Au}}$ for RHIC was introduced in Chapter 2.1 in terms of the average beam luminosity L and Au+Au cross section $\sigma_{\text{Au+Au}}$. Using the PHENIX minimum bias triggering system efficiency $\epsilon_{\text{trigger}}$, and ion beam bunch-crossing frequency b_{crossing}, the recorded event rate $R_{\text{Au+Au}}$ is expected as

$$\begin{aligned} R_{\text{Au+Au}} &= L(10^{26}\frac{1}{\text{cm}^2\text{s}}) \times \sigma_{\text{Au+Au}}(6.8 \text{ barns} \times 10^{-24}\frac{\text{cm}^2}{\text{barn}}) & (47) \\ &\times \epsilon_{\text{trigger}}(0.93) \times b_{\text{crossing}}(10^{-7}\frac{\text{s}}{\text{b.crossing}}) & (48) \\ &= 10^{-4} \text{ events per bunch crossing.} & (49) \end{aligned}$$

In other words one in every 10,000 bunch crossings of the beam produces a single Au+Au interaction observed in the minbias data. Thus pile-up of two Au+Au interactions in a single bunch crossing is expected to be within the collection of minbias data at the same rate of 10^{-4}, and this is in fact the rate observed in the data

$$R_{\text{pile up}} = 10^{-4} \text{ pile up events per minbias event.} \quad (50)$$

Note that head on or central events are more rare than grazing peripheral events and this affect is not accounted for in the above approximation.

The left plot in Figure 44 on page 181 is the BBC North vs. South plot and the pile-up are the correlated events extending to the highest BBC charge values;

the right plot is event ZDC energy in the North arm vs. that in the South arm where again the pile-up are the correlated events extending to the highest ZDC energies. It is unclear if the events appearing as strongly uncorrelated and far from the central lobe is background or not – coulomb dissociation contamination likely makes up some of these events.

The pile-up background events have a few features which were unexpected and are issues which remain unresolved: Figure 41 on page 179 shows $E_{T\ (\mathrm{EMC})}$ vs. BBC charge before and after background removed; note that the pile up is not evenly distributed around the main part of the distribution which corresponds to the single Au+Au interactions, but rather only about half of that distribution. It is not clear why this is but appears that (when comparing the pile-up to single interaction events) there is pile-up with twice the BBC charge and twice the E_T, and with twice the BBC charge and one times the E_T, but not with one times the BBC charge and twice the E_T. The left plot in Figure 48 on page 183 is the time the event was triggered as determined by the BBC's (vertical axis) vs. the time as determined by the ZDC's (horizontal axis); the right plot is the Zvertex as reconstructed in BBC timing (vertical axis) vs. the Zvertex as reconstructed in ZDC timing (horizontal axis). The pile-up appears in the correlated and very central parts of the two plots and not in the out-lier regions as expected; because of this it is not removable from the single interaction events using timing or Zvertex information at the nano-dst level where individual arm event times are not available. It's possible the pile-up might be removable from single interaction events in a plot of BBC (or ZDC) event time determined in the north arm vs. the event time determined in the south arm.

3.5 Electromagnetic calorimeter faulty PbSc tower removal

There are faulty PbSc towers which are dead (or off) and do not record event energy. There are faulty PbSc towers which are constantly reporting a false energy deposition, some which add an enormous amount of spurious energy into each event. The corruption to event-by-event E_T due to noisy or "hot" PbSc towers is serious and it was very important to remove it. Hot tower energy was removed in all 6 sectors for all analyses, and along with the dead towers were accounted for in the acceptance correction part of the mean E_T measurement. Sector West 3 was the worst sector with approximately 20% of its towers faulty. Figure 49 on page 184 are projections of sector West 3 showing the multiplicity distribution summed over several events before (left plot) and after (right plot) hot tower removal. The empty gaps in the left plot are the dead tower regions. The "Lego plots" in Figure 50 on page 185 show the multiplicity distribution in West 3 – the number of clusters is summed over all events and is indicated on the vertical axis. The 3 plots show views zoomed further in along the Z axis illustrating just how hot some towers in the sector are. Sector West 1 was the best sector having only 5% of its towers faulty. Each of the other four sectors had approximately 10% of its towers faulty.

The method of hot tower removal requires analyzing all events twice, the first time to identify faulty towers and to construct hot tower maps, which then become part of the analysis the second time (and every other time) those events are analyzed. The following procedure was used. The coordinates in the sector of the PbSc tower were recorded every time that tower was identified as the central tower in a cluster, and a representative entry placed in "tower cell" of a Lego plot made of the sector as shown in Figure 50 on page 185. Each entry then represents a particle shower and the entry was weighted by the central tower energy. Each sector's Lego plot is an energy deposition histogram filled for all clusters on all events used in the entire analysis. Next the energy weighted hits were used to fill a 1 dimensional histogram of energy-per-tower shown in the left plot of Figure 51 on page 186. A +3.5 sigma cut about this distribution mean was applied to remove hot towers; an additional cut was applied to remove all neighboring towers in a 3×3 tower area around every hot tower to reduce the likelihood of including hot tower energy in the data analysis. The location of dead towers and removed hot towers were recorded in a sector map which is shown in the right plot of Figure 51 on page 186. The bottom plot in Figure 51 on page 186 is the actual energy across all events used from the West 3 sector after the bad towers were removed. Figure 52 on page 187 and Figure 53 on page 187 are the Sector West 1 energy deposition Lego plot, energy per tower histogram, and resultant sector map, showing the before and after hot tower removal.

3.6 Global energy scale baseline: π^0 kinematics

The neutral pion decays to two photons $\pi^0 \to 2\gamma$ which are detected in the EMC, and the π^0 invariant mass, m_0, and transverse momentum, p_T, are determined using the nano-dst variables for EMC cluster energy and particle hit position. The π^0 mass is reconstructed using the equation relating the total energy, 3-momentum, and invariant mass [36]

$$E_{\text{total}}^2 = \vec{p}^{\,2} c^2 + m_0^2 c^4 = \vec{p}^{\,2} + m_0^2 \tag{51}$$

And in the notation $c \equiv 1$

$$m_0^2 = E_{\text{total}}^2 - \vec{p}^{\,2} \tag{52}$$

An equation for the π^0 3-momentum is obtained by summing the two photon momentum vectors:

$$\vec{p} = |\vec{p}|\hat{p} = \vec{p}_{\gamma_1} + \vec{p}_{\gamma_2} \tag{53}$$

and thus p_T for the π^0 is:

$$p_T = \sqrt{(p_{x,\gamma_1} + p_{x,\gamma_2})^2 + (p_{y,\gamma_1} + p_{y,\gamma_2})^2} \tag{54}$$

For the photon $m_\gamma = 0$ thus $|p_\gamma| = E_\gamma$, and energy can be used to determine the magnitude of momentum components; since the photon trajectories are not affected by the PHENIX central magnet $\vec{B}$-field the photon momentum vectors coincide with the two photon hit position vectors at the calorimeter, and after correcting for the Z-vertex using $z - z_{vtx}$:

$$\vec{p}_\gamma = |\vec{p}_\gamma|\hat{p} = E_\gamma \frac{\vec{x} + \vec{y} + \vec{z}}{\sqrt{x^2 + y^2 + (z - z_{vtx})^2}} \tag{55}$$

thus:

$$p_{x,\gamma_1} = E_{\gamma_1} \frac{x_1}{\sqrt{x_1^2 + y_1^2 + (z_1 - z_{vtx})^2}} \tag{56}$$

$$p_{x,\gamma_2} = E_{\gamma_2} \frac{x_2}{\sqrt{x_2^2 + y_2^2 + (z_2 - z_{vtx})^2}} \tag{57}$$

$$p_{y,\gamma_1} = E_{\gamma_1} \frac{y_1}{\sqrt{x_1^2 + y_1^2 + (z_1 - z_{vtx})^2}} \tag{58}$$

$$p_{y,\gamma_2} = E_{\gamma_2} \frac{y_2}{\sqrt{x_2^2 + y_2^2 + (z_2 - z_{vtx})^2}} \tag{59}$$

$$p_{z,\gamma_1} = E_{\gamma_1} \frac{z_1 - z_{vtx}}{\sqrt{x_1^2 + y_1^2 + (z_1 - z_{vtx})^2}} \tag{60}$$

$$p_{z,\gamma_2} = E_{\gamma_2} \frac{z_2 - z_{vtx}}{\sqrt{x_2^2 + y_2^2 + (z_2 - z_{vtx})^2}} \tag{61}$$

The π^0 invariant mass is obtained by summing the photon energies and vector momenta:

$$m_0^2 = E_{\text{total}}^2 - \vec{p}^{\,2} \tag{62}$$

$$= (E_{\gamma_1} + E_{\gamma_2})^2 - (\vec{p}_{\gamma_1} + \vec{p}_{\gamma_2})^2 \tag{63}$$

$$m_0 = \sqrt{(E_{\gamma_1} + E_{\gamma_2})^2 - ([p_{x,\gamma_1} + p_{x,\gamma_2}]^2 + [p_{y,\gamma_1} + p_{y,\gamma_2}]^2 + [p_{z,\gamma_1} + p_{z,\gamma_2}]^2)} \tag{64}$$

Note that m_0 can also be determined by using:

$$m_0^2 = E_{\gamma_1}^2 + E_{\gamma_2}^2 + 2E_{\gamma_1}E_{\gamma_2} - p_{\gamma_1}^2 - p_{\gamma_2}^2 - 2\vec{p}_{\gamma_1}\vec{p}_{\gamma_2} \tag{65}$$

$$= 2(E_{\gamma_1}E_{\gamma_2} - |p_{\gamma_1}||p_{\gamma_2}|\cos\theta_{1,2}) = 2(E_{\gamma_1}E_{\gamma_2} - E_{\gamma_1}E_{\gamma_2}\cos\theta_{1,2}) \tag{66}$$

$$m_0 = \sqrt{2E_{\gamma_1}E_{\gamma_2}(1 - \cos\theta_{1,2})} \tag{67}$$

where $\theta_{1,2}$ is the separation angle between $\vec{p}_{\gamma_1}$ and $\vec{p}_{\gamma_2}$ (which is also the separation angle between the two photon hits) [22]:

$$\cos\theta_{1,2} = \frac{x_1 x_2 + y_1 y_2 + (z_1 - z_{vtx})(z_2 - z_{vtx})}{\sqrt{x_1^2 + y_1^2 + (z_1 - z_{vtx})^2}\sqrt{x_2^2 + y_2^2 + (z_2 - z_{vtx})^2}} \tag{68}$$

The reconstructed π^0 mass peaks were used for a correction to cluster energy measured in each EMC sector. The actual π^0 corrections were done previously by the PHENIX Photon Working Group experts (see for example [6] for the case of 62.4 GeV data). In this thesis the π^0 mass was reconstructed in each sector, for each analysis (Au+Au, $p+p$, and d+Au), using the procedure outlined in [6], as a double check and ultimately as a gauge for absolute energy scale accuracy on the event – note that using the π^0 mass peak works to gauge energy per particle, but by itself cannot gauge energy produced on the event where multiplicity is also a factor. Figure 54 on page 188, Figure 55 on page 188, and Figure 56 on page 189 are the π^0 mass reconstructions for 200 GeV Au+Au. To obtain the mass peak Gaussian fits were applied with a single exponential background subtraction for mid to low p_T events and a double exponential background subtraction for higher p_T events. The π^0 peak is expected in the EMC at 138 MeV which is about 3 MeV higher than the actual mass due to known detector systematic affects. Figure 57 on page 190 shows the peak to within 1% accuracy in the peripheral collisions but only about 2% accurate in central collisions. This is thus the percent accuracy in the global scale E_T measurement on each event. Figure 58 on page 191 are π^0 mass reconstructions for 62.4 GeV Au+Au. The peaks were reconstructed with the nano-dst variable of photon energy labeled “ecore” as opposed to the cluster energy variable “e” which was used for event E_T reconstruction as discussed in Chapter 2.2.2. ecore has a higher probability of being a photon than does e and thus better to use for π^0 reconstruction. The % difference in measured to absolute value of e versus measured to absolute value of ecore was reported previously by PHENIX to be negligible, and thus the mass peak is usable to calibrate event E_T. In summary, the peaks were reconstructed with the following selection and cuts:

1. The nano-dst variable of photon energy labeled “ecore” was used with no energy scale corrections beyond those inherent in the PHENIX data analysis offline Master ReCalibrator.

2. Photon pairing was limited (by preference) to individual sectors, however the reconstructed π^0's were collected in all 6 sectors.

3. Photon energy asymmetry was limited to a difference of < 0.8.

4. Photon spread was limited to $\chi^2 < 3$.

4 $\langle E_T \rangle$ PRODUCTION AND FLUCTUATIONS

4.1 E_T and multiplicity production – model of nucleons or quarks

The first physics analysis conducted in this thesis is a test to see if the Wounded Nucleon Model (WNM) [16] accounts for the scale of E_T production in relativistic collisions. Wounded nucleons are also referred to in the literature as *participant nucleons*. A related application of the model was tested for *participant quarks*. This is done using the average values for events separated into centrality classes of data. In Chapter 3.2 an introduction was given about how modeling the nuclear geometry of the collision is used, and also about dividing up the data in centrality and representing each class of the measured data with a mean number of participants. Immediately following is a description of the participant model, and at the end of this Section is a standard procedure which is used to bin events in centrality.

The WNM model counts the number of nucleons which are expected to contribute to the scaling of the multiplicity production, and describes low collision-energy p+A multiplicity and E_T data well. First the relationship between produced energy and multiplicity is examined. Event E_T is the sum of all the individual particle energy as was discussed in chapter 2.2.2. Energy production in nuclear interactions rises with collision impact due to an increase in the multiplicity produced and apparently not due to any significant changes in the average energy per created particle, this can be seen in the plots of Figure 59 on page 193. The particle energy as measured in the PbSc calorimeters (cluster E_T) does slightly rise with centrality however this is not understood and some believe it to be a systematic artifact of the calorimeter's limitations, such as cluster merging, or imperfect response as a function of transverse momentum p_T (it is noted however that a small rise in charged particle p_T with impact is also observed by PHENIX). Thus mid-rapidity "mean energy production" and "mean particle production" in relativistic nuclear interactions are very much correlated; from this simple perspective if the WNM describes mean multiplicity production over impact parameter it would also describe $\langle E_T \rangle$ production over impact parameter. The model was evaluated by comparing the average $\langle E_T \rangle$ in event-by-event $p + p$, d+Au, and Au+Au distributions as a function of centrality.

Such models can be used to examine average particle production for a select class of events in impact parameter and can also be used to examine an entire event-by-event multiplicity inclusive distribution. Both applications of the model are discussed as they are relevant to the study of this thesis.

In simple terms the WNM makes the following two assumptions: firstly, that the multiplicity scales with the number of nucleon-nucleon collisions when for one of the nucleons it was a first-time it was involved in any collision; and secondly, the multiplicity is proportional to half the number of first-struck nucleons, not the number of collisions. A nucleon is free to continue striking other nucleons, and those then produce additional multiplicity on the event. Thus using this model together with a geometrical description of the nucleus proposes a way to account for the multiplicity production. The following example is an application of the WNM for p+A interactions where, for example, A represents a nucleus (like a Au ion), and p represents a proton. The number of nucleons in A which participate is represented by n and thus in a p+A collision the total number of participant nucleons is $n+1$. Measured multiplicity in p+A is compared to that in $p+p$ to evaluate if they are merely scale factor multiples of each other. For example when $n=4$ (here the event-by-event "average" notation $\langle\rangle$ is left off of the multiplicity variable, N, to simplify notation)

$$N^{p+\mathrm{A}}_{\mathrm{multiplicity}} = \frac{n+1}{2} N^{p+p}_{\mathrm{multiplicity}} = \frac{4+1}{2} N^{p+p}_{\mathrm{multiplicity}} = 2.5 N^{p+p}_{\mathrm{multiplicity}}. \tag{69}$$

where $n+1 \equiv N_{\mathrm{nuc-part}}$ is the number of participant nucleons in this example p+A collision. The interesting result is that when 4 nucleons in A are struck, the multiplicity production expected is not 4 times that of a $p+p$ collision, nor 2 times that, but rather 2.5 times as much. Thus the formula relating multiplicity production across the different species collisions is

$$N^{p+\mathrm{A}}_{\mathrm{multiplicity}} = 0.5 N^{p+\mathrm{A}}_{\mathrm{nuc-part}} N^{p+p}_{\mathrm{multiplicity}}, \tag{70}$$

where $N^{p+\mathrm{A}}_{\mathrm{nuc-part}}$ is estimated from a model of the nuclear geometry of A in the collision, together with the model for counting participant nucleons. This was shown to work very well in low energy fixed target experiments a few decades ago [1], and this thesis evaluates it in higher energy relativistic collider experiments.

For Au+Au $N^{\rm Au+Au}_{\rm nuc-part}$ is estimated as a function of Au+Au impact parameter using the nuclear geometry model, and then mean values $\langle N^{\rm Au+Au}_{\rm nuc-part}\rangle$ are used to normalize the average multiplicity measured in different centrality classes of data corresponding to the same impact parameter. Multiplicity in Au+Au is compared to $p+p$

$$\langle N^{\rm Au+Au}_{\rm multiplicity}\rangle = 0.5\langle N^{\rm Au+Au}_{\rm nuc-part}\rangle\langle N^{p+p}_{\rm multiplicity}\rangle, \tag{71}$$

$$\frac{\langle N^{\rm Au+Au}_{\rm multiplicity}\rangle}{0.5\langle N^{\rm Au+Au}_{\rm nuc-part}\rangle} = \langle N^{p+p}_{\rm multiplicity}\rangle. \tag{72}$$

In $p+p$ collisions the only allowed number of nucleon participants is $n=2$, thus

$$\frac{\langle N^{p+p}_{\rm multiplicity}\rangle}{0.5\times(n=2)} = \langle N^{p+p}_{\rm multiplicity}\rangle, \tag{73}$$

and the $p+p$ collision is a fundamental element which can be evaluated in a prediction of multiplicity production in larger collision systems. Each proton contains 3 valence quarks and this then introduces a more fundamental mechanism for multiplicity production which is used in a quark participant framework. The computation of the number of participant nucleons from the geometrical model of the nucleus was not performed in this thesis work, rather the official PHENIX collaboration results were utilized [37], [27], [18]. However a brief and general description of the formulation used by PHENIX and others to estimate $N_{\rm nuc-part}$ as a function of impact parameter is presented here (see [37] for details). The Woods-Saxon geometrical model for the density of the nucleus is utilized and is given by

$$\rho(r) = \frac{\rho_0}{1 + e^{(r-R)/d}}, \tag{74}$$

where ρ_0 is a constant density term, r the distance out from the center of the nucleus, d a diffuseness parameter, and R the nuclear radius estimated from the atomic weight A of the nucleus, $R = (1.19A^{1/3} - 1.61A^{-1/3})$ fm. Ranges for the various input parameters ρ_0, R, and d are assumed and an associated error determined; typical values are $R = 6.38$ fm, and $d = 0.54$ fm. To estimate the number of participants on an A+B collision where A and B are the mass numbers of the two nuclei, as a function of impact parameter b, for example in the Nuclear Overlap Model [21], [28], and [19]

$$N^{\mathrm{A+B}}_{\mathrm{nuc-part}} = \int d^2 s T_A(\vec{s}) \left[1 - \left[1 - \frac{\sigma_{NN} T_B(\vec{s} - \vec{b})}{B}\right]^B\right] \tag{75}$$

$$+ \int d^2 s T_B(\vec{s}) \left[1 - \left[1 - \frac{\sigma_{NN} T_A(\vec{s} - \vec{b})}{A}\right]^A\right], \tag{76}$$

where $T(b) = \int dz\ \rho_A(\sqrt{b^2 + z^2})$ is a "thickness function" for the hadronic media traversed, and $[1 - \sigma_{NN} T_A(b)/A]^A$ is the probability a nucleon will pass through without interacting. The nucleon-nucleon cross section $\sigma_{NN} = 42$ millibarns (mb, or mbarn) is typically used.

In a related application of the model the number of participant quarks is obtained $N^{\mathrm{A+B}}_{\mathrm{nuc-part}} \to N^{\mathrm{A+B}}_{\mathrm{quark-part}}$ by making substitutions into the integral estimation for participants. The following example was obtained from [21], [28], and [19]. In a nucleon-nucleon collision if one quark-quark collision occurs, the other quarks remaining spectator quarks, only part of the energy is spent in multiplicity production

$$\sqrt{s_{qq}} \sim \frac{\sqrt{s_{NN}}}{3} \tag{77}$$

The actual number of quarks per nucleon which participate has to be estimated from a model, and at RHIC energies was calculated at about 1.2 to 1.3. In a Au+Au collision more than one quark per nucleon interacts because, due to the large nucleus size those which would have been spectator quarks now interact with different target nucleons. In the calculation of the cross section one takes into account the ratio of the radius of the quark to the radius of the nucleon $(r_q/R_N)^2$. In the quark constituent estimation a value of $(r_q/R_N)^2 \sim 1/9$ was utilized [21]. Note that the integral over the collision geometry involves the thickness function which depends on the density distribution now in the quark framework. Thus in the integral $N^{\mathrm{A+B}}_{\mathrm{nuc-part}} \rightarrow N^{\mathrm{A+B}}_{\mathrm{quark-part}}$ the corresponding three substitutions are made

$$\rho_0 \rightarrow 3\rho_0, \tag{78}$$

$$A \rightarrow 3A, \quad B \rightarrow 3B \tag{79}$$

$$\sigma_{NN} \rightarrow \sigma_{qq}, \text{ where } \sigma_{qq} \sim \sigma_{NN} \times (r_q/R_N)^2 \sim \frac{\sigma_{NN}}{9} = 4.56 \text{ mbarn.} \tag{80}$$

These substitutions into the integral provide the relationship between quark participants and nucleon participants, and this shape is illustrated in the top plot of

Figure 67 on page 201. In terms of E_T Equation 72 takes the analogous form

$$\frac{\langle E_T^{\mathrm{Au+Au}}\rangle}{0.5\langle N_{\mathrm{nuc-part}}^{\mathrm{Au+Au}}\rangle} = \langle E_T^{p+p}\rangle, \tag{81}$$

and in the quark participant estimation in the Nuclear Overlap Model equation 81 becomes

$$\frac{\langle E_T^{\mathrm{Au+Au}}\rangle}{\langle N_{\mathrm{quark-part}}^{\mathrm{Au+Au}}\rangle} = \frac{\langle E_T^{p+p}\rangle}{\langle N_{\mathrm{quark-part}}^{p+p}\rangle}. \tag{82}$$

Standard procedure which is used to bin events in centrality

Thus we use a model to estimate the number of participants for centrality classes of events in percentiles of impact parameter. Now we need a binning method to shuffle the data into centrality classes of events. The definition of centrality was introduced in Chapter 3.2. For PHENIX Run 4 estimates on the part of the total cross section which was observed by the minimum bias trigger were, for 200 GeV Au+Au 93% $\sim \pm 3\%$ (which involved the ZDC and BBC detectors together), and for 62.4 GeV Au+Au 83.7% $\pm$ 3.2% [32] (which was limited to the BBC detectors). Although a limited part of the cross section is observed the centrality classes that the events are shuffled into are percentiles relative to the total cross section; therefore although each 5% wide distribution of events has the same number of events, that number of events is more than 5% of the recorded events. The following example using 62.4 GeV data illustrates how events are binned in centrality classes. The total number of recorded events in the inclusive distribution measured is N_{events}, and to divide them up into 5% wide bins, or classes, the following number of events are put into each bin

$$0.05 \times \frac{100\%}{83.7\%} \times N_{events} = 0.06 \times N_{events} \tag{83}$$

It is estimated that the part of the cross section we do not observe corresponds to the most peripheral events, which in turn are assumed to have the lowest BBC charge in the inclusive event-by-event BBC charge distribution. The BBC distribution is divided up to categorize events in centrality for the other detectors; therefore the charge range along the BBC distribution, starting from the highest charge, which contains $0.06 \times N_{events}$ events defines the top 5% centrality class, and so on.

4.1.1 The E_T distribution – described by the participant model

The Wounded Nucleon Model uses a geometrical picture to estimate the number of participants in the interaction as a function of impact parameter, which are then used to normalize the semi-inclusive multiplicity (or E_T) production measured in binned centrality classes of events, to evaluate the model. Another way to use the Wounded Nucleon Model is as functions in n convolutions of an E_T inclusive distribution made from a small and fundamental collision system such as $p + p$; for example $n = 197$ convolutions would be required to recreate an E_T inclusive distribution of the larger collision system ^{197}Au+^{197}Au. A more detailed discussion of the inclusive E_T distribution is useful here to understand how the nuclear geometry models are used to describe that distribution. Event-by-event p+A inclusive and A+A semi-inclusive E_T distributions have been extensively studied and are known to be fit well by the gamma distribution

$$f_\Gamma(E_T, p, b) = N\frac{b}{\Gamma(p)}(bE_T)^{p-1}e^{-bE_T}, \tag{84}$$

which includes the term N for scale normalization, the gamma function Γ, a power law term with shape parameter p (not to be confused with the p denoting a proton collision), and an exponential term with shape parameter b ($p,\ b > 0,\ 0 \leq E_T \leq \infty$) [41]. The first two moments of a distribution are the mean value denoted by μ, and the RMS width denoted by σ, and characterize the distribution. The gamma distribution parameters of p and b provide these first two moments

$$\langle E_T \rangle = \frac{1}{N_{\text{events}}}\sum_{i=1}^{N_{\text{events}}} E_{Ti} \tag{85}$$

$$\mu \equiv \langle E_T \rangle = \frac{p}{b}, \quad \sigma \equiv \sqrt{\langle E_T^2 \rangle - \langle E_T \rangle^2} = \frac{\sqrt{p}}{b}, \tag{86}$$

Products of these moment's are used in the fluctuations analysis and are

$$\frac{\sigma}{\mu} = \frac{1}{\sqrt{p}}, \quad \frac{\sigma^2}{\mu} = \frac{1}{b} \tag{87}$$

and alternatively

$$p = \frac{\mu^2}{\sigma^2}, \quad b = \frac{\mu}{\sigma^2}. \tag{88}$$

The $p + p$, d+Au, and semi-inclusive Au+Au measured here were all fit to gamma distributions. The gamma distribution is asymmetric unlike the symmetric and more familiar Gaussian distribution, and has an exponentially shaped high E_T tail. A fundamental reason why the E_T distribution is asymmetric is due to the fact that production of negative energy is not possible, thus the inclusive distribution is one-sided (no events less than zero energy) and fluctuations add to the upper E_T tail. The physical processes in nuclear interactions show up as characteristic features in the E_T distribution, and these are described well by the two functions in the gamma distribution

$$E_T^{p-1} \text{ and } e^{-bE_T}. \tag{89}$$

The features are best seen on a log ordinate scale. Figure 60 on page 194 shows the 200 GeV Au+Au inclusive and semi-inclusive E_T plots. In the inclusive distribution the bulk of the events produce relatively low multiplicity and thus event yield is highest at low E_T; there is an initial drop in yield (or fall-off) with energy, followed by a broad plateau where the yield decreases only slightly with energy, a rolling turn downward called the "knee", and finally a sharp exponential drop. Most events are of low energy as grazing collisions are much more probable than high impact collisions. In A+A collisions the number of interacting nucleons varies according to impact parameter thus the inclusive distribution contains events of all collision centralities and overlapping fluctuations in energy production, these events fill the plateau region. The knee is where the number of available nucleons begins to saturate, and the exponential drop corresponds to the physical cut off where no more energy can be produced. The sharpness of the drop depends on fluctuations in energy production – since energy on the event is the sum of all the individual particle energy E_T contains fluctuations from both multiplicity production and from energy per particle production.

Convolution models are used to determine what the underlying interaction is which accounts for inclusive multiplicity (and associated energy) production in nucleus collisions: projectile nucleons, projectile+target nucleons, wounded nucleons, multiple binary collisions, or quark collisions. The procedure is to fit a measured inclusive distribution produced by the events of a small collision system (where few nucleons are involved), and to convolve this fit to try and recreate the measured inclusive distribution of a larger collision system (where more nucleons are involved). If the distribution made of a large collision system is no more than the sum of random combinations of an underlying distribution (that of the smaller collision system), then convolutions are useful. Simple convolutions work when the only thing which is being added is more of the same type of nuclear collisions.

The number of summed convolutions required to recreate one distribution from another distribution is the difference between the atomic masses, and each successive convolution (1, 2, 3, ...) is weighted with model dependent terms. The WNM and the Additive Quark Model (AQM) [17] use a modeled number of participant nucleons, and participant quarks respectively, and have been shown to recreate larger species E_T distributions; Figure 61 on page 195 and Figure 62 on page 196 show that convolutions of a gamma distribution from the fit of a fixed target ^1p+Au distribution reproduces O+Cu and O+Au distributions at 14.5

GeV/nucleon (measured in $1.25 < \eta < 2.44$), and also reproduces O+Pb at 200 GeV/nucleon [41], [1] and [10], where these energies are that of the beam on the fixed target. The convolved ^1p+Au distribution describes the heavier species data very well demonstrating that at low beam energy the fundamental mechanism for E_T production are wounded nucleons.

If a gamma distribution which is parametrized by p_0 and b_0 is convolved n successive times the result is a higher order gamma distribution which is parametrized by p and b, and given by

$$f_n(E_T, p, b) = N \frac{b_0}{\Gamma(np_0)} (b_0 E_T)^{np_0 - 1} e^{-b_0 E_T}, \tag{90}$$

where $p = np_0$ and $b = b_0$ (is unchanged). The distribution moments scale with the $n-$fold convolution as

$$\mu_n = \frac{np_0}{b_0} = n\mu_0, \quad \sigma_n = \frac{\sqrt{np_0}}{b_0} = \sqrt{n}\sigma_0, \tag{91}$$

and the combinations of moments which measure fluctuations

$$(\frac{\sigma}{\mu})_n = \frac{1}{\sqrt{np_0}} = \frac{1}{\sqrt{n}} \frac{\sigma_0}{\mu_0}, \quad (\frac{\sigma^2}{\mu})_n = \frac{1}{b} = \frac{1}{b_0}; \tag{92}$$

the parameters of the distribution expressed in terms of the moments are

$$p = \frac{\mu^2}{\sigma^2} = n\frac{\mu_0^2}{\sigma_0^2} = np_0, \quad b = \frac{\mu}{\sigma^2} = \frac{\mu_0}{\sigma_0^2} = b_0. \tag{93}$$

This illustrates that the gamma distribution mean and RMS width evolve proportionally to the number of convolutions of the underlying distribution n, and to

$\sqrt{n}$ respectively. The remaining question is what is n in relativistic interactions? n parametrizes the multiplicity production and this thesis explores whether n is the number of nucleon participants or quarks participants.

For completeness the mathematical formulation of one such convolution model which describes E_T production at low $\sqrt{s_{NN}}$ energies is inserted here. In the Wounded Projectile Nucleon Model (WPNM) the probability (or yield) for an event of given E_T to be produced in a B+A collision is given by [41]

$$(\frac{d\sigma}{dE_T})_{\mathrm{WPNM}} = \sigma_{BA} \sum_{n=1}^{B} \omega_n P_n(E_T) \tag{94}$$

where σ_{BA} is the measured B+A cross section in the detector, ω_n is the relative weight or probability for n of the B projectile nucleons to participate in the reaction, and $P_n(E_T)$ is the predicted E_T distribution on the detector when n projectile nucleons independently participate. Each sequential term ($n = 1, \ldots,$ B) of $P_n(E_T)$ contained in the sum $\frac{d\sigma}{dE_T}$ involve ($i = 0, 1, 2, \ldots,\ n$) recursive convolutions of the measured fundamental reaction, f_1, obtained from fitting an $n = 1$ projectile distribution

$$P_n(E_T) = \sum_{i=0}^{n} \frac{n!}{(n-i)!i!} p_0^{n-i}(1-p_0)^i f_i(E_T) \tag{95}$$

$$f_i(E_T) = \int dE'_T f(E'_T) f_{i-1}(E_T - E'_T), \text{ and } f_0(E_T) = \delta(E_T) \tag{96}$$

The calculated fundamental E_T distribution, $P_1(E_T)$, contains the measured probability p_0 for the 1-participant elementary collision, f_1, to have resulted in zero multiplicity in the detector's limited acceptance:

$$P_1(E_T) = (1 - P_0) f_1(E_T) + p_0 \delta(E_T). \tag{97}$$

4.1.2 E_T distribution and distribution mean – prior results

In summary, results obtained in the late 1980's and early 1990's on the AGS at Brookhaven National Laboratory, at CERN, and at Fermi National Accelerator Laboratory illustrated the following: at $\sqrt{s_{NN}} = 5$ GeV (AGS) the WPNM works at mid rapidity, but the WNM over-predicts indicating that in low energetic collisions the projectile nucleons themselves account for multiplicity production; at $\sqrt{s_{NN}} = 20$ GeV (CERN/Fermilab) the WNM works to account for multiplicity production as originating from each first-struck nucleon, whether it be in the projectile or in the target; and finally, at $\sqrt{s_{NN}} = 31$ GeV the WNM under-predicts leading to the speculation that quark-quark interactions may play a dominant role [41].

The investigation to determine which underlying interaction accounts for multiplicity (and associated energy) production in relativistic collisions continues and recent RHIC results look promising. Early PHENIX analyses of $\langle E_T \rangle$ and $\langle N_{\text{ch tracks}} \rangle$ in Au+Au collisions at 19 GeV, 130 GeV, and 200 GeV are shown in: Figure 63 on page 197 [2], Figure 64 on page 198 [3], Figure 65 on page 199 [4], and Figure 66 on page 200 [4]. In Figure 63 on page 197 the points in the bottom plot are the mean multiplicity values taken from the semi-inclusive distributions, four of which are shown (in their raw measured form) in the middle plot; each point is normalized by the modeled number of mean participant nucleons as described earlier in this Chapter. The fact that the points illustrate a rising trend in centrality suggest the modeled number of participant nucleons does not account for the multiplicity production at 130 GeV. Likewise the points in the bottom left plot of Figure 64 on page 198 are the normalized mean E_T measurements at 130 GeV; these were taken from the semi-inclusive raw $E_{T\ (\mathrm{EMC})}$ distributions shown in the top plot of that Figure, corrected as discussed in Chapter 2.2.2, and normalized by the modeled number of mean participant nucleons. Again there is a rising trend in centrality. The bottom panels in Figure 65 on page 199 show the mean multiplicity and E_T measurements at 19 GeV, 130 GeV, and 200 GeV, normalized to participant nucleons, all have rising trends. Thus the Wounded Nucleon Model which was used here to estimate participant nucleons does not describe the multiplicity nor energy production at mid-rapidity in RHIC relativistic interactions. The top left panel (and right panel) in Figure 66 on page 200 illustrates that the scale dependency E_T (and multiplicity) has on centrality is essentially the same – to within the systematic error – for the different energies. The bottom left panel illustrates the E_T and multiplicity have the same scaling with centrality.

The multiplicity production per participant nucleon measured by PHOBOS in 130 GeV and 200 GeV Au+Au showed similar results as PHENIX; these however were re-evaluated in the constituent-quark framework first by Eremin and

Voloshin [21] in year 2003. This method was described by equation 76 together with equations 78, and 80 presented earlier in this Chapter. The top plot in Figure 67 on page 201 gives their model estimates for the relationship between participant quarks to participant nucleons for the two different choices of σ_{qq} of 4.56 mbarn and 6 mbarn. Note that for these choices of the quark-quark cross section, even in the most central collisions, the number of quark participants never is three times the number of nucleon participants. The bottom plot in the Figure shows the quark framework better explains the mid-rapidity multiplicity production. After the Eremin and Voloshin paper others quickly renormalized multiplicity and E_T mid-rapidity data in the quark framework.

Figure 68 on page 202 is a recent model calculation for the number of constituent quarks for various Au+Au energies, and also for $p+p$ collisions estimated by the PHOBOS collaboration in a very similar fashion as was done by Eremin and Voloshin [35]. Figure 69 on page 203, and Figure 70 on page 204 are PHOBOS multiplicity results normalized in both the nucleon and quark models, illustrating the quark-constituent model which describes the $\langle N_{\text{ch tracks}}\rangle$ production well at mid-rapidity, does not describe the data in the forward and backward (beam) directions, where the WNM does a better job [34]. The reason for this has not yet been thoroughly explained. Figure 71 on page 205 is a quark participant renormalization of midrapidity multiplicity and also E_T data in A+A collisions from SPS to RHIC energies, using the model as did Eremin and Voloshin; the results illustrate the quark framework better explains the production [28]. Finally Figure 72 on page 206 illustrates that in the constituent quark framework (again an application like that by Eremin and Voloshin) the multiplicity production at mid-rapidity in $p+p$, Au+Au, and Pb+Pb collisions, at lower (SPS) energies, and also at relativistic energies all fall on the equation of a logarithmic line [19]. This result demonstrates that the multiplicity production per quark is proportional across systems and energies.

In this thesis mid-rapidity $\langle E_T \rangle$ was examined in the WNM and quark participant model for Au+Au at 200 GeV and 62.4 GeV, and results illustrate the quark framework better describes the data. $p + p$ and d+Au 200 GeV $\langle E_T \rangle$ was examined in the WNM and compared to Au+Au; some correction factors for $p+p$ and d+Au are still needed, however initial indication suggests production in Au+Au might scale with that in $p + p$ and d+Au.

4.2 Fluctuations over centrality – search for the QGP

The second goal of the thesis is examination of fluctuations in E_T production over collision centrality for a QGP phase transition signature. The third goal of the thesis (discussed in the next section) is examination of fluctuations in E_T production over geometric $\Delta\phi$ acceptance for spatially correlated particle emission. Centrality and acceptance are different "topologies" over which E_T production would increase barring any change in the internal dynamics of the collisions. For example E_T events are measured in different acceptances and each acceptance comprises a class of events of that topology. The event-by-event distributions are examined by looking for non-random behavior in the evolution of the relative width $\frac{\sigma}{\mu}$, and the scaled variance $\frac{\sigma^2}{\mu}$.

It is well known that there are interactions in relativistic collisions which produce an atypical amount of multiplicity and E_T on the event, such as jet production [11] from hard quark-quark interactions, and expansion patterns in elliptic flow [38]. Figure 73 on page 207, and Figure 74 on page 208 illustrate that the fluctuations due to jets are, although small, more dominant in higher energy interactions [5], [30]. The presence of such known fluctuations in the E_T distributions, or absence there of, was not evaluated in the work presented here; in a future and more thorough search for a fluctuation signature of a QGP phase transition these affects should be identified and monitored over centrality. References which discuss QGP phase transition induced fluctuations are [24], and [26].

It is useful to discuss some basic properties of distributions such as the fundamental Poisson distribution [13], and the symmetric Gaussian distribution [13], followed by properties of the gamma distribution which fits E_T [41]. If the outcome of several repeated measurements are identical the event-by-event distribution is nothing more than a delta function. Random and/or dynamic fluctuations produce a distribution. The quantity being measured in a histogram of events is often called the abscissa x, and the number of times it occurs called the ordinate y. A

Poisson distribution describes particular outcomes of sharp events occurring in a continuum, and has the property that its standard deviation equals the square root of its mean $\sigma = \sqrt{\langle x \rangle} \equiv \sqrt{\mu}$ (see equation 86). Thus if an event-by-event distribution for one class of events fits a Poisson distribution then $\frac{\sigma^2}{\mu} = 1$ for that distribution representing that specific class of events; if the evolution of fluctuations over a topology remain purely random then $\frac{\sigma^2}{\mu}$ remains valued at 1 over that topology. A Poisson distribution can be asymmetric about its mean and have a characteristically long upper tail – in this case the mean is not equal to the mode (the mode, x_{mode}, is the value of x corresponding to y_{max}).

In the limit when μ becomes "large" the Poisson distribution tends to a Gaussian distribution, also having $\sigma = \sqrt{\mu}$, which can be used as an approximation; how large a value of μ depends on the agreement one requires. The Gaussian distribution has various notable properties: it is a bell-shaped curve symmetric about μ; the magnitude of σ determines its width; changing the origin and/or scale reduces any Gaussian distribution to a standard form; $x = \mu \pm \sigma$ are inflexion points in the shape of this curve, and also correspond to where $y = 0.61 \times y_{\mathrm{max}}$. The mean, the mode, and the median are all equal (the median, x_{median}, is the middle value of x along the abscissa). A distribution produced by the combined effects of many independent variables will be approximately a Gaussian regardless of the individual distributions of the independent variables. The most central E_T distributions in Figure 83 on page 219 are gamma distributions but are more symmetric in shape as E_T has become very large. Measurement errors are also well described by the Gaussian distribution and individual measurements are usually quoted to within an error referenced in multiples of σ: for the Gaussian distribution 75% of events fall within $\pm 1\sigma$ of the mean, 95% within $\pm 2\sigma$, and 99.5% within $\pm 3\sigma$. For repeated measurements if in the limit the probability of the outcome of interest is small the uncertainty of the result scales with $1/\sqrt{N}$ for the N measurements.

In Chapter 4.1 it was stated that the inclusive $p+p$ E_T distribution and semi-inclusive Au+Au E_T distributions in centrality fit the gamma distribution which has parameters p and b; and that in summing n convolutions of a gamma distribution *in purely random* combinations an n^{th} order gamma distribution is produced with the moments given by Equations 91, 92, and 93; in these equations the number of summed convolutions, n, could be that describing the internal dynamics of the collision over centrality, that is as impact parameter becomes small. An important conclusion here is that like with the Poisson distribution of random-only fluctuations the gamma distribution, added in random combinations, preserves $\frac{\sigma^2}{\mu}$ = constant. In the case of changing dynamical fluctuations $\frac{\sigma^2}{\mu}$ would not remain constant.

It should be noted for completeness that multiplicity is a dimensionless variable and so is its width σ, thus its scaled variance $\frac{\sigma^2}{\mu}$ is also dimensionless. However E_T has a dimension (typically MeV or GeV) and thus so does the magnitude of its scaled variance $\frac{\sigma^2}{\mu}$, making direct comparison of the E_T and multiplicity scaled variance measurements a bit tricky. The relative width $\frac{\sigma}{\mu}$ is dimensionless and therefore can be used in a dimensionless comparison of E_T and multiplicity fluctuations.

Modeled location of a QGP phase transition

QGP formation is expected to occur at collision energy densities between 1 and 3 GeV/fm^3 [38], and a model (see Equation 100) is used to estimate the energy density from the E_T produced on the event. Mean E_T measurements thus indicate where dynamical fluctuations might be located in collision centrality. It is useful to discuss here the physical scales obtained in RHIC interactions, such scales where the quantum description is appropriate. In quantum theory an exchange of a boson, which is associated with the interaction, carries momentum Δp, and energy ΔE, and this process takes place within a time scale Δt limited by the Heisenberg Uncertainty Principle [36]

$$\Delta E \Delta t \sim \frac{h}{2\pi}, \tag{98}$$

where $h = 6.626 \times 10^{-34}$ Joules $\times$ s is Planck's constant. As was introduced in Equation 3, in $\sqrt{s_{NN}} = 200$ GeV collider experiments the entire collision energy is available in the c.m.s frame and represented here by 200 GeV $\equiv E$; thus the energy E, separation length L, and interaction time t, achieved on collision are

$$L = \frac{hc}{2\pi E} = 10^{-18} \text{ m}, \quad t = \frac{h}{2\pi E} = 10^{-27} \text{ s} \tag{99}$$

and the length scales obtained are much smaller than the size of the nucleon.

As discussed in Chapter 2.2.2 $\langle E_T \rangle$ measured in the PHENIX geometric acceptance is scaled to a reference acceptance of 1 unit pseudorapidity $\Delta\eta$ and 360^o $\Delta\phi$, obtaining $\frac{dE_T}{d\eta}|_{\text{lab frame}}$; this is an observable of the interaction which is proportional to the energy density ϵ of the collision zone as

$$\epsilon = \frac{1}{\tau_0 \pi R^2} \frac{dE_T}{dy}|_{\text{cms frame}}, \tag{100}$$

where $\tau_0 \sim 1$ fm$/c$ is the formation time of the initial medium created on the collision, and $\pi R^2 \equiv A_\perp$ is the effective transverse overlap area of the colliding nuclei calculated by the use of a nuclear geometry model. E_T per unit pseudorapidity is measured in the lab frame but the formula for energy density ϵ is given per unit rapidity, and in the cms frame, thus the conversions $\eta \to y$ and $|_{\text{lab frame}} \to |_{\text{cms frame}}$ at midrapidity are needed. The conversion for $\eta \to y$ at midrapidity was modeled by PHENIX for each 5% wide centrality class as [4]

$$\frac{dE_T}{dy}|_{\text{cms frame}} \sim 1.25 \pm 5\% \times \frac{dE_T}{d\eta}|_{\text{cms frame}}; \tag{101}$$

in a collider, if the two beams have the same momenta, then the lab frame is also the cms frame

$$\frac{dE_T}{d\eta}|_{\text{cms frame}} = \frac{dE_T}{d\eta}|_{\text{lab frame}}, \tag{102}$$

and thus

$$\epsilon = \frac{dE_T}{dy} \frac{1}{\tau_0 A_\perp}|_{\text{cms frame}} \sim 1.25 \times \frac{dE_T}{d\eta} \frac{1}{\tau_0 A_\perp}|_{\text{lab frame}}. \tag{103}$$

Using $\tau \sim 1$ fm/c, and values of $A_\perp$ as modeled by PHENIX [4] the energy densities are calculated. The 1-3 GeV/fm^3 levels required for QGP formation were attained in both of the RHIC 62.4 GeV Au+Au collisions (not shown here), and the 200 GeV Au+Au collisions. In 200 GeV Au+Au interactions in the 60-65% collision centrality class of events $\langle N_{\mathrm{nuc-part}} \rangle = 30$, $A_\perp = 40.9$ fm^2, and the transverse energy (see Table 3 on page 131) and associated energy density measured are

$$\frac{dE_T}{d\eta} = 34.09 \text{ GeV} \tag{104}$$

$$\epsilon = 1.25 \times (34.09 \text{ GeV}) \times (1\frac{\text{fm}}{\text{c}})^{-1} \frac{1}{40.9 \text{ fm}^2} = 1.04 \frac{\text{GeV}}{\text{fm}^3} \pm 22\% \tag{105}$$

In the 25-30% collision centrality class $\langle N_{\mathrm{nuc-part}} \rangle = 151$, $A_\perp = 82.2$ fm^2, and the transverse energy (see Table 3 on page 131) and associated energy density measured are

$$\frac{dE_T}{d\eta} = 217.17 \text{ GeV} \tag{106}$$

$$\epsilon = 1.25 \times (217.7 \text{ GeV}) \times (1\frac{\text{fm}}{\text{c}})^{-1} \frac{1}{82.2 \text{ fm}^2} = 3.31 \frac{\text{GeV}}{\text{fm}^3} \pm 13\% \tag{107}$$

In this thesis work no dynamical fluctuations were measured over impact parameter above the systematic error introduced by the centrality cut. There is a natural relation between E_T fluctuations, phase transitions, and the observation of a new state of matter like QGP. Specifically, near energy densities which would create the deconfinement of quarks and gluons modifications to event-by-event fluctuations are expected in net electric-charge production and multiplicity production [23]. The expected strength of these fluctuations is a critical topic however it was not estimated here and is left for a separate analysis.

In summary in adding n random combinations of a gamma distribution of moments μ_0 and σ_0 produces a higher order gamma distribution with moments $\mu_n = n\mu_0$ and $\sigma_n = \sqrt{n}\sigma_0$; this relationship between the higher order and lower order moments are characteristic of a process evolving under random fluctuations. Thus if E_T is described by a gamma distribution, in the absence of dynamical fluctuations its scaled variance is expected to remain constant over centrality, and likewise the relative width is expected to scale with $\frac{1}{\sqrt{n}}$. Figure 75 on page 209 are NA49 results for scaled variance multiplicity and p_T fluctuation measurements for fixed target experiments of different species collisions at 158-A-GeV ($\sim \sqrt{s_{NN}}$ =17 GeV) [33]; although in the paper which reported these results the authors do claim that the observed rise and fall of the fluctuations can be explained by non physical affects, it was not until the following year that more was understood about the centrality cut systematic error.

4.3 Fluctuations over acceptance – correlated particle emission

The last analysis performed in this thesis is measurement of fluctuations over acceptance in a search for correlated particle emission. The measurement is essentially the same as that done over centrality other than being in various acceptances. The mean E_T was measured in varying azimuthal solid angle and found to scale linearly with acceptance to within better than 1%. The remaining question is how is the E_T distribution width expected to scale with acceptance? Reference [33] reports that in purely random behavior the expectations for the evolution of fluctuations is a flat scaled variance. $\frac{\sigma^2}{\mu}$ was measured and found to have a significant dependence on azimuthal solid angle. Results for all the analyses are presented and discussed in Chapter 5.

5 $\langle E_T \rangle$ PRODUCTION AND FLUCTUATION - RESULTS

5.1 Error analysis

For all E_T analyses here the statistical errors and components of centrality-independent systematic error were estimated and added in quadrature

$$Total\ Error = \sqrt{(stat.\ error)^2 + (sys.\ error_1)^2 + (sys.\ error_2)^2 + ...} \tag{108}$$

E_T distribution moments were also obtained from fitting the histograms to gamma distributions. The differences in results between data and *acceptable* fits to the gamma distribution were negligible thus, although the results of fitting are shown, the fit results were not used in the final physics results for $\langle E_T \rangle$, σ/μ, or σ^2/μ. All errors are indicated on the plots and the methodology is presented in this section.

5.1.1 Statistical errors

For all analyses the statistical error for the different moments and products of the moments was computed in a standard procedure outlined in [13]. The E_T was measured in high statistics of more than $\sim$ 1 million events per semi-inclusive distribution; thus the statistical errors on the distribution moments are negligible at values less than 0.5% for each measurement in centrality. In the products of the moments used in the fluctuations the statistical error remains below 1.5%.

To avoid confusion here in the meaning of the symbols δ is used to represent the error on a moment, or product of moments, and σ to represent the E_T distribution

R.M.S. width; N_{events} represents the number of events in an E_T distribution. The formula for the statistical error on the moments is given below, and also for the error on a product or ratio of two moments, $F = xy$ or $F = x/y$, which is the same:

$$\delta_\mu = \frac{\sigma}{\sqrt{N_{events}}}, \tag{109}$$

$$\delta_\sigma = \frac{\sigma}{\sqrt{2(N_{events}-1)}}, \tag{110}$$

$$\delta_{F=xy,x/y} = \sqrt{\left(\frac{\delta_x}{x}\right)^2 + \left(\frac{\delta_y}{y}\right)^2} \times F \quad \text{(in the units of F)}, \tag{111}$$

and dividing Equation 111 by F produces that error given in decimal percent. When a correlation exists between moments an extra cross term appears in Equation 111 given by

$$+2\frac{\delta F}{\delta x}\frac{\delta F}{\delta y}\rho\delta_x\delta_y, \tag{112}$$

this is dependent on the correlation strength ρ. This term should be evaluated but for the analyses presented here was determined to be negligible and thus dropped. Thus for the relative width fluctuation σ/μ, and scaled variance fluctuation σ^2/μ the statistical errors are respectively

$$\delta_{\sigma/\mu} = \sqrt{\left(\frac{\delta_\sigma}{\sigma}\right)^2 + \left(\frac{\delta_\mu}{\mu}\right)^2} = \sqrt{\frac{1}{2(N_{events}-1)} + \frac{\sigma^2}{\mu^2 N_{events}}} \tag{113}$$

$$\delta_{\sigma^2/\mu} = \sqrt{\left(\frac{\delta_{\sigma^2}}{\sigma^2}\right)^2 + \left(\frac{\delta_\mu}{\mu}\right)^2} = \sqrt{\frac{1}{(N_{events}-1)} + \frac{\sigma^2}{\mu^2 N_{events}}} \tag{114}$$

5.1.2 Systematic errors

Systematic errors for Au+Au mean E_T in centrality $\frac{1}{0.5\langle N_{part}\rangle}\langle\frac{dE_T}{d\eta}\rangle$

Various systematic errors were identified. The errors are of two general types, centrality-independent and centrality-dependent. The components of error within each type are added in quadrature but the two types themselves are accounted for separately and not added in quadrature; this is because the measurements of semi-inclusive distribution moments (i.e. the "points" on the plots) are, to within the error, constrained to move together but in a different relative fashion depending on the error type; thus adding the two types in quadrature would result in an incorrect error estimate. The centrality-independent error is a "global scale" error on the energy measurement and all points are constrained to move together up or down by an equal percent. For the centrality-dependent error (referred to as "tilt" error, or "bending" error in PHENIX specific literature) all points are constrained to move together within the error but the error is always smaller in the more central class of interactions; this arises from the fact that the smaller the impact parameter class of events the larger the E_T, and consequentially the centrality-dependent error has a smaller relative effect. Listed below are the components of error followed by a brief description of how some of them were estimated.

The centrality-independent global scale error was estimated at 7.1% for 62.4 GeV and 5.5% for 200 GeV and includes the following components listed in their order of significance:

1. discrepancy across the multiplicity measurements made with individual sectors of the calorimeter;

2. a component of the error on the model N_{part} estimation in reference [27];

3. error on particle identification discussed in chapter 2.2.2, and on the hadronic $k-$factor [4]; for 62.4 GeV data the 19 GeV Au+Au errors for these terms were accepted as a "worse-case";

4. error on the energy scale accuracy estimated by π^0 reconstruction discussed in chapter 3.6.

The centrality-dependent error has three components listed in their order of significance (error totals appear in tables in Section A):

1. an error which results from binning the data in centrality while observing a limited part of the total cross section due to the limited acceptance: see Equations 83, 115, and 116;

2. an error due to spurious energy from measured electronic noise in the calorimeter PbSc towers;

3. a component of the error on the model N_{part} estimation in reference [27].

The error on the multiplicity measurements made by individual sectors of the calorimeter was evaluated for both 62.4 GeV and 200 GeV Au+Au. This was done over centrality, and for each sector. The maximal difference in the mean multiplicity of a sector from the 6-sector mean was 3.6% – see Figure 105 on page 241 and Figure 106 on page 242. There was also a measured error on the energy measurement due to sector edge effects of 1.5%. These two added in quadrature result in a 4% error (note this is somnetimes noted here as a 5% error).

The PbSc tower electronic noise was measured by selecting events from the 62.4 GeV Run 4 minbias data which had an interaction Zvertex of +50 to +60 cm and −50 to −60 cm. The 200 GeV Au+Au minbias definition excluded events in this Zvertex range and thus the 62.4 GeV data was used to define this error for both energies. When moving away from the beam line the large PHENIX iron magnet poles are situated between these two Zvertex locations and the PbSc calorimeters, thus the iron masks the calorimeters from the event multiplicity and perfectly screened and noise-free calorimeter is expected to receive zero energy. E_T distributions were measured on the selected masked events and each sector found to contribute an average amount of noise energy per event of 25 to 35 MeV. The measurements were made for various centrality classes and a centrality-dependence was observed but this was not investigated any further. A fixed noise contribution of 35 MeV has a smaller relative affect in the more central high-energy producing collisions; this produces the centrality-dependent shape of the error.

Equation 83 is the 62.4 GeV Au+Au case example of how events are binned into centrality classes; the following illustrates how the associated error of ±3.2%

on the observable cross section, $\sigma_{\mathrm{Au+Au}} = 83.7\% \pm 3.2\%$ [32], is accounted for in the measurement of $\langle E_T \rangle$. Shuffling the events into centrality bins defined at the limits of the cross section error estimate results in classes of events having a different $\langle E_T \rangle$. Estimating this particular error correctly is important as it is the largest, and becomes relatively larger toward the peripheral centrality classes. The limits of the cross section estimate are used in the calculation to determine how many events are placed into each 5% wide centrality bin; if N_{events} represents the total number of events in the inclusive distribution then:

$$0.05 \times \frac{100\%}{80.5\%} \times N_{events} = 0.062 \times N_{events} \tag{115}$$

$$0.05 \times \frac{100\%}{86.9\%} \times N_{events} = 0.057 \times N_{events}. \tag{116}$$

Systematic error on Au+Au energy density measurement ϵ

For the estimation of the energy density, ϵ, in 200 GeV Au+Au (see Chapter 4.2) various errors were identified and added in quadrature. The components are an E_T scale error and calorimeter noise error (both discussed above in the error estimates for mean E_T); error on the modeling of the transverse overlap area, and error in the conversion between lab and c.m.s. frames previously estimated by PHENIX [4]. The total error estimated is 13% for the energy density in the 25-30% centrality class, and 22% for the energy density measured in the 60-65% centrality class.

Systematic error in Au+Au fluctuations in centrality

The dominant error for 62.4 and 200 GeV Au+Au fluctuations is due to the limitations of the centrality definitions. This arises from clipping the upper and lower tails of those distributions made by one detector (the BBC, and/or ZDC) to measure fluctuations measured in another detector (EMC and/or Drift Chambers). Equal numbers of events are distributed into centrality bins which by definition requires an uneven distribution of events in BBC charge, this results in the error. For the centrality clock method in 200 GeV this introduces non-monotonic behavior in σ. This was examined and shown qualitatively in a first attempt to evaluate the error. Error due to the known uncertainty on the estimation of the observed cross section σ_{Au+Au} was not evaluated but should be in a more thorough analysis. A relatively small run-by-run systematic error was obtained by measuring the physical quantities $\frac{\sigma}{\langle E_T \rangle}$, $\frac{\sigma^2}{\langle E_T \rangle}$, and α which describes the dependency of $\frac{\sigma}{\langle E_T \rangle}$ on $N^{\alpha}_{\mathrm{nuc-part}}$, in 30 separate subsets of the data, and the standard deviation of each of the variables calculated across the 30 data subsets. The error on $^{\alpha}$ due to the error on the estimate of the observed cross section was not considered as it was in the $\langle E_T \rangle$ analysis. For $\frac{\sigma}{\langle E_T \rangle}$ and $\frac{\sigma^2}{\langle E_T \rangle}$ this was done for every centrality bin and the errors were consistently less than 1%. Geometry fluctuation corrections were applied to the 200 GeV 6-sector measurements and results are shown; however in some of the final results the geometry fluctuation corrections were not used as is indicated on the plots.

Systematic error in Au+Au fluctuations in acceptance

Error estimated on $\frac{\sigma^2}{\mu}$ and $\frac{\mu^2}{\sigma^2}\frac{1}{n}$ for the 200 GeV Au+Au 0-5% centrality class are as follows. The dominant systematic error identified results from the different responses across the calorimeter sectors, in part due to the different numbers of included towers. To quantify this error the fluctuation measurement was made for each of the six sectors individually and a standard deviation calculated. The errors were 3% for $\frac{\mu^2}{\sigma^2}\frac{1}{n}$ and 2% for $\frac{\sigma^2}{\mu}$, and were assigned not only to the single sector measurement but additionally to the larger acceptance measurements. Geometry fluctuation corrections were not applied.

Systematic errors on $p + p$ and d+Au measurements

For the $p + p$ and d+Au $\langle E_T \rangle$ measurements from the inclusive distributions the systematic error analysis was estimated as follows but not completed. What remains to be done is outlined.

1. the spurious energy due to calorimeter PbSc electronic noise was not measured in the RHIC Run 3 data and this may be the largest source of error;

2. the second largest source of error could result from an incorrect handling of the missed interactions, and/or minbias triggers which resulted in zero E_T: for $p + p$ the E_T measurement was decreased by the estimation on interactions missed due to the limited PHENIX acceptance (trigger bias) as described in Chapter 5.3 but the associated error on this estimation was not calculated; and for d+Au neither the trigger bias nor its associated error were estimated. The percentage of minbias triggered data which resulted in

zero E_T to the calorimeter was 19% in $p+p$ and 6% in d+Au, these events are included and no associated error was investigated.

3. The value of $k-$ factor $= 1.3$ was borrowed from 200 GeV Au+Au and applied from equation 24, and this value includes terms for hadronic response, inflow, and outflow. Other very different estimates on the value of the $k-$factor are shown in Chapter 2.2.2, and thus a full evaluation for $p+p$ and d+Au is necessary. When there is zero inflow and zero outflow $k = 1.3 \rightarrow 1.33$, a difference of less than 3%; thus an additional error component of 3% was added in quadrature to the standard error on k [4]. An unlikely but extreme case error on k is $k = 1.3^{+31\%}_{-22\%}$, see Chapter 2.2.2 equation 29;

4. the sector discrepancy error measured in Au+Au was applied;

5. for $p+p$ a value of $\langle N_{\mathrm{nuc-part}} \rangle = 2$ was accepted without error, and for the inclusive d+Au measurement the value of $\langle N_{\mathrm{nuc-part}} \rangle$ and its associated error was obtained from reference [29];

6. the π^0 invariant mass was reconstructed and distributions made, the average π^0 invariant mass was found to differ by less than 2% from the expected value.

For the $p+p$ and d+Au inclusive distribution $E_{T\ (\mathrm{EMC})}$ fluctuations the systematic error analysis was estimated as follows but not completed. What remains to be done is outlined.

1. Geometry fluctuation corrections were not applied on the final results and this may be the largest source of error;
2. No corrections were applied for trigger bias nor for minbias triggers which resulted in zero E_T, these may be the largest source of error;
3. error was not estimated for spurious energy from PbSc electronic noise;
4. faulty PbSc towers were removed but corrections were not made for the different numbers of included towers, as this would result in measuring fluctuations in different acceptances which was found to introduce a large error;
5. the $k-$factor was not used in any way in this analysis.

5.2 PHENIX E_T distributions, raw, corrected, and fitted

As discussed in chapter 2.2.2 the transverse energy measured in the PHENIX acceptance is labeled $E_{T\ (\mathrm{EMC})}$. For Au+Au typically all 6 PbSc sectors were used which amounted to 5.5 equivalent sectors after removal of faulty towers; in $p+p$ and d+Au typically 5 PbSc sectors were used resulting in 4.5 equivalent sectors after removal of faulty towers. When a smaller acceptance was used it is indicated so on the plots. Approximately 10% of the PbSc towers were removed from the designed acceptance due to systematic problems. After applying the $k-$factor correction (including hadronic response, inflow and outflow if known), correction for faulty towers, and scaling to the reference acceptance of $\Delta\eta = 1$ and $\Delta\phi = 360°$, the transverse energy measurement is referred to as E_T. Figure 76 on page 212 through Figure 100 on page 235 are the $E_{T\ (\mathrm{EMC})}$ and E_T distributions measured and used consistently in the analyses, and discussed in the following text.

5.2.1 $p + p$ and d+Au E_T distributions

Figure 76 on page 212 shows the 200 GeV minbias inclusive $p + p$ and d+Au $E_{T\ (\mathrm{EMC})}$ distributions measured in the same acceptance of 4.5 equivalent PbSc sectors. The physics analysis results for mean E_T, and $E_{T\ (\mathrm{EMC})}$ fluctuations in centrality were obtained from these $E_{T\ (\mathrm{EMC})}$ distributions and their characteristic values are listed in Table 2 on page 130. The striking difference between the two distributions is the beginning of a "plateau" region (as introduced in Chapter 4.1) in d+Au which has an average number of participant nucleons of 9.1 ± 0.4 [29], many more than in $p+p$ where there are only 2 participants. The inclusive distribution contains interactions over the entire range of impact parameter and thus the wide number of participants, and multiplicity resulting from successive collisions, shapes the d+Au plateau region. The plateau is followed by a sharp drop in E_T as the limited number of nucleons from the deuteron are quickly saturated in the Au. In d+Au as in Au+Au the centrality estimation of the number of participant nucleons uses the Glauber model Monte Carlo and the Woods-Saxon distribution of the nucleus. However because d+Au is an asymmetric collision system this estimation is handled a bit different than with the symmetric $p+p$ and Au+Au interactions. The number of hits incident on the Beam Beam Counter located on the opposite side of the interaction region from the incident Au beam is assumed to be (1) proportional to the number of Au participants on the event (${}^{\mathrm{Au}}N_{\mathrm{nuc-part}}$), (2) to have a response which follows a negative binomial distribution NBD. For each ${}^{\mathrm{Au}}N_{\mathrm{nuc-part}}$ a NBD distribution is calculated and added to the resulting distribution with Glauber weights, then fitted to the BBC data to find the best fit parameters [20]. The d+Au plots in Figure 77 on page 213 are BBC-hits distribution of events from the model and from data, and the emergence of the plateau region is illustrated. For the minimum bias data an estimate that 88% of the cross section is observed, and the modeled trigger efficiency is also accounted for.

5.2.2 $p+p$ and d+Au E_T fitted to the gamma distribution

The plots in Figure 78 on page 214 and Figure 79 on page 215 are 200 GeV minbias inclusive $E_{T\ (\mathrm{EMC})}$ measured in 4.5 equivalent PbSc sectors, and after scale corrected to E_T are shown in Figure 80 on page 216 and Figure 81 on page 217; the plots are evaluated in a fit to the gamma distribution $N\frac{b}{\Gamma(p)}(bE_T)^{p-1}e^{-bE_T}$. As was discussed in Chapter 2.2.2 a trigger bias accounts for missed interactions and this creates a discontinuity at zero E_T; in addition a portion of the minbias triggered events result in zero E_T ("EMC zeroes"). Due to its lower multiplicity environments $p+p$ contains the largest number of such missed interactions and zero-E_T events. The EMC zeroes were initially discarded from the $p+p$ distribution shown in Figure 76 on page 212, but they were included in Figure 78 on page 214. To avoid the discontinuity at zero E_T the fit was started after the first histogram bin. The behavior of the measured E_T distribution at zero E_T was not explored further (see [15] for further details regarding the zeros). The plots of Figure 78 on page 214 show the $p+p$ distribution begins to break away from the exponential shape of the fit at high E_T, 3 to 4 orders down, this is possibly due to jets as are seen in Figure 74 on page 208. In a future analysis and search for QGP it would be illustrative to examine in the minbias $p+p$ distribution all interactions which triggered as jet producing events, and monitor the percentage of such events over collision centrality. Figure 79 on page 215 shows that d+Au inclusive E_T did not fit the gamma distribution failing specifically at low E_T. Although the reason was not investigated here it is thought related to the fact that this is an inclusive distribution, and the gamma distribution does not fit the plateau region. The gamma distribution fits the inclusive E_T in $p+p$, and also often fits (as will be shown in the Figures ahead) the centrality binned semi-inclusive Au+Au distributions. Figure 80 on page 216 and Figure 81 on page 217 are the scale corrected E_T, and the errors were expanded on the low E_T bins in the lower plots to provide a fit to the high E_T tail which, upon afterthought would have been more accurately done by leaving out the low E_T points all together.

5.2.3 Au+Au $E_{T\ (\mathrm{EMC})}$ distributions: background affects

Figure 82 on page 218 shows Au+Au inclusive and semi-inclusive E_T distributions before and after background removal. This illustrates just how much background was removed from the two Au+Au data sets by the cuts developed and discussed in Chapter 3.3 and Chapter 3.4. The physics analysis results for Au+Au mean E_T, and $E_{T\ (\mathrm{EMC})}$ fluctuations in centrality were obtained from these much cleaner distributions, and their characteristic values are listed in Table 3 on page 131 and Table 4 on page 132. The error on the moments due to background depends on the shape of the background and this was not evaluated as the background was simply removed. It is worth noting that, in one case, when due to background a semi-inclusive E_T distribution had a $\sim 2\%$ error on the distribution mean μ, there was a corresponding error of 8% on the fluctuation σ^2/μ. The lower plots in Figure 82 on page 218 show the 62.4 GeV $E_{T\ (\mathrm{EMC})}$ before and after background removal; note that the background appears 3 orders down in the semi-inclusive distributions and this corresponds to a 50% distortion of the fluctuations as seen in Figure 26 on page 167. The previously published PHENIX $\langle E_T \rangle$ papers (see Figure 64 on page 198 and Figure 65 on page 199) have used much smaller numbers of events than were used in this thesis. Using high statistics as opposed to low statistics affects the shape of the semi-inclusive centrality binned $E_{T\ (EMC)}$ distributions, and this is discussed in Chapter 5.2.5.

5.2.4 Au+Au $E_{T\ (\mathrm{EMC})}$ distributions: comparison to convolutions in participant nucleon model

The Au+Au histograms in Figure 83 on page 219 and Figure 84 on page 220 were filled using a 100 MeV bin size to better resolve the events in each of the 5% wide centrality distributions. It is illustrative to compare these real $E_{T\ (\mathrm{EMC})}$ distributions to the 1, 2, ..., 16-fold convolutions of the real p+Au inclusive distribution in Figure 61 on page 195 which were created in a participant nucleon model. Notable differences in the features of the model to the data are as follows. In the O+Au model the highest order convolutions (which correspond to the most central interactions) have a higher relative yield in the mid part of those distributions; the reason for this is because the Au target is so much larger than the oxygen projectile that the relative probability is higher for the oxygen to be completely absorbed into the Au target. This is not observed in the O+Cu model convolutions nor the real Au+Au data. It is less likely to completely saturate oxygen into copper, or gold into gold. Another observation is the model convolutions of the most central distributions illustrate asymmetric shaped gamma distributions, whereas the most central Au+Au distributions, although gamma distributions, they are a bit more symmetric. The reason for this was given in Chapter 4.2: in the limit when μ becomes large the Poisson distribution tends to a Gaussian distribution; this is also understood mathematically: to recreate the most central Au+Au distribution would require $n = 197$ recursive convolutions, and the relative widths drop as $\sigma/\mu \sim 1/\sqrt{n}$ (see Equation 92).

5.2.5 200 GeV Au+Au $E_{T\ (\mathrm{EMC})}$ and E_T distributions fit to the gamma distribution

Figure 85 on page 221 shows the 200 GeV fully corrected (and scale shifted) inclusive E_T distribution. Figure 86 on page 221 shows the inclusive Au+Au distributions by themselves both before and after normalizing each bin contents by the total number of events. Figure 87 on page 222 are the results for fitting a gamma distribution to the upper tails of the 200 GeV Au+Au 0-5% semi-inclusive distribution (top plot), and to the inclusive distribution (bottom plot): the fit parameters of p, and b are essentially the same illustrating the effectiveness of the centrality cut for this high E_T upper tail.

There are two situations when the gamma distribution fails to fit the E_T distribution as evidenced by the χ^2/dof becoming very large: one is the imperfect centrality definition and the other is when some (but not all) of the semi-inclusive distributions are measured in high statistics. Although it was not investigated and remains unclear these two cases appear to be related, that is, in going to higher statistics the imperfect centrality definition might be becoming more noticeable. The χ^2/dof becomes large systematically depending on how the BBC charge is treated in the centrality cut's definition of semi-inclusive distributions, and this is explained a bit further in this Section.

The purpose of binning the E_T data in centrality is to group events of the interaction cross section into percentiles of impact parameter; the expectation is that a perfectly binned class of interactions is well described by the gamma distribution. In Figure 61 on page 195 each convolution corresponds to a given number of participant nucleons, or a class of interactions in impact parameter; the various curves overlap as the fluctuations in energy production overlap class to class. This overlap can also be seen in the simulations in the right plot of Figure 21 on page 164 where each colored group of events is a class of simulated interactions. Because of this overlap the centrality cuts, for example the vertical cuts into the BBC inclusive distribution of Figure 20 on page 163, and the radial cuts in the left plot of Figure 21 on page 164, are unable to separate the data into perfect classes of impact parameter. Thus, one thing is percentile classes of *interactions* in impact parameter, and another is percentile classes of *recorded events* of minbias data. Because the centrality binning of data is imperfect each centrality class of events contains an abundant amount of events from other classes of impact parameter. How well the gamma distribution fits the data is a consequence of the efficiency of the centrality cut.

The top two plots in Figure 88 on page 223 show that the χ^2/dof is good for the gamma distribution fit to the most central $E_{T\ (\mathrm{EMC})}$ distribution measured in low statistics, but not in high statistics. The affect statistics has on the results for the $\langle E_T \rangle$ and fluctuations analyses was not carefully quantified, however the following observations were made. In one case the $\langle E_T \rangle$ obtained from the data was different in low and high statistics, and this was related to low statistics data from specific run numbers. In general the $\langle E_T \rangle$ results are not significantly different when measured in high statistics as long as the mean values from the data are used; the mean values extracted from gamma fits were consistent in low and high statistics however the gamma distributions do not always fit the centrality-binned classes. The distribution moments extracted from the manually minimized NBD fits were significantly different and this should be explored further.

Figure 88 on page 223 through Figure 90 on page 225 show the central through peripheral 5% wide $E_{T\ (\mathrm{EMC})}$ distributions fitted to a gamma distribution. The fits were not good for the most central and most peripheral distributions, and become worse the further away in centrality from the $\sim$ 30-35% class. It appears the reason for the bad fits is as follows. The centrality-by-clock definition uses the ZDC-BBC scatter plot to classify the data (see left plot in Figure 21 on page 164); due to the arbitrarily chosen location of the clock origin the angle between a clock radial line and the centroid of the ZDC-BBC scatter plot moves away from 90° when moving away from the $\sim$ 30-35% class. An alternate PHENIX centrality method referred to as "centrality-by-perpendicular" slices perpendicularly into the clock and should be evaluated for an improved centrality prescription. When the gamma fit fails it raises a question as to the accuracy of the distribution moments used in the physics analysis.

The imperfect centrality cut is thought to have a large impact on the low E_T side of the distributions and so the low E_T errors were expanded in an attempt to account for this unquantified and assumed error; Figure 91 on page 226 through Figure 93 on page 228 show central through peripheral $E_{T\ (\mathrm{EMC})}$ distributions, and Figure 94 on page 229 through Figure 96 on page 231 show the corresponding scale-adjusted hadronic E_T distributions fitted to gamma distributions.

5.2.6 200 GeV Au+Au $E_{T\ (\mathrm{EMC})}$ distributions fitted to the Negative Binomial Distribution

The mathematical terms of the gamma distribution used to fit the E_T, and $E_{T\ (\mathrm{EMC})}$ distributions were assembled, and the ROOT histogramming software, and its MINUIT minimization technique were used to do the fits. At the time during this thesis work some in PHENIX at BNL believed that MINUIT might have problems properly determining the minimum values while estimating a best fit to the data; therefore the 200 GeV Au+Au $E_{T\ (\mathrm{EMC})}$ distributions were also fit "by hand," which means making small, incremental changes to one fit parameter while holding the other constant, until the best χ^2/dof is obtained, and then repeating the process for the other fit parameter. This was done fitting the 200 GeV Au+Au $E_{T\ (\mathrm{EMC})}$ distributions to the negative binomial distribution (NBD) by

Jeffrey Mitchell at BNL. The results for the $\chi^2/$ dof were much better than those obtained in fitting with the MINUIT package. The plots are shown in Figure 97 on page 232 through Figure 100 on page 235, and the results for the fits are in Table 5 on page 133. The distribution means, $\langle E_{T\ (\mathrm{EMC})} \rangle$, and the R.M.S. widths, σ, estimated from these fits were for some of the semi-inclusive distributions significantly different than their values in the data, and also different than values obtained from the gamma fits; however the ratio of these moments in the scaled variance, $\sigma^2/\langle E_{T\ (\mathrm{EMC})} \rangle$, were not significantly different as can be seen in the top left plot in Figure 116 on page 253. No further investigation was done as to what the difference in the NBD moments might mean for the physics results obtained.

5.2.7 62.4 GeV Au+Au $E_{T\ (\mathrm{EMC})}$ distributions fitted to the gamma distribution

Figure 101 on page 236 through Figure 104 on page 239 show the 62.4 GeV Au+Au central through peripheral 5% wide $E_{T\ (\mathrm{EMC})}$ distributions fitted to a gamma distribution. The distributions were measured in 5.5 equivalent sectors, and in centrality-by-BBC. Starting from the 5-10% centrality class the χ^2/dof for the gamma fits to E_T become large systematically as the BBC charge range for the distributions becomes large, that is 5-10% has the best χ^2/dof, then 10-15%, then 15-20%, and so on. The fit to the 0-5% E_T class is a special case, it has a relatively large χ^2/dof as it is the only distribution which has the BBC charge cut only on one side.

5.3 Mean E_T over collision centrality

The differential hadronic E_T measurements $\frac{dE_T}{d\eta}$ were performed for fully-inclusive $p+p$ and d+Au distributions, and for 5% wide in centrality (semi-inclusive) 62.4 and 200 GeV Au+Au distributions. Preliminary results for 200 GeV Au+Au were published in [9], and described in the associated PHENIX Analysis Note [8], and these published plots are given in Section B.5.5. As discussed in Chapter 4.1 each E_T measurement in centrality was divided by its modeled mean number of participant nucleons $\langle N_{\mathrm{nuc-part}}\rangle$, and in the case of Au+Au also by its mean number of participant quarks $\langle N_{\mathrm{quark-part}}\rangle$. Figure 107 on page 243 through Figure 114 on page 250 present all the results obtained, with key results provided in Figure 108 on page 244, Figure 112 on page 248, and Figure 114 on page 250.

Before discussing the physics results it is worth mentioning that the 6 PbSc sectors were each used individually to measure E_T, and each result scaled to the total hadronic reference. This was done as a systematic check on performance across the sectors (introduced in Chapter 5.1.2). The results, illustrated in Figure 105 on page 241 and Figure 106 on page 242 show a maximum differences in E_T of about ~4-5%; this measured descrepancy was factored into the error estimation of $\frac{1}{0.5\langle N_{\mathrm{nuc-part}}\rangle}\langle\frac{dE_T}{d\eta}\rangle$. Included in this 4% error are a 1.5% error due to known sector edge affects, and a 3.6% error due to different observed multiplicities in the different sectors, added in quadrature. The different multiplicities might be correlated to sector location on the PHENIX Arms: the outer sectors (West 0, West 3, and East 3) measured a slightly smaller multiplicity than the inner sectors. This systematic error has not previously been considered by PHENIX and should be evaluated more carefully to draw a firm conclusion. The absolute energy scale on the event is calibrated with the π^0, and/or minimum ionization potential (MIP), both of which are calibrations based on expected energy deposition; there is currently no check on the E_T measurement based on cluster multiplicity, so if for example each sector were losing a similar amount of clusters per event this would go unnoticed and the E_T quoted would be inaccurate.

5.3.1 Mean E_T over collision centrality: Au+Au

The Au+Au results are as follows. The plots in Figure 107 on page 243 are the 62.4 and 200 GeV Au+Au mean E_T measurements $\frac{1}{0.5\langle N_{\mathrm{nuc-part}}\rangle}\langle\frac{dE_T}{d\eta}\rangle$ plotted versus the modeled $\langle N_{\mathrm{nuc-part}}\rangle$, and fitted to a power law function. The results are expressed in the form

$$\langle E_T\rangle \sim \langle N_{\mathrm{nuc-part}}\rangle^{\alpha}, \tag{117}$$

$$\langle E_T\rangle_{62\ \mathrm{GeV}} = A \times \langle N_{\mathrm{nuc-part}}\rangle^{1.26\ \pm\ 0.06}, \tag{118}$$

$$\langle E_T\rangle_{200\ \mathrm{GeV}} = B \times \langle N_{\mathrm{nuc-part}}\rangle^{1.15\ \pm\ 0.06}, \tag{119}$$

where A and B are constants, and α is the power extracted from the fit. The error on α is obtained by fitting the results after incorporating the centrality-dependent error into the measurements. These results are also listed in Table 8 on page 136 and Table 9 on page 137. Figure 108 on page 244 shows the 200 GeV and 62.4 GeV results together. As was discussed in Chapter 4.2, in collisions an energy density of ~ 3 GeV/fm^3 is at the high end of the expectation for a QGP formation, and in 200 GeV Au+Au interactions this occurs at about 150 participant nucleons. Equivalent levels of transverse energy are measured in the 62.4 GeV interactions but at higher numbers of participants (~ 250 participant nucleons in a very rough estimate). PHENIX results for 200 GeV $\langle E_T \rangle$ normalized in the participant nucleon model were obtained prior in PHENIX Run 2 [4], and they were obtained again in this thesis as a cross-check having comparable results to within the systematic error (see Figure 109 on page 245).

The measurement of E_T at 62.4 GeV for Au+Au had not been done prior by PHENIX; as is shown in Figure 108 on page 244 the scale dependency with participant nucleons of $\alpha = N_{\mathrm{nuc-part}}^{1.26}$ is greater than that in 200 GeV where $\alpha = N_{\mathrm{nuc-part}}^{1.15}$. This was an unexpected result because if E_T production scales with quark participants, since the number of quark participants per nucleon participants is lower at 62.4 GeV than at 200 GeV (see Figure 68 on page 202), one might expect α to be smaller in 62.4 GeV interactions. In a separate PHENIX analysis done with the Drift Chambers the multiplicity production at 62.4 GeV was measured to scale faster with $N_{\mathrm{nuc-part}}$ than it does at 200 GeV Au+Au, this is illustrated in Figure 110 on page 246, taken from [31]. Thus if there is in fact an error in the measured value of α at 62.4 GeV, in E_T and in multiplicity, it could have been introduced at the level of the centrality definition; it would be wise to re-evaluate the correction which is applied to the BBC charge in the centrality definition to see if there is an underestimated systematic error (see Chapter 3.2).

As was discussed in Chapter 4.1 modeled numbers of participant quarks and participant nucleons $\langle N_{\rm part}^{\rm Au+Au}\rangle$ estimated for a given impact parameter, are used to normalize the $\langle E_T^{\rm Au+Au}\rangle$ measured in a centrality class of events corresponding to the same impact parameter. This is given in equations 81 and 82 and are repeated here

$$\frac{\langle E_T^{\rm Au+Au}\rangle}{0.5\langle N_{\rm nuc-part}^{\rm Au+Au}\rangle} = \langle E_T^{p+p}\rangle, \tag{120}$$

$$\frac{\langle E_T^{\rm Au+Au}\rangle}{\langle N_{\rm quark-part}^{\rm Au+Au}\rangle} = \frac{\langle E_T^{p+p}\rangle}{\langle N_{\rm quark-part}^{p+p}\rangle}. \tag{121}$$

The participant model which better describes the data would flatten out the E_T measured over centrality. Figure 111 on page 247 through Figure 113 on page 249 compare the E_T results normalized in the nucleon and quark models. The values for quark participants used are those given in reference [21], which were not intended for the 62.4 GeV data but used here as a preliminary estimation. However as can be seen in the top plot in Figure 68 on page 202, a very similar quark constituent calculation, the maximal difference in quark constituents between 62.4 GeV and 200 GeV is only $\sim$ 4%, occurring in the central collision region. In Figure 112 on page 248 it is clear that the quark model better describes E_T production.

5.3.2 Mean E_T over collision centrality: $p+p$, d+Au, Au+Au

Figure 114 on page 250 shows the $p+p$, d+Au, and Au+Au $\langle E_T \rangle$ in the nucleon participant model, compared to Au+Au $\langle E_T \rangle$ in the quark participant model. These measurements are also located in Table 10 on page 138 and Table 11 on page 139. Although the $p+p$ and d+Au measurements presented here are reasonable estimates these analyses are not complete and the results should not be quoted. The Au+Au simulated k-factor of 1.3 was applied to $p+p$ and d+Au as discussed in Chapter 2.2.2, with an increase in its associated systematic error of 3% (see equation 24, equation 29, and Chapter 5.1.2). Additionally the PbSc calorimeter electronic noise component of the systematic error should be measured and included.

The $p+p$ and d+Au $\langle E_{T\ (\mathrm{EMC})} \rangle$ distributions were measured twice, first while including, then while excluding the minbias triggered events which resulted in zero E_T: in $p+p$ 81.3% of events result in E_T, and in d+Au 94% of events result in E_T. The $p+p$ and d+Au distributions used in the final $\langle E_T \rangle$ analyses were those where the minbias events of zero E_T had been discarded, but the zero E_T events are required to measure $\langle E_T \rangle$ so they were reinserted into that measurement via the corrections $0.813 \times E_T$ $(p+p)$, and $0.94 \times E_T$ (d+Au). The $p+p$ mean measurement was further decreased due to the trigger bias as seen by the EMC $\frac{\sigma_{\mathrm{BBC}}/\sigma_{p+p}}{\epsilon_{\mathrm{EMC}}} = \frac{21.8\ \mathrm{mb}/41\ \mathrm{mb}}{0.75} = 0.52/0.75 = 0.69$.

The trend of the $p+p$ and d+Au measurements appear to follow into the trend observed in Au+Au suggesting the quark participant model may also describe E_T production in 200 GeV $p+p$ and d+Au; however since the various corrections were not completed further discussion of these measurements is not useful.

5.4 E_T fluctuations over centrality

Measurements of the E_T distribution relative width $\frac{\sigma}{\langle E_T \rangle}$, and the scaled variance fluctuations $\frac{\sigma^2}{\langle E_T \rangle}$, were performed in a high-statistics analysis using 5% wide centrality binned data, for both 62.4 GeV Au+Au and 200 GeV Au+Au $E_{T\ (\mathrm{EMC})}$ distributions. Scaled variance fluctuations were also measured in inclusive $p+p$ and d+Au distributions. It is important to note the following. In the fluctuations analyses $E_{T\ (\mathrm{EMC})}$ was used, not the scale-corrected, hadronic-corrected, and missing-tower-corrected "E_T;" this is because scale shifting the events in an event-by-event distribution changes (maybe even ruins) the σ^2/μ fluctuation being measured, this is demonstrated in Chapter 5.5. "$E_{T\ (\mathrm{EMC})}$," "E_T," and "μ" are used interchangeably in this Section to represent $E_{T\ (\mathrm{EMC})}$. Each centrality based measurement is plotted against its associated mean number of participant nucleons $\langle N_p \rangle$ (where $N_p \equiv N_{\mathrm{nuc-part}}$), and/or the associated centrality percentile of the binned data.

As was discussed in the Chapter 4.2: (1) levels of energy density estimated for QGP formation were measured in both 62.4 GeV Au+Au, and 200 GeV Au+Au interactions (for 200 GeV see Equations 105, and 107) and, (2) over collision centrality, under purely random behavior the fluctuations obey Equation 92, that is $\frac{\sigma^2}{\langle E_T \rangle} = constant$, $\frac{\sigma}{\langle E_T \rangle} = \frac{1}{\sqrt{n}}$, and where n is the number of convolutions of the fundamental distribution. Thus a transition to a QGP may be observable as a change in event-by-event fluctuations.

Figure 115 on page 252 through Figure 125 on page 262 are presentation of all the results discussed within this Section. Looking a bit ahead the key results are: Figure 117 on page 254, Figure 122 on page 259, Figure 124 on page 261, and the bottom plot in Figure 125 on page 262. The following are the main conclusions obtained in this analysis and apply to both the 200 GeV Au+Au and 62.4 GeV Au+Au measurements

1. the observed changes in the magnitude of the fluctuations in $\sigma^2/\langle E_T \rangle$ over centrality are no more than systematic error from the imperfect centrality definitions;

2. the observed deviation of $\sigma/\langle E_T \rangle$ from the expectation of random behavior scaling (in the quark participant model) of $\sim 1/\sqrt{N_{\mathrm{quark-part}}}$, over centrality, is due to systematic error from the imperfect centrality definitions;

3. no dynamical fluctuations were observed over centrality above the systematic error of the centrality definitions; further work is needed to find an improved method of shuffling events into percentiles of impact parameter.

Preliminary results for 62.4 and 200 GeV Au+Au were published in [9], and described in the associated PHENIX Analysis Note [8]. These published plots are given in Chapter B.5.5.

5.4.1 E_T fluctuations: noticing centrality problems

Figure 115 on page 252 shows Au+Au results for the scaled variance fluctuations illustrating a 20% rise in 62 GeV fluctuations and a 40% rise in 200 GeV fluctuations; these measurements are logged in Table 12 on page 140 and Table 13 on page 141. As discussed in Chapter 3.2 the centrality-by-BBC method categorizes event classes by slicing up the BBC charge distribution with simple vertical cuts, where "vertical" means selecting all events between two fixed values of BBC charge. The centrality-by-clock method categorizes event classes by slicing into the distribution of ZDC energy vs. BBC charge, a correlation or scatter plot; this results in making angular cuts on the BBC charge. The error introduced into the fluctuations by the centrality cut will now be evaluated.

The various Au+Au plots in Figure 116 on page 253 provide many useful comparisons and illustrate that using detectors (in this case the BBC's and ZDC's) to look for dynamic fluctuations in other detectors (like the EMC or Drift Chambers) introduces the largest systematic error. The bottom left plot are measurements of $\frac{\sigma^2}{\mu}$ (where here $\mu = \langle BBC_{\text{charge}} \rangle$) from the clipped BBC distributions which are used to define centrality; more discussion of this plot appears further in the Chapter but for now it is sufficient to point out that these are not actual fluctuation measurements as the tails of the distributions are purposefully cut; the various features observed in these BBC "fluctuations" are also observed in the E_T and multiplicity fluctuations. The top plots are E_T scaled variance fluctuations $\frac{\sigma^2}{\mu}$ measured in the 5.5 equivalent sectors; the top left plot are 200 GeV comparison of data, data + geometry fluctuation corrections, gamma distribution fits (some of which were bad fits), and fits to the negative binomial distribution which were done by searching for a best χ^2/dof manually for each fit parameter; results from the fits do not provide a significant change in the results other than at very low N_p; the application of geometry fluctuation corrections do begin to flatten out the results very nicely. In the top right plot the two different centrality definitions were used and results are compared. Regarding the measurements first recall that the location of each point along the $x-$axis (i.e. the $N_{\mathrm{nuc-part}}$ coordinate) remains fixed regardless of which centrality method is used, and differs only very slightly between 62.4 GeV and 200 GeV interactions. Note that the relative ordinates of the points, i.e. the "shape of the fluctuations" when centrality-by-BBC is used looks the same in 200 GeV and 62.4 GeV, but is different when centrality-by-clock is used; this immediately illustrates that the fluctuation magnitude (i.e. the ordinate of any given point) depends on which centrality definition is used, and this is a systematic error. The bottom right plot shows multiplicity fluctuations for charged tracks $\frac{\sigma^2}{\langle N_{\mathrm{ch\ tracks}}\rangle}$, where for 200 GeV the centrality-by-clock was used and for 62.4 GeV the centrality-by-BBC was used. In comparing the multiplicity fluctuations and the E_T fluctuations (the two plots on the right), it is obvious that they share the following characteristic features with the "fluctuations" observed in the BBC charge (plot on lower left); all of these features are systematic error and not to be confused with dynamic fluctuations

1. when centrality-by-BBC is used: over the range $N_{\mathrm{nuc-part}} < 100$ there is a sharp rise in fluctuations with increasing $N_{\mathrm{nuc-part}}$;

2. when centrality-by-BBC is used: over the range $N_{\mathrm{nuc-part}} > 100$ there is a moderate rise in fluctuations with increasing $N_{\mathrm{nuc-part}}$;

3. when centrality-by-clock is used: over range $N_{\mathrm{nuc-part}} < 10$ there is rise in fluctuations with increasing $N_{\mathrm{nuc-part}}$;

4. when centrality-by-clock is used: over range $10 < N_{\mathrm{nuc-part}} < 50$ there is a drop in fluctuations with increasing $N_{\mathrm{nuc-part}}$;

5. when centrality-by-clock is used: over range $50 < N_{\mathrm{nuc-part}} < 200 - 250$ there is a rise in fluctuations with increasing $N_{\mathrm{nuc-part}}$; this rise is not so apparent in multiplicity fluctuations which may be due to the different cuts used;

6. when centrality-by-clock is used: over range $N_{\mathrm{nuc-part}} > 250$ there is a drop in fluctuations with increasing $N_{\mathrm{nuc-part}}$.

Interpreting the different magnitudes of the E_T fluctuations and multiplicity fluctuations in Figure 116 on page 253 is not straightforward for the various reasons, (1) E_T has a dimension and multiplicity does not, (2) different geometric acceptances were used, (3) a cut on particle p_T was used for the multiplicity fluctuations. Thus in the analysis here the main focus is on how flat $\frac{\sigma^2}{\mu}$ is and not the magnitude of the fluctuations.

5.4.2 E_T fluctuations: $\frac{\sigma}{\mu}$ fits a power law – error in σ

Figure 117 on page 254 are the 200 GeV and 62.4 GeV Au+Au relative width measurements $\frac{\sigma}{\mu}$, and these are also logged in Table 12 on page 140 and Table 13 on page 141. As discussed in chapter 4.2, for the case of purely random behavior with centrality the expectation for the evolution of the distribution relative width is $\sigma/\mu = 1/\sqrt{\mu}$ (where $\mu \equiv \langle E_T \rangle$), thus

$$\begin{aligned} \text{if } \frac{\sigma^2}{\langle \mathrm{E_T} \rangle} &= \mathrm{A}, && (122) \\ \text{and if } \langle \mathrm{E_T} \rangle &= B \times \langle N_{\mathrm{nuc-part}} \rangle^{\alpha}, && (123) \\ \text{then expect } \frac{\sigma}{\langle \mathrm{E_T} \rangle} &= C \times \frac{1}{\sqrt{\langle N_{\mathrm{nuc-part}} \rangle^{\alpha}}} && (124) \end{aligned}$$

where A, B, and C are constants, and α is the fit parameter from the power law fit. The results obtained for the evolution of $\langle E_T \rangle$ in 62.4 GeV and 200 GeV (discussed in Chapter 5.3) are $\alpha = 1.26$ and $\alpha = 1.15$ respectively. These measurements for $\sigma/\langle E_T\rangle$, and α from the fit are

$$\frac{\sigma}{\langle E_T\rangle}_{62\ \text{GeV}} = D \times \frac{1}{\sqrt{N_{\text{nuc-part}}^{1.16\ \pm\ 0.002}}}, \tag{125}$$

$$\frac{\sigma}{\langle E_T\rangle}_{200\ \text{GeV}} = E \times \frac{1}{\sqrt{N_{\text{nuc-part}}^{0.93\ \pm\ 0.01}}}, \tag{126}$$

where D and E are constants. The only error on α considered was a small run-by-run error. These values for α are reasonably close to those obtained in the $\langle E_T\rangle$ analysis which concluded with Equations 118 and 119. If the model $N_{\text{nuc-part}}^{\alpha}$ accounts for the evolution of E_T over impact parameter, and if the fluctuations over impact parameter are purely random, and if our measurement technique is good enough, then the value of α measured should be the same in $\langle E_T\rangle = N_{\text{nuc-part}}^{\alpha}$ and $\sigma = \sqrt{N_{\text{nuc-part}}^{\alpha}}$. However the values obtained for α may be slightly different across energies as can be inferred from the the top plot in Figure 68 on page 202.

For a given collision energy the deviations in the observed value of α in the $\langle E_T\rangle$ and $\frac{\sigma}{\langle E_T\rangle}$ measurements are largely due to the error introduced by the centrality cut, and dependent on what centrality region is fitted. The bottom right plot in the Figure 117 on page 254 is a close up view of the fit to the model illustrating the centrality-by-clock definition introduces a larger point-to-point error.

Figure 118 on page 255 are measurements of the Au+Au distribution RMS widths σ_{E_T} (here a change in notation is used $\sigma \equiv \sigma_{E_T}$), normalized by the $\langle N_{\text{part}}\rangle$ expectations from the models. As was discussed in Chapter 5.3.1, in the absence of dynamical fluctuations, the participant model which better describes the data would flatten out these measurements made over centrality. It is clear that the quark participant model better describes the evolution of σ_{E_T}. The fact that the points normalized in the quark participant model are still not flat is largely (if not entirely) due to the error introduced by the centrality definitions.

Two differences are noted between the fluctuation measurements made in different $\Delta\phi$ acceptances by comparing the bigger (5.5 PbSc sectors) measurements of Figure 118 on page 255 to the much smaller ($\sim$ 1 PbSc sector) measurements of Figure 119 on page 256. The first difference is that the fluctuations in the bigger acceptance are larger than they are in the smaller acceptance; they are expected to be larger but not by this much, and this is discussed in Chapter 5.5 in the context of correlated particle emission. The second difference is that the fluctuations measured in the bigger acceptance appear to have a larger slope over centrality; much of this however is, again, the error of the centrality definitions, and another part is just visual parallax due to differences of scale.

5.4.3 E_T fluctuations: identifying the centrality error

The plots in Figure 116 on page 253 in Chapter 5.4.1 were used to illustrate that the change in scaled variance fluctuations σ^2/μ over centrality observed in E_T measurements follow the σ^2/μ measurements in the BBC detector and are thus likely non-physical. It is somewhat simpler to follow this argument while comparing only σ_{BBC} and σ_{E_T}.

Figure 120 on page 257 are the Au+Au event-by-event distributions in 5% wide centrality of (top plot) BBC charge and (middle plot) ZDC energy used in the 200 GeV centrality-by-clock definition. The bottom plot in this Figure compares the most central of the 200 GeV centrality-by-clock BBC distributions to the most central BBC distribution in the centrality-by-BBC method for 62.4 GeV data. In the centrality-by-BBC method the semi-inclusive distribution tails in all except the most central distribution are completely clipped on both sides, and the most central is only clipped on the low E_T side. The error introduced into the E_T fluctuations from the centrality definitions comes from these distributions not accurately representing percentiles of impact parameter.

The moments σ and μ from the BBC and ZDC distributions in the top two plots in Figure 120 on page 257 are plotted as a function of $\langle N_{\mathrm{nuc-part}} \rangle$ in Figure 121 on page 258 and many things are noted. The top right plot shows that σ_{BBC} is not monotonic in this centrality definition – at about 50 participant nucleons it has a kink corresponding to where the angle the BBC is cut at goes from negative to positive (when the BBC is cut at 0° all events of that centrality class are chosen from between two fixed values of BBC charge). This kink at 50 participants also appears in the measurements of σ_{E_T} shown in the bottom plot. This is a clear indication that this kink in measured E_T fluctuations is non-physical. The measurement of σ_{BBC} in the top right plot drops with centrality in the most central region; σ_{E_T} in the most central region follows suite and also drops with centrality, an indication that it is non-physical. Note that σ_{ZDC} versus centrality bends upward in this centrality region as is seen in the middle right plot. The response in the ZDC is inverse to that in the BBC. There had been speculation in PHENIX about jet suppression possibly being the cause for this drop in fluctuations at high centrality, but it is more likely due to the centrality definition and non-physical; the most likely reason is that the scatter plot of ZDC vs. BBC used for this centrality (the bottom plot in Figure 123 on page 260) becomes very narrow in central collisions and thus a narrowing BBC range is used for the centrality bins.

The following compares the changes observed in $\sigma^2_{E_T}/\mu$ over centrality to the changing density of events in BBC-centrality space which is a consequence of the binning procedure. Figure 122 on page 259 shows a direct comparison of the inverted E_T fluctuations (bottom plot) to the density of events over the plane of BBC charge vs. percent centrality, for both 200 GeV centrality-by-clock (top plots) and 62.4 GeV centrality-by-BBC (middle plots). The large central peak in the top plots correspond to where the BBC in the centrality-by-clock is sliced at an angle close to 0°; it is also where the clock is thickest and thus the range allowed in BBC charge per percentile is a minimum. In the top right and middle right plots the rolling rise of events seen in the peripheral region is where the BBC charge range assigned to the centrality bins drops to a minimum, and fluctuations are greatly cut. This shows that clipping the tails of BBC charge distributions decreases the magnitude of the E_T fluctuations being measured. The biggest suppression to E_T fluctuations is when the BBC charge is cut vertically.

At this point it is useful to revisit what the physics is that this analysis is trying to measure. In order to observe dynamical fluctuations in E_T the centrality definition has to bin the data in percentiles of impact parameter without removing the fluctuations. This is not an easy task. Figure 123 on page 260 shows the measured fluctuations in E_T simply follow the "fluctuations" in the BBC, which are caused by the changing angular cut, and width, of BBC bins used in the centrality definition. Figure 124 on page 261 identifies the E_T fluctuations with the BBC cuts.

5.4.4 E_T fluctuations: $p+p$, d+Au, and Au+Au

The top plot in Figure 125 on page 262 provides a comparison of 200 GeV Au+Au scaled variance fluctuations from the moments taken directly from the data compared to those taken from gamma fits, where the fits were made with increased errors on the low E_T bins to get a better fit to the upper E_T tails; also compared are post geometry fluctuation corrections. The bottom plot compares the fluctuations measured in $p+p$ and d+Au to Au+Au, and these values are also listed in Table 11 on page 139. The fluctuation measured in $p+p$ is smaller than in d+Au, and in Au+Au, and this might be due in part to the trigger bias and/or minbias triggers which resulted in zero E_T.

5.5 E_T fluctuations over geometric acceptance

This analysis compares fluctuations in the 200 GeV Au+Au $E_{T\ (\mathrm{EMC})}$ distributions made in sequentially larger slices of azimuthal solid angle to search for spatially directed correlations in particle multiplicity. The event-by-event $E_{T\ (\mathrm{EMC})}$ distributions were measured with 1 sector, 2 sectors together, 3 sectors together, ... and 6 sectors together. The faulty PbSc towers were removed from each sector which amounted to eliminating approximately 10% of towers in each of four sectors, but sector West 1 only had 5% removed, and sector West 3 had 20% removed. It was determined that the slightly different effective acceptances of the sectors has little to do with the observed change in fluctuations, and these differences in numbers of included towers were incorporated into the systematic error as discussed in Chapter 5.1. Figure 126 on page 264 through Figure 134 on page 272 are presentation of all results. The key results are in Figure 130 on page 268, Figure 132 on page 270, and the top plot in Figure 134 on page 272, and these results are tabulated in Table 14 on page 142.

The five goals of this analysis were to

1. Determine if the E_T distribution RMS width σ scales with the square root of the acceptance.

2. Compare the "overshoot" of the smaller acceptance upper E_T tails which occurs after acceptance scaling.

3. Determine the effect acceptance scaling a distribution has on measured fluctuations.

4. Quantify the observed changes in fluctuations.

5. Extract a correlation length.

This analysis was done following much of the procedure outlined in [15]. Figure 126 on page 264 and the top two plots in Figure 127 on page 265 are respectively the inclusive, and 0-5% central semi-inclusive distributions made in the six acceptances shown before and after having scale shifted, or "acceptance corrected" the distributions. In Figure 105 on page 241 and Figure 106 on page 242 it was shown that the semi-inclusive mean E_T scales one to one with acceptance n. The bottom left plot in Figure 126 on page 264 shows the inclusive mean E_T also scales with n. However the bottom plot in Figure 127 on page 265 shows the semi-inclusive distribution width does not scale with $\sqrt{n}$.

In acceptance scaling, the E_T on all the events in the 1 sector measurement ($n = 1$) were multiplied by a factor of 6, and in the normalization the number of events in each bin of the new histogram was divided by six to maintain a distribution with yield referenced to a 1 GeV bin size. Likewise the events in the

2 sector measurement were multiplied and normalized by a factor of 3 and so on.

$$
\begin{aligned}
n &= 1, \quad \text{scale factor} = 6.0, \quad \text{normalization} = 1/6 && (127)\\
n &= 2, \quad \text{scale factor} = 3.0, \quad \text{normalization} = 1/3 && (128)\\
n &= 3, \quad \text{scale factor} = 2.0, \quad \text{normalization} = 1/2 && (129)\\
n &= 4, \quad \text{scale factor} = 6/4, \quad \text{normalization} = 1/1.5 && (130)\\
n &= 5, \quad \text{scale factor} = 6/5, \quad \text{normalization} = 1/1.2 && (131)\\
n &= 6, \quad \text{scale factor} = 1.0, \quad \text{normalization} = 1 && (132)
\end{aligned}
$$

There is speculation concerning whether or not the large overshoot in the upper E_T tails of the scaled distributions, an overshoot which is largest for the smallest acceptance measurements, is of physical importance [15]. For a measured distribution of N events, when scale shifting the value of each i^{th} event by a constant factor A, both of the moments of the distribution also scale by the same factor A

$$
\begin{aligned}
\mu_{scaled} &= \frac{1}{N}\sum_{i=1}^{N} Ax_i = A\frac{1}{N}\sum_{i=1}^{N} x_i = \quad A \times \mu_{measured} && (133)\\
\sigma_{scaled} &= \sqrt{\frac{1}{N}\sum_{i=1}^{N}(Ax_i)^2 - \left(\frac{1}{N}\sum_{i=1}^{N} Ax_i\right)^2} && (134)\\
&= \sqrt{\frac{A^2}{N}\sum_{i=1}^{N} x_i^2 - \left(\frac{A}{N}\sum_{i=1}^{N} x_i\right)^2} && (135)\\
&= A\sqrt{\frac{1}{N}\sum_{i=1}^{N} x_i^2 - \left(\frac{1}{N}\sum_{i=1}^{N} x_i\right)^2} \quad = \quad A \times \sigma_{measured} && (136)
\end{aligned}
$$

Thus scaling a distribution by a constant A produces a new distribution that has a RMS width $\sqrt{A}$ times larger than might be expected in the purely random expectation. In any ratio of the two moments if, in the ratio each moment is raised to the same power, then the scale factor cancels out thus:

$$\frac{\sigma}{\mu}_{scaled} = \frac{\sigma}{\mu}_{measured} \tag{137}$$

$$\frac{\sigma^2}{\mu}_{scaled} = A\frac{\sigma^2}{\mu}_{measured} \tag{138}$$

$$\frac{\mu^2}{\sigma^2}_{scaled} = \frac{\mu^2}{\sigma^2}_{measured}. \tag{139}$$

The bottom plot in Figure 127 on page 265 illustrates that the RMS widths of the scale corrected distributions are in actuality smaller, not larger, than what might be expected for the RMS width when scale shifting a distribution. An additional observation is that the overshoot in E_T tails might not be anything more than a scale shift effect.

The plots in Figure 128 on page 266 illustrate the effect on the fluctuation analysis when scaling of the distributions is done: a clear artifact in the scaled variance fluctuation is introduced by the scale factor and thus it is concluded that examining fluctuations in acceptance is better done on the measured distributions and not the scaled distributions. Thus no acceptance scaling was used in the remainder of this analysis.

As was discussed in Chapter 4.2 an n-fold convolution of a single gamma distribution produces another gamma distribution with $p \to np_0$ thus

$$p = \frac{\mu^2}{\sigma^2} = n\frac{\mu_0^2}{\sigma_0^2} = np_0 \tag{140}$$

If E_T distributions made in increasing acceptance can be compared to an n-fold convolution of an underlying gamma distribution, say for example the $n = 1$ sector measurement, then $\mu^2/\sigma^2 n$ is a test for fluctuations, and expect

$$\frac{\mu^2}{\sigma^2}\frac{1}{n} = \text{constant.} \tag{141}$$

Figure 129 on page 267 shows that the $\mu^2/\sigma^2 n$ is not flat in acceptance, and this might be the result of correlated particle emission from the interactions. Some checks were done to rule out known physical and systematic affects: (1) the sectors were chosen in different combinations (see the top plot in Figure 129 on page 267) to explore if jets might be causing the fluctuations, and results concluded that the shape of the fluctuations do not have a significant dependency on how the sectors are arranged relative to one another; (2) the bottom plot in Figure 129 on page 267 illustrates the identified systematic error estimated by the different single sector measurements; (3) energy from the two rows of PbSc towers along each sector edge was removed and the fluctuations measured again (not shown here); the results concluded that this had no significant effect on the shape of the fluctuations. The width of two PbSc towers is about 11 cm and removing the edge towers reduces the known effect of particle showers which bleed across the sectors as registering as particles in two sectors simultaneously on the event. The final result for the fluctuations in Figure 130 on page 268 did not fit a simple power law function but do fit an exponential

$$\frac{\mu^2}{\sigma^2 n}_{(200\ \text{GeV}\ 0-5\%)} = 50e^{-0.5\sqrt{n}} \tag{142}$$

It was not determined if this fit has any physical relationship to the fluctuations.

The plots in Figure 131 on page 269 show the scaled variance fluctuations in acceptance for various centralities, and are compared to fluctuations measured in CERN Pb+Pb and $p+p$ collisions at much lower energies. Figure 132 on page 270 are the final results for σ^2/μ for the 0-5% centrality class showing a clear 115% rise in fluctuations when the azimuthal solid angle is increased to 6 times the size.

Finally, the mean transverse energy per cluster, e_T, was measured for the 0-5% centrality class to be 0.25 GeV (see Figure 133 on page 271). This was used in an attempt to relate the observed fluctuations to a physical effect by estimating a correlation length; this was done following the method outlined in [39]. The cumulant k for a distribution is given by

$$\frac{1}{k} = \frac{\sigma^2}{\mu^2} - \frac{1}{\mu}. \tag{143}$$

k is typically used with multiplicity distributions and thus dimensionless. For this E_T analysis e_T was used in the expression for k to produce a dimensionless result (however it is not clear if this procedure is accurate)

$$\frac{1}{k} \rightarrow \frac{\sigma^2}{\mu^2} - \frac{e_T}{\mu}. \tag{144}$$

k was plotted as a function of the $n = 1,\ 2,\ ..,\ 6$ acceptance measurements as is shown in Figure 134 on page 272, and the result fitted to a particle correlation function [39]: one of the fit parameters is the correlation length ζ. The value obtained for ζ from the fit is 0.14 of a PbSc sector, which is equivalent to 28 cm (about the size of 5 PbSc towers). Each sector subtends an angle of 22° in $\Delta\phi$ from the interaction region which is 5.1 meters distant, thus the measured correlation is 3.1°

$$\zeta = 3.1^\circ \tag{145}$$

$$\sim 28 \text{ cm} \sim 5 \text{ PbSc towers}; \tag{146}$$

Correlations due to π^0 shower spread, reaction plane rotation, and elliptic flow were not addressed and these issues should be considered before drawing any further conclusions.

6 CONCLUSIONS

The main results are as follows:

1. A nuclear geometry model which counts participant quarks better describes both the Au+Au mean E_T production over centrality, and the evolution of the second distribution moment the RMS width, than does the Wounded Nucleon Model.

2. In Au+Au interactions estimated energy densities required for QGP formation were produced, however no dynamical E_T fluctuations over centrality were observed above the systematic error introduced by the centrality definitions.

3. An unidentified 115% rise in the 200 GeV Au+Au 0-5% centrality E_T fluctuations were measured over a 6-fold increase in ϕ acceptance, from this a 3.1° correlation length is estimated.

These results are described below in more detail, and they are tabulated in Section A, which have corresponding Figures appearing in Section B.5 as follows:

1. Figure 76 (top plot) on page 212 corresponds to Table 2 on page 130.

2. Figure 83 on page 219 corresponds to Table 3 on page 131.

3. Figure 84 on page 220 corresponds to Table 4 on page 132.

4. Figure 97 on page 232, Figure 98 on page 233, Figure 99 on page 234, and Figure 100 on page 235 correspond to Table 5 on page 133.

5. Figure 105 on page 241, and Figure 106 on page 242 correspond to Table 6 on page 134 and Table 7 on page 135 respectively.

6. Figure 107 on page 243 corresponds to Table 8 on page 136 and Table 9 on page 137.

7. Figure 114 on page 250 corresponds to Table 10 on page 138 and Table 11 on page 139.

8. Figure 115 on page 252 and Figure 117 on page 254 correspond to Table 12 on page 140 and Table 13 on page 141.

9. Figure 125 (the $p+p$ and d+Au points in the bottom plot) on page 262 appear in Table 11 on page 139.

10. Figure 130 on page 268, Figure 132 on page 270, and the top plot in Figure 134 on page 272 correspond to Table 14 on page 142.

E_T distributions

Gamma distributions were fit to the 200 GeV inclusive minbias $p+p$ and d+Au E_T distributions, and semi-inclusive 62.4 GeV and 200 GeV Au+Au E_T distributions. The fit to d+Au did not work well in the low E_T "plateau region" of that distribution. The 200 GeV Au+Au semi-inclusive E_T distributions were made in the ZDC vs. BBC centrality centrality-by-clock definition – the best fits were obtained in the 30-35% centrality class where the clock is sliced transverse, and the fits worsened systematically on both sides of this class. This suggests that the alternate centrality method referred to as centrality-by-perpendicular could be evaluated for an improved centrality prescription, as this method determines all centrality classes with perpendicular slices of the clock.

Energy densities measured

Collision energy densities in both 62.4 GeV and 200 GeV Au+Au interactions were measured to be within the levels expected for QGP formation; specifically for 200 GeV, in the centrality classes of 60-65% ($\langle N_{\mathrm{nuc-part}}\rangle = 30$), and 25-30% ($\langle N_{\mathrm{nuc-part}}\rangle = 151$), the levels were respectively

$$\epsilon = 1.04\ \mathrm{GeV/fm^3}\ \pm 22\% \tag{147}$$

$$\epsilon = 3.31\ \mathrm{GeV/fm^3}\ \pm 13\%. \tag{148}$$

$\langle E_T\rangle$ in centrality

62.4 GeV and 200 GeV Au+Au mean E_T production across collision centrality rises faster than predicted by counting nucleons in the Wounded Nucleon Model, where for the constants A and B

$$\langle E_T \rangle_{62 \text{ GeV}} = A \times \langle N_{\text{nuc-part}} \rangle^{1.26 \pm 0.06} \tag{149}$$

$$\langle E_T \rangle_{200 \text{ GeV}} = B \times \langle N_{\text{nuc-part}} \rangle^{1.15 \pm 0.06}. \tag{150}$$

The 200 GeV Au+Au $\langle E_T \rangle$ across collision centrality is constant when normalized to a counted number of quarks in the Participant Quark framework. Inclusive 200 GeV $p+p$ and d+Au $\langle E_T \rangle$ per wounded nucleon follows the rising trend observed in semi-inclusive Au+Au $\langle E_T \rangle$ production; however the correction terms for particle inflow and losses to the electromagnetic calorimeters should be simulated and applied to the $p+p$ and d+Au measurements before drawing further conclusions.

Fluctuations in centrality

The dominant structure in the 62.4 GeV and 200 GeV Au+Au scaled variance $\frac{\sigma^2}{\langle E_T \rangle}$ fluctuation measurements in centrality are shown to be clear artifacts of the centrality definitions. Specifically the systematic limitation inherent in clipping the tails of event-by-event distributions measured in one detector to define centrality classes in another are observed. $\frac{\sigma^2}{\langle E_T \rangle}$ for inclusive $p+p$ is half that measured in d+Au and Au+Au; an evaluation of the effect of the $p+p$ trigger bias of lost interactions on the fluctuation is recommended. Measurements of the relative widths illustrate an $N^{\alpha}_{\text{nuc-part}}$ dependency, where for the constants D and E

$$\frac{\sigma}{\langle E_T\rangle}_{62\ \text{GeV}} = D \times \frac{1}{\sqrt{N^{1.16\ \pm\ 0.002}_{\text{nuc-part}}}} \tag{151}$$

$$\frac{\sigma}{\langle E_T\rangle}_{200\ \text{GeV}} = E \times \frac{1}{\sqrt{N^{0.93\ \pm\ 0.01}_{\text{nuc-part}}}}. \tag{152}$$

The difference in the value obtained for α between the $\langle E_T\rangle$ and $\frac{\sigma}{\langle E_T\rangle}$ measurements is due to the fact that the systematic limitation of the centrality definition introduces a larger error on the distribution width σ, than it does on the distribution mean $\langle E_T\rangle$.

Fluctuations in acceptance

The 200 GeV Au+Au 0-5% centrality class E_T distribution fluctuations, cast in three forms, were measured over a $\Delta\phi$ = 6-fold increase of the azimuthal solid angle. This was done using the n = 1, 2, ..., 6 PbSc calorimeters. Over this increase in acceptance the scaled variance $\frac{\sigma^2}{\langle E_T\rangle}$ rises 115%. The fluctuation cast in terms of $\frac{\langle E_T\rangle^2}{\sigma^2 n}$ fit

$$\frac{\langle E_T\rangle^2}{\sigma^2 n}_{(200\ \text{GeV}\ 0-5\%)} = 50e^{-0.5\sqrt{n}}; \tag{153}$$

the physical significance of this fit was not explored further. To check the systematic effect of shower spread across sectors, and for correlated jets, incrementation of the acceptance was done in the various trial configurations of neighboring sectors, back-to-back sectors, and not-neighbor nor back-to-back sectors; results show negligible effect on the rise in fluctuations. Finally the fluctuation was cast in terms of the distribution cumulant k (making use of the measured mean cluster transverse energy e_T to produce a dimensionless k)

$$k = \frac{\sigma^2}{\mu^2} - \frac{e_T}{\mu}. \tag{154}$$

A correlation length ζ was obtained by fitting k vs. ϕ-acceptance (Δn) to a particle correlation function; a result of $\zeta = 0.14$ PbSc sectors, which is equivalent to 28 cm was obtained (about the size of 5 PbSc towers). The EMC, which is out at a distance of 5.1 meters from the interaction region, subtends an angle in $\Delta\phi$ of $22°$, thus the correlation length measured is $3.1°$

$$\begin{aligned} \zeta &= 3.1° \quad (155) \\ &\sim 28 \text{ cm} \sim 5 \text{ PbSc towers}; \quad (156) \end{aligned}$$

Correlations due to π^0 shower spread, reaction plane rotation, and elliptic flow were not addressed and these issues should be considered before drawing any further conclusions.

Background removal in Au+Au: design of cuts

Two sources of background were identified and removed in the 200 GeV Au+Au minbias cleaning up the data down to ~ 6 orders of magnitude. Over the 50-93% peripheral centrality range the data still contains pile-up events 5 to 6 orders down. The 200 GeV Au+Au background was of two types. Triggers with event times right outside the BBC dynamic range resulting in a $10^{-3} - 10^{-4}$ background; this is removed by retaining only events having a valid BBC Zvertex. The second type is pile-up of two events in the same bunch crossing; this was removed via a geometrical cut placed above the ZDC energy vs. BBC charge scatter plot of events (the centrality-by-clock). The 62.4 GeV Au+Au background identified and removed was that due to a scheduled electronic reset in Pad Chamber 1 which corrupted minbias triggered events in bunch crossings 57-71.

Faulty PbSc tower removal, an enhanced method

Analysis code for a faulty PbSc tower identification, mapping, and removal technique was written. The process locates dead and hot towers by comparing the response of individual towers to the average response of all towers summed over many events. Specifically, only the responses in towers identified as the central tower in each cluster were compared to the average response of all central towers. This is done on a sector by sector basis. The comparison was done by summing the central tower energy over many events and towers having more energy than the average plus 3.5 σ are considered hot, dumping spurious energy into the events. Hot towers were removed. Additionally all neighboring towers in a 3×3 tower area around each hot tower were removed (the average shower size of a π^0, which make up a lot of the particles on each event, is about a 3×3 tower area). Thus removing the neighboring towers eliminates hot tower energy from getting into the events when the hot tower is not the central tower in the cluster. Towers which had recorded zero energy over the events are considered dead and were identified. The geometric acceptance of the total number of removed plus dead towers was computed and accounted for in the physics analyses. Previous faulty tower identification and removal used in PHENIX compared only the multiplicity in central towers but not the energy. In E_T analyses energy is the variable being measured and as such the energy-per-tower method to remove faulty towers is more appropriate. A qualitative comparison of the two methods was performed however results did not indicate that either method was significantly better than the other. A conclusion was drawn that both energy-per-tower and multiplicity-per-tower should be checked in removing faulty towers, as long as the resultant smaller acceptance does not have any larger negative effect (than the faulty towers did) on the physics being investigated.

PHENIX Preliminary plots

The plots shown in Figures 135 on page 274 through Figure 140 on page 279 were made during the course of this thesis work and have been approved in the PHENIX Global Working Group to PHENIX "Preliminary Status" in preparation for publication. They were published in Proceedings of the 19th International Particles and Nuclear Interactions Conference (PANIC) [9]. Two new results are

1. in 62.4 GeV Au+Au event-by-event distributions no dynamical fluctuations are observed above the approximate 20% systematic error; this result is illustrated in Figure 137 on page 276.

2. the second distribution moment, σ_{E_T}, scales with $N^{\alpha}_{\mathrm{nuc-part}}$ as does E_T, and shown in Figure 139 on page 278 and Figure 140 on page 279.

A TABLES SECTION

LEAD PROPERTY	VALUE
density	$\rho = 11.35$ g/cm^3
atomic number	$Z = 82$
atomic weight	$A = 207.2$
total cross section	$\sigma_T = 2.96$ barns
absorption cross section	$\sigma_{abs} = 1.77$ barns
radiation length	$X_0 = 6$ g/cm^2
radiation length (cm)	$X_{0\ (\mathrm{cm})} = 0.53$ cm
interaction length	$L_I = 116.2$ g/cm^2
interaction length (cm)	$L_{I\ (\mathrm{cm})} = 10.2$ cm
absorption length	$\lambda_{abs} = 194$ g/cm^2
absorption length (cm)	$\lambda_{abs\ (\mathrm{cm})} = 17$ cm
PbSc PROPERTY	**VALUE**
PbSc absorption lengths	0.51
PbSc radiation lengths	18
PbSc Interaction lengths	0.85
PbSc Energy resolution	$\frac{\Delta E}{E} = \frac{0.08}{\sqrt{E\ (\mathrm{GeV})}}$

Table 1: Properties of lead and specifications for the PHENIX PbSc EMC calorimeters (discussed in Chapter 2.2.1).

SPECIES	NUMBER OF EVENTS	$\langle E_{T\ (\mathrm{EMC})}\rangle$ (GeV)	$\frac{dE_T}{d\eta}$ (GeV)	$\sigma_{E_{T\ (\mathrm{EMC})}}$ (GeV)	$\sigma^2_{E_{T\ (\mathrm{EMC})}}$ (GeV^2)
$p+p$	15.18E6	0.505	1.71	0.53	0.28
d+Au	10.81E6	1.51	8.60	1.29	1.67

Table 2: 200 GeV $p+p$ and d+Au minbias inclusive $\langle E_{T\ (\mathrm{EMC})}\rangle$, $\frac{dE_T}{d\eta}$, $\sigma_{E_{T\ (\mathrm{EMC})}}$, and $\sigma^2_{E_{T\ (\mathrm{EMC})}}$ measured in 4.53 ($p+p$) and 4.51 (d+Au) "equivalent sectors" after removal of faulty towers – from the data (not fits). Minbias triggers having zero EMC energy were discarded amounting to ~19% of $p+p$ events and 6% of d+Au events. For the measurement of $\frac{dE_T}{d\eta}$ corrections included: values of 6.03 for $p+p$ and 6.07 for d+Au (which includes a k-correction of 1.3 borrowed blindly from Au+Au simulations, plus corrections for faulty towers and geometric acceptance), and the minbias triggers having zero EMC energy were re-included amounting to factors of 0.813 ($p+p$) and 0.94 (d+Au), and for $p+p$ an additional correction was applied for inelastic collisions which did not trigger the BBC of $\frac{\sigma_{\mathrm{BBC}}/\sigma_{p+p}}{\epsilon_{\mathrm{EMC}}} = \frac{21.8\ \mathrm{mb}/41\ \mathrm{mb}}{0.75} = 0.52/0.75 = 0.69$. Thus for $p+p$: $\frac{dE_T}{d\eta} = 6.03 \times 0.813 \times 0.69 \times \langle E_{T\ (\mathrm{EMC})}\rangle$, and for d+Au: $\frac{dE_T}{d\eta} = 6.07 \times 0.94 \times \langle E_{T\ (\mathrm{EMC})}\rangle$; the systematic error is provided on the physics results in Table 11. Discussed in Chapter 5.2.1. For corresponding Figure see list in Chapter 6.

CENTRALITY	NUMBER OF EVENTS	$\langle E_{T\ (\mathrm{EMC})} \rangle$ (GeV)	$\frac{dE_T}{d\eta}$ (GeV)	$\sigma_{E_{T\ (\mathrm{EMC})}}$ (GeV)	$\sigma^2_{E_{T\ (\mathrm{EMC})}}$ (GeV^2)
0% - 93%	42,939,350	32.41	161.17	35.34	1248.92
0% - 5%	2,321,373	118	586.81	13.73	188.51
5% - 10%	2,318,003	96.29	478.85	12.80	163.84
10% - 15%	2,319,586	79.16	393.66	11.59	134.33
15% - 20%	2,318,475	65.21	324.29	10.42	108.58
20% - 25%	2,310,642	53.55	266.30	9.25	85.58
25% - 30%	2,308,504	43.67	217.17	8.127	66.05
30% - 35%	2,306,359	35.27	175.40	7.082	50.15
35% - 40%	2,306,312	28.14	139.94	6.122	37.48
40% - 45%	2,305,233	22.12	110.00	5.266	27.73
45% - 50%	2,303,372	17.07	84.89	4.518	20.41
50% - 55%	2,304,443	12.91	64.20	3.879	15.05
55% - 60%	2,296,549	9.523	47.36	3.333	11.11
60% - 65%	2,300,982	6.856	34.09	2.875	8.27
65% - 70%	2,300,955	4.788	23.81	2.479	6.14
70% - 75%	2,296,024	3.281	16.32	2.113	4.46
75% - 80%	2,302,282	2.261	11.24	1.757	3.09

Table 3: 200 GeV Au+Au minbias $\langle E_{T\ (\mathrm{EMC})} \rangle$, $\frac{dE_T}{d\eta}$, σ_{E_T}, $\sigma^2_{E_T}$ from data (not fits), in 5.5 equiv. PbSc sectors, centrality-by-clock assuming 93% $\sigma_{\mathrm{Au+Au}}$ visible. $\frac{dE_T}{d\eta} = 4.973 \times \langle E_{T\ (\mathrm{EMC})} \rangle$ includes corrections $k = 1.3$, for faulty towers, geometric acceptance. Error given in Table 8. For corresponding Figure see list in Chapter 6.

CENTRALITY	NUMBER OF EVENTS	$\langle E_{T\ (\mathrm{EMC})}\rangle$ (GeV)	$\frac{dE_T}{d\eta}$ (GeV)	$\sigma_{E_{T\ (\mathrm{EMC})}}$ (GeV)	$\sigma^2_{E_{T\ (\mathrm{EMC})}}$ (GeV^2)
0% - 83.7%	22,401,880	21.71	108.92	22.90	524.41
0% - 5%	1,370,543	75.33	377.93	9.464	89.57
5% - 10%	1,337,487	60.80	305.03	8.594	73.86
10% - 15%	1,337,903	49.29	247.29	7.541	56.87
15% - 20%	1,337,890	40.01	200.73	6.733	45.33
20% - 25%	1,337,665	32.32	162.15	6.026	36.31
25% - 30%	1,336,212	25.90	129.94	5.365	28.78
30% - 35%	1,336,219	20.53	103.00	4.754	22.60
35% - 40%	1,335,911	16.04	80.47	4.165	17.35
40% - 45%	1,335,638	12.34	61.91	3.602	12.97
45% - 50%	1,337,308	9.313	46.72	3.057	9.34
50% - 55%	1,336,913	6.879	34.51	2.534	6.42
55% - 60%	1,335,651	4.941	24.79	2.055	4.22
60% - 65%	1,336,332	3.428	17.20	1.63	2.66
65% - 70%	1,335,633	2.286	11.47	1.271	1.61

Table 4: 62.4 GeV Au+Au $\langle E_{T\ (\mathrm{EMC})}\rangle$, $\frac{dE_T}{d\eta}$, $\sigma_{E_{T\ (\mathrm{EMC})}}$, and $\sigma^2_{E_{T\ (\mathrm{EMC})}}$ from data (not fits), in 5.46 equivalent PbSc sectors, in centrality-by-BBC assuming 83.7% of $\sigma_{\mathrm{Au+Au}}$ visible. $\frac{dE_T}{d\eta} = 5.017 \times \langle E_{T\ (\mathrm{EMC})}\rangle$ which includes corrections $k = 1.3$, for faulty towers, and geometric acceptance. Systematic error provided in Table 9. Data is minbias plus requirement of 2 hits per BBC, which includes a small number ($< 1\%$) of minbias triggers which resulted in zero $E_{T\ (\mathrm{EMC})}$. For corresponding Figure see list in Chapter 6.

CENTRALITY	$\langle E_{T\ (\mathrm{EMC})} \rangle$ data (GeV)	$\langle E_{T\ (\mathrm{EMC})} \rangle$ fit (GeV)	$\frac{\sigma^2}{\langle E_{T\ (\mathrm{EMC})} \rangle}$ data (GeV)	$\frac{\sigma^2}{\langle E_{T\ (\mathrm{EMC})} \rangle}$ fit (GeV)	$\frac{\chi^2}{\mathrm{dof}}$ fit
0% - 5%	118	116.0	1.60	1.61	$\frac{996.6}{107} = 9.31$
5% - 10%	96.29	94.8	1.70	1.72	$\frac{57.9665}{101} = 0.58$
10% - 15%	79.16	77.5	1.70	1.72	$\frac{40.6873}{95} = 0.43$
15% - 20%	65.21	63.5	1.66	1.71	$\frac{178.449}{87} = 2.05$
20% - 25%	53.55	51.9	1.60	1.62	$\frac{276.769}{76} = 3.64$
25% - 30%	43.67	42.1	1.51	1.53	$\frac{480.852}{67} = 7.18$
30% - 35%	35.27	33.8	1.42	1.43	$\frac{662.252}{59} = 11.22$
35% - 40%	28.14	26.8	1.33	1.34	$\frac{869.353}{53} = 16.40$
40% - 45%	22.12	20.8	1.25	1.30	$\frac{1097.89}{46} = 23.86$
45% - 50%	17.07	15.8	1.20	1.24	$\frac{1295.77}{39} = 33.22$
50% - 55%	12.91	11.7	1.17	1.22	$\frac{1212.78}{35} = 34.65$
55% - 60%	9.52	8.32	1.17	1.27	$\frac{768.332}{28} = 27.44$
60% - 65%	6.86	5.60	1.21	1.37	$\frac{229.715}{24} = 9.57$
65% - 70%	4.79	3.70	1.28	1.55	$\frac{29.7367}{21} = 1.42$
70% - 75%	3.28	2.37	1.36	1.81	$\frac{601.15}{19} = 31.64$

Table 5: 200 GeV Au+Au $E_{T\ (\mathrm{EMC})}$ distributions fitted to the Negative Binomial Distribution. 5.5 equivalent PbSc sectors measured in centrality-by-clock. The entries in the Table are from Figures 97, 98, 99, and 100 (fits to the NBD courtesy Jeff Mitchell (BNL)). For corresponding Figure see list in Chapter 6.

$\langle N_{\mathrm{nuc-part}} \rangle$	W0 (GeV)	W1 (GeV)	W2 (GeV)	W3 (GeV)	E2 (GeV)	E3 (GeV)	6 sectors (GeV)
353	3.313	3.377	3.440	3.327	3.270	3.227	3.326
300	3.178	3.241	3.310	3.193	3.138	3.098	3.192
254	3.086	3.147	3.206	3.101	3.048	3.008	3.100
215	3.003	3.063	3.119	3.018	2.966	2.928	3.017
181	2.930	2.986	3.044	2.945	2.893	2.856	2.943
151	2.863	2.920	2.975	2.879	2.828	2.792	2.876
125	2.792	2.850	2.904	2.809	2.760	2.723	2.806
103	2.704	2.759	2.812	2.720	2.673	2.636	2.718
83.3	2.627	2.681	2.734	2.644	2.598	2.562	2.641
66.7	2.532	2.584	2.635	2.550	2.504	2.468	2.546
52.5	2.430	2.481	2.533	2.450	2.405	2.372	2.445
40.2	2.339	2.391	2.439	2.363	2.317	2.285	2.356
30.2	2.243	2.289	2.339	2.263	2.222	2.190	2.258
22	2.148	2.193	2.242	2.170	2.129	2.102	2.165
α_{fit}	1.153	1.152	1.151	1.151	1.152	1.152	1.155

Table 6: 200 GeV Au+Au $\frac{1}{0.5\langle N_{\mathrm{nuc-part}} \rangle}\langle \frac{dE_T}{d\eta} \rangle$ measured in the 6 individual PbSc sectors (W0, W1, W2, W3, E2, and E3) and in the 6-sector combination, for the different number of participant nucleons $\langle N_{\mathrm{nuc-part}} \rangle$. Also indicated is the value of α_{fit} obtained from the power law fit $\langle E_T \rangle \sim \langle N_{\mathrm{nuc-part}} \rangle^{\alpha}$. Table entries correspond to Figure 105.

$\langle N_{\mathrm{nuc-part}} \rangle$	W0 (GeV)	W1 (GeV)	W2 (GeV)	W3 (GeV)	E2 (GeV)	E3 (GeV)	6 sectors (GeV)
345.1	2.150	2.197	2.269	2.206	2.174	2.133	2.190
296.3	2.021	2.065	2.132	2.073	2.044	2.006	2.059
250.3	1.940	1.981	2.045	1.990	1.962	1.926	1.976
211	1.867	1.908	1.971	1.917	1.889	1.853	1.903
177.7	1.790	1.831	1.890	1.839	1.811	1.777	1.825
148.7	1.714	1.753	1.811	1.762	1.736	1.701	1.748
123.8	1.631	1.669	1.725	1.678	1.653	1.620	1.664
102.1	1.545	1.580	1.634	1.589	1.566	1.534	1.576
82.9	1.463	1.498	1.548	1.506	1.484	1.453	1.493
66.2	1.383	1.416	1.463	1.423	1.403	1.373	1.411
51.9	1.302	1.333	1.379	1.342	1.322	1.292	1.330
α_{fit}	1.260	1.258	1.257	1.257	1.258	1.260	1.258

Table 7: 62.4 GeV Au+Au $\frac{1}{0.5\langle N_{\mathrm{nuc-part}} \rangle}\langle \frac{dE_T}{d\eta} \rangle$ measured in the individual PbSc sectors (W0, W1, W2, W3, E2, and E3) and in the 6-sector combination, for the different number of participant nucleons $\langle N_{\mathrm{nuc-part}} \rangle$. Also indicated is the value of α_{fit} obtained from the power law fit $\langle E_T \rangle \sim \langle N_{\mathrm{nuc-part}} \rangle^{\alpha}$. Table entries correspond to Figure 106.

CENTRALITY	$\langle N_{\mathrm{nuc-part}} \rangle$	$\frac{1}{0.5\langle N_{\mathrm{nuc-part}}\rangle}\langle\frac{dE_T}{d\eta}\rangle$ (GeV)	Bending Error ($\pm$ GeV)
0% - 5%	353	3.33	0.01
5% - 10%	300	3.19	0.03
10% - 15%	254	3.10	0.05
15% - 20%	215	3.02	0.07
20% - 25%	181	2.94	0.09
25% - 30%	151	2.88	0.12
30% - 35%	125	2.81	0.14
35% - 40%	103	2.72	0.17
40% - 45%	83.3	2.64	0.19
45% - 50%	66.7	2.55	0.23
50% - 55%	52.5	2.44	0.29
55% - 60%	40.2	2.36	0.33
60% - 65%	30.2	2.26	0.39
65% - 70%	22	2.16	0.48

Table 8: 200 GeV Au+Au $\frac{1}{0.5\langle N_{\mathrm{nuc-part}}\rangle}\langle\frac{dE_T}{d\eta}\rangle$: systematic error 5.5%, statistical error $< 0.035\%$. (values for $\langle\frac{dE_T}{d\eta}\rangle$ used here obtained from Table 3). For corresponding Figure see list in Chapter 6.

CENTRALITY	$\langle N_{\mathrm{nuc-part}}\rangle$	$\frac{1}{0.5\langle N_{\mathrm{nuc-part}}\rangle}\langle\frac{dE_T}{d\eta}\rangle$ (GeV)	Bending Error ($\pm$ GeV)
0% - 5%	345.1	2.19	0.014
5% - 10%	296.3	2.06	0.031
10% - 15%	250.3	1.98	0.043
15% - 20%	211	1.90	0.057
20% - 25%	177.7	1.82	0.075
25% - 30%	148.7	1.75	0.10
30% - 35%	123.8	1.66	0.10
35% - 40%	102.1	1.58	0.12
40% - 45%	82.9	1.49	0.14
45% - 50%	66.2	1.41	0.16
50% - 55%	51.9	1.33	0.17

Table 9: 62.4 GeV Au+Au $\frac{1}{0.5\langle N_{\mathrm{nuc-part}}\rangle}\langle\frac{dE_T}{d\eta}\rangle$: systematic error $<$ 7.1%, statistical error $<$ 0.035%. (values for $\langle\frac{dE_T}{d\eta}\rangle$ used here obtained from Table 4). For corresponding Figure see list in Chapter 6.

CENTRALITY	$\frac{\langle N_{\text{quark-part}}\rangle}{\langle N_{\text{nuc-part}}\rangle}$	$\frac{1}{0.5\langle N_{\text{quark-part}}\rangle}\langle\frac{dE_T}{d\eta}\rangle$ (GeV)	Top Bend (GeV)	Bottom Bend (GeV)
0% - 5%	2.44	1.360	1.364	1.357
5% - 10%	2.38	1.341	1.353	1.329
10% - 15%	2.32	1.339	1.360	1.317
15% - 20%	2.25	1.339	1.370	1.308
20% - 25%	2.19	1.344	1.385	1.302
25% - 30%	2.13	1.353	1.410	1.296
30% - 35%	2.06	1.362	1.431	1.293
35% - 40%	2.00	1.361	1.448	1.274
40% - 45%	1.93	1.370	1.472	1.269
45% - 50%	1.86	1.370	1.493	unav.
50% - 55%	1.79	1.369	1.529	unav.
55% - 60%	1.71	1.378	1.574	unav.
60% - 65%	1.63	1.384	1.626	unav.
65% - 70%	1.55	1.398	1.711	unav.

Table 10: 200 GeV Au+Au $\frac{1}{0.5\langle N_{\text{quark-part}}\rangle}\langle\frac{dE_T}{d\eta}\rangle$: statistical error $< 0.035\%$, systematic error 5.5%. The top and bottom "Bend" is the bending error discussed in the text. $\langle N_{\text{nuc-part}}\rangle/\langle N_{\text{quark-part}}\rangle$ error not estimated. Values for $\langle\frac{dE_T}{d\eta}\rangle$ obtained from Table 3, and values of $\langle N_{\text{quark-part}}\rangle$ taken from [21]. For corresponding Figure see list in Chapter 6.

SPECIES	$\langle N_{\mathrm{nuc-part}} \rangle$	$\frac{1}{0.5\langle N_{\mathrm{nuc-part}}\rangle}\langle\frac{dE_T}{d\eta}\rangle$ (GeV)	Error on $\frac{1}{0.5\langle N_{\mathrm{nuc-part}}\rangle}\langle\frac{dE_T}{d\eta}\rangle$ (GeV)	$\frac{\sigma^2}{\langle E_{T\ (\mathrm{EMC})}\rangle}$ (GeV)
$p+p$	2	1.712	$\pm$ 0.13	0.542
d+Au	9.1	1.89	$\pm$ 0.14	1.102

Table 11: 200 GeV minbias inclusive $p+p$ and d+Au $\frac{1}{0.5\langle N_{\mathrm{nuc-part}}\rangle}\langle\frac{dE_T}{d\eta}\rangle$ and $\frac{\sigma^2}{\langle E_{T\ (\mathrm{EMC})}\rangle}$, measured in 4.53 ($p+p$) and 4.51 ($d$+Au) equivalent sectors from the data (not fits). For the measurement of $\frac{\sigma^2}{\langle E_{T\ (\mathrm{EMC})}\rangle}$: minbias triggers having zero EMC energy were discarded amounting to 19% of $p+p$ events and 6% of d+Au events; systematic errors were not estimated and the affect of the zeros should be examined; statistical vertical scale errors are negligible. For the measurements of $\frac{1}{0.5\langle N_{\mathrm{nuc-part}}\rangle}\langle\frac{dE_T}{d\eta}\rangle$ the values of $\langle\frac{dE_T}{d\eta}\rangle$ used here were obtained from Table 2; error shown is Systematic error; error was not determined for PbSc sector electronic noise; statistical vertical scale error $< 0.035\%$. For corresponding Figure see list in Chapter 6.

CENTRALITY	$\langle N_{\mathrm{nuc-part}} \rangle$	$\frac{\sigma}{\langle E_{T\ (\mathrm{EMC})} \rangle}$ (dimensionless)	$\frac{\sigma^2}{\langle E_{T\ (\mathrm{EMC})} \rangle}$ (GeV)
0% - 5%	353	0.116	1.60
5% - 10%	300	0.133	1.70
10% - 15%	254	0.146	1.70
15% - 20%	215	0.160	1.66
20% - 25%	181	0.173	1.60
25% - 30%	151	0.186	1.51
30% - 35%	125	0.201	1.42
35% - 40%	103	0.217	1.33
40% - 45%	83.3	0.238	1.25
45% - 50%	66.7	0.265	1.20

Table 12: 200 GeV Au+Au $\frac{\sigma}{\langle E_{T\ (\mathrm{EMC})} \rangle}$ and $\frac{\sigma^2}{\langle E_{T\ (\mathrm{EMC})} \rangle}$ measured in 6 PbSc sectors – or 5.5 equivalent sectors after removal of faulty towers – with centrality-by-clock, from the data (not fits). Geometry fluctuation corrections not applied. Systematic run-by-run vertical scale error $< 1\%$, statistical vertical scale error $< 0.1\%$. For corresponding Figure see list in Chapter 6.

CENTRALITY	$\langle N_{\text{nuc-part}} \rangle$	$\frac{\sigma}{\langle E_{T\ (\text{EMC})} \rangle}$ (dimensionless)	$\frac{\sigma^2}{\langle E_{T\ (\text{EMC})} \rangle}$ (GeV)
0% - 5%	345.1	0.126	1.19
5% - 10%	296.3	0.141	1.21
10% - 15%	250.3	0.153	1.15
15% - 20%	211	0.168	1.13
20% - 25%	177.7	0.186	1.12
25% - 30%	148.7	0.207	1.11
30% - 35%	123.8	0.231	1.10
35% - 40%	102.1	0.260	1.08
40% - 45%	82.9	0.292	1.05
45% - 50%	66.2	0.328	1.00

Table 13: 62.4 GeV Au+Au $\frac{\sigma}{\langle E_{T\ (\text{EMC})} \rangle}$ and $\frac{\sigma^2}{\langle E_{T\ (\text{EMC})} \rangle}$ measured in 6 PbSc sectors – or 5.45 equivalent sectors after removal of faulty towers – with centrality-by-BBC, from the data (not fits). Geometry fluctuation corrections not applied. Systematic run-by-run vertical scale error $< 1\%$, statistical vertical scale error $< 0.1\%$. For corresponding Figure see list in Chapter 6.

n ($\Delta\phi$)	μ (GeV)	σ (GeV)	k (dimensionless)	$\frac{p}{n}$ (dimensionless)	$\frac{\sigma^2}{\mu}$ (GeV)
0.92 sectors	19.65	3.81	40.16	29.09	0.73
1.90 sectors	41	6.26	58.14	22.65	0.95
2.81 sectors	61.3	8.33	69.35	19.26	1.13
3.66 sectors	79.47	10.07	77.52	17.03	1.28
4.58 sectors	98.92	11.93	83.3	15.02	1.44
5.50 sectors	118	13.74	87	13.43	1.60

Table 14: 200 GeV Au+Au $0-5\%$ centrality E_T fluctuations in $\Delta\phi$ acceptance. $\langle E_{T\ (\mathrm{EMC})}\rangle \equiv \mu$, $\sigma_{E_{T\ (\mathrm{EMC})}} \equiv \sigma$, cumulant $k \equiv \frac{\sigma^2}{\mu^2} - \frac{e_T}{\mu}$, and $\frac{p}{n} \equiv \frac{\mu^2}{n\sigma^2}$. Measured with centrality-by-clock, results from the data (not fits). The nominal acceptance of 1 PbSc sector is 22.5° in $\Delta\phi$ and 45° in $\Delta\theta$. The PbSc sector combinations used in the measurements were: W0, W0+W1, W0+W1+W2, W0+W1+W2+W3, W0+W1+W2+W3+E2, and W0+W1+W2+W3+E2+E3, where the maximal difference in number of faulty towers removed from individual sectors was 15%. Systematic vertical scale error $< 3\%$ on p/n and σ^2/μ (not estimated independently for k); statistical vertical scale errors negligible. For corresponding Figure see list in Chapter 6.

B FIGURES SECTION

B.1 Figures referenced in Introduction

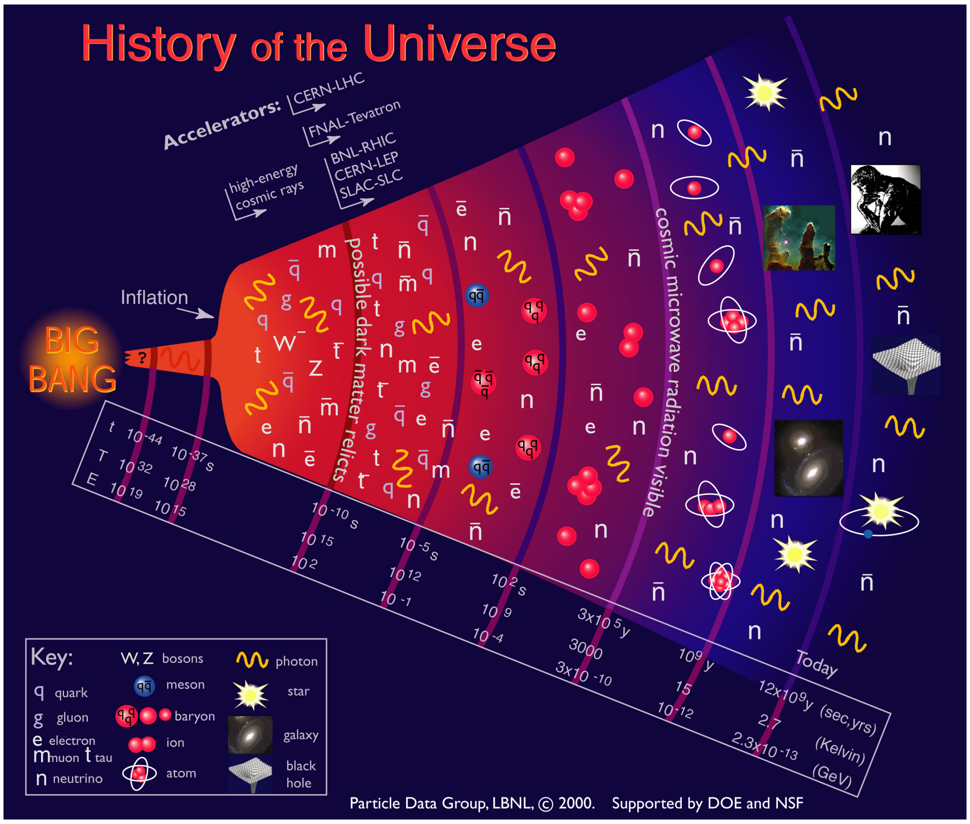

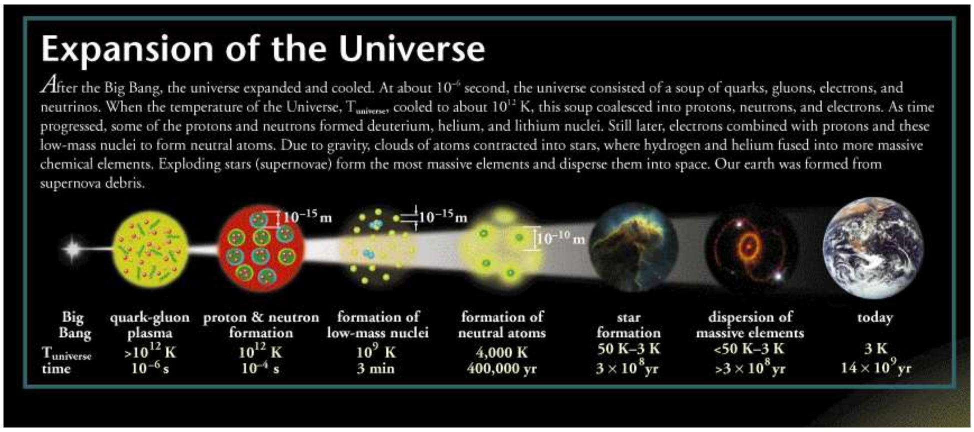

Figure 1: Big Bang creation of the universe and formation of matter into structure in various phases as the universe expanded and sub-sequentially cooled. Figure referneced in Chapter 1 (courtesy: permission for use of this figure by the copyright Contemporary Physics Education Project).

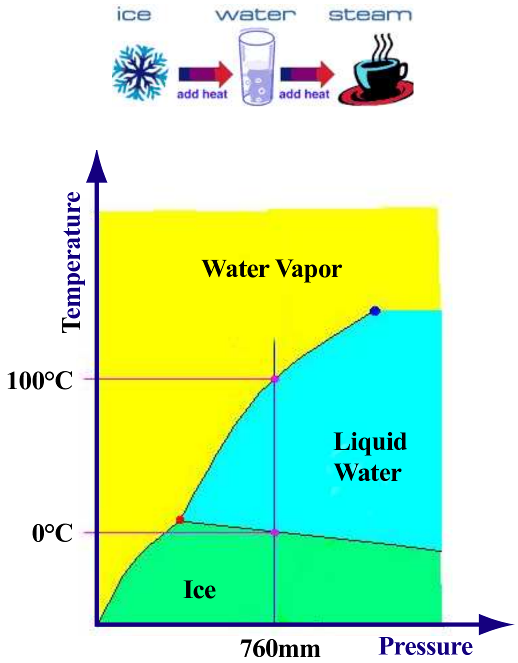

Figure 2: H_2O changes phases from ice, to water, to steam, and the associated phase transition diagram. Figure refernced in Chapter 1

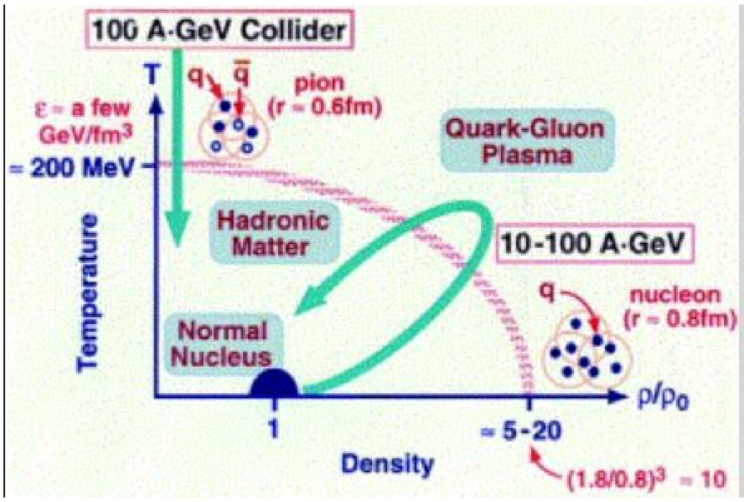

Figure 3: Hadronic-matter to QGP-matter phase change is illustrated in the phase transition diagram. Figure refernced in Chapter 1.

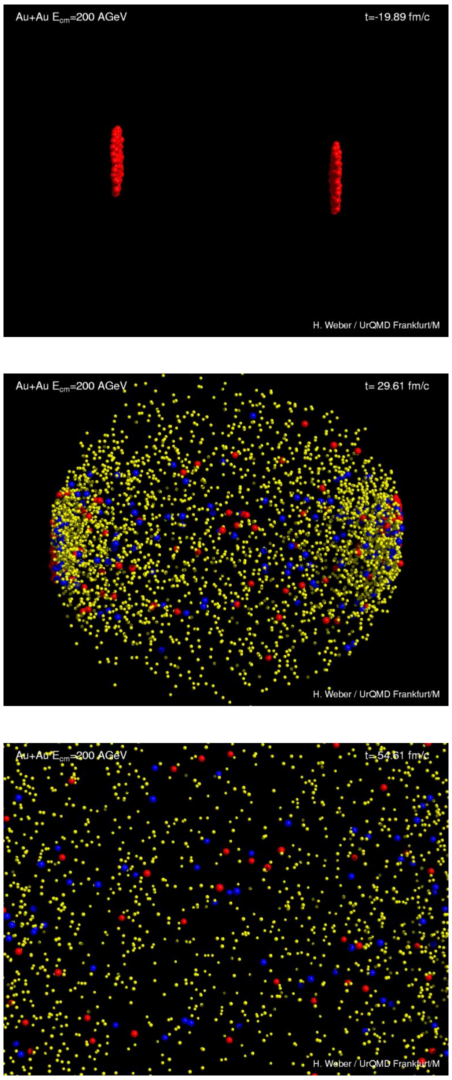

Figure 4: Computer simulation of a BNL-RHIC Au+Au collision at $\sqrt{s_{NN}} =$ 200 GeV per nucleon pair in the Ultra-relativistic quantum molecular dynamics (UrQMD) model: (top) before collision, (middle) much after the collision, and (bottom) a long time after the collision. The hadrons, in red, are relativistically flattened transverse to the collision axis before the collision, and afterward mesons are produced, in yellow, and excited baryons, in blue. Figure refernced in Chapter 1 (courtesy: H. Webber, J.W. Goethe-University, Frankfurt).

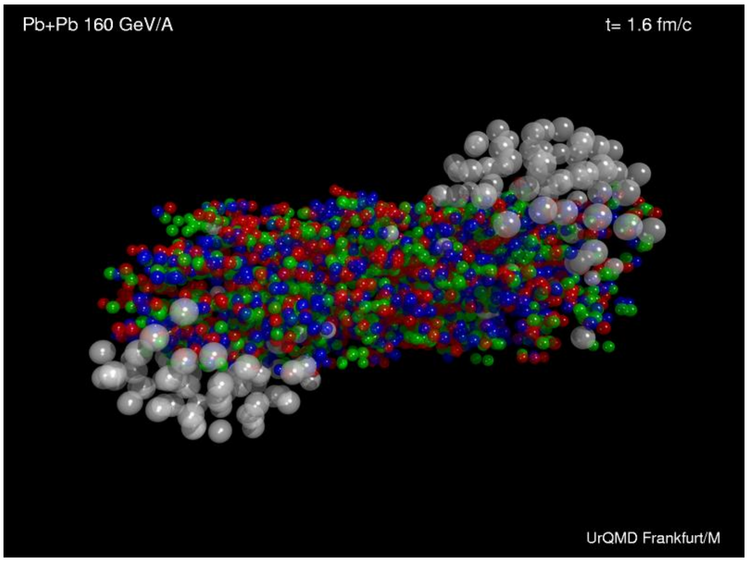

Figure 5: Computer simulation of a SPS CERN Pb+Pb nuclei collision at 160 GeV per nucleon (GeV/A) in the Ultra-relativistic quantum molecular dynamics (UrQMD) model. Shown at t = 1.6 fm/c which is immediately after the collision: the hadrons are in white, and the quarks in red, blue, and green, are stretched along the collision axis. Figure refernced in Chapter 1 (courtesy: H. Webber, J.W. Goethe-University, Frankfurt).

B.2 Figures referenced in Chapter 2

Figure 6: Sketch of RHIC accelerator facility at Brookhaven National Laboratory. Figure referenced in Chapter 2.

Figure 7: Satellite photos of RHIC ring on Long Island, NY

Figure 8: Aerial photo of the RHIC ring. Figure referenced in Chapter 2.

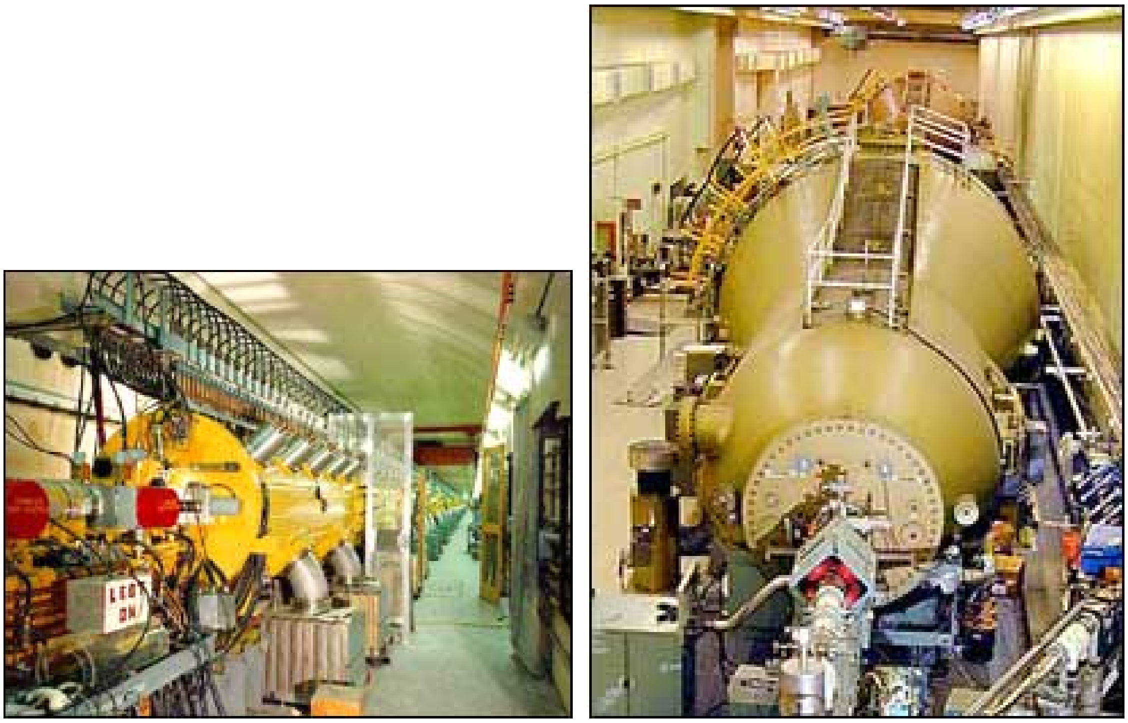

Figure 9: (left) 200 MeV Proton Linear Accelerator supplies protons, and (right) Heavy ion Tandem Van de Graaf accelerator supplies heavy ions to the AGS. Figure referenced in Chapter 2.

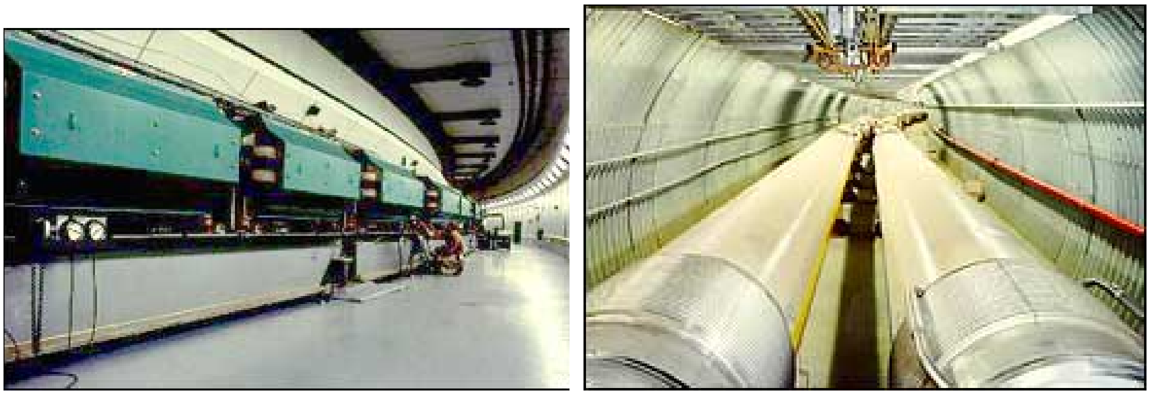

Figure 10: Alternating Gradient Synchrotron (AGS) increases the acceleration of protons and heavy ions, then feeds them to the (right) Relativistic heavy ion collider which speeds them up to 99.995% the speed of light and collides them. Figure referenced in Chapter 2. (courtesy: BNL Collider Accelerator Department).

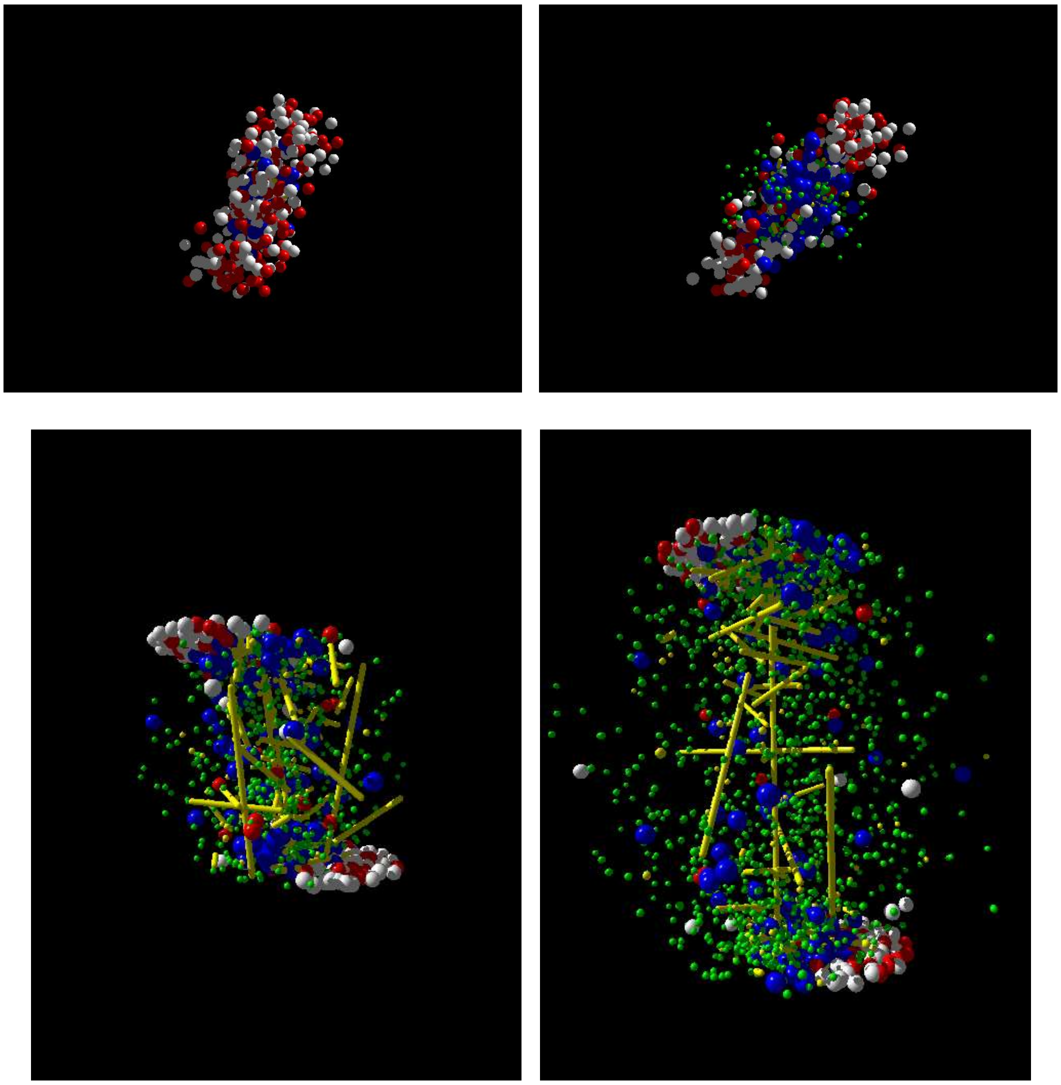

Figure 11: Computer simulations of a Au+Au collision with same impact parameter but for the different energies of (top left) 1.5 GeV/u, (top right) 10.6 GeV/u, (bottom left) 200 GeV/u, and (bottom right) 5 TeV/u, in the Ultra-relativistic quantum molecular dynamics (UrQMD) Cascade model. Note the increasing number of partons in higher collision energies. Color scheme: white and red are colliding nucleons, then after the collision are produced hadrons are in blue, quarks in green, and the long yellow bars are gluons. Figure referenced in Chapter 2. (courtesy: H. Webber, J.W. Goethe-University, Frankfurt).

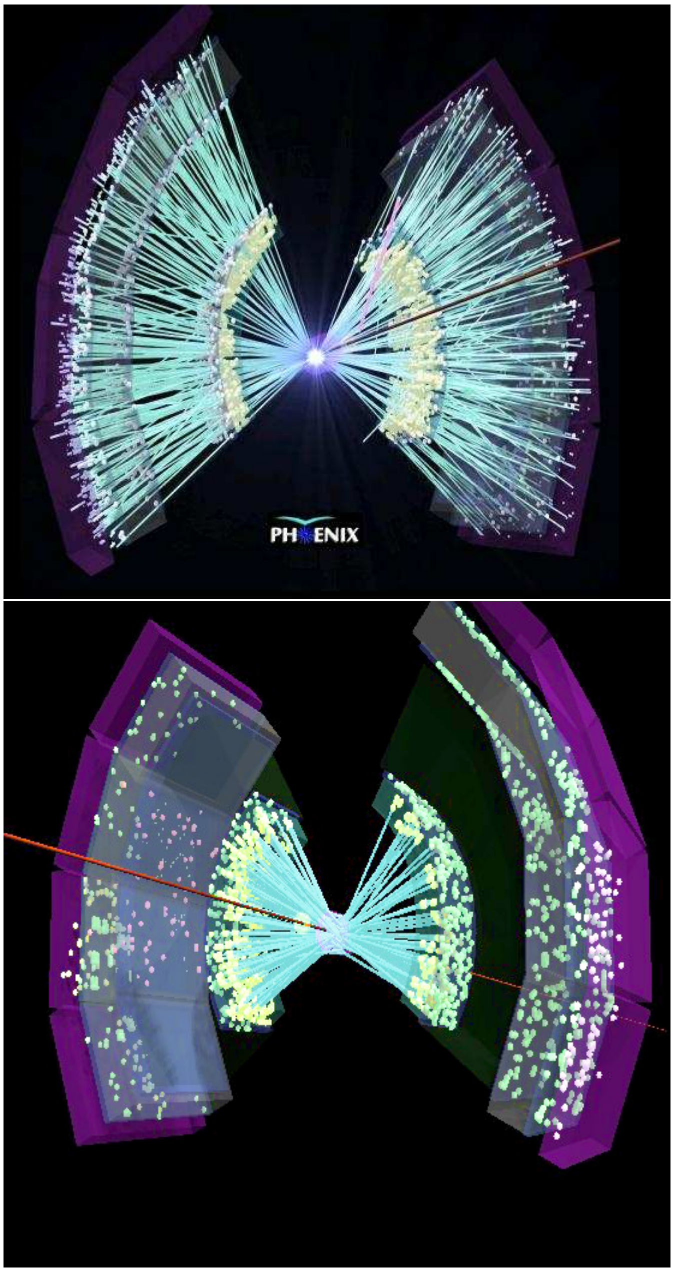

Figure 12: Computer reconstruction of a real RHIC single Au+Au central collision as detected by PHENIX: the Drift Chamber tracks and EMC hits (shown in green) emanate from the collision vertex; the beam path is shown in red Figure referenced in Chapter 2. (courtesy Dr. Jeffrey Mitchell, RHIC Run 2, BNL 2002)

Figure 13: PHENIX Group picture in front of the detectors. Figure referenced in Chapter 2.

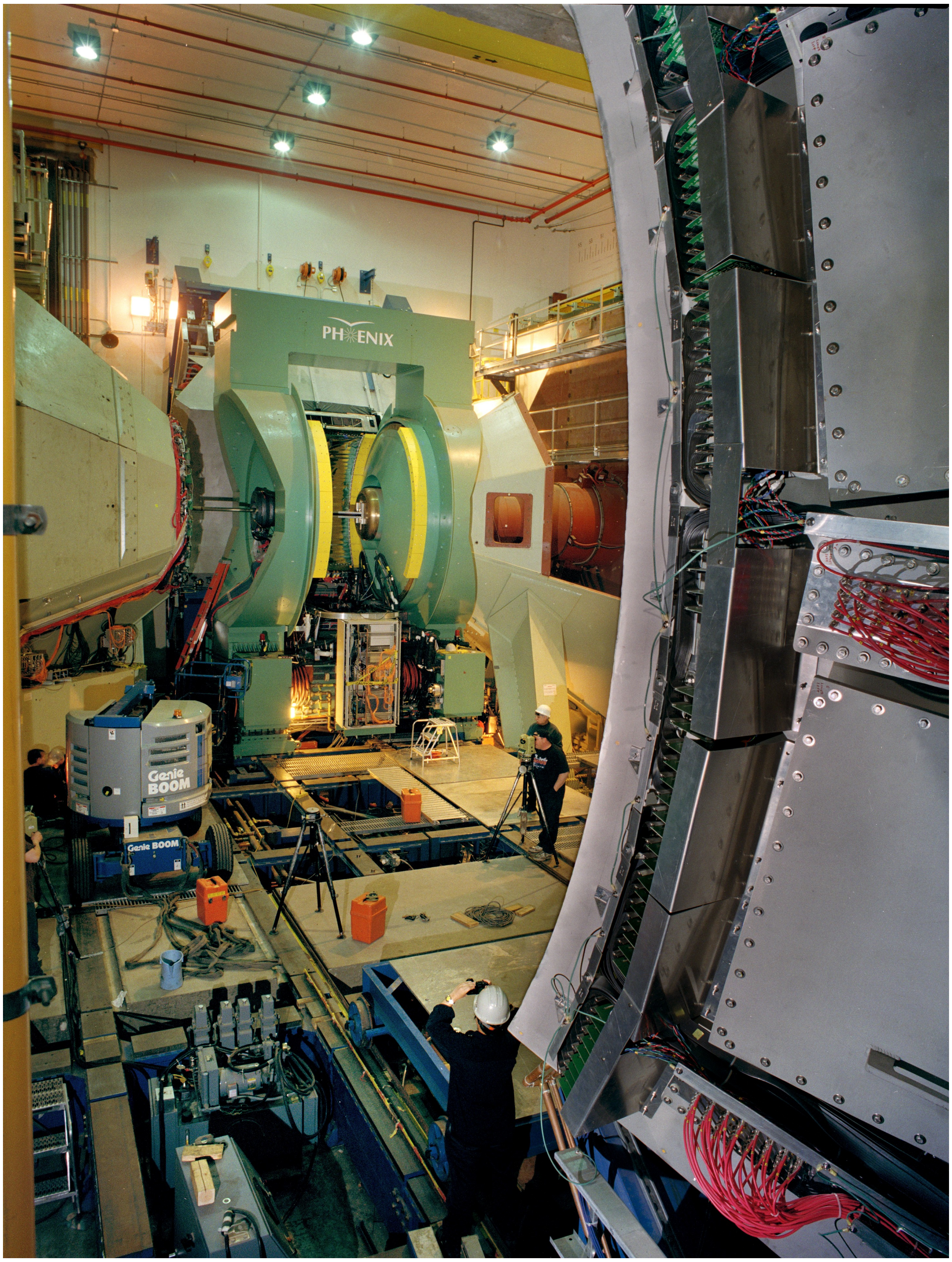

Figure 14: PHENIX experimental hall. Figure referenced in Chapter 2.

Figure 15: Photograph illustrating orientation of EMC and BBC detectors relative to the collision beam pipe. Figure referenced in Chapter 2.

Figure 16: The top plot shows the assembly of one PbSc EMC sector consisting of 18 PbSc supermodules; each supermodule consists of 36 PbSc modules, and each module contains 4 PbSc towers; thus there are 2592 towers per sector. The bottom plot shows the mounting of a PbSc sector onto the EMC arm; there are 4 sectors in the West Arm and two in the East Arm. Figure referenced in Chapter 2.

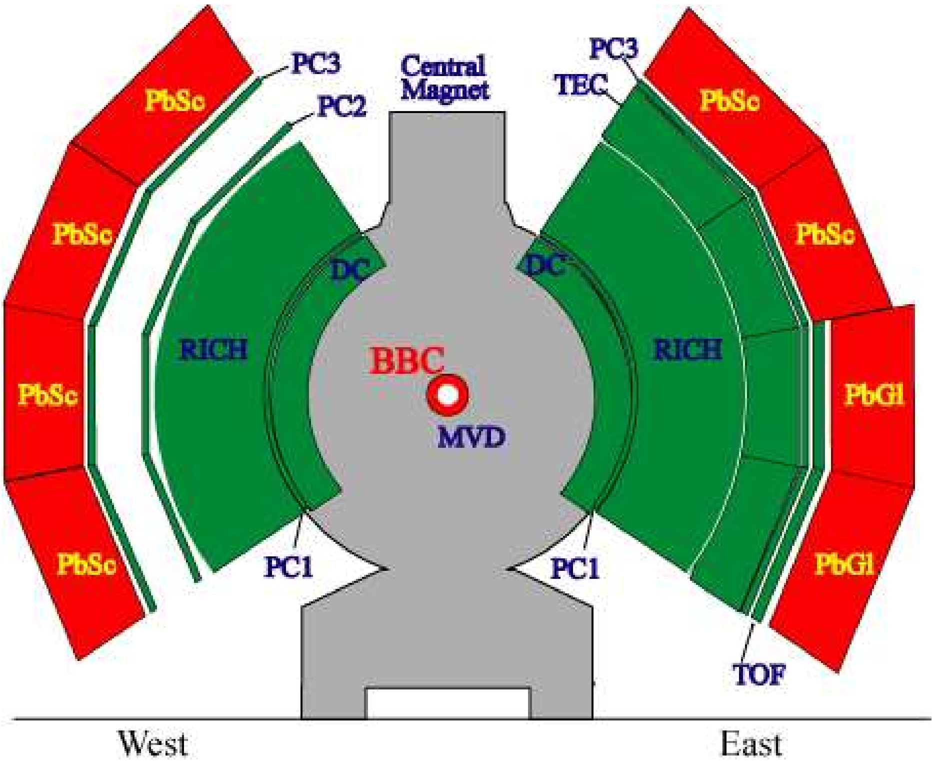

Figure 17: Sketch of the PHENIX PbSc EMC relative to other subsystems. Figure referenced in Chapter 2.

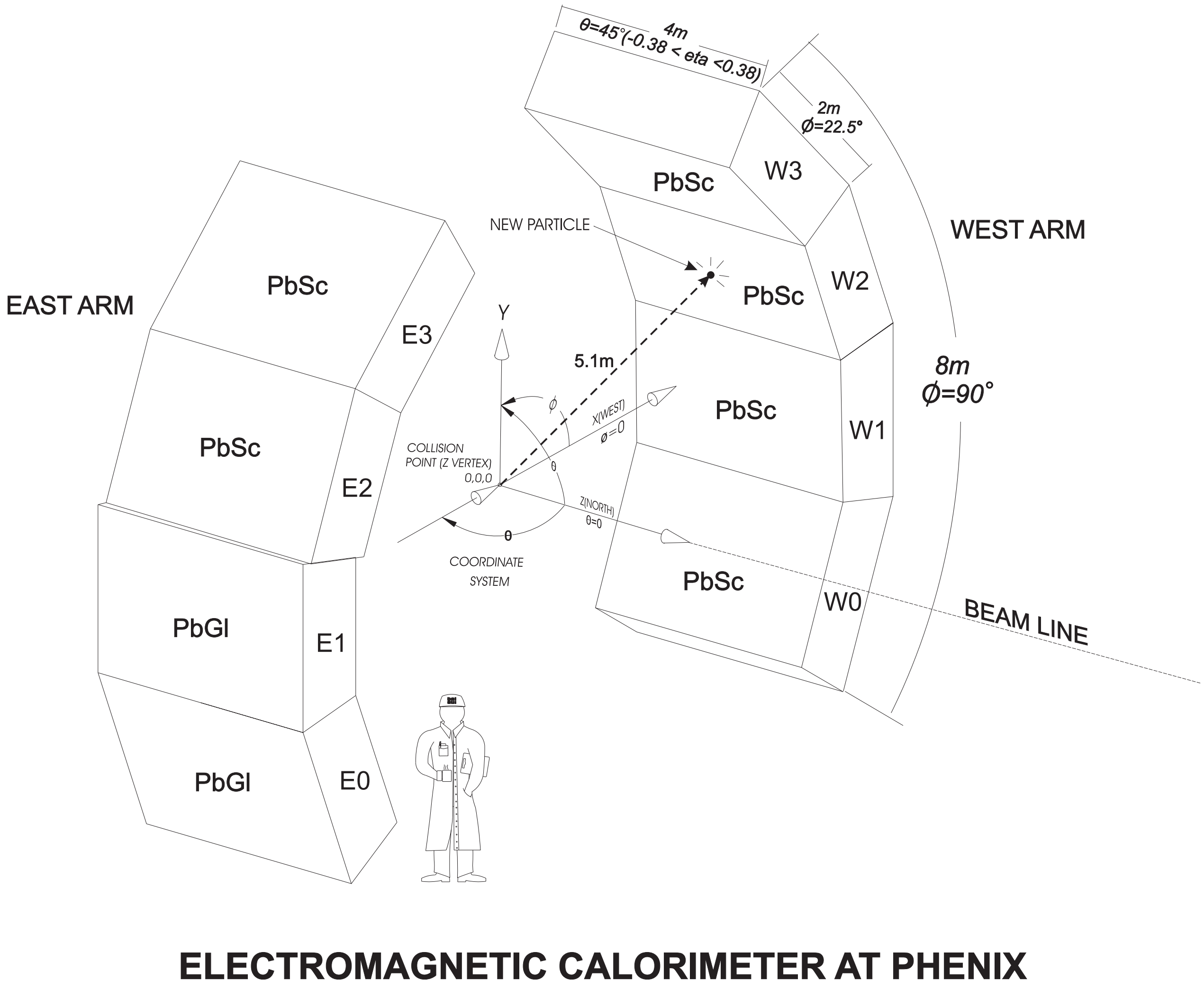

Figure 18: Sketch of the PHENIX EMC and coordinate systems (X, Y, Z), and (θ, ϕ). Figure referenced in Chapter 2. (drawn by Raul Armendariz and Richard Ruggiero at PHENIX).

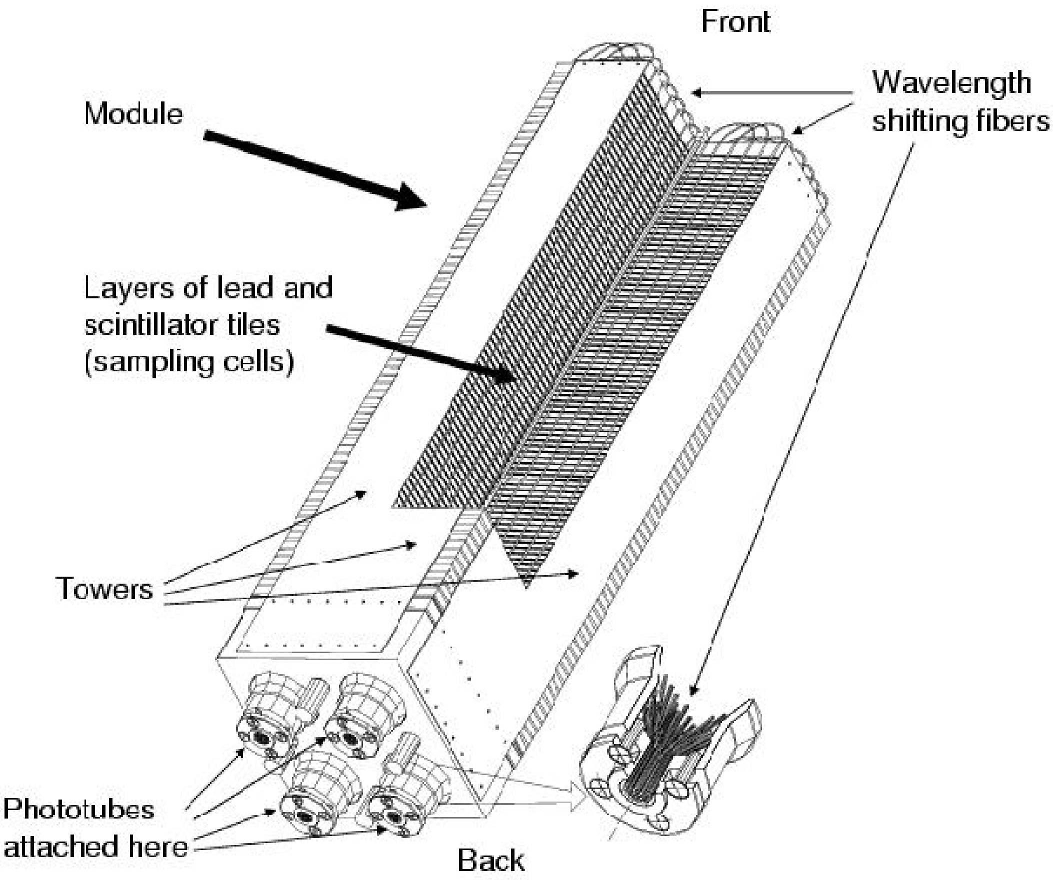

Figure 19: EMC calorimeter module of 4 PbSc towers. Each individual tower measures 5.535×5.535 cm^2. Figure referenced in Chapter 2.

B.3 Figures referenced in Chapter 3

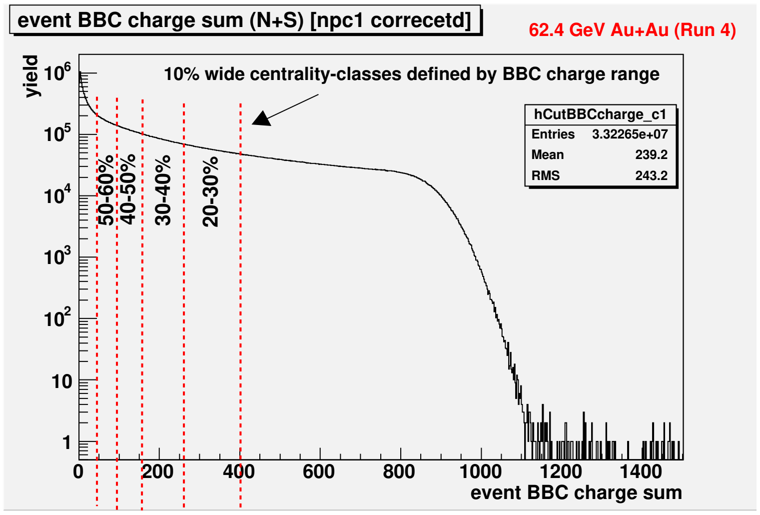

Figure 20: 62.4 GeV Au+Au event-by-event inclusive BBC charge distribution of events used to define collision centrality classes for PHENIX Run 4 official analyses. Figure referenced in Chapter 3.

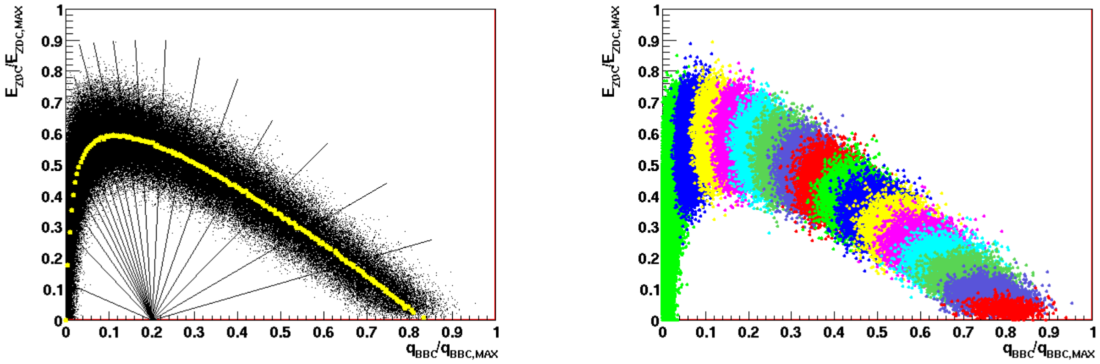

Figure 21: The left plot is a 200 GeV Au+Au scatter plot of event ZDC energy vs. event BBC charge made from real events, where radial lines define collision centrality classes for PHENIX Run 4 official analyses. The right plot is a simulation of the ZDC and BBC responses for simulated interactions over the range of $N_{\mathrm{nuc-part}}$. Figure referenced in Chapter 3. (Courtesy of PHENIX internal Analysis Note 33 [27]).

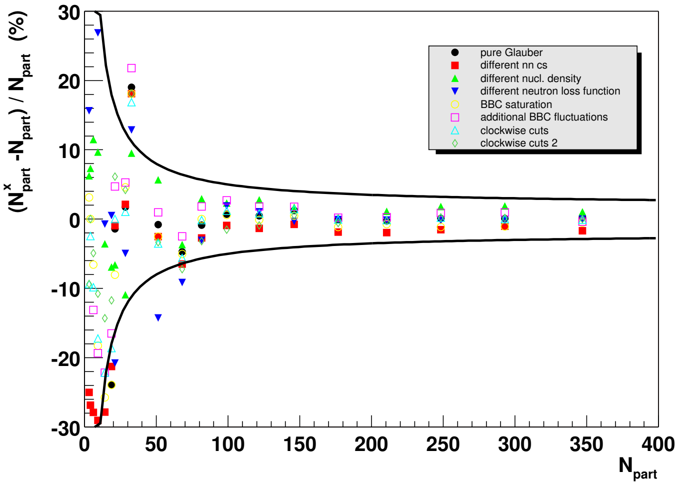

Figure 22: Error estimation on the modeled $N_{\mathrm{nuc-part}}$ determination used in the 200 GeV Au+Au analyses. Figure referenced in Chapter 3. (courtesy: Klaus Reygers (BNL) [27]).

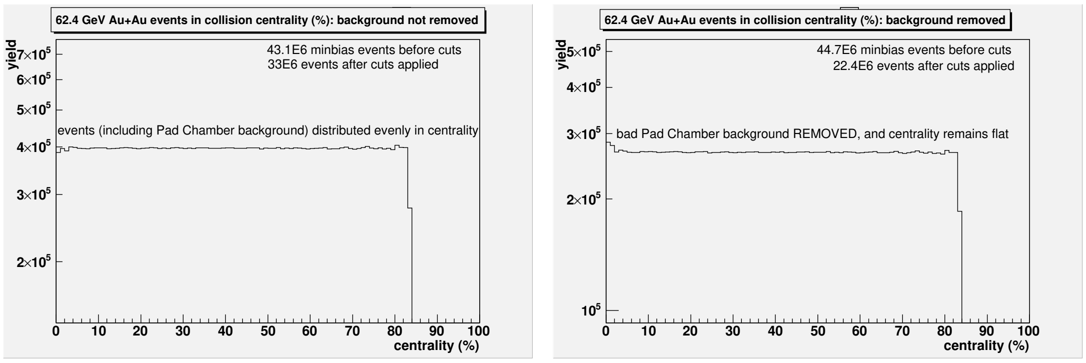

Figure 23: 62.4 GeV Au+Au distribution of events in centrality before (left) and after (right) background removal. The amount of Pad Chamber bad-event background is small enough such that even after its removal the centrality distribution remains sufficiently flat (note: disregard difference in quantities of events). Figure referenced in Chapter 3.

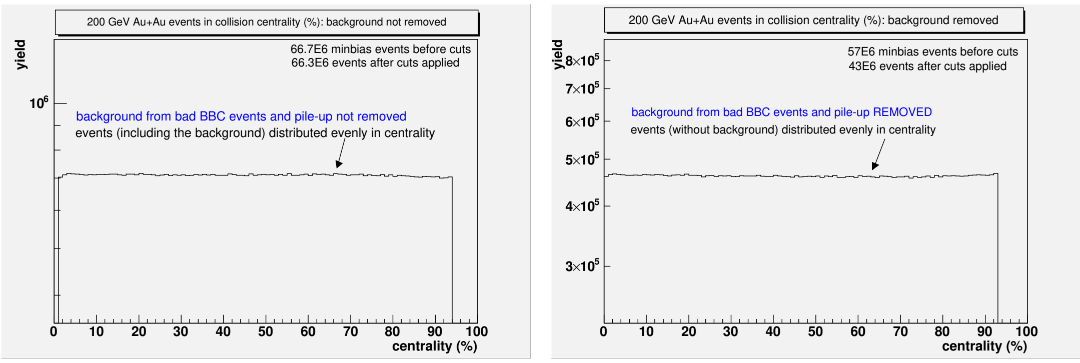

Figure 24: 200 GeV Au+Au distribution of events in centrality before (left) and after (right) background removal. The amount of background from bad BBC events and pile-up is small enough such that even after their removal the centrality distribution remains sufficiently flat (note: disregard difference in quantities of events). Figure referenced in Chapter 3.

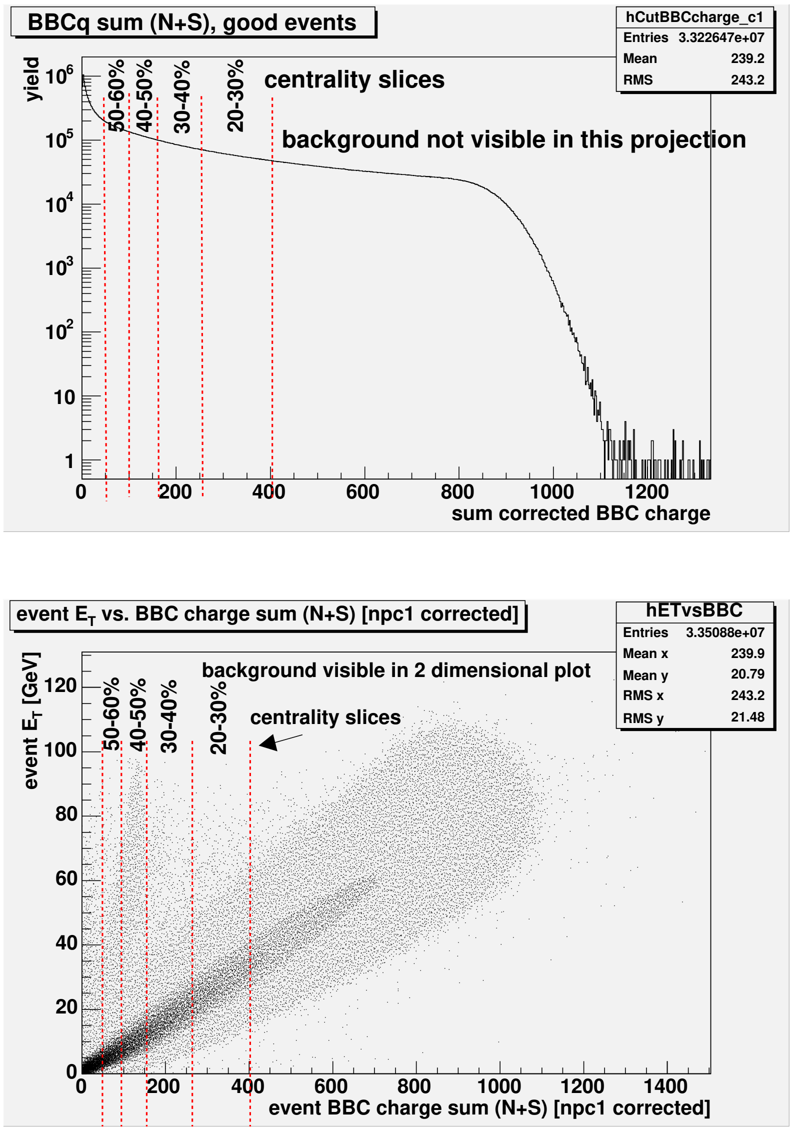

Figure 25: 62 GeV Au+Au: (top plot) the 1-dimensional BBC charge distribution of events does not appear unusual and thus the centrality problem not visible; one has to plot another variable such as E_T against BBC charge (bottom plot) to see the background and centrality distortion. Figure referenced in Chapter 3.

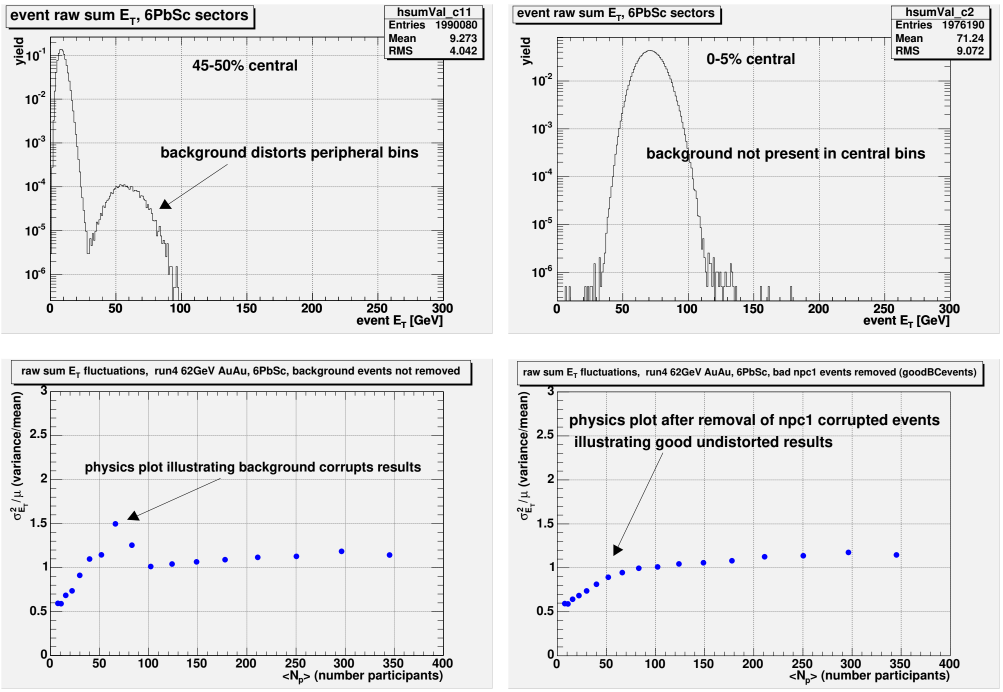

Figure 26: 62 GeV Au+Au: (top left plot) the event centrality is distorted due to background in the peripheral semi-inclusive $E_{T\ (\mathrm{EMC})}$ distributions but not the (top right) more central distributions. The affect this has on the fluctuation measurements $\sigma^2/\langle E_{T\ (\mathrm{EMC})}\rangle$ can be seen in the bottom left plot shown for the case where fits were not applied to the semi-inclusive distributions, but rather the ROOT histogram-ming package was used to compute the widths and the means from the data over the entire distributions including the background. The bottom right plot shows $\sigma^2/\langle E_{T\ (\mathrm{EMC})}\rangle$ after background was removed by cutting events in bunch crossing region 57-71. Figure referenced in Chapter 3.

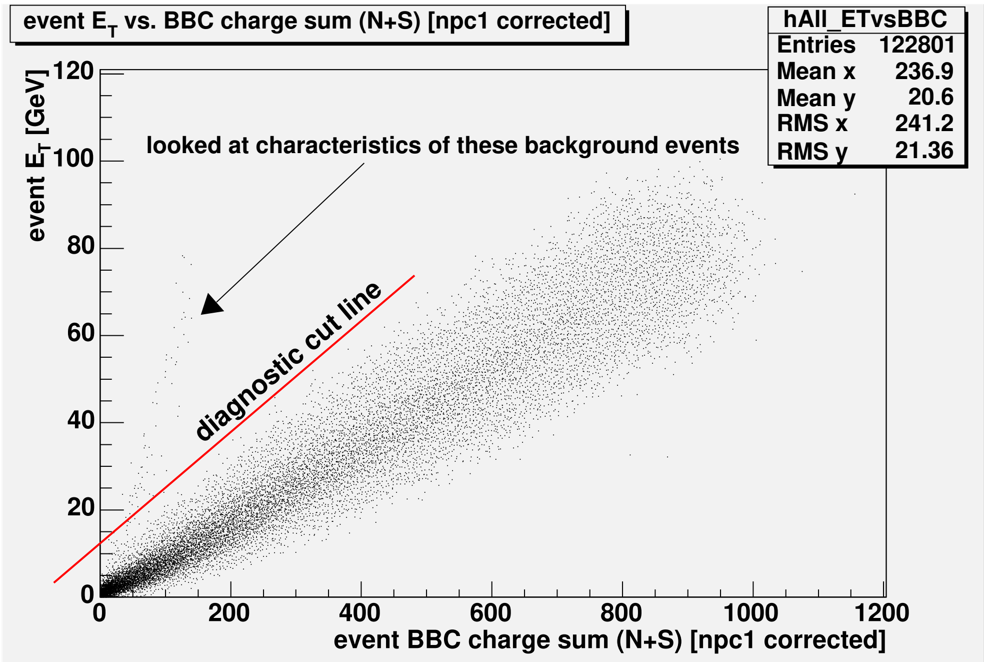

Figure 27: 62 GeV Au+Au: in order to track down the source of the background problem various characteristics of the events situated above the diagnostic cut line were looked at; it was determined that all these background events are contained to the bunch crossings numbered 57-71. Figure referenced in Chapter 3.

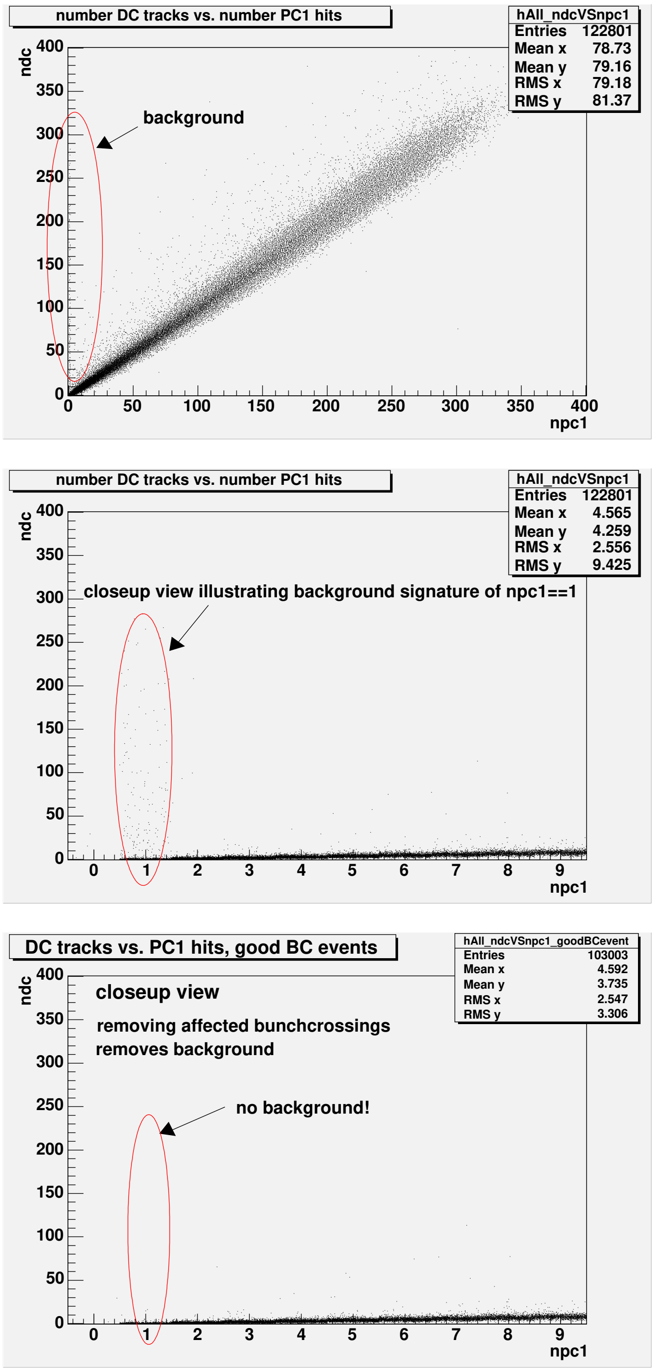

Figure 28: 62 GeV Au+Au: background events appear as uncorrelated events in scatter plots of Drift Chamber track multiplicity vs. Pad Chamber-1 hit multiplicity; although hard to see in the top plot the closeup view (middle) illustrates these background events have a specific signature of 1 hit to pad chamber 1 ($npc1 = 1$). Bottom plot shows the background is removed after cutting all events in the beam bunch crossing region 57-71. Figure referenced in Chapter 3.

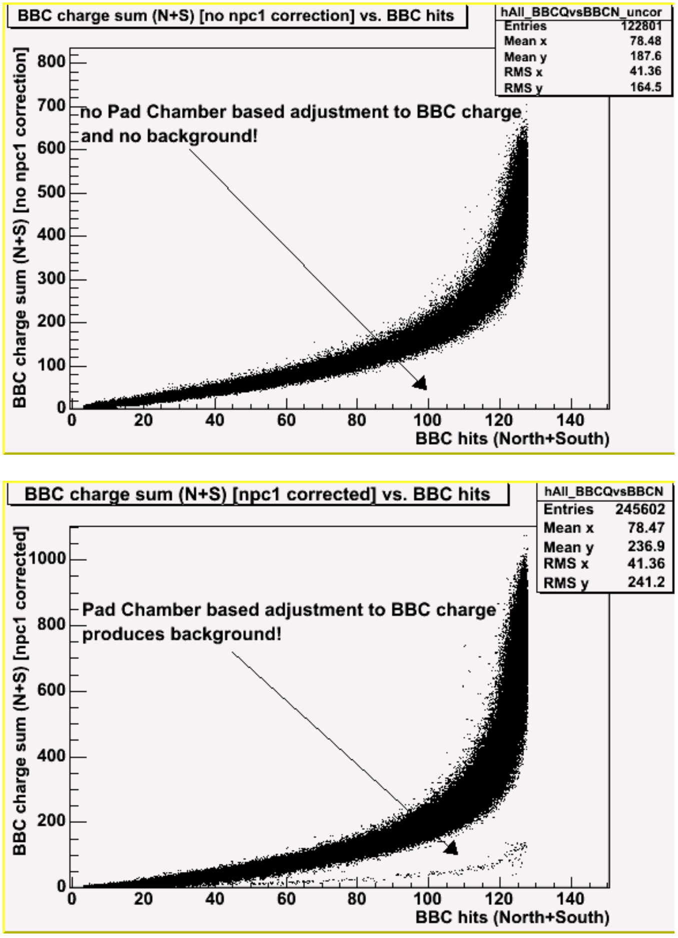

Figure 29: 62 GeV Au+Au: the horizontal axes in both plots are the event multiplicity in the BBC, and the vertical axes a measure of the BBC charge. Both distributions follow a correlated curve which saturates and turns upwards at about 120 hits due to the limited number of BBC Cerenkov counters. The top plot contains the raw measured BBC charge; in the bottom plot the BBC charge on each event was adjusted off-line according to what the Pad Chamber-1 multiplicity was (*npc*1-adjusted), and this resulted in a background of some uncorrelated events, illustrating that the source of the background is the pad chamber. Figure referenced in Chapter 3.

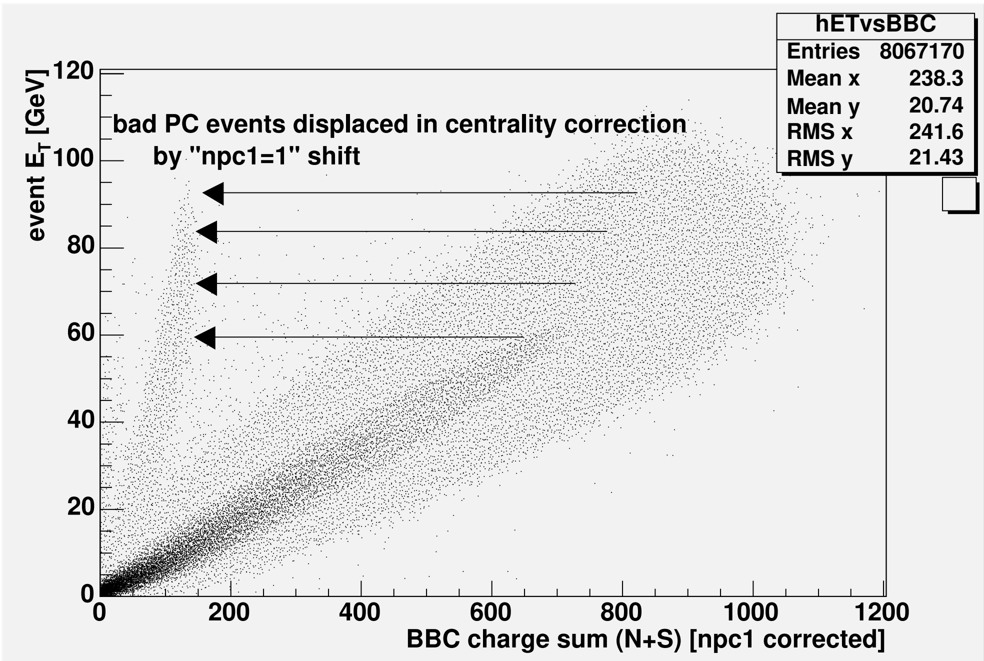

Figure 30: 62 GeV Au+Au: scatter plot of event E_T vs. event BBC charge after the charge was adjusted by using the Pad Chamber-1 multiplicity. The events having incorrect Pad Chamber data are consequentially assigned an incorrect collision centrality and are seen here as shifted to the peripheral or low BBC charge region. Figure referenced in Chapter 3.

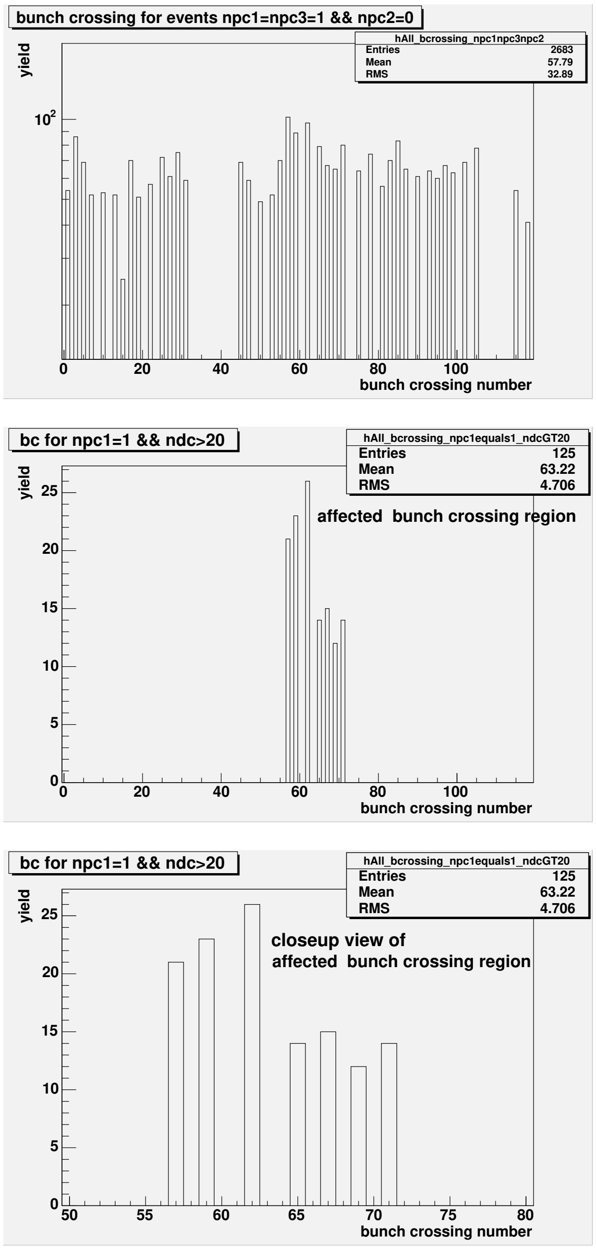

Figure 31: 62 GeV Au+Au: the top plot is the RHIC beam bunch crossing numbers for minbias triggered events which contain both good events and background events; the middle plot are bunch crossing numbers only for the background events which were selected by requiring the incorrect simultaneous signature of 1 hit to Pad Chamber-1 and more than 20 tracks in the Drift Chamber; the close up view in the bottom plot shows the background to be contained to the bunch crossing region 57-71. Figure referenced in Chapter 3.

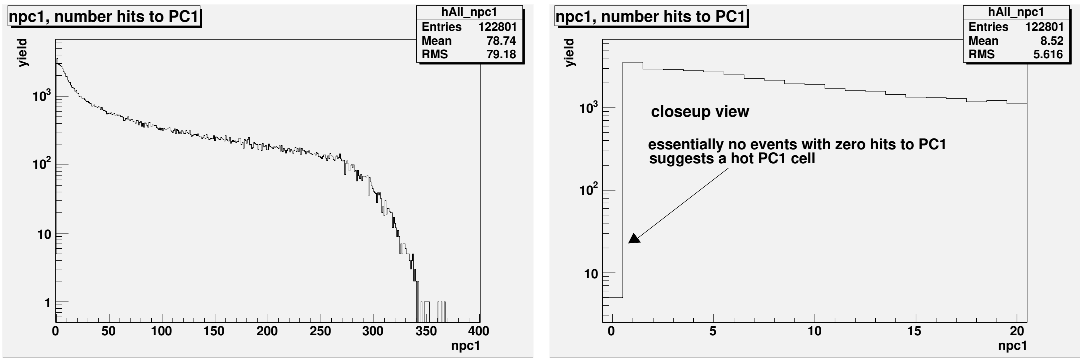

Figure 32: 62 GeV Au+Au: in the left plot the Pad chamber-1 multiplicity distribution of minbias events (including good events plus background) does not look unusual; however when viewed up close in the right plot there are essentially no events having zero hits to Pad Chamber-1 – the explanation for this is the presence of a “hot” pad chamber-1 cell falsely reports being hit on every event. Figure referenced in Chapter 3.

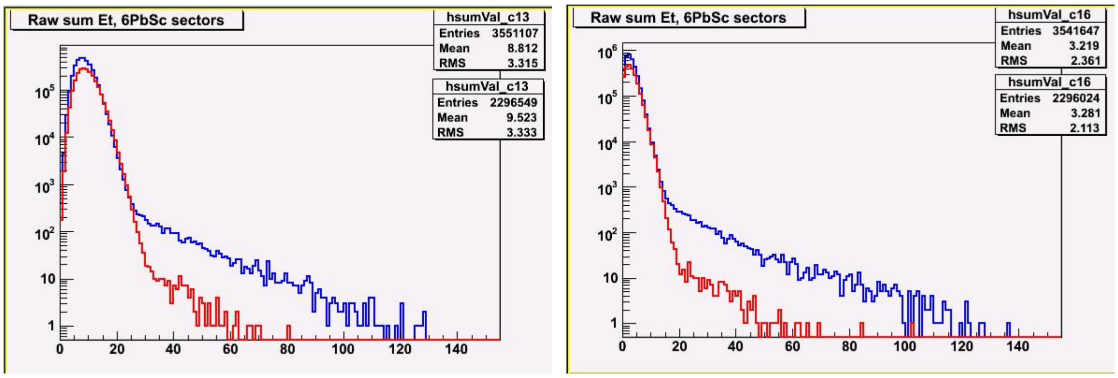

Figure 33: 200 GeV Au+Au: two types of background in semi-inclusive $E_{T\ (\mathrm{EMC})}$ distributions. The left plot is the 55-60% centrality class, and the right plot the 70-75% centrality class. The larger background (shown in blue) are the minbias single events having no valid BBC-timing nor BBC-Zvertex, and has features like two interactions in sequential bunch crossings. The smaller background (shown in red) are minbias single events due to pile-up of two interactions in the same bunch crossing. Both background appears in peripheral to central event classes but becomes smaller in the more central events. Figure referenced in Chapter 3.

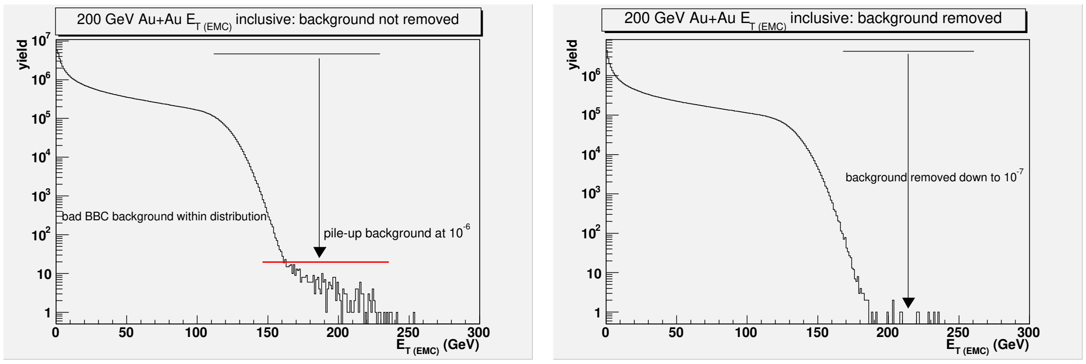

Figure 34: 200 GeV Au+Au inclusive $E_{T\ (\mathrm{EMC})}$ distribution before (left) and after (right) background cuts applied to remove BBC background and pile-up. Figure referenced in Chapter 3.

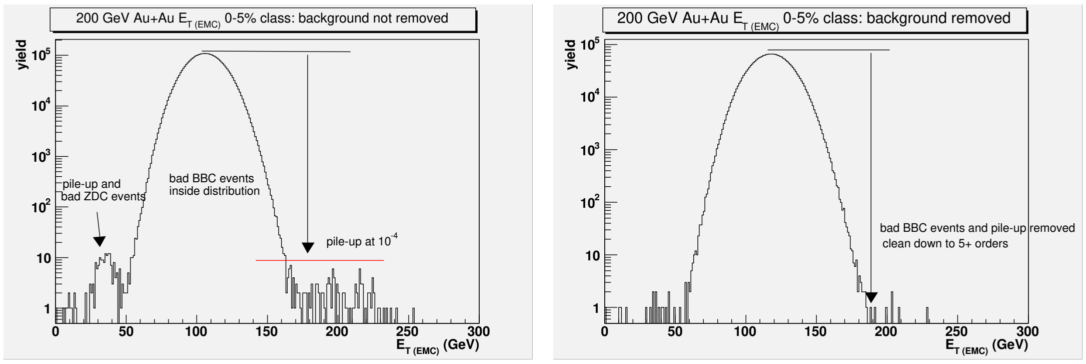

Figure 35: 200 GeV Au+Au 0-5% central $E_{T\ (\mathrm{EMC})}$ distribution before (left) and after (right) background cuts applied to remove BBC background and pile-up. Figure referenced in Chapter 3.

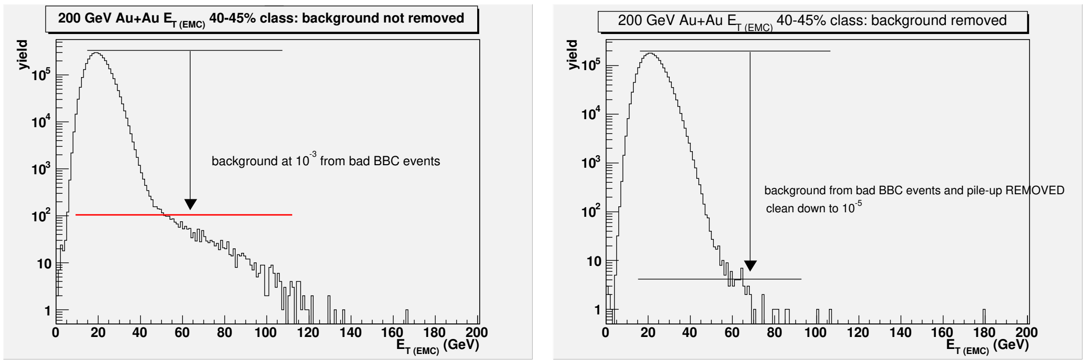

Figure 36: 200 GeV Au+Au 40-45% central $E_{T\ (\mathrm{EMC})}$ before (left) and after (right) background cuts to remove BBC background and pile-up. Figure referenced in Chapter 3.

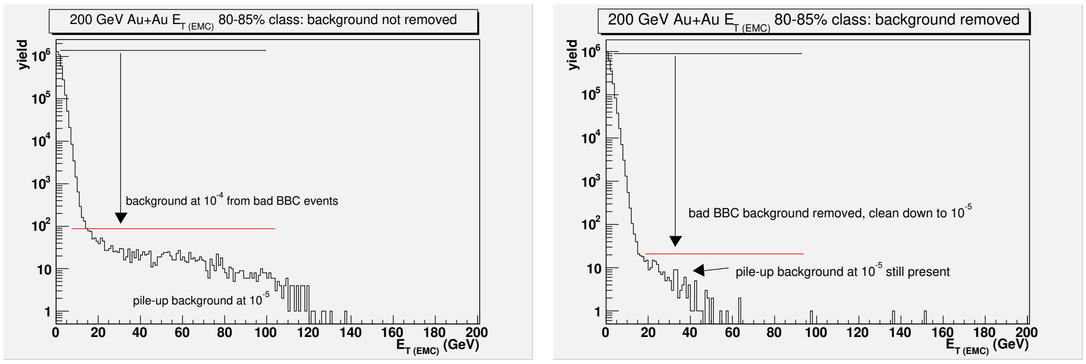

Figure 37: 200 GeV Au+Au 80-85% central $E_{T\ (\mathrm{EMC})}$ distribution before (left) and after (right) background cuts to remove BBC background and pile-up. Figure referenced in Chapter 3.

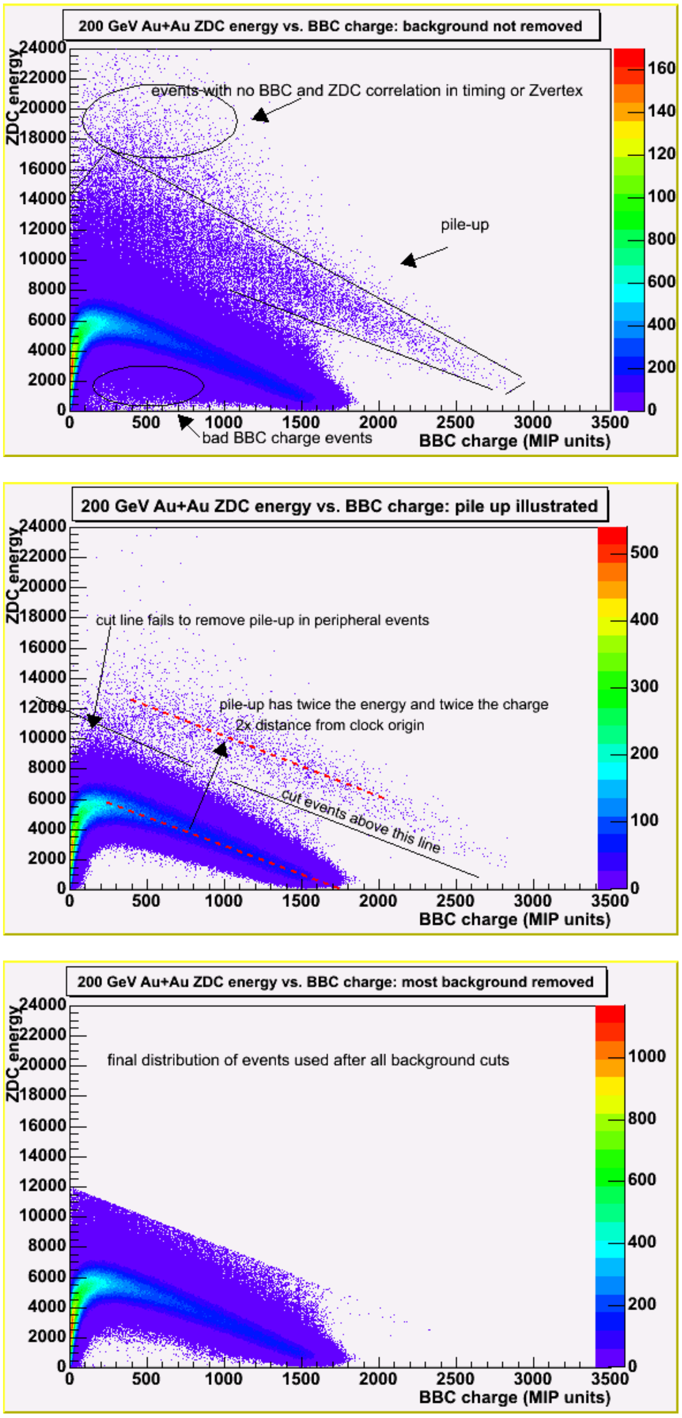

Figure 38: 200 GeV Au+Au scatter plots of event ZDC energy vs. BBC charge. Top plot is before any background cuts. The middle plot is after bad BBC background events removed by only keeping events with a Zvertex determined by the BBC's, and also shows a cut line in ZDC-BBC space to remove pile-up. Bottom plot is after both the BBC background events and pile-up events removed. Figure referenced in Chapter 3.

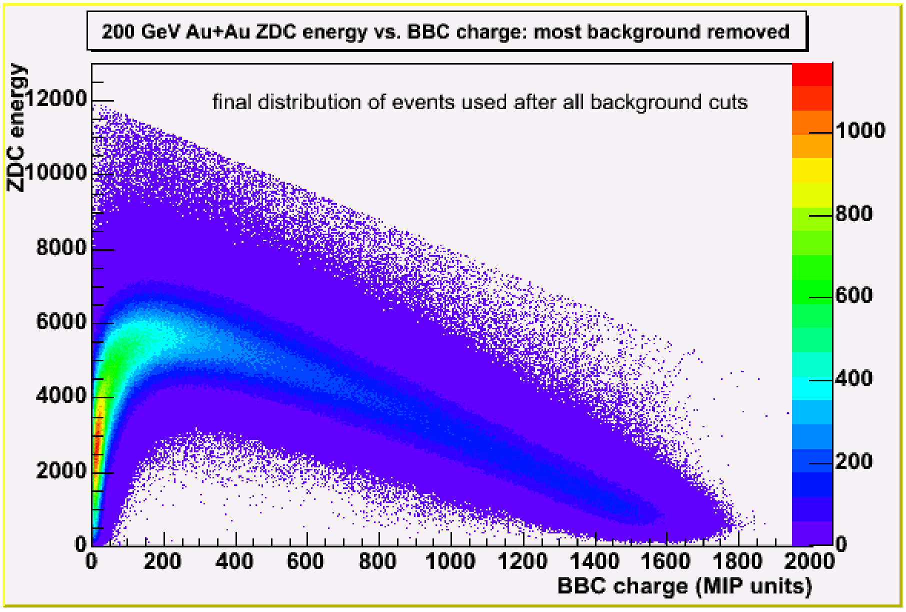

Figure 39: close up view of 200 GeV Au+Au scatter plot of event ZDC energy vs. BBC charge after most background removed; the remaining background is pile-up in the peripheral event region which is mixed into the good part of the distribution. Figure referenced in Chapter 3.

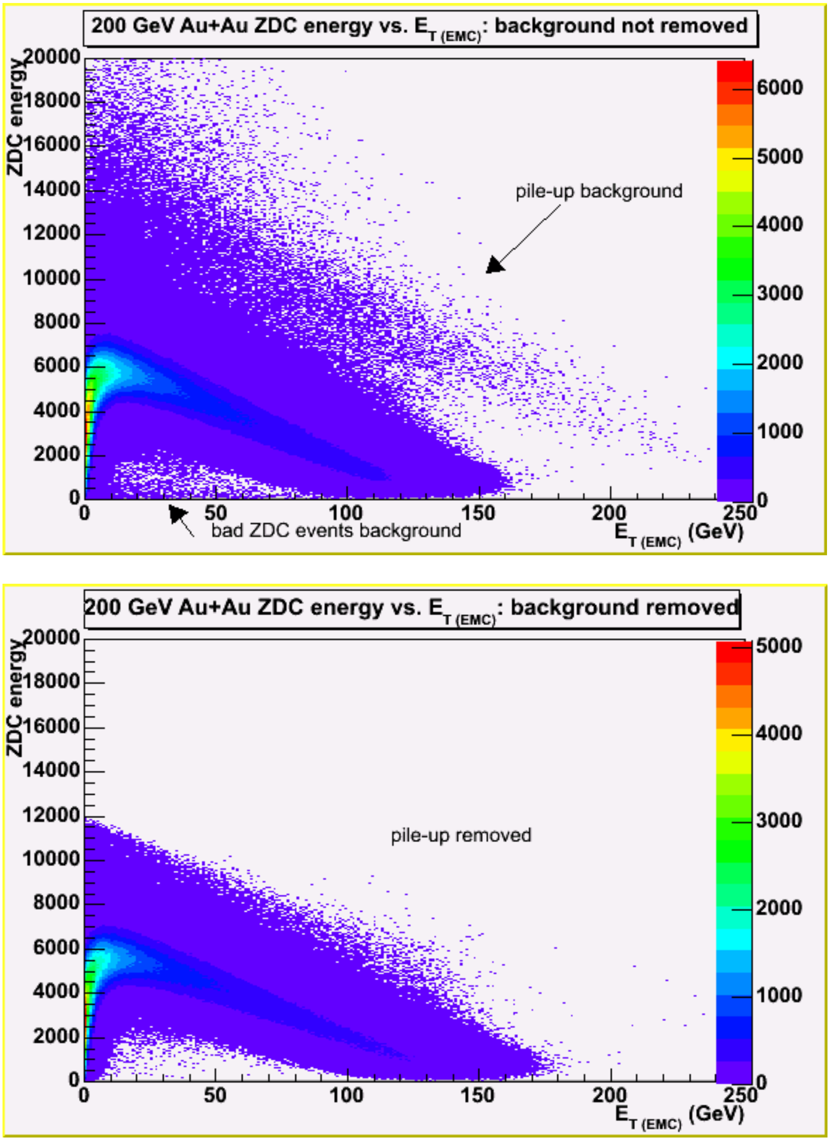

Figure 40: 200 GeV Au+Au scatter plot of event ZDC energy vs. $E_{T\ (\mathrm{EMC})}$ before and after background removal. Figure referenced in Chapter 3.

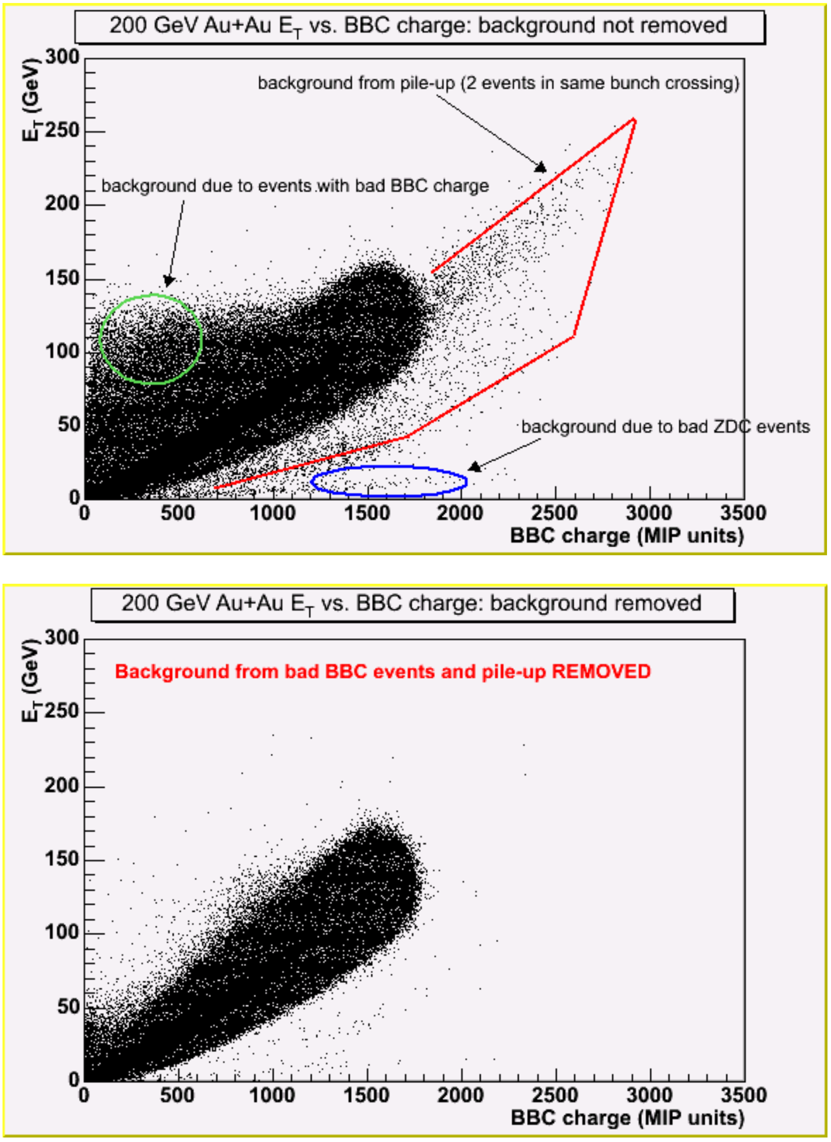

Figure 41: 200 GeV Au+Au scatter plot of event $E_{T\ (\mathrm{EMC})}$ vs. BBC charge before (top) and after (bottom) background removal. The pile up are two interactions in the same beam bunch crossing which triggered as one event. Note that in the top plot the pile up is not evenly distributed around the normal single interaction distribution, but rather only below the correlated line $E_T = BBC$. It is not clear why this is. Figure referenced in Chapter 3.

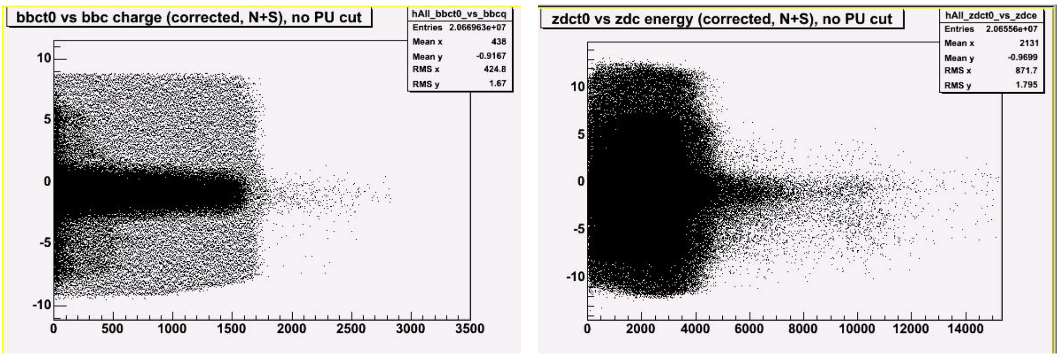

Figure 42: 200 GeV Au+Au minbias events before background cuts. The left plot shows the event trigger time as determined by the BBC's (vertical axis in nano seconds) vs. the sum BBC charge (MIP units). The right plot shows the event trigger time as determined by the ZDC's (vertical axis in nano seconds) vs. the sum ZDC energy (in neutron equivalent energy [GeV]). The BBC's can determine event trigger times at a limited $\pm$ 10.5 nsec relative to the RHIC beam clock, but the ZDC's have a larger timing dynamic range shown here out to $\pm$ 12 nsec. In both plots the pile-up is seen centered around zero time and extending out to twice the charge and energy. There is a second component of background having very high amounts of ZDC energy with event times out to $\sim \pm 10$ nsec, the origin of this is not clear. Figure referenced in Chapter 3.

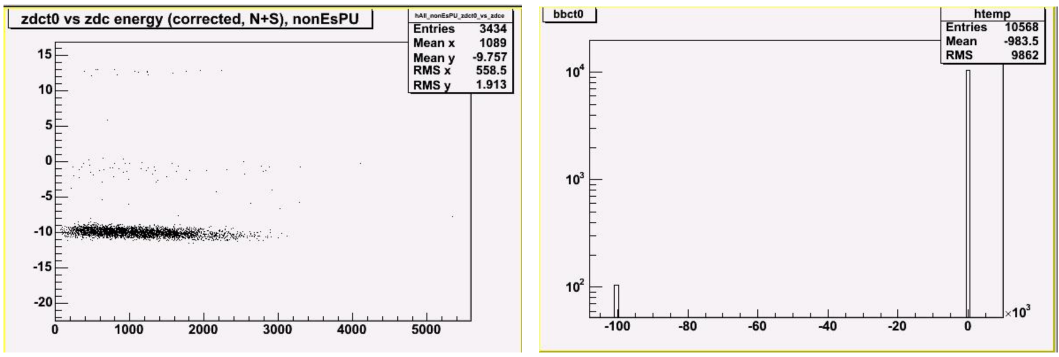

Figure 43: 200 GeV Au+Au bad BBC charge background events. Only the background events appearing in the upper left corner of the E_T vs. BBC charge scatter plot (see the top plot in Figure 41) were hand selected and used to fill the plot on the left which is the event trigger time as determined by the ZDC's (vertical axis in nsec) vs. the sum ZDC energy (in GeV); for simplicity a cut isolating only one ZDC arm was used which explains why only negative times are shown. It is clear that this specific background has trigger times at the 10.5 nsec edge of the BBC timing dynamic range. The right plot shows this background is nominally labeled as BBC underflow and given an event time = −99 nsec. Figure referenced in Chapter 3.

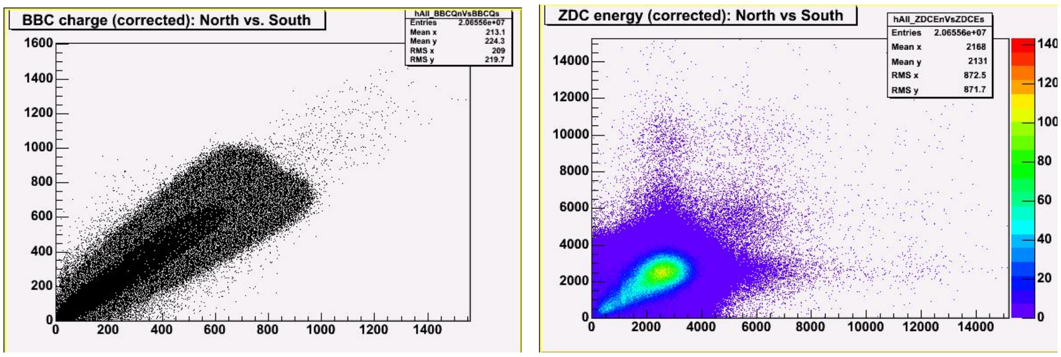

Figure 44: 200 GeV Au+Au minbias: the left plot is event BBC charge in MIP units in the North arm (vertical axis) vs. that in the South arm. The pile-up are the correlated events extending to the highest BBC charge values. The bad BBC charge background events are strongly anti-correlated and located far from the central lobe. The right plot is event ZDC energy (in GeV) in the North arm vs. that in the South arm; again the pile-up are the correlated events extending to the highest ZDC energy values. Figure referenced in Chapter 3.

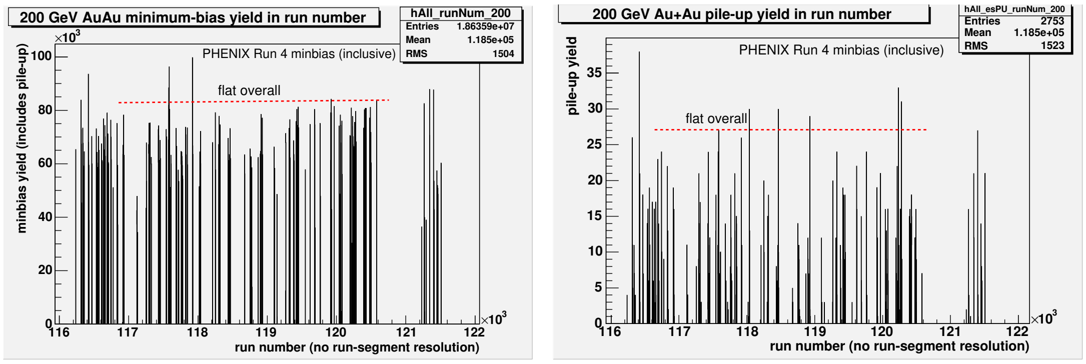

Figure 45: 200 GeV Au+Au: number of minbias triggered events as a function of RHIC Run 4 run-number sequence. The left plot contains all minbias and the right plot contains only events above the pile-up cut line defined in the ZDC-BBC scatter plot (see middle plot in Figure 38). Both plots are flat illustrating the background is distributed across the run-numbers. Figure referenced in Chapter 3.

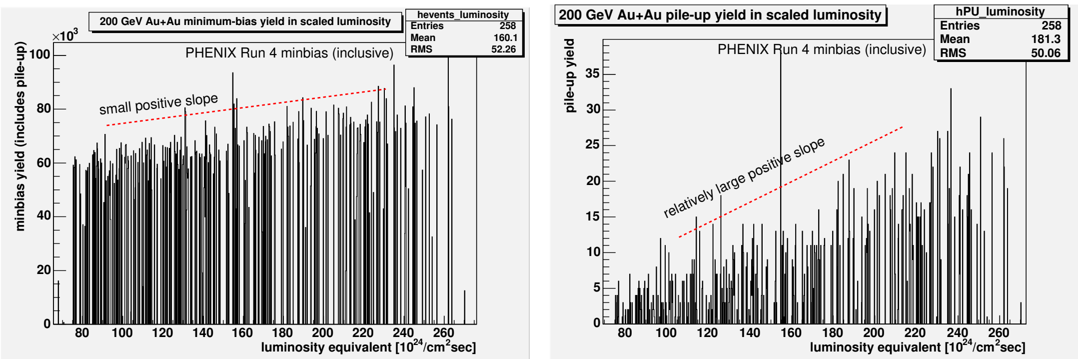

Figure 46: 200 GeV Au+Au number of minbias triggered events as a function of RHIC Run 4 luminosity. The left plot contains all minbias events and the right plot contains only events above the pile-up cut line defined in the ZDC-BBC scatter plot (see middle plot in Figure 38). The pile-up has the expected characteristic of a larger slope than the minbias. Figure referenced in Chapter 3.

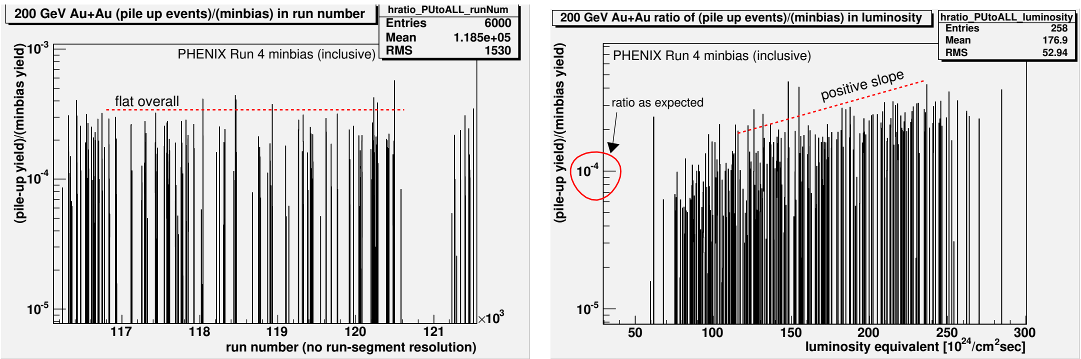

Figure 47: 200 GeV Au+Au ratio of pile-up events to minbias triggered events as a function of the RHIC Run 4 (left plot) run-number sequence and (right plot) luminosity: the ratio in luminosity has the characteristic rising slope of pile-up, and additionally, occurs at a 10^{-4} rate expected from the RHIC beam luminosity and bunch crossing frequency. Figure referenced in Chapter 3.

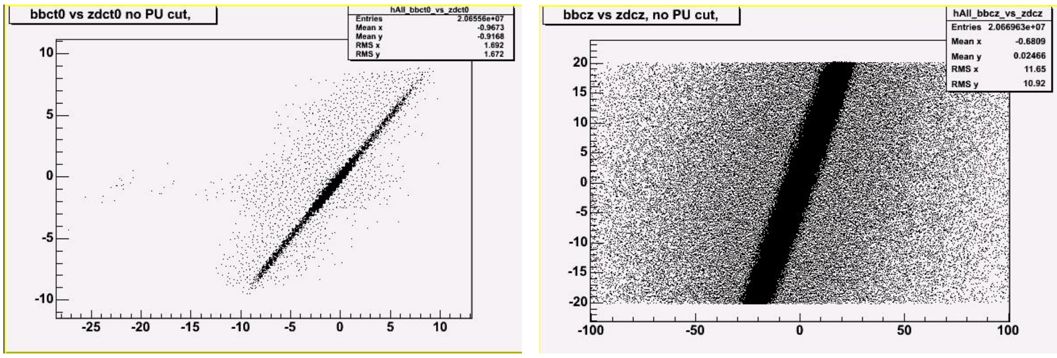

Figure 48: 200 GeV Au+Au. The left plot is the time the event was triggered in nsec as determined using both the BBC's together (vertical axis) vs. the time determined by the two ZDC's (horizontal axis). The right plot is the Zvertex in cm as determined by the two BBC's (vertical axis) vs. the Zvertex determined by the two ZDC's (horizontal axis), constructed from their respective event times. The pile-up events appear in the correlated and central part of the two plots and not in the outliers event regions, thus not removable from single interaction events using this dual-arm timing and Zvertex information with nano-dst data. Figure referenced in Chapter 3.

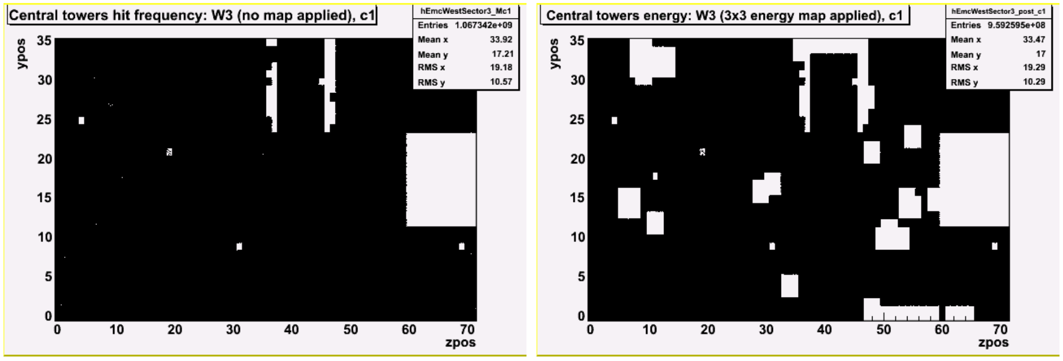

Figure 49: Projections of the EMC sector West 3 tower energy accumulated over many 200 GeV Au+Au events, before (left plot) and after (right plot) hot towers removed. The large gaps on the left plot are regions of dead towers. Figure referenced in Chapter 3.

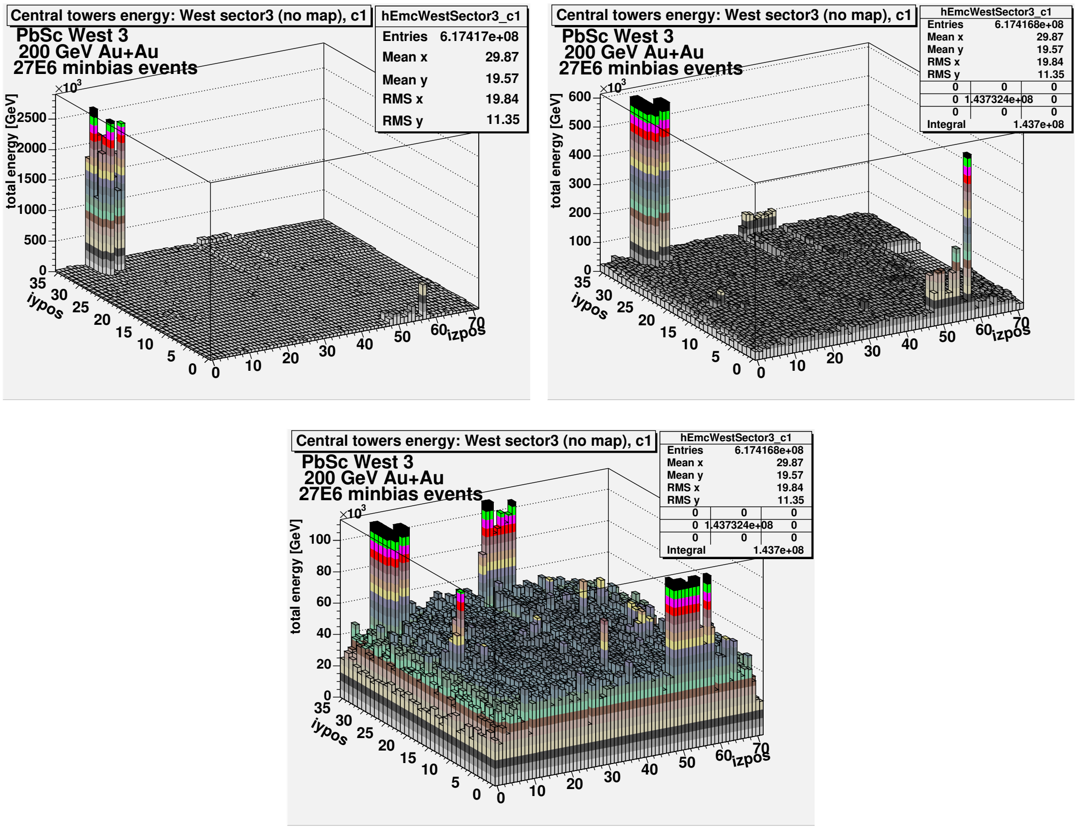

Figure 50: Distribution of energy across the EMC sector West 3 before the faulty PbSc hot towers were removed in 200 GeV Au+Au events. The top left plot shows all the spurious energy accumulated from the hottest towers, and the other two plots are zoomed in to resolve the real event energy spread more evenly across the sector. Figure referenced in Chapter 3.

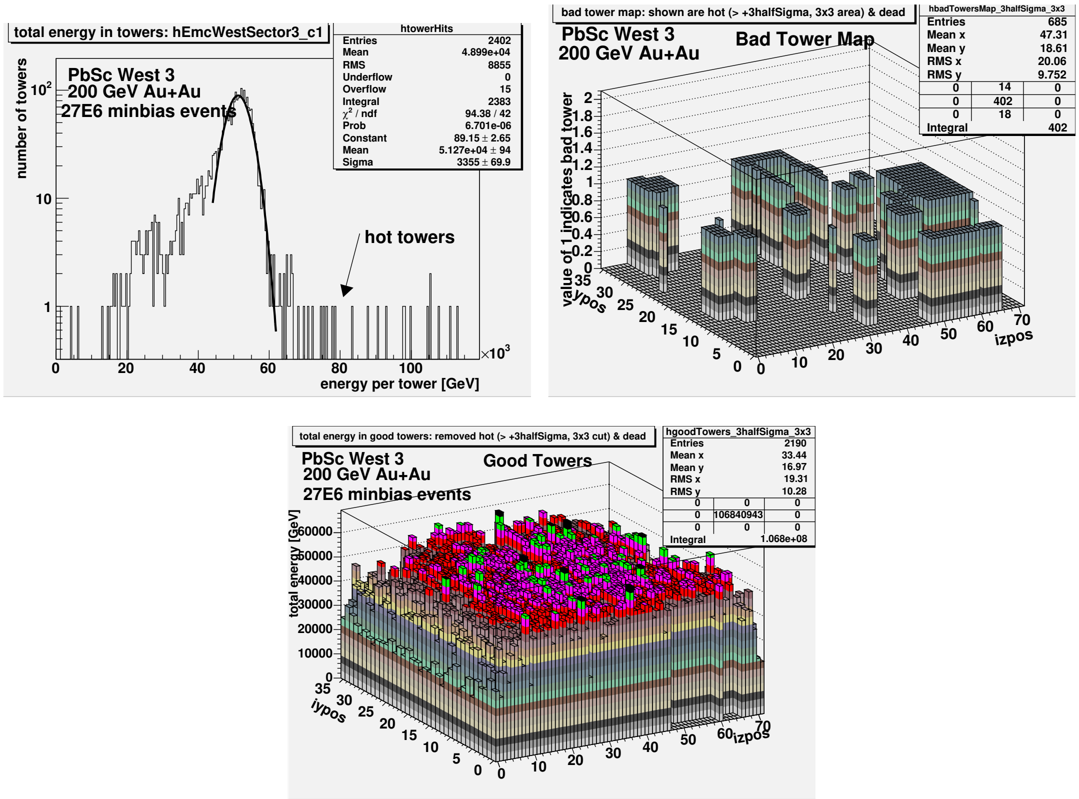

Figure 51: 200 GeV Au+Au: the top left plot is the EMC PbSc sector West 3 energy per tower histogram fitted to a simple Gaussian about which a $> +3.5\ \sigma$ cut is used to identify and remove hot towers by making a map; the low energy towers shown are due to sector edge affects and intermittent supermodules within the sector. The top right plot is the sector West 3 bad tower map which includes dead, and hot towers plus all towers which neighbor in a 3x3 tower area around a hot tower. The bottom plot is the energy distributed across sector West 3 after removal of bad towers using the map. Figure referenced in Chapter 3.

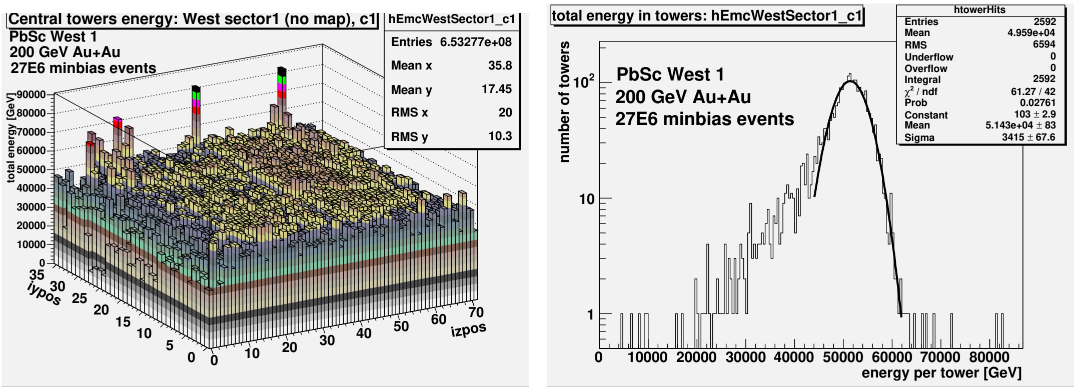

Figure 52: The left plot is the distribution of energy across the PbSc sector West 1 before hot towers were removed in 200 GeV Au+Au events. The right plot is the PbSc sector West 1 energy per tower histogram fitted to a simple Gaussian about which a $> +3.5\ \sigma$ cut is used to identify and remove hot towers. Throughout RHIC Run 3 and Run 4 sector West 1 was the cleanest sector and sector West 3 had the highest number of faulty (hot + dead) towers. Figure referenced in Chapter 3.

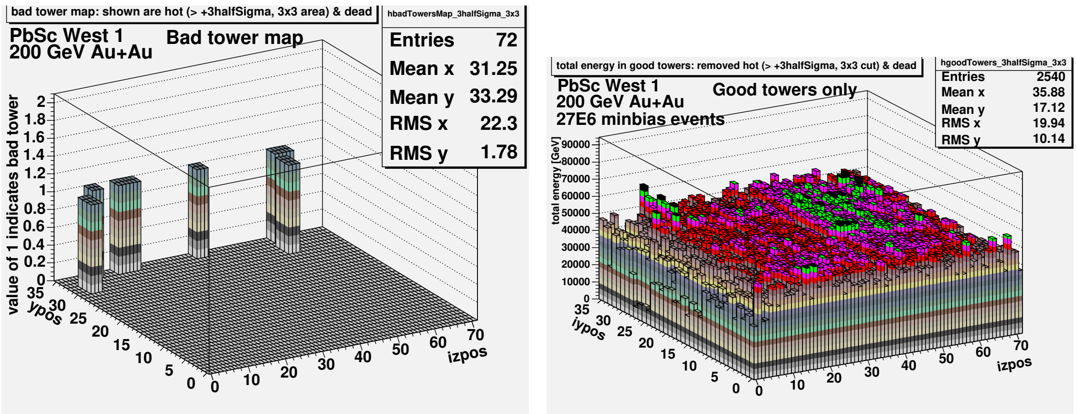

Figure 53: 200 GeV Au+Au PbSc sector West 1 bad tower map (left plot), and (right plot) distribution of energy across the sector after removal of bad towers via the map. Figure referenced in Chapter 3.

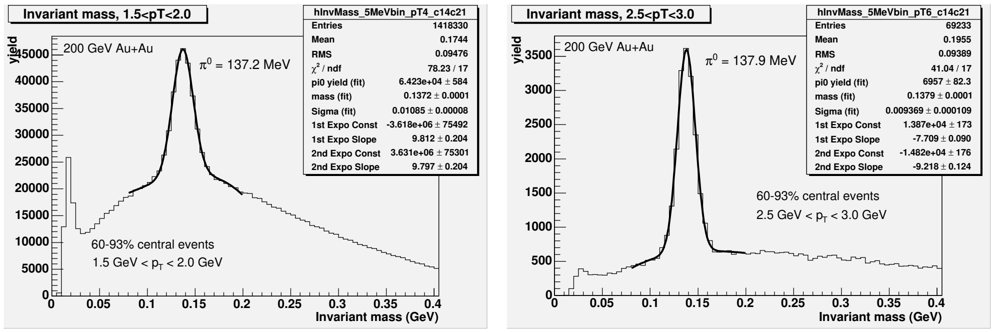

Figure 54: 200 GeV Au+Au reconstructed π^0 mass peaks in the peripheral events (60-93% centrality) for (left plot) low p_T and (right plot) mid p_T, fitted to a Gaussian plus two exponentials for combinatorial background subtraction. Figure referenced in Chapter 3.

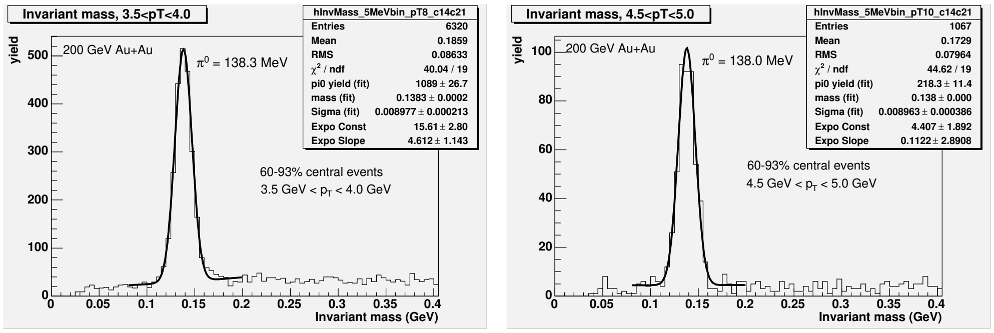

Figure 55: 200 GeV Au+Au reconstructed π^0 mass peaks in peripheral events (60-93% centrality) for (left plot) mid p_T and (right plot) higher p_T, fitted to a Gaussian plus one exponential for combinatorial background subtraction. Figure referenced in Chapter 3.

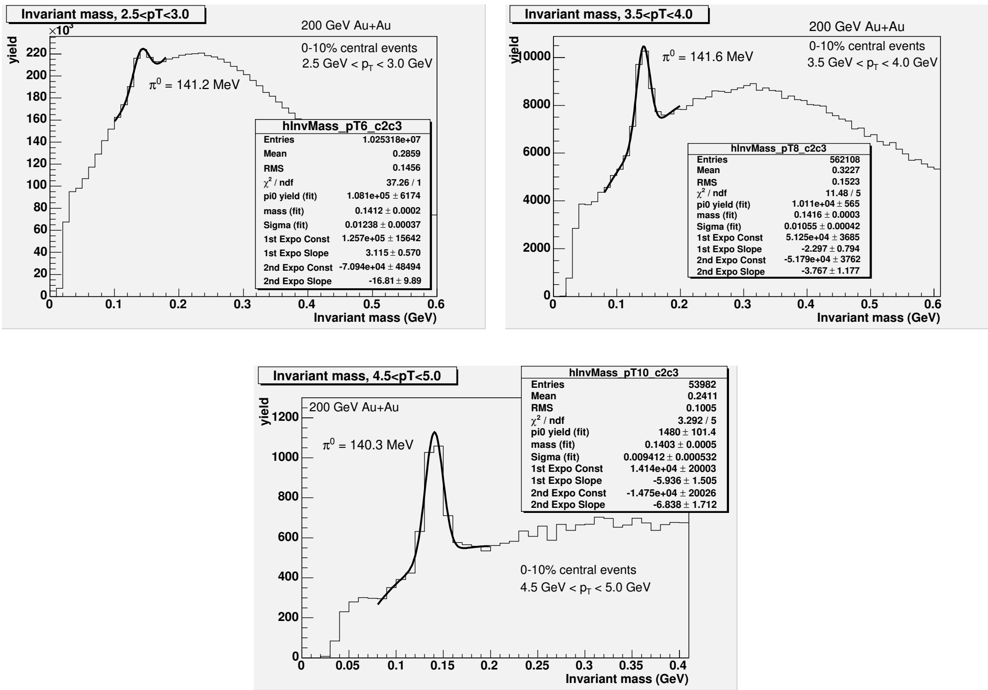

Figure 56: 200 GeV Au+Au reconstructed π^0 mass peaks in central events (0-10% centrality) for different ranges of p_T. The plots are fitted to a Gaussian plus two exponentials for combinatorial background subtraction. Figure referenced in Chapter 3.

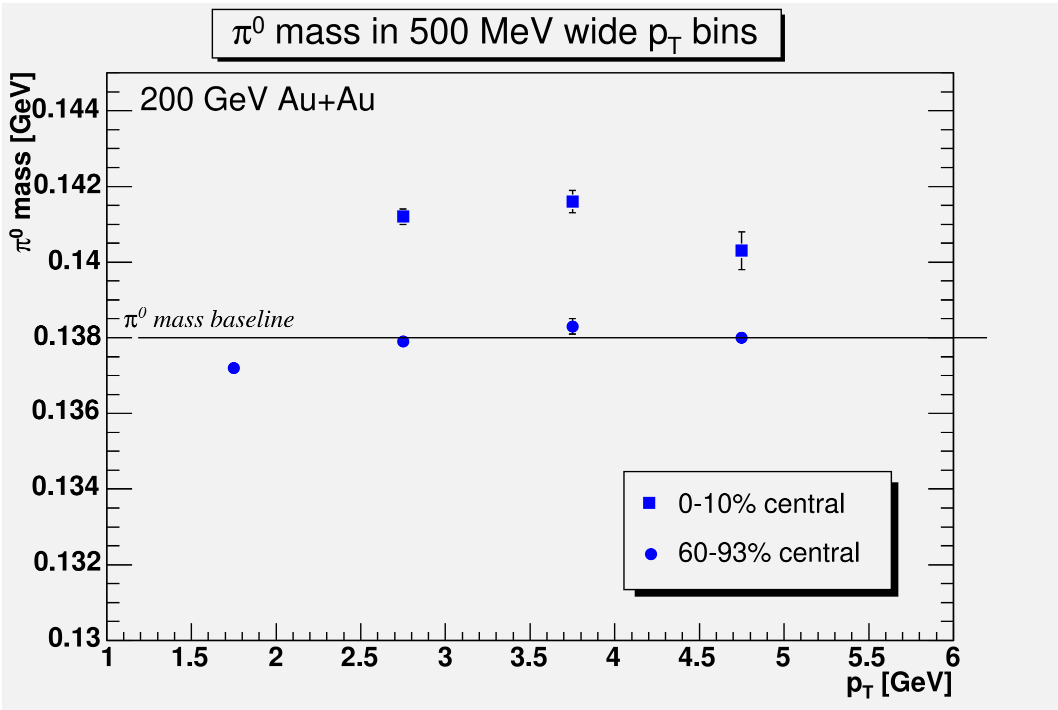

Figure 57: 200 GeV Au+Au reconstructed π^0 mass measurements. Due to a known systematic smearing affect in the EMC the π^0 mass is expected to be measured at 138 MeV. The points were taken from the Gaussian fits. Figure referenced in Chapter 3.

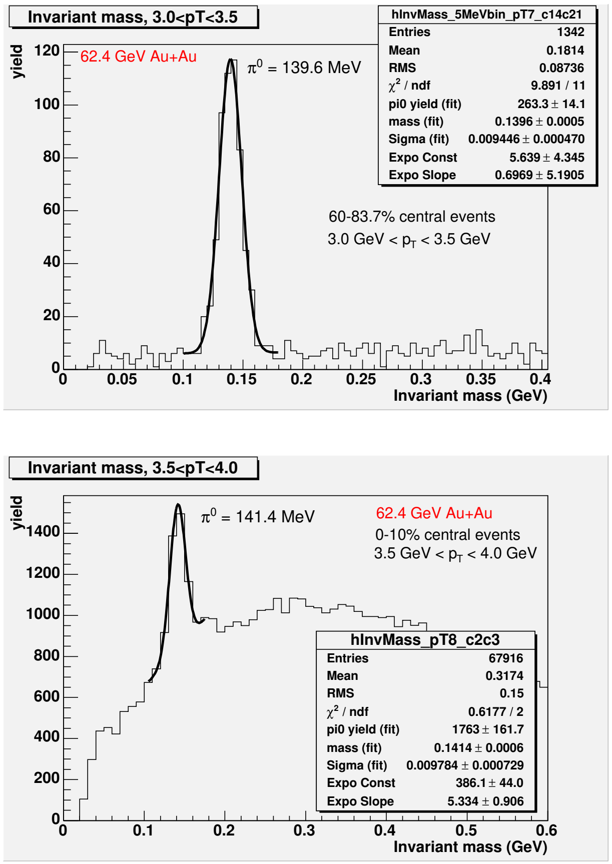

Figure 58: 62.4 GeV Au+Au reconstructed π^0 mass peaks in peripheral events (top plot) and central events (bottom plot); the plots are fitted to a Gaussian plus one exponential for combinatorial background subtraction. Figure referenced in Chapter 3.

B.4 Figures referenced in Chapter 4

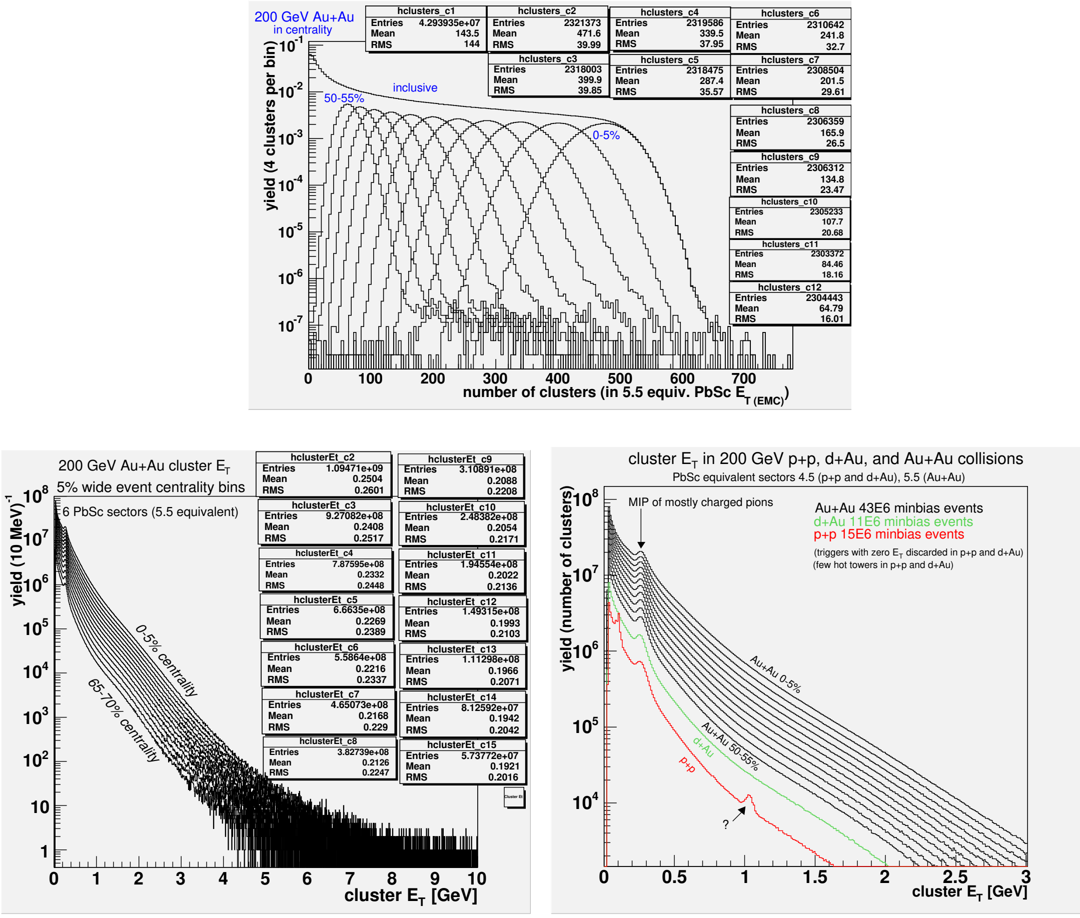

Figure 59: The top plot shows the expected rise in the number of produced clusters with collision centrality in 200 GeV Au+Au events. The bottom left plot shows an unexpected slight rise in the mean cluster energy with collision centrality in 200 GeV Au+Au (see the statistics boxes). The bottom right plot are the cluster energy distributions for $p+p$, d+Au, to the most central Au+Au, all which show the unexpected slight rise in mean cluster energy. This rise is not understood and some think it may be a systematic artifact due to limitations of the electromagnetic calorimeter. Figure referenced in Chapter 4.

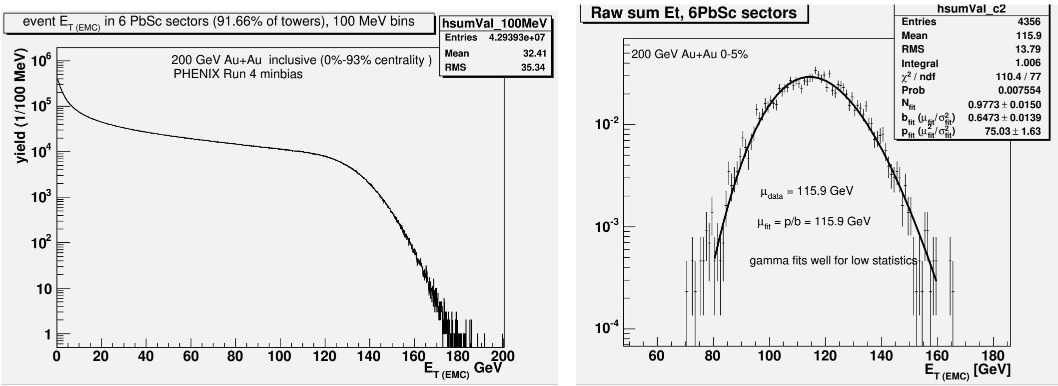

Figure 60: 200 GeV Au+Au event-by-event $E_{T\ (\mathrm{EMC})}$ distributions. In the left plot the characteristic features of the inclusive distribution can be seen: the initial drop in yield, the plateau, the knee, and the exponential cut off in energy production as the number of available nucleons is saturated. The right plot is the low statistics 0-5% centrality distribution fitted to a gamma distribution; the fit is good as is indicated by the χ^2 per degree of freedom. Figure referenced in Chapter 4.

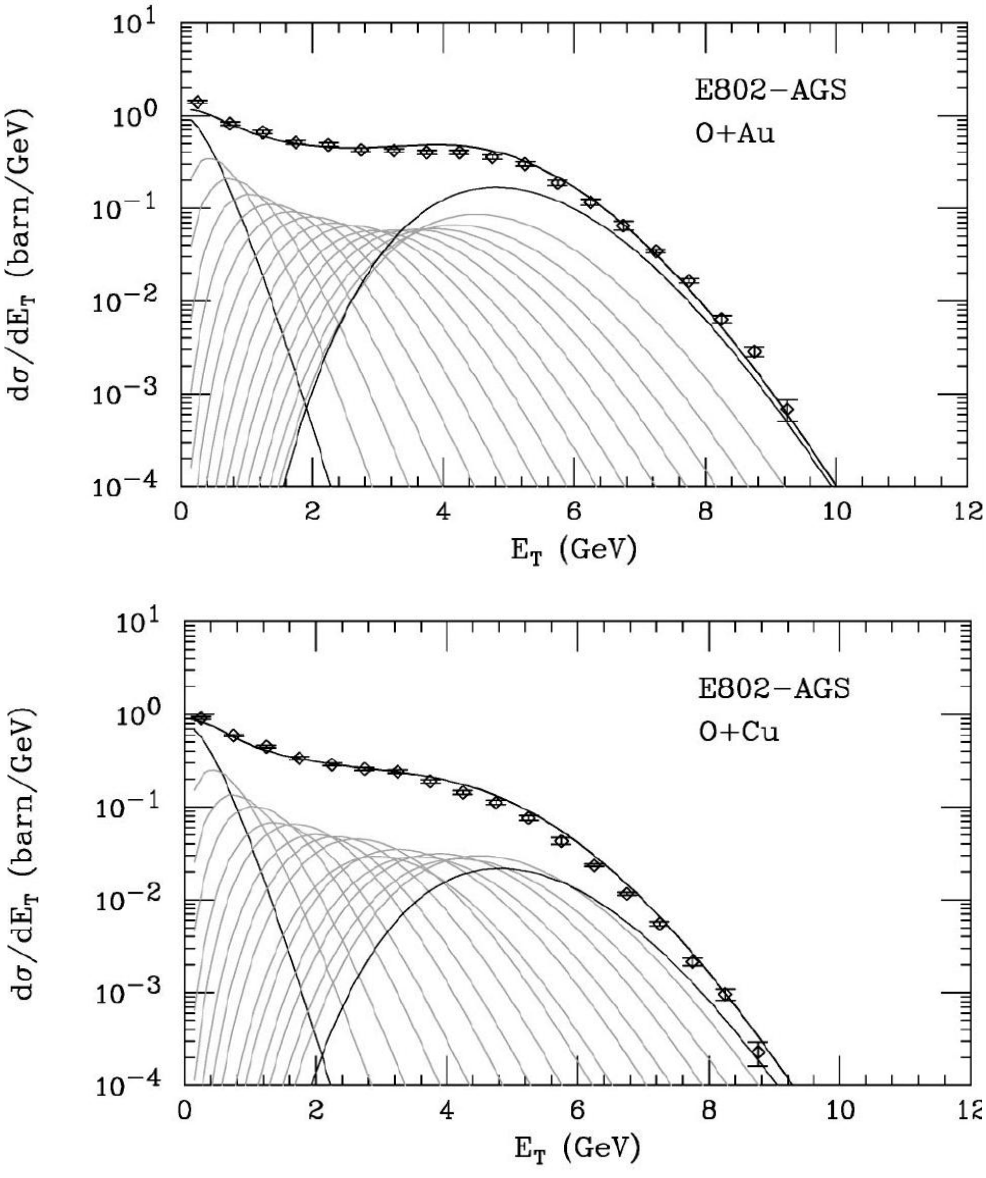

Figure 61: E-802 results (1987): 14.5 GeV/nucleon fixed target E_T measurements. In both figures the solid curve of least energy is the measured ${}^{1}p$+Au inclusive E_T distribution, and the data points are the measured (top plot) ^{16}O+Au, and (bottom plot) ^{16}O+Cu E_T. Various other curves are sum of convolutions of the ${}^{1}p$+Au weighted in the Wounded Nucleon Model probability for the projectile nucleon to interact in the target. The highest energy curve running through the points is the 1 to 16-fold recursive convolution which reproduces ^{16}O+Au and ^{16}O+Cu E_T, demonstrating (at low $\sqrt{s_{NN}}$) the mechanism for energy production are wounded nucleons. It is illustrative to compare to Figure 83. Figure referenced in Chapter 4. (Courtesy M. Tannenbaum (BNL) [41]).

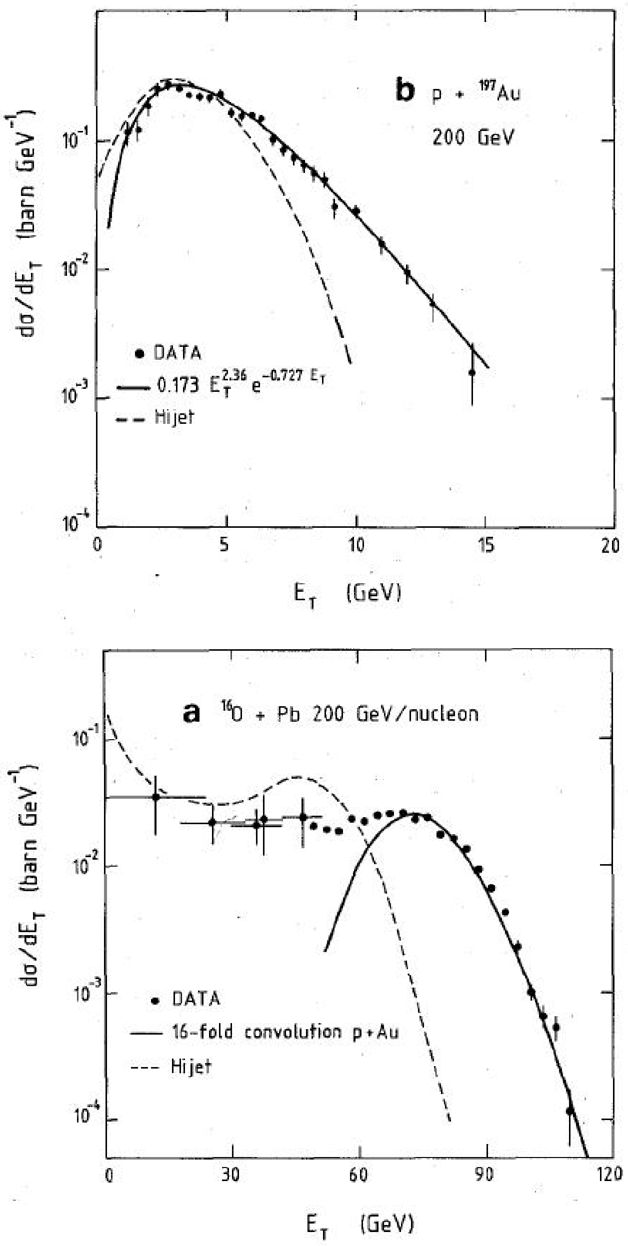

Figure 62: NA35 results (1987): 200 GeV/nucleon fixed target inclusive E_T measured at rapidity $2.2 < y < 3.8$. In the top figure the data points are the measured ^1p+Au inclusive E_T and the solid line traversing the points is a fit to the gamma distribution. In the bottom figure the data points are the measured ^{16}O+Pb E_T; the solid line traversing the points is the sum of the 1 to 16-fold recursive convolutions of ^1p+Au weighted in the Wounded Nucleon Model probability for the projectile nucleon to interact in the target. The convolution reproduces ^{16}O+Pb E_T demonstrating that (at low $\sqrt{s_{NN}}$) the mechanism for energy production are wounded nucleons (courtesy [10]). Figure referenced in Chapter 4.

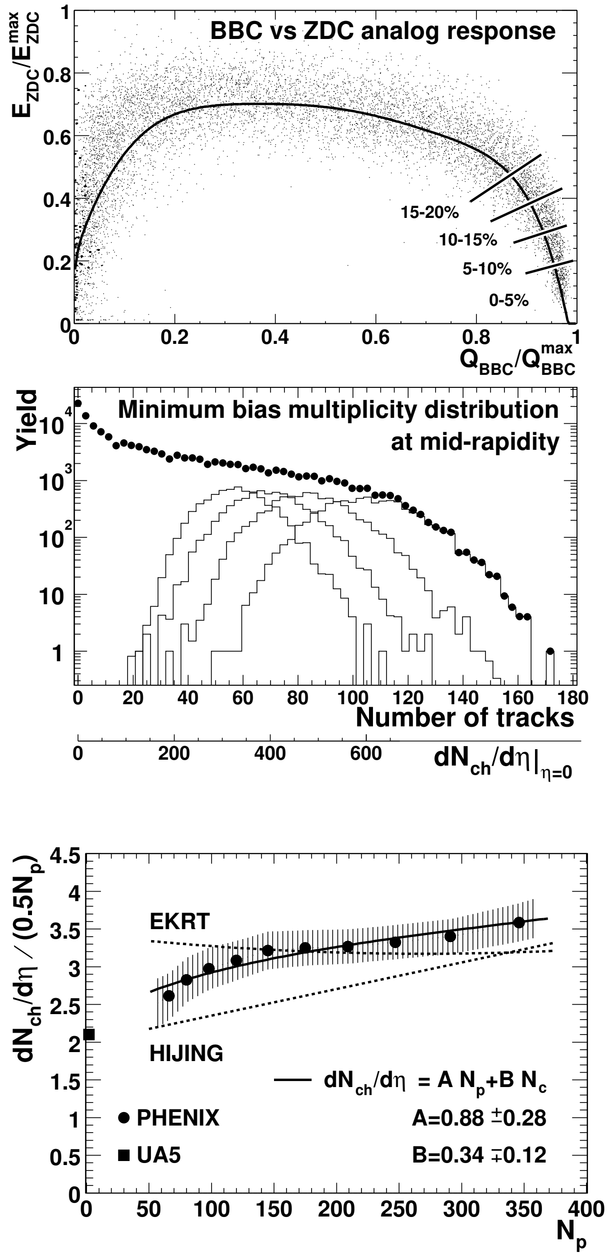

Figure 63: PHENIX previous results (2001): 130 GeV Au+Au. The top plot is a scatter plot of events in ZDC energy vs. BBC charge used to classify events in the "centrality clock". The middle plot are the inclusive, and semi-inclusive $N_{\rm ch\ tracks}$ distributions at midrapidity made from the centrality clock. The points in the bottom plot are the semi-inclusive multiplicity measurements in the Wounded Nucleon Model $\langle N_{\rm ch\ tracks}\rangle/\langle N_{\rm nuc-part}\rangle$: the rising trend with centrality suggests the model does not account for the multiplicity production at 130 GeV. Figure referenced in Chapter 4. (courtesy Alexander Bazilevsky (BNL) [2]).

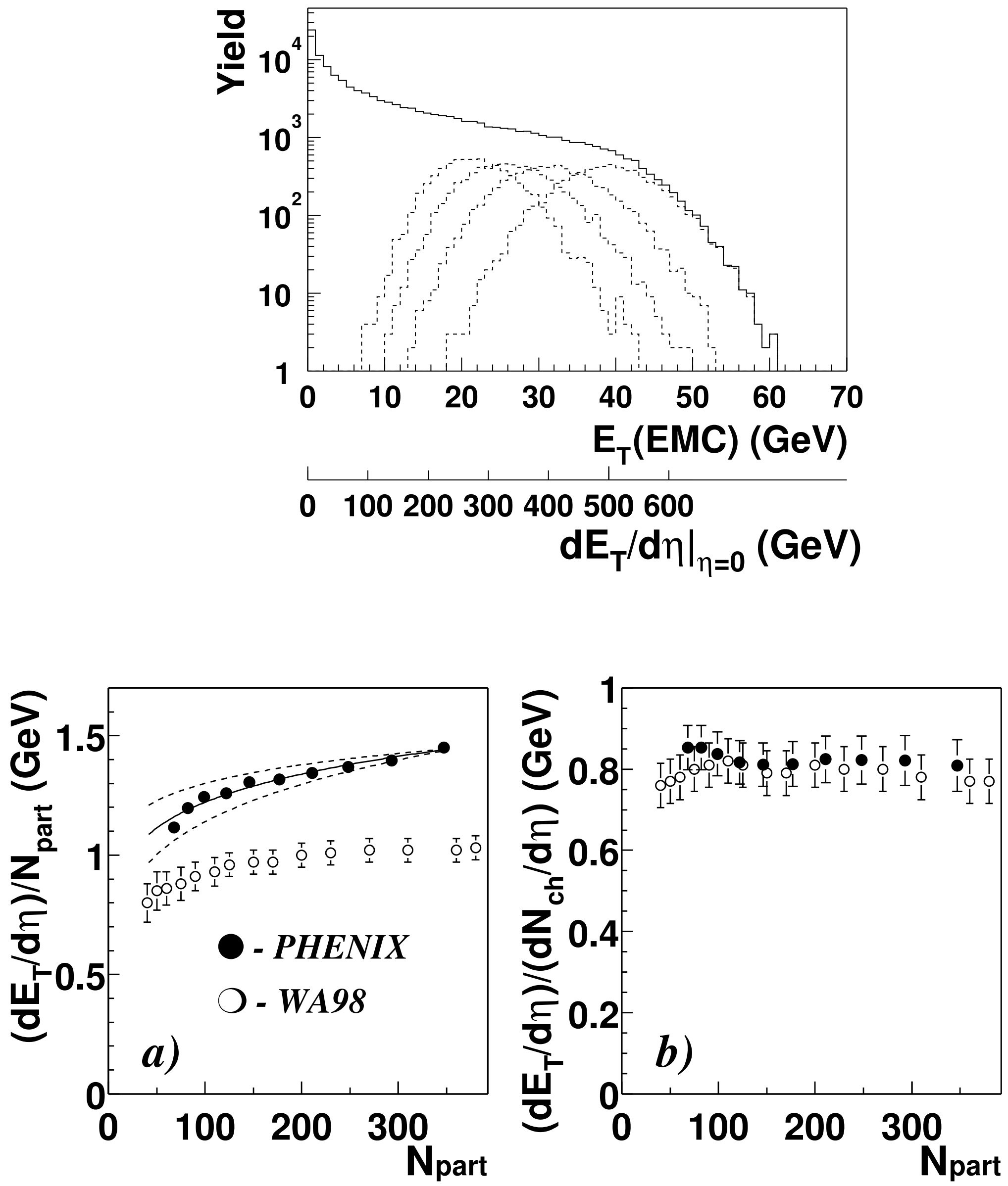

Figure 64: PHENIX previous results (2001): 130 GeV Au+Au. The top plot shows event-by-event $E_{T\ (\mathrm{EMC})}$ inclusive and semi-inclusive distributions at mid-rapidity. The bottom left plot are the mean E_T measurements in centrality in the Wounded Nucleon model $\langle E_T \rangle / \langle N_{\mathrm{nuc-part}} \rangle$, the rising trend with centrality suggests the model does not account for the E_T production at 130 GeV. The bottom right plot shows the ratio $\langle E_T \rangle / \langle N_{\mathrm{ch\ tracks}} \rangle$ is flat to within the errors suggesting that E_T scales with multiplicity. Figure referenced in Chapter 4. (courtesy Alexander Bazilevsky (BNL) [3]).

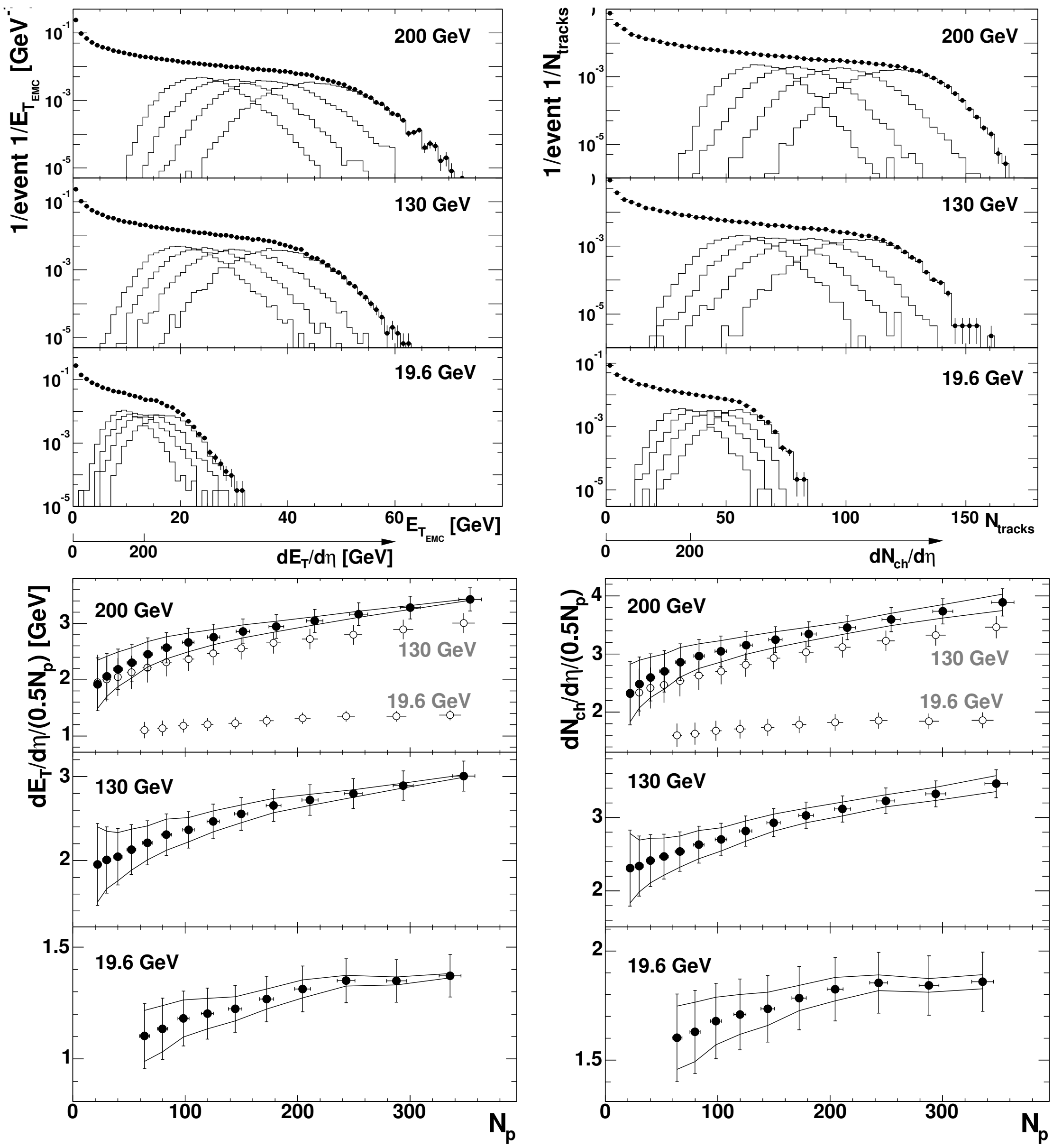

Figure 65: PHENIX previous results (2005): 19.6, 130, and 200 GeV Au+Au midrapidity measurements. The top plots are the E_T and $N_{\mathrm{ch\ tracks}}$ distributions in centrality. The bottom plots are the respective $\langle E_T\rangle/\langle N_{\mathrm{nuc-part}}\rangle$, and $\langle N_{\mathrm{ch\ tracks}}\rangle/\langle N_{\mathrm{nuc-part}}\rangle$ measurements. Figure referenced in Chapter 4. (courtesy Alexander Milov (BNL) [4]).

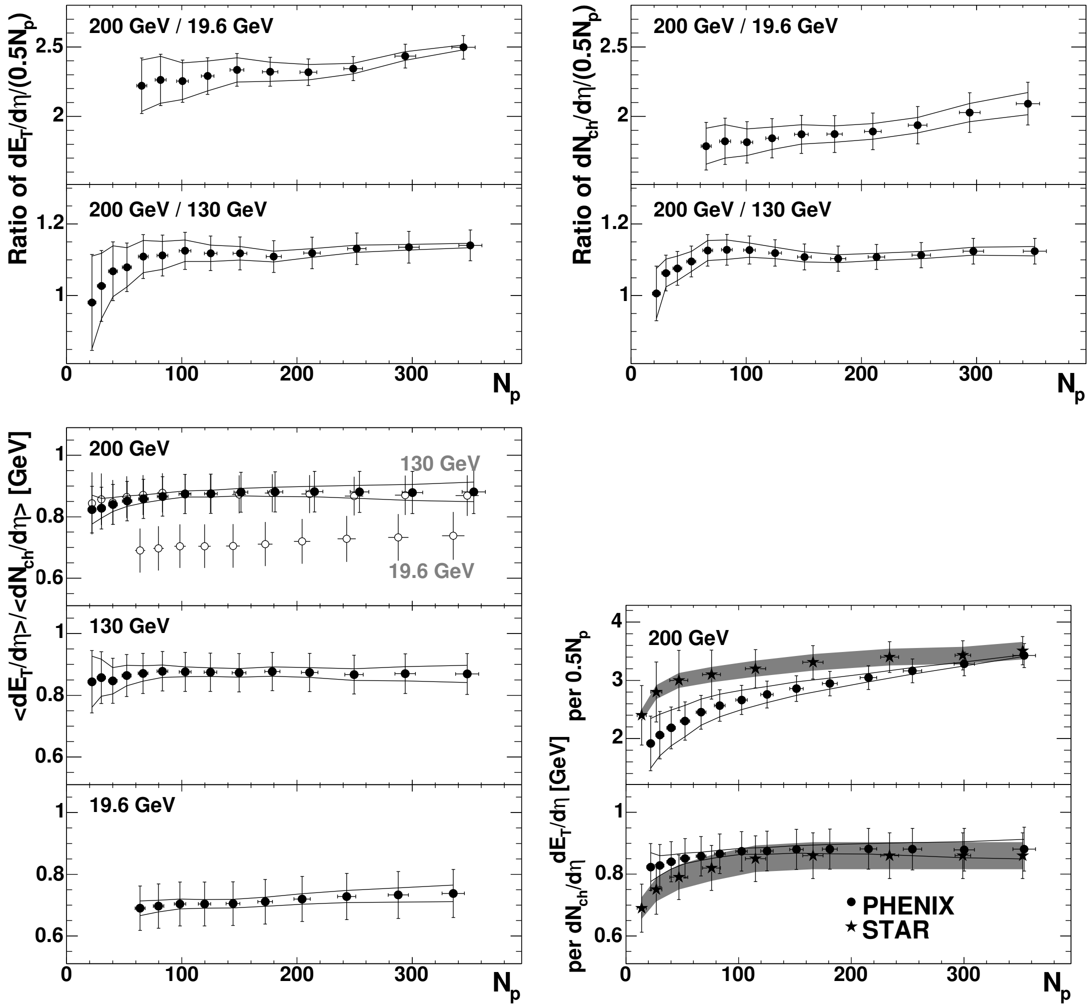

Figure 66: PHENIX and STAR previous results (2005) at midrapidity: The top plots are $\langle E_T \rangle / \langle N_{\text{nuc-part}} \rangle$ ratios and $\langle N_{\text{ch tracks}} \rangle / \langle N_{\text{nuc-part}} \rangle$ ratios for the different collision energies which are flat to within the errors. The bottom left plot is the E_T to multiplicity ratios for specific energies. The bottom right plot show the PHENIX and STAR measurements are in agreement. Figure referenced in Chapter 4. (courtesy Alexander Milov (BNL) [4]).

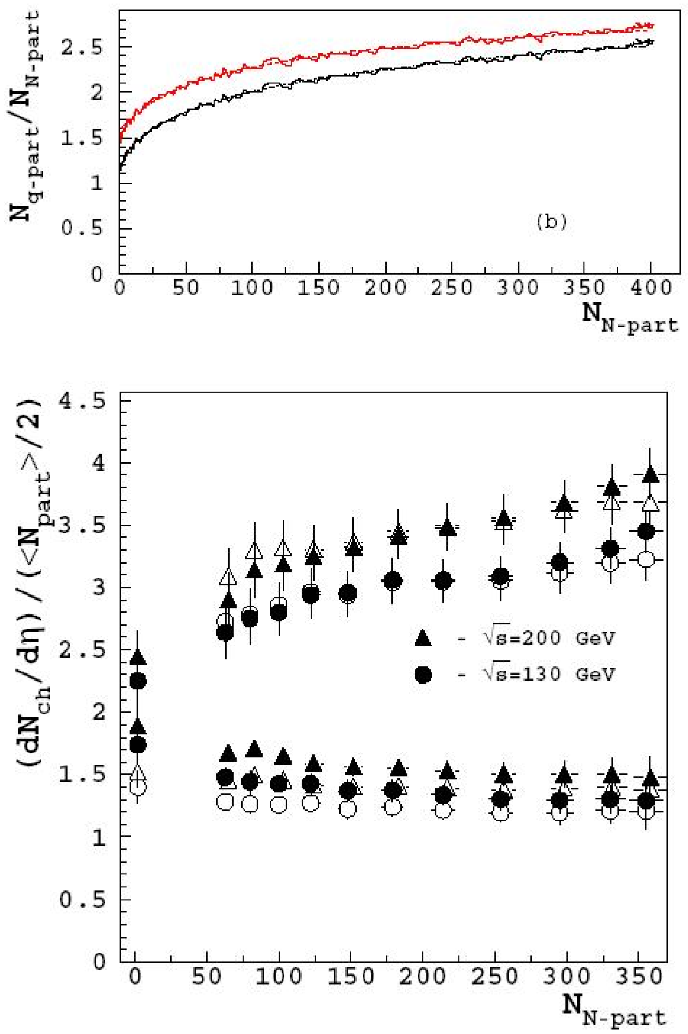

Figure 67: PHOBOS results renormalized (2003): PHOBOS 130 and 200 GeV Au+Au event-by-event multiplicity mid-rapidity results. The top plot shows a model relation between nucleon participants and quark participants in the Nuclear Overlap Model calculated by Eremin and Voloshin (see Chapter 4.1, Equation 76). In the bottom plot the PHOBOS multiplicity data are compared in the two models - the upward sloping points are normalized to nucleon participants $\langle N_{\mathrm{ch\ tracks}}\rangle/\langle N_{\mathrm{nuc-part}}\rangle$, and the flatter points to quark participants $\langle N_{\mathrm{ch\ tracks}}\rangle/\langle N_{\mathrm{quark-part}}\rangle$. This work by Eremin and Voloshin was an early demonstration – if not the first demonstration – that multiplicity production at mid-rapidity for RHIC energies is explained by a quark participant model (courtesy [21]). Figure referenced in Chapter 4.

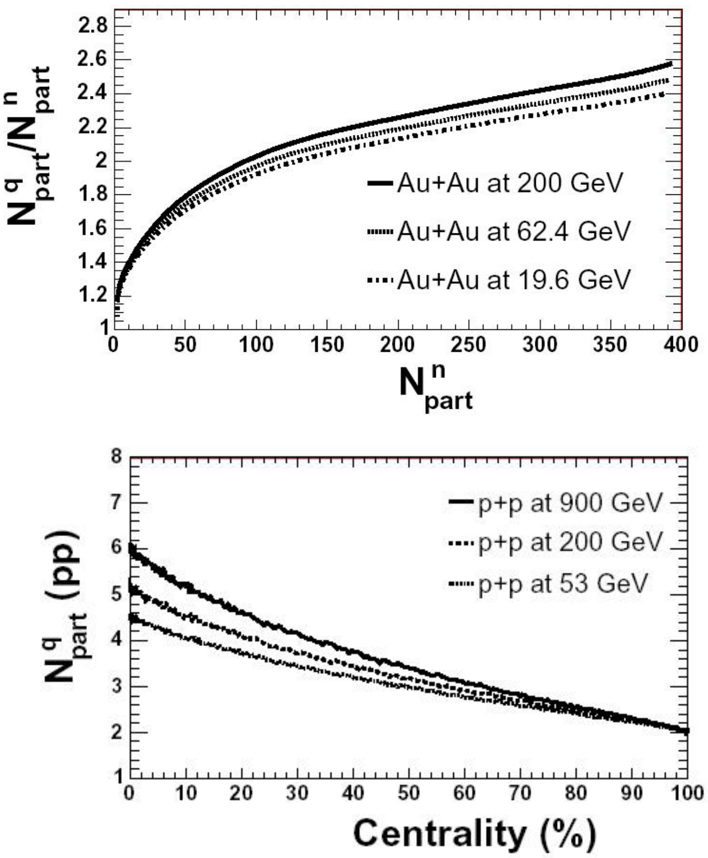

Figure 68: PHOBOS results: modeled $N_{\mathrm{quark-part}}$ estimations compared to $N_{\mathrm{nuc-part}}$ over centrality, used by PHOBOS for $p+p$ and Au+Au interactions. Figure referenced in Chapter 4. (courtesy R. Nouicer (BNL) [35]).

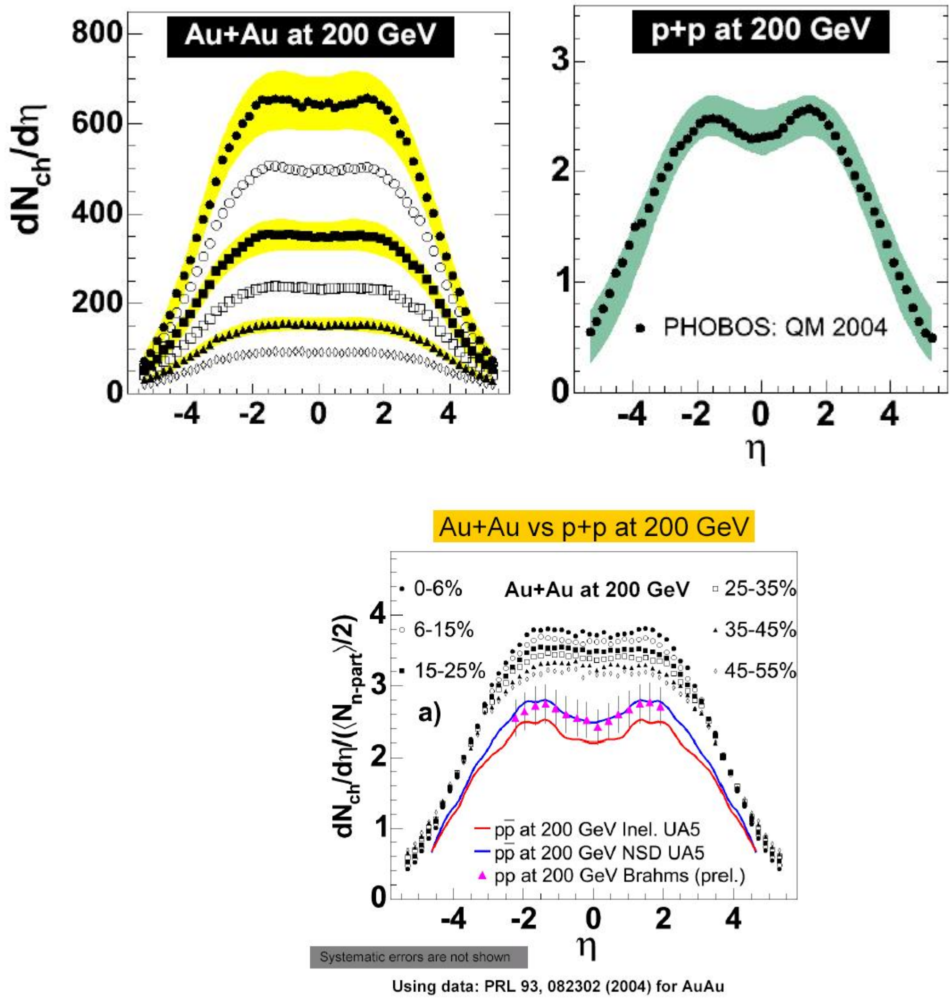

Figure 69: PHOBOS results (2005): $\langle N_{\mathrm{ch\ tracks}} \rangle$ measurements in 200 GeV Au+Au for various centralities, and $p + p$ measurements from other experiments, shown over a large range of pseudorapidity. The top plot shows the number of tracks. The bottom plot shows in the different centrality classes the number of tracks normalized to $\langle N_{\mathrm{nuc-part}} \rangle$ do not agree at mid-rapidity; the fact that they do agree at $\eta \sim \pm 3.8$ is suspicious as this happens to be where the BBC triggers are - coincidence or maybe a systematic artifact? In the model $p + p$ does not line up with Au+Au. Figure referenced in Chapter 4. (courtesy R. Nouicer (BNL) [34]).

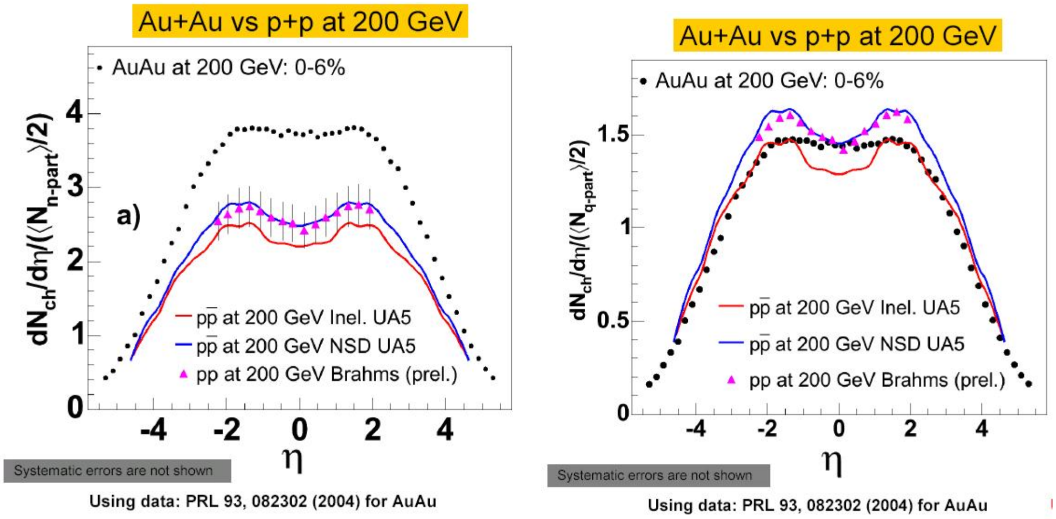

Figure 70: PHOBOS results (2005): $\langle N_{\text{ch tracks}}\rangle$ production in 200 GeV central Au+Au collisions compared to $p+p$, over a large range of pseudorapidity: (left plot) when normalized to $\langle N_{\text{nuc}-\text{part}}\rangle$ does not line up, but (right plot) when normalized to $\langle N_{\text{quark}-\text{part}}\rangle$ lines up other than a discrepancy at mid-rapidity. Figure referenced in Chapter 4. (courtesy R. Nouicer (BNL) [34]).

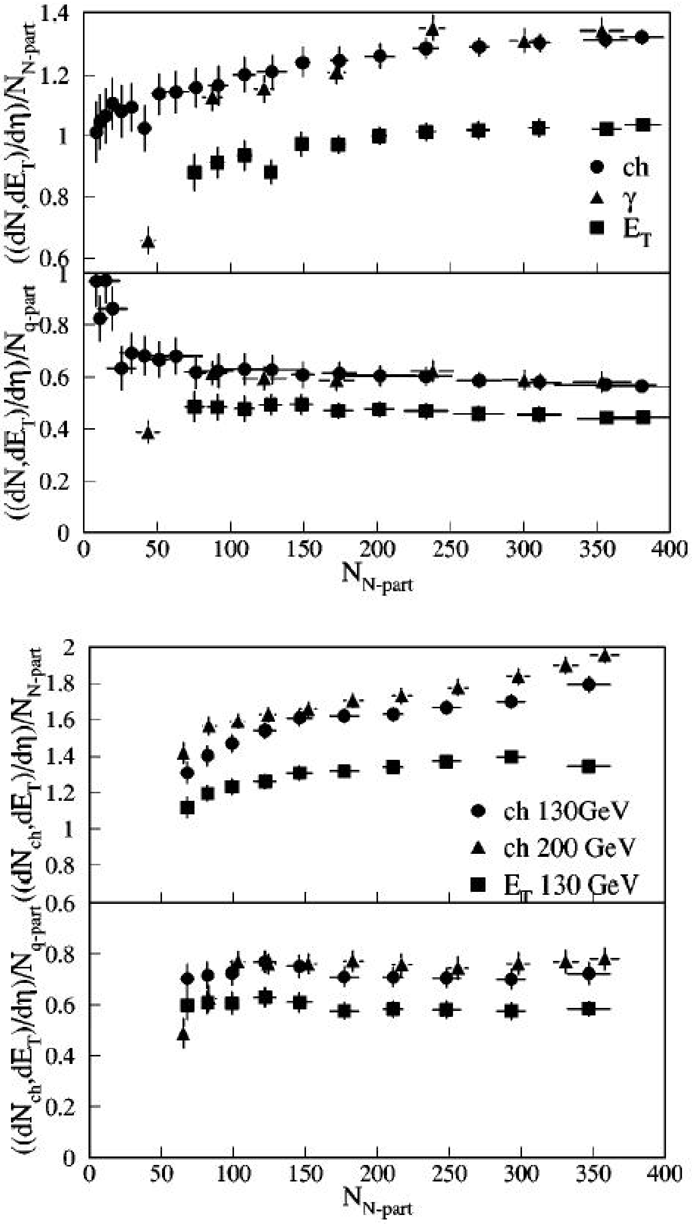

Figure 71: SPS and RHIC previous results (2004): comparison of production in the nucleon and quark models at mid-rapidity. The top plot are WA98 results for 158 GeV/A Pb+Pb $\langle N_{\mathrm{ch}}\rangle$, $\langle N_{\gamma}\rangle$, and $\langle E_T\rangle$. The bottom plot are PHOBOS results for 130 and 200 GeV Au+Au $\langle N_{\mathrm{ch\ tracks}}\rangle$, and PHENIX 130 GeV Au+Au results for $\langle E_T\rangle$. Results are flatter in the quark normalization which better describes the multiplicity and E_T production. Figure referenced in Chapter 4. (courtesy Netrakanti and Mohanty [28]).

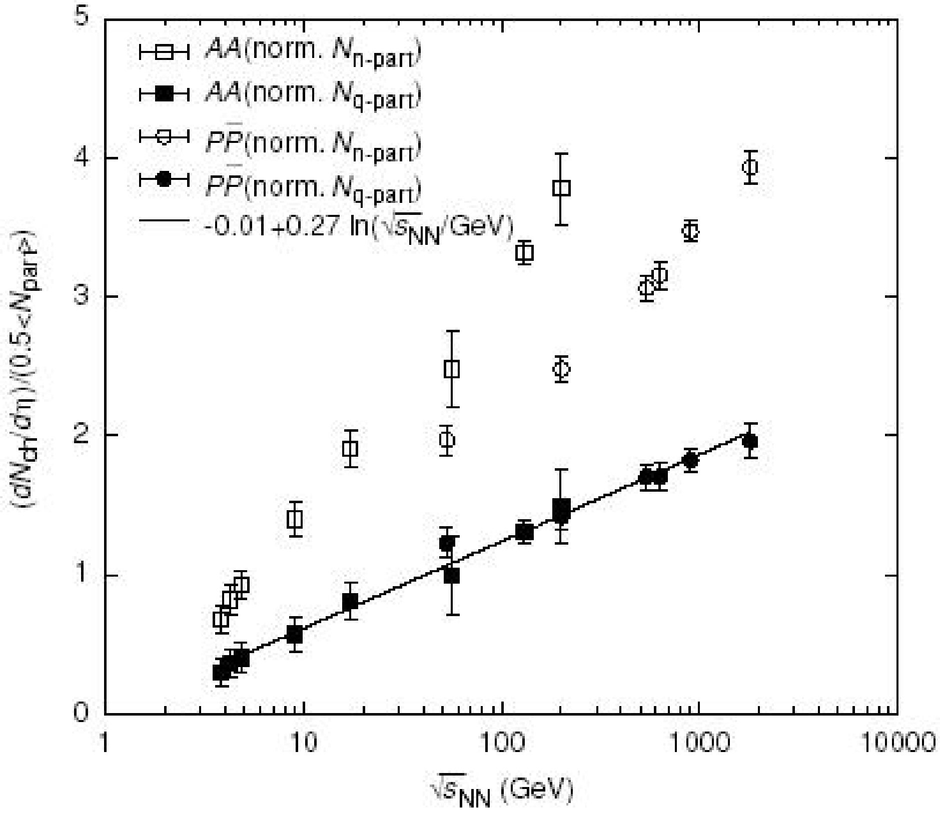

Figure 72: SPS and RHIC previous results (2005): Illustration that at mid-rapidity the measurements for $\langle N_{\rm ch}\rangle/\langle N_{\rm quark-part}\rangle$ (closed symbols) for the different species $p+p$, Pb+Pb, and Au+Au, and from SPS to RHIC energies all fall on an equation of a line; but that $\langle N_{\rm ch}\rangle/\langle N_{\rm nuc-part}\rangle$ do not (open symbols). Figure referenced in Chapter 4. (courtesy Bhaskar De and S. Bhattacharyya [19]).

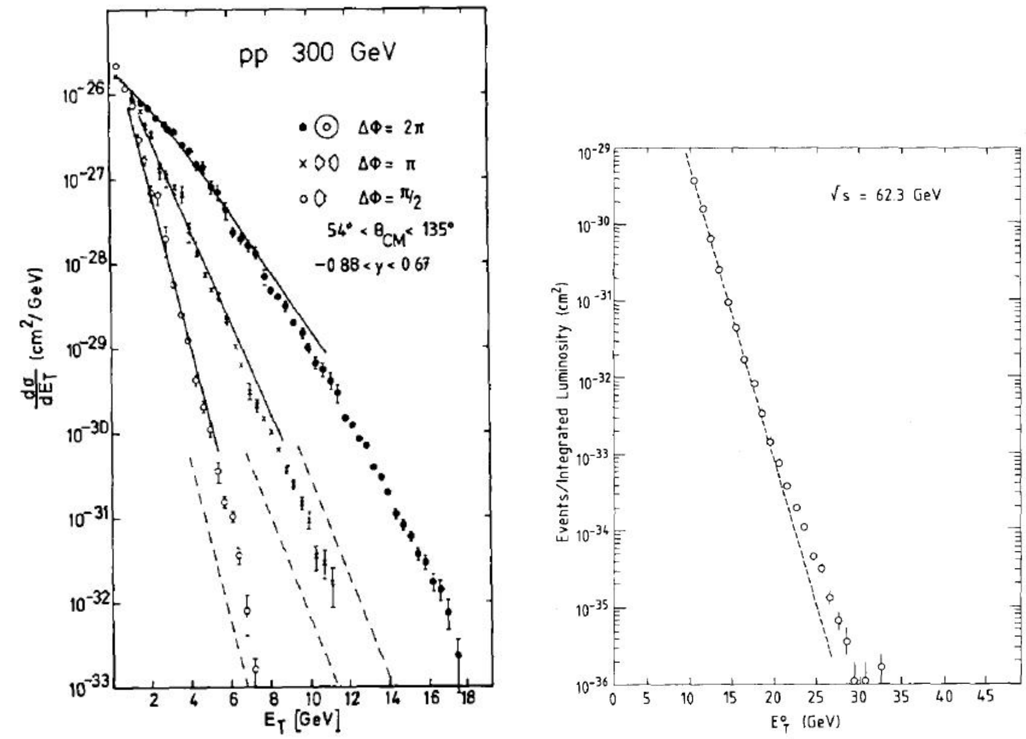

Figure 73: NA5 (1980) and CCOR (1983) results: event-by-event E_T distributions fitted to gamma distributions which have the characteristic of exponentially shaped tails at high E_T. Jets are highly energetic events and produce fluctuations in the E_T distributions. The left plot (NA5) shows for $\sqrt{s_{NN}} = 23$ GeV $p+p$ fixed target collisions the upper E_T tail does not break away from the exponential fit 7 orders of magnitude down suggesting the absence of jets. The right plot (CCOR) shows in $\sqrt{s_{NN}} = 62.3$ GeV $p+p$ jets appear 8 orders of magnitude down the tail (courtesy [5]). Figure referenced in Chapter 4.

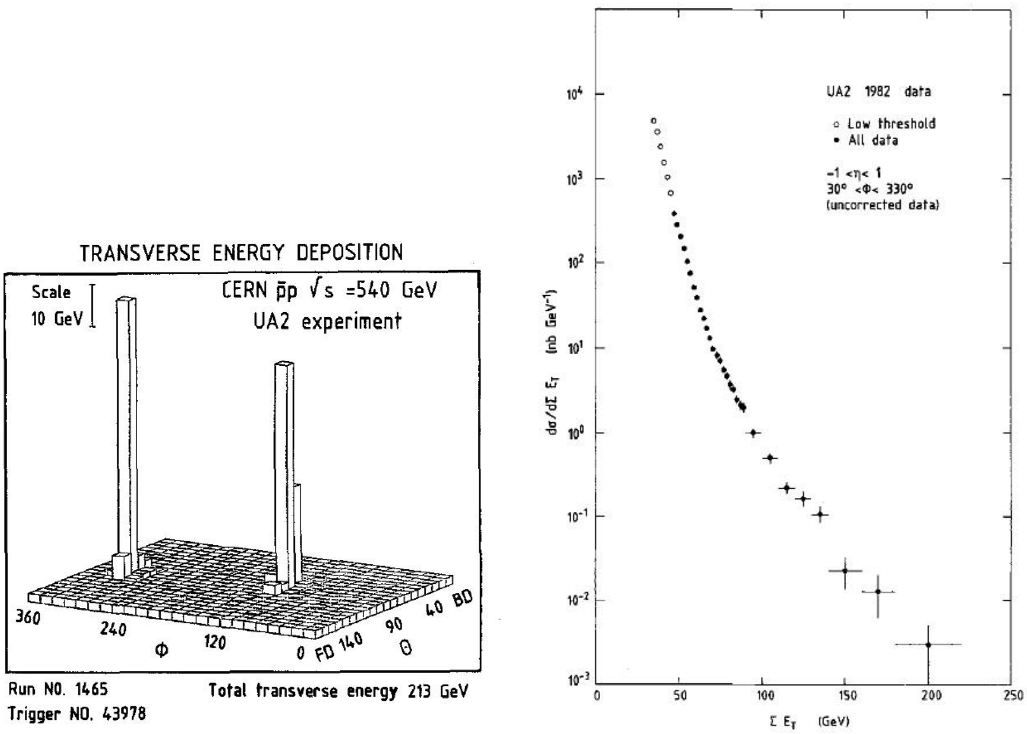

Figure 74: UA2 results (1983): $\sqrt{s_{NN}} = 540$ GeV $p + \overline{p}$ collisions. The left plot is the energy deposition for the single event having largest transverse energy – the two spikes are two back-to-back jets. The right plot shows jets appear at the "knee" in the distribution at about 120 GeV, at about 5 to 6 orders of magnitude down (courtesy [30]). Figure referenced in Chapter 4.

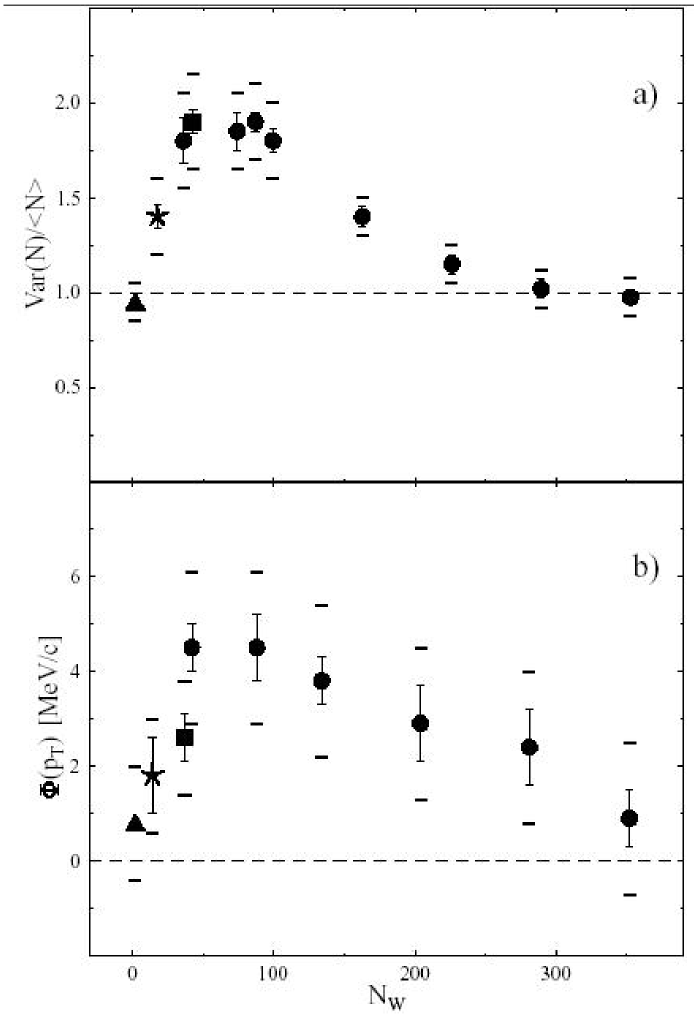

Figure 75: NA49 results (2004): fixed target $\sqrt{s_{NN}} = 17$ GeV scaled variance fluctuations $\frac{\sigma^2}{\mu}$ for multiplicity (top plot) and p_T (bottom plot) of negative particles vs. centrality. The triangle is $p + p$, asterisk is C+C, square is Si+Si, and circles are Pb+Pb. Vertical bars are statistical errors and dashes are the statistical plus systematic total error. These published results by NA49 were in large part motivational for the fluctuations analysis performed with PHENIX data in this thesis. However within the first year after the release of this paper more was understood about systematic affects to the fluctuations such as the centrality cut (courtesy [33]). Figure referenced in Chapter 4.

B.5 Figures referenced in Chapter 5

B.5.1 Figures of E_T distributions

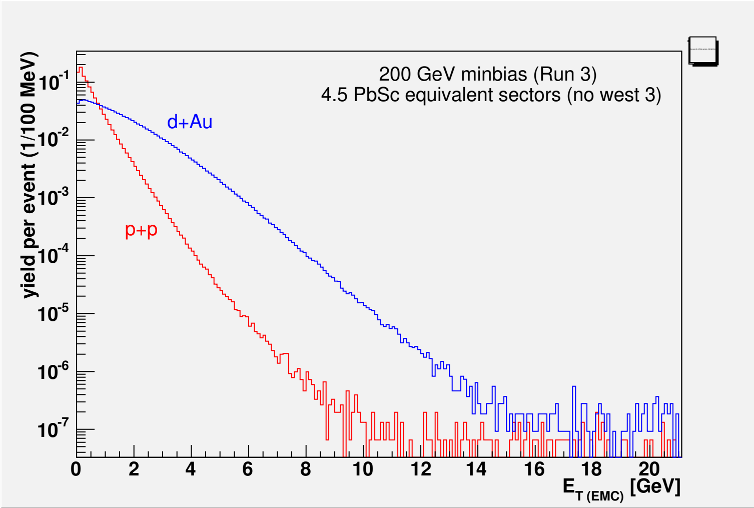

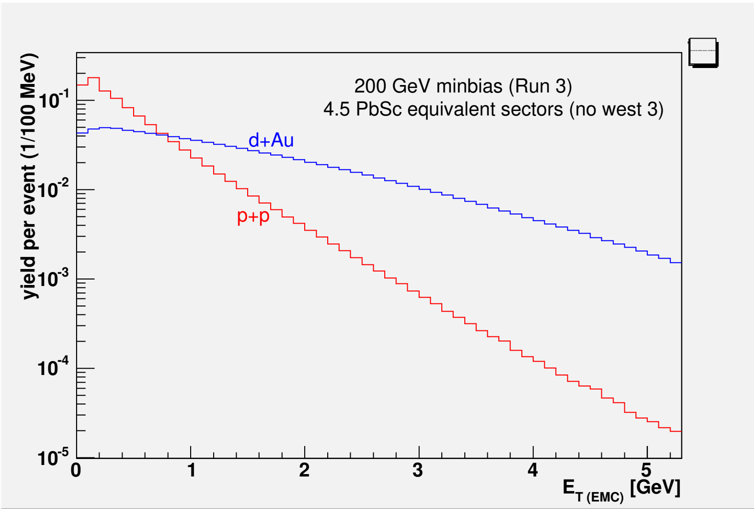

Figure 76: 200 GeV $p + p$ and d+Au event-by-event inclusive $E_{T\ (\mathrm{EMC})}$ distributions obtained in 4.5 equivalent PbSc sectors. The bottom plot is the low E_T region viewed up close. The $p + p$ distribution is sharply exponential with evidence of a slightly breaking tail possibly due to jets. The d+Au distribution shows the low E_T plateau region characteristic of successive collisions, but jets are not clearly observed in the upper tail. The minbias triggers which had zero E_T in the EMC were discarded. Some nebulous EMC hot towers are evident at high energies, and the possibility of pile-up events was not investigated. Figure referenced in Chapter 5.

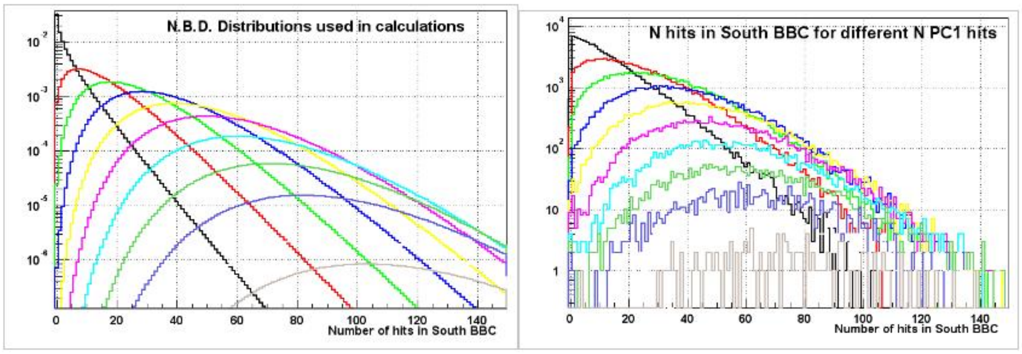

Figure 77: PHENIX previous results (2003): d+Au 200 GeV distributions of hits to the Beam Beam Counter located on the other side of the interaction region from the oncoming Au beam; (left plot) modeled N.B.D distributions for the number of BBC hits weighted with Glauber probability and, (right plot) the measured BBC hits distributions obtained by using a cut on Pad Chamber 1 number of hits to constrain centrality. The measured distributions are broader due to additional fluctuations introduced by the cut. Figure referenced in Chapter 5. (courtesy PHENIX Analysis Note 210 [20] (BNL)).

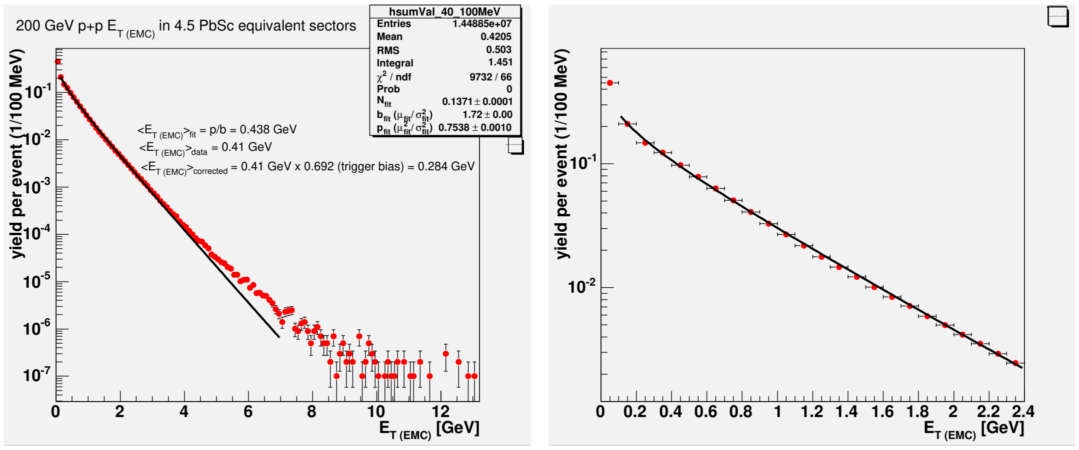

Figure 78: 200 GeV $p + p$ event-by-event $E_{T\ (\mathrm{EMC})}$ inclusive histogram fitted to a gamma distribution $N\frac{b}{\Gamma(p)}(bE_T)^{p-1}e^{-bE_T}$, where N is the normalization, and b and p the fit parameters. The fit excluded the first 100 MeV bin which contains minbias triggers which resulted in zero E_T. The right plot is a close up view. Figure referenced in Chapter 5.

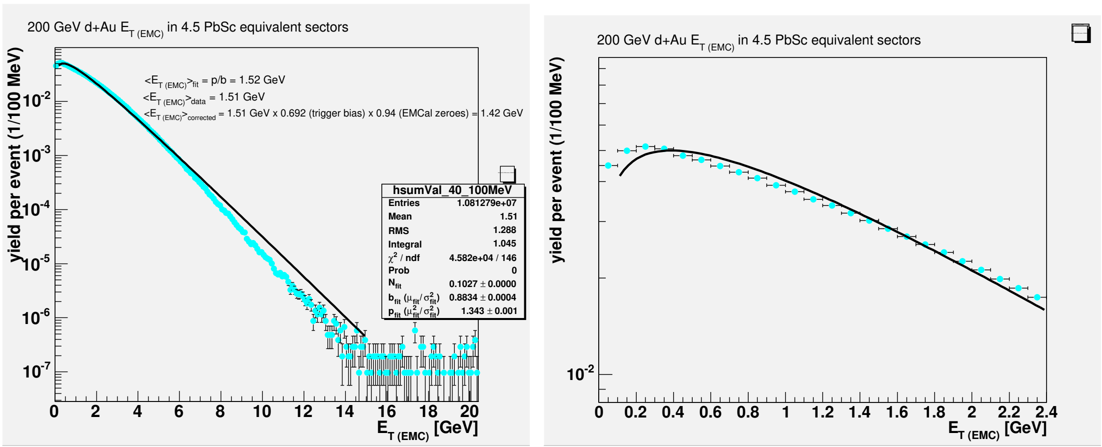

Figure 79: 200 GeV d+Au event-by-event $E_{T\ (\mathrm{EMC})}$ inclusive histogram fitted to a gamma distribution. The fit excluded the first 100 MeV bin. Note that the minbias triggers which had zero $E_{T\ (\mathrm{EMC})}$ were not included in the histogram. The right plot is a close up view showing the fit fails at low E_T. Figure referenced in Chapter 5.

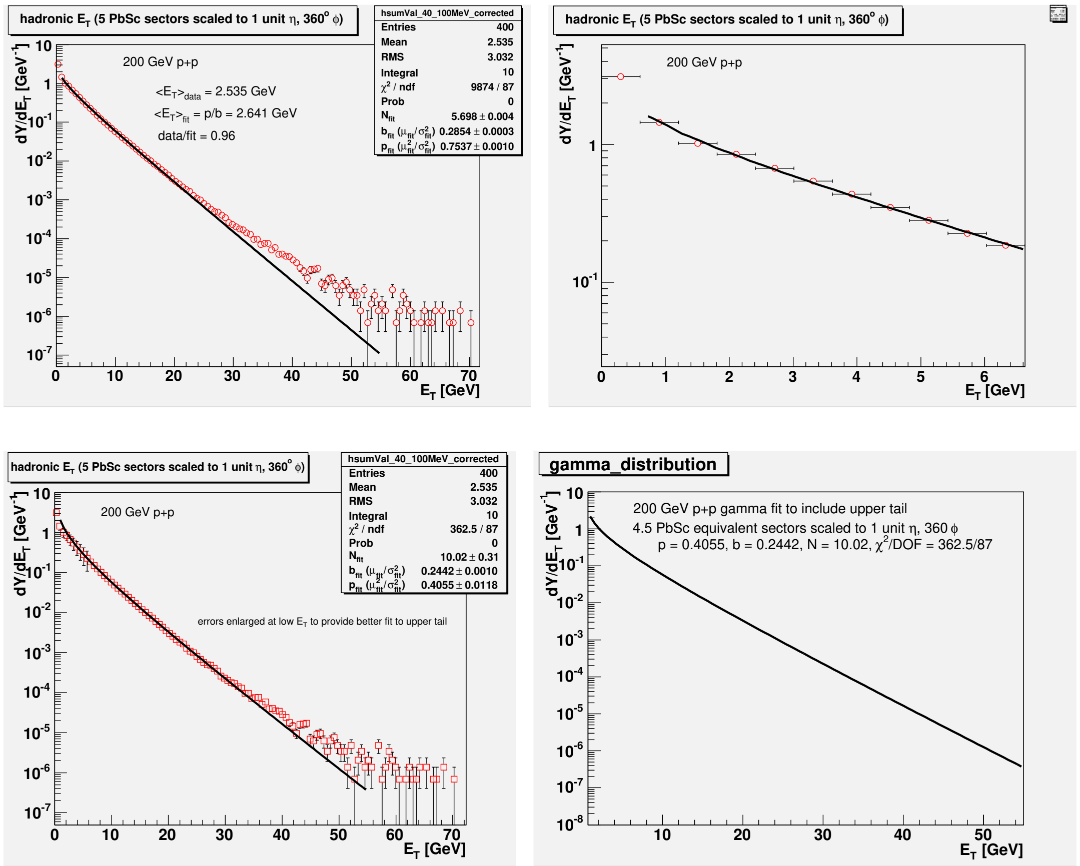

Figure 80: 200 GeV p+p event-by-event inclusive hadronic E_T fitted to a gamma distribution. These were measured in 4.5 equivalent PbSc sectors, corrected for faulty towers, scaled to 1 unit of $\Delta\eta$ and 360° in $\Delta\phi$, and scaled by the Au+Au $k-$factor of 1.30. The top right plot is the low E_T region. In the top plots the fit was begun at the 2nd histogram bin to avoid the discontinuity at zero E_T. In the bottom plots the error was expanded on the low E_T points with purpose to fit the high E_T tail which, upon afterthought this would have been more accurately done by leaving out the low E_T points all together. The bottom right plot is this gamma distribution by itself. The binning is 100 MeV but the yield per bin referenced to a 1 GeV bin size. Figure referenced in Chapter 5.

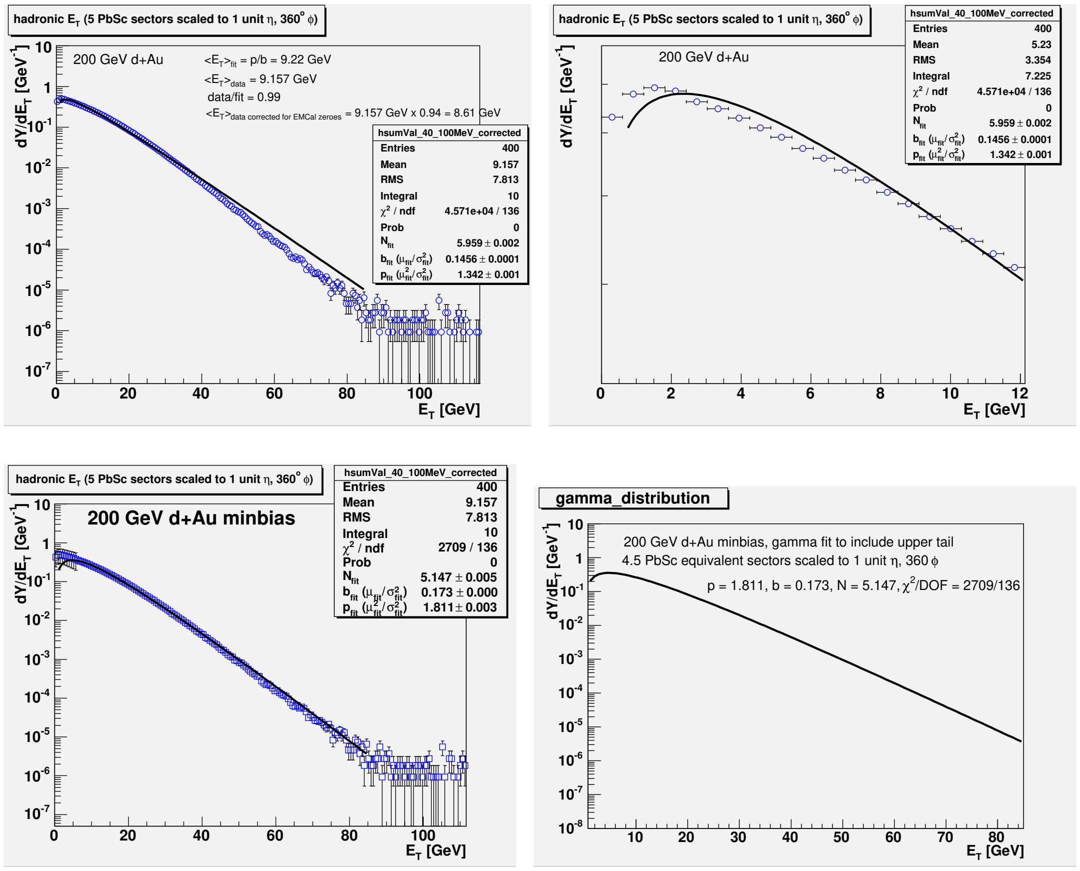

Figure 81: 200 GeV d+Au event-by-event inclusive hadronic E_T fitted to a gamma distribution. These were measured in 4.5 equivalent PbSc sectors, corrected for faulty towers, scaled to 1 unit of $\Delta\eta$ and 360° in $\Delta\phi$, and scaled by the Au+Au $k-$factor of 1.30. The top right plot is the low E_T region. In the top plots the fit was begun at the 2nd histogram bin to avoid any discontinuity near zero E_T. In the bottom plots the error was expanded on the low E_T points with purpose to fit the high E_T tail which, upon afterthought this would have been more accurately done by leaving out the low E_T points all together. The bottom right plot is this gamma distribution by itself. The binning is 100 MeV but the yield per bin referenced to a 1 GeV bin size. Figure referenced in Chapter 5.

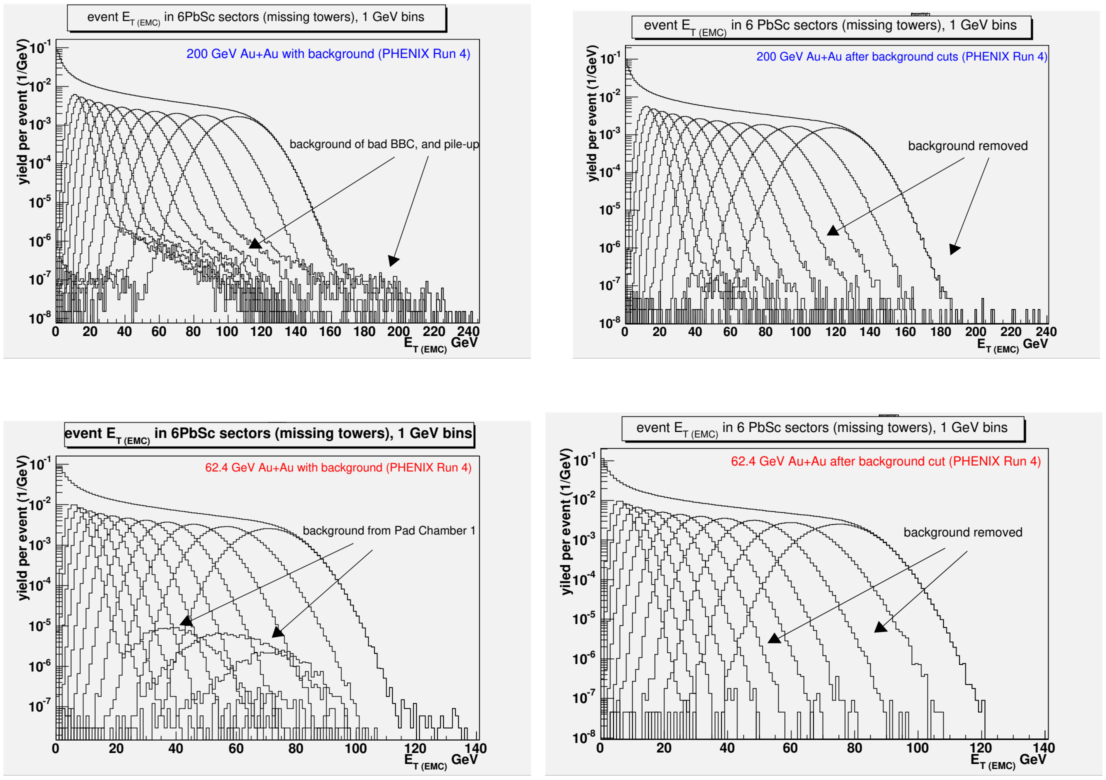

Figure 82: 200 GeV (top plots) and 62.4 GeV (bottom plots) Au+Au event-by-event $E_{T\ (\mathrm{EMC})}$ inclusive and semi-inclusive distributions 0-5%, 5-10%, ..., 50-55% centrality, before (left plots) and after (right plots) background cuts. In 200 GeV interactions events having no valid BBC timing and also pile-up events are displaced in centrality. The BBC timing background (top left plot) is an order of magnitude larger than the pile-up. In 62.4 GeV interactions events with an incorrect Pad Chamber multiplicity are displaced in centrality. In the (lower left plot) 62.4 GeV the pile-up is barely visible in the inclusive distribution at 7 orders down, due to lower luminosity (additional note: after background cuts more PbSc towers were included but fewer events analyzed.) Figure referenced in Chapter 5.

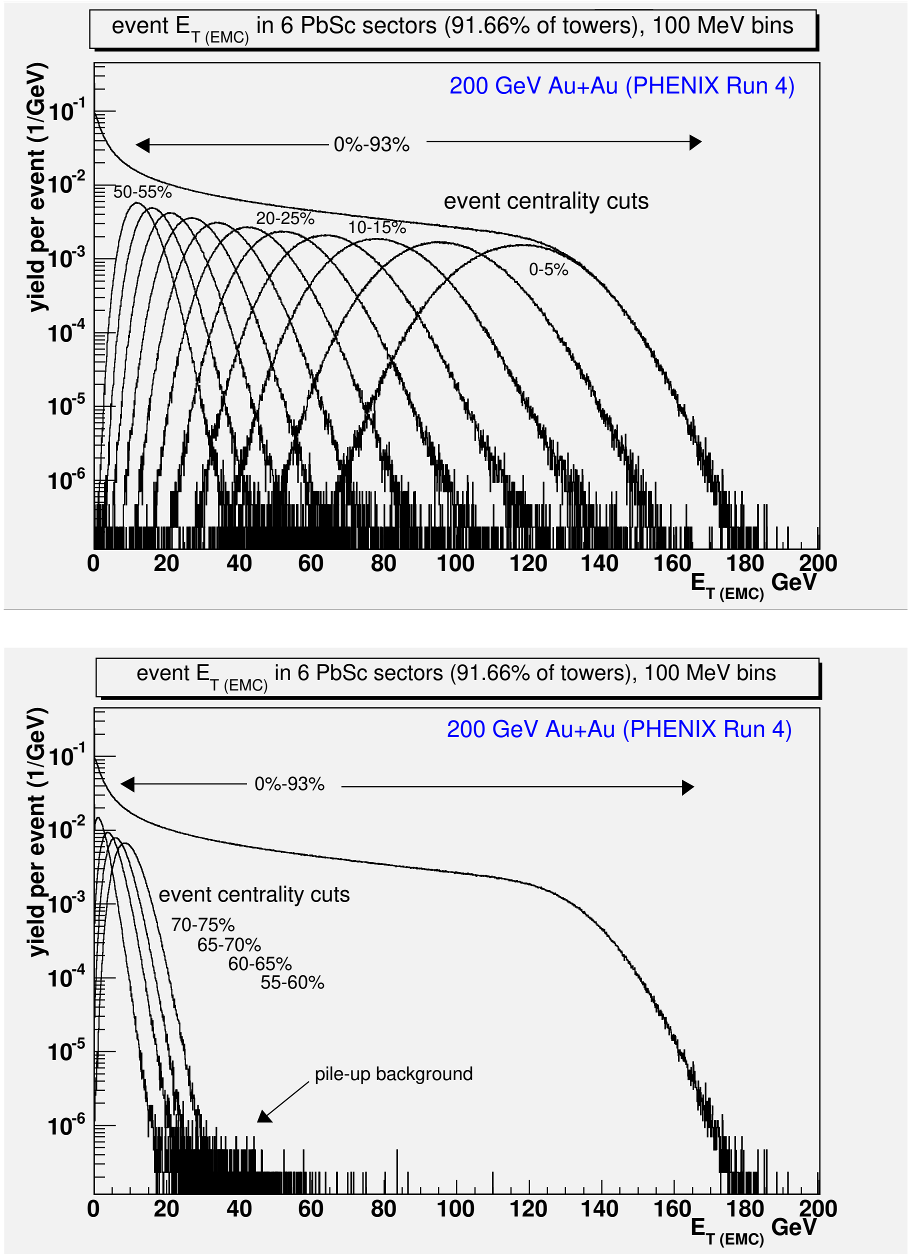

Figure 83: 200 GeV Au+Au event-by-event $E_{T\ (\mathrm{EMC})}$ inclusive and semi-inclusive distributions of (top plot) 0-5%, 5-10%, ..., 50-55% centrality, and (bottom plot) 55-60%, 60-65%, 65-70%, 70-75% centrality, after background cuts. Pile up is still present in the most peripheral distributions where the cut line in the ZDC-BBC space fails to remove it. It is illustrative to compare these measurements to the convolutions in Figure 61. Figure referenced in Chapter 5.

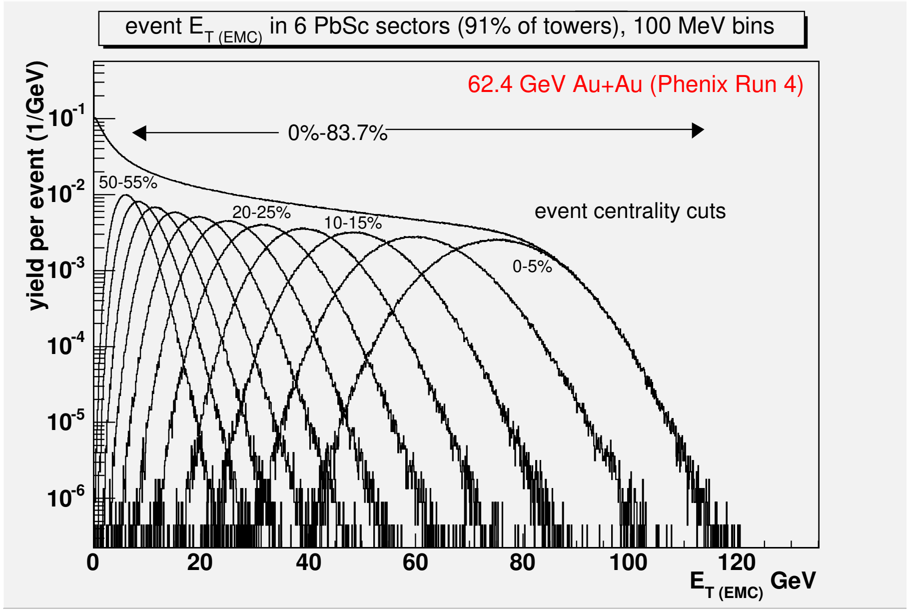

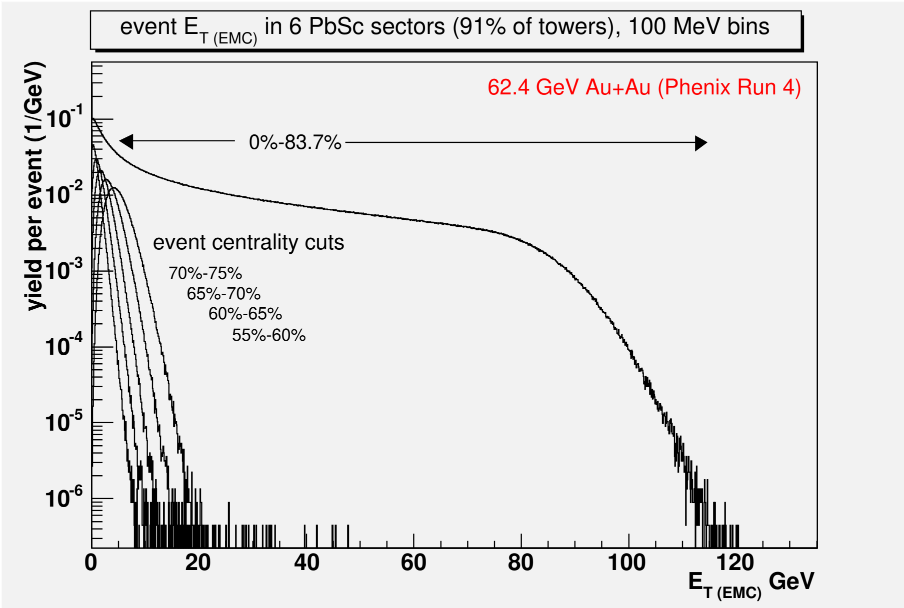

Figure 84: 62.4 GeV Au+Au event-by-event $E_{T\ (\mathrm{EMC})}$ inclusive and semi-inclusive distributions of (top plot) 0-5%, 5-10%, ..., 50-55% centrality, and (bottom plot) 55-60%, 60-65%, 65-70%, 70-75% centrality, after the background cut. It is illustrative to compare these measurements to the convolutions in Figure 61. Figure referenced in Chapter 5.

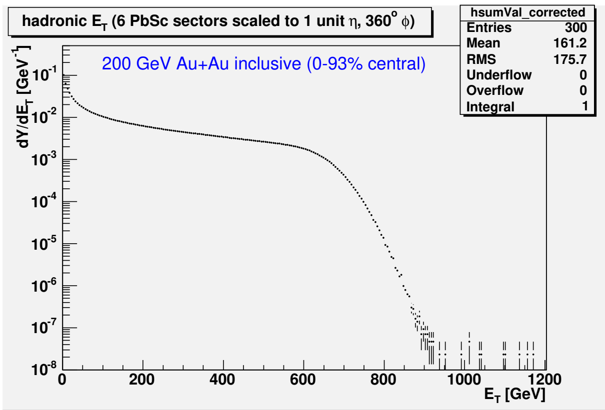

Figure 85: 200 GeV Au+Au minbias event-by-event inclusive hadronic E_T distribution. This was measured in 5.5 equivalent PbSc sectors, corrected for faulty towers, scaled to 1 unit of $\Delta\eta$ and 360° in $\Delta\phi$, and scaled by the Au+Au $k-$factor of 1.30. Figure referenced in Chapter 5.

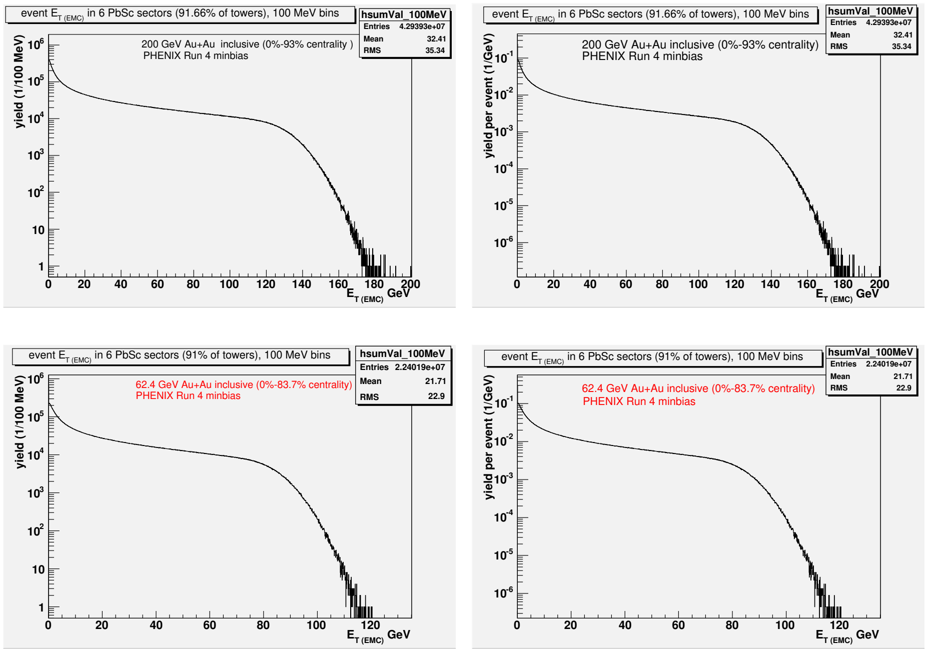

Figure 86: Top plots are 200 GeV Au+Au and bottom plots are 62.4 GeV Au+Au event-by-event $E_{T\ (\mathrm{EMC})}$ inclusive distributions with 100 MeV binning resolution shown (left plots) unnormalized, and (right plots) after each bin content is normalized to the distribution sum of events, and referenced to a 1 GeV bin size, providing a probability distribution. Figure referenced in Chapter 5.

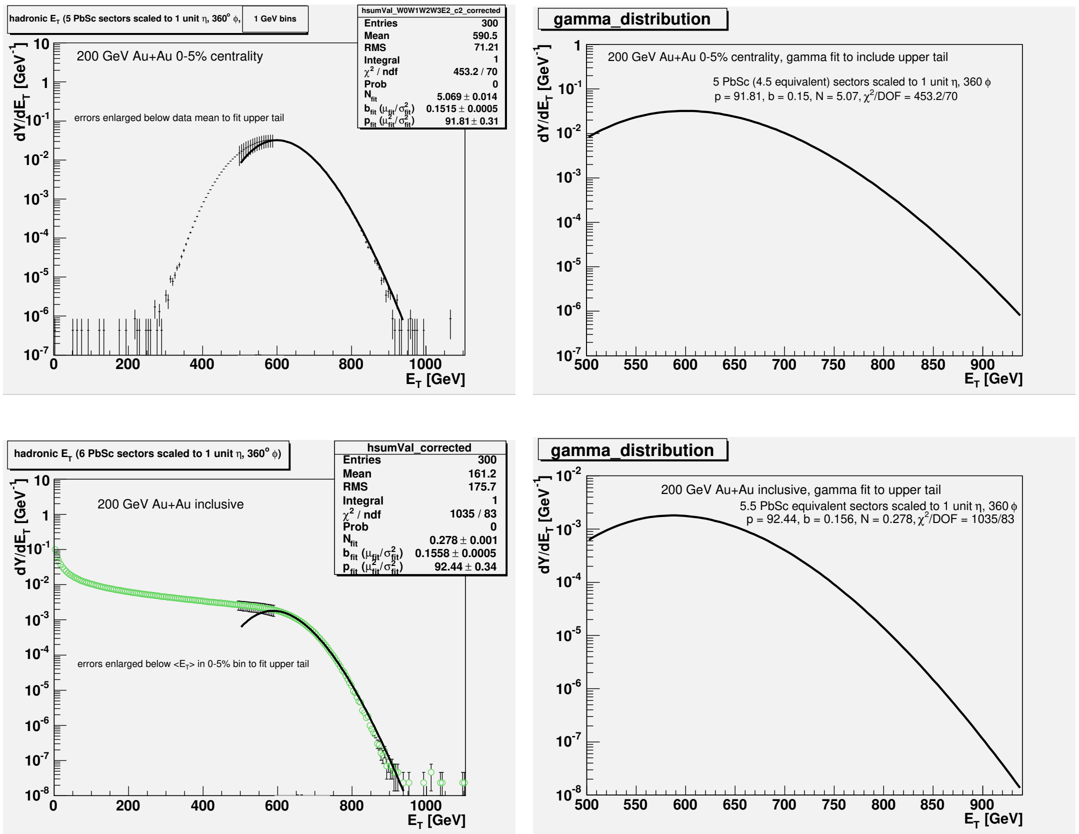

Figure 87: 200 GeV Au+Au event-by-event hadronic E_T. Top left plot is the 0-5% centrality measurement scale corrected from 4.5 equivalent sectors, and the bottom left plot is the inclusive distribution scale corrected from 5.5 equivalent sectors. The high E_T tails were fit to the gamma distribution, where the errors were expanded on the low E_T bins lying below the knee of the distributions (upon afterthought this would have been more accurately done by leaving out the low E_T bins all together). The right side plots are the gamma distributions. The 0-5% class is extracted from the inclusive distribution via the centrality cut, and thus similar results are obtained for the fit parameters (although it is noted that the distributions here were made in different acceptances, and this has an affect as explained in Chapter 5.5). Figure referenced in Chapter 5.

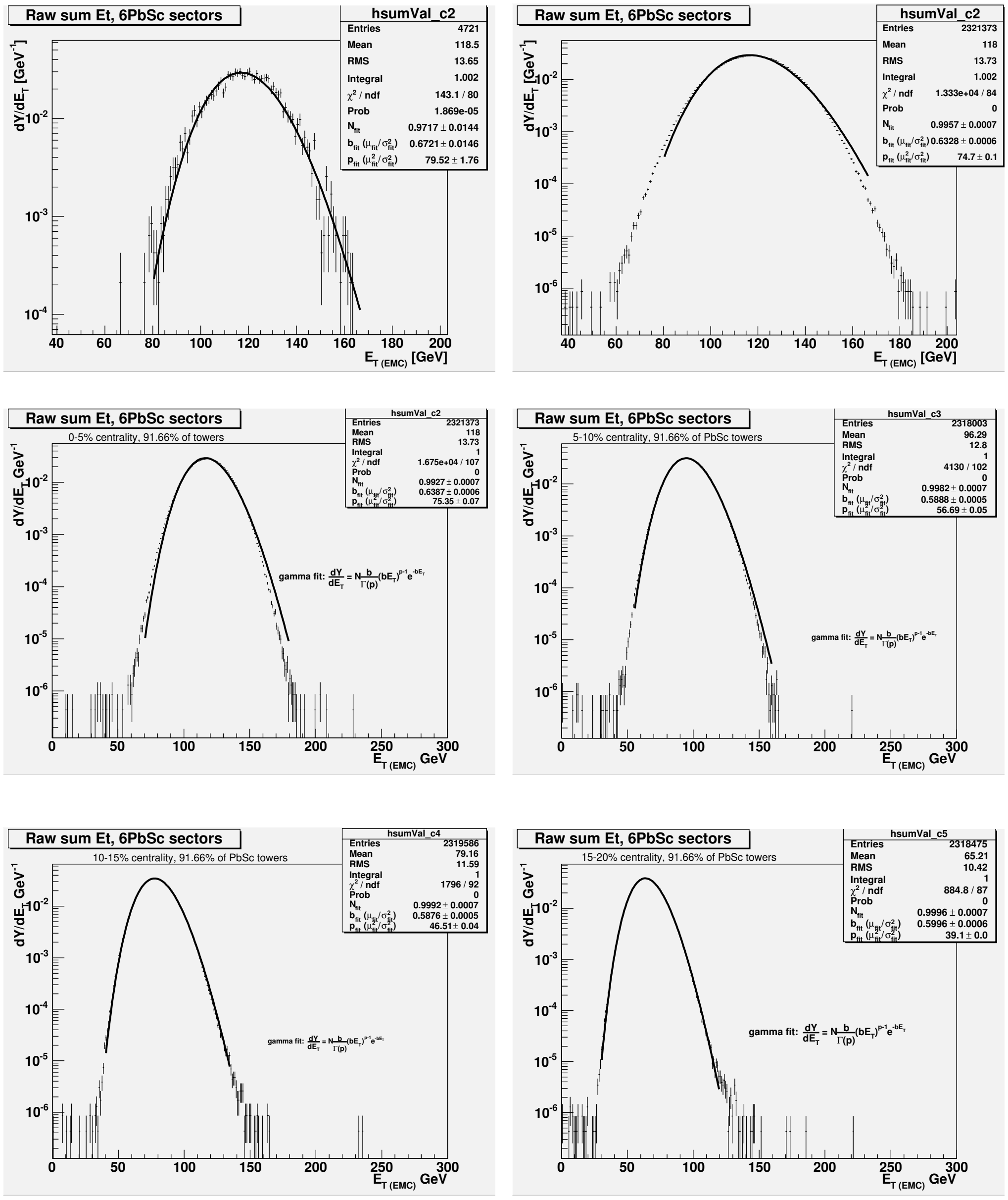

Figure 88: 200 GeV Au+Au 5% wide centrality $E_{T\ (\mathrm{EMC})}$ distributions fitted to gamma distribution. Measured in 5.5 equivalent sectors. The top two plots are both 0-5% centrality, the only difference is the right plot has much higher statistics – notice the χ^2/dof is much worse in high statistics. The other plots are 5-10%, 10-15%, and 15-20% centrality. Made in centrality-by-clock. Figure referenced in Chapter 5.

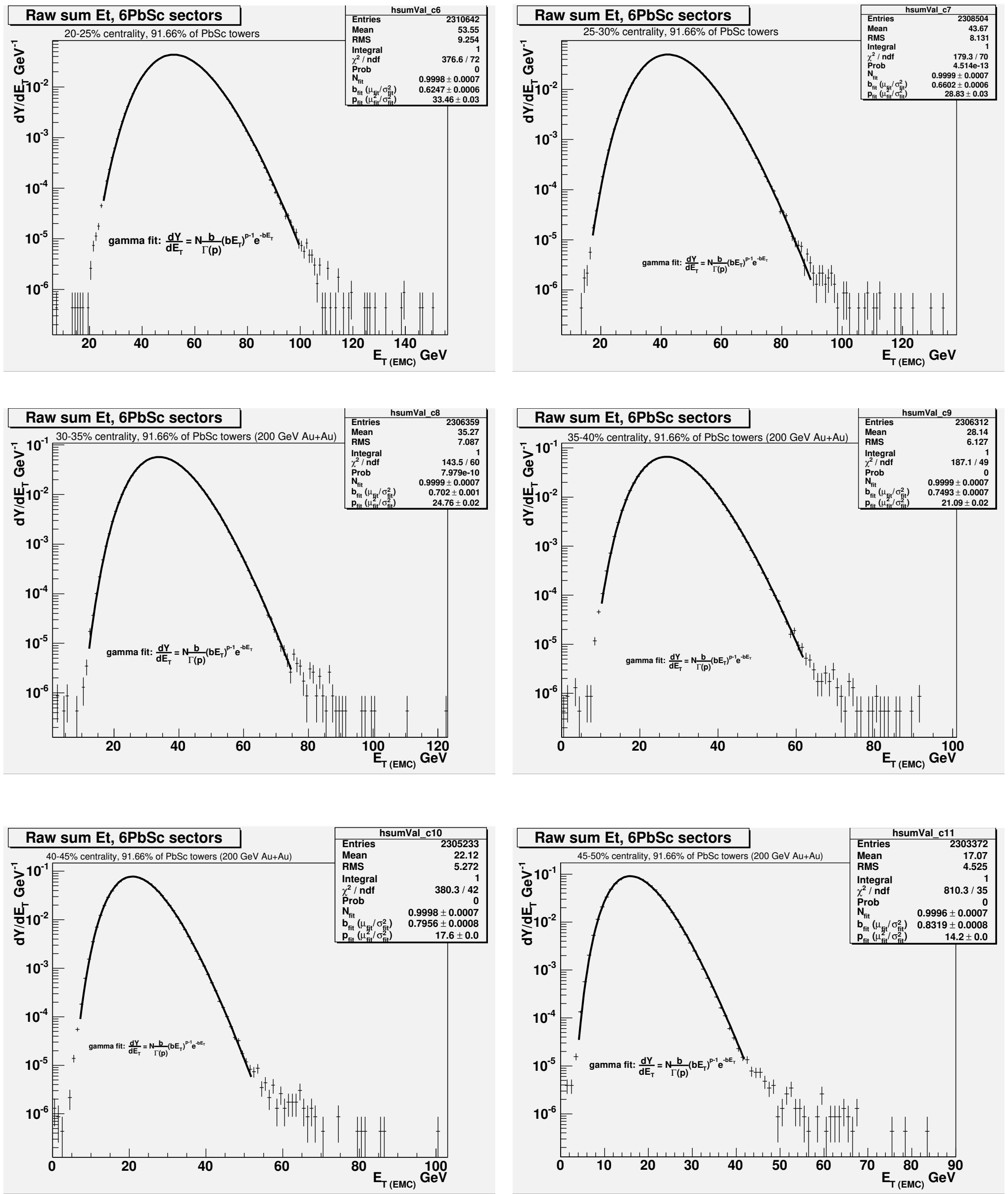

Figure 89: 200 GeV Au+Au 5% wide centrality $E_{T\,(\mathrm{EMC})}$ distributions fitted to gamma distribution. Measured in 5.5 equivalent sectors. Shown are 20-25%, 25-30%, 30-35%, 35-40%, 40-45%, and 45-50% centrality. Notice the background at high E_T in the peripheral distributions, this is the remaining pile up which the cut did not remove. Made in centrality-by-clock. Figure referenced in Chapter 5.

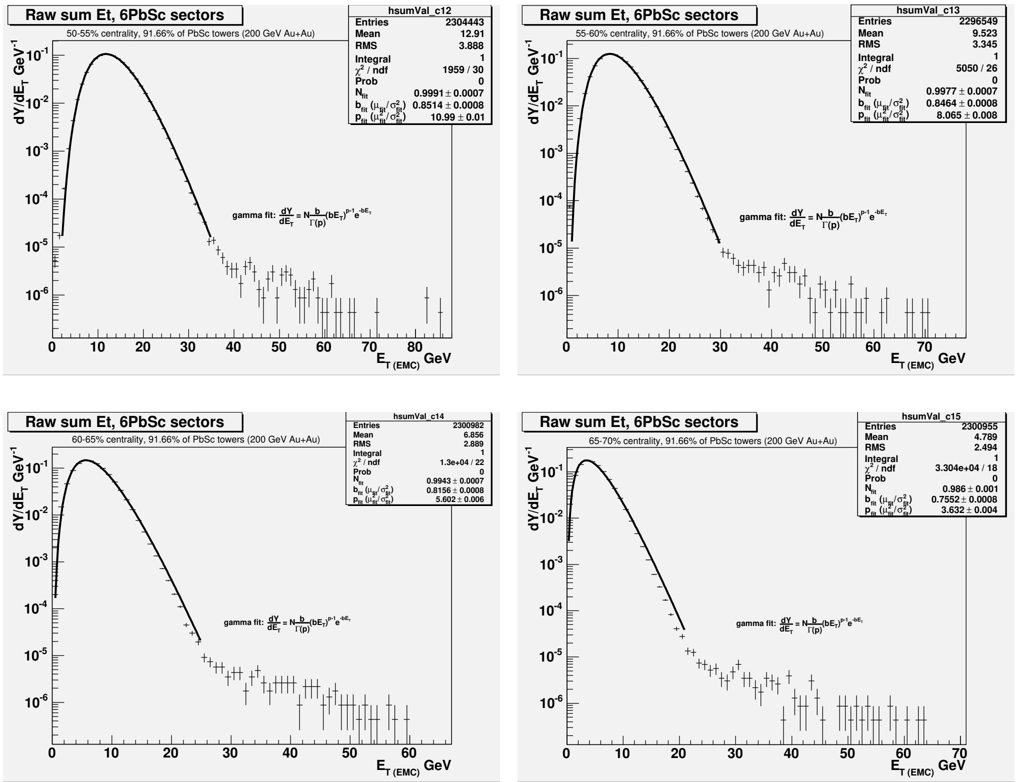

Figure 90: 200 GeV Au+Au 5% wide centrality $E_{T\ (\mathrm{EMC})}$ distributions fitted to gamma distribution. Measured in 5.5 equivalent sectors. Shown are 50-55%, 55-60%, 60-65%, and 65-70% centrality. Notice the background at high E_T in these peripheral distributions, this is the remaining pile up which the cut did not remove. Made in centrality-by-clock. Figure referenced in Chapter 5.

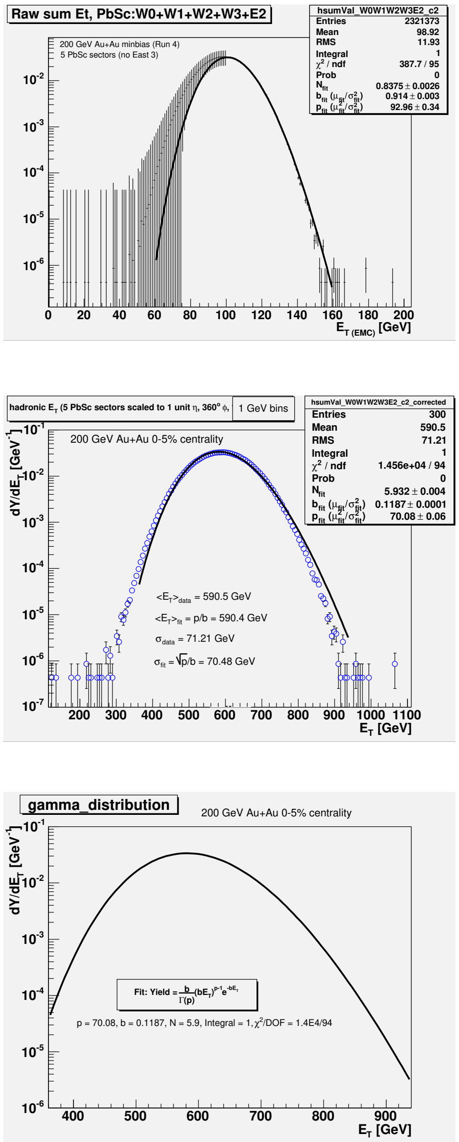

Figure 91: 200 GeV Au+Au event-by-event 0-5% centrality $E_{T\ (\mathrm{EMC})}$ measured in 4.5 equivalent PbSc sectors (top plot) and scaled to the reference acceptance for E_T (middle plot), made in centrality-by-clock. Both are fitted to a gamma distribution. As the middle plot illustrates the fit is not good; this might be due to the imperfect centrality definition distorting the low energy side of the distribution, thus, in the top plot the errors on the low energy bins were enlarged. This distribution made in 4.5 equavalent sectors is included here as it can be used in a future analysis of convolutions of the $p+p$ measurement, which was made in the same acceptance (see Figures 78 and 80). The bottom plot is the gamma fit to E_T by itself. Figure referenced in Chapter 5.

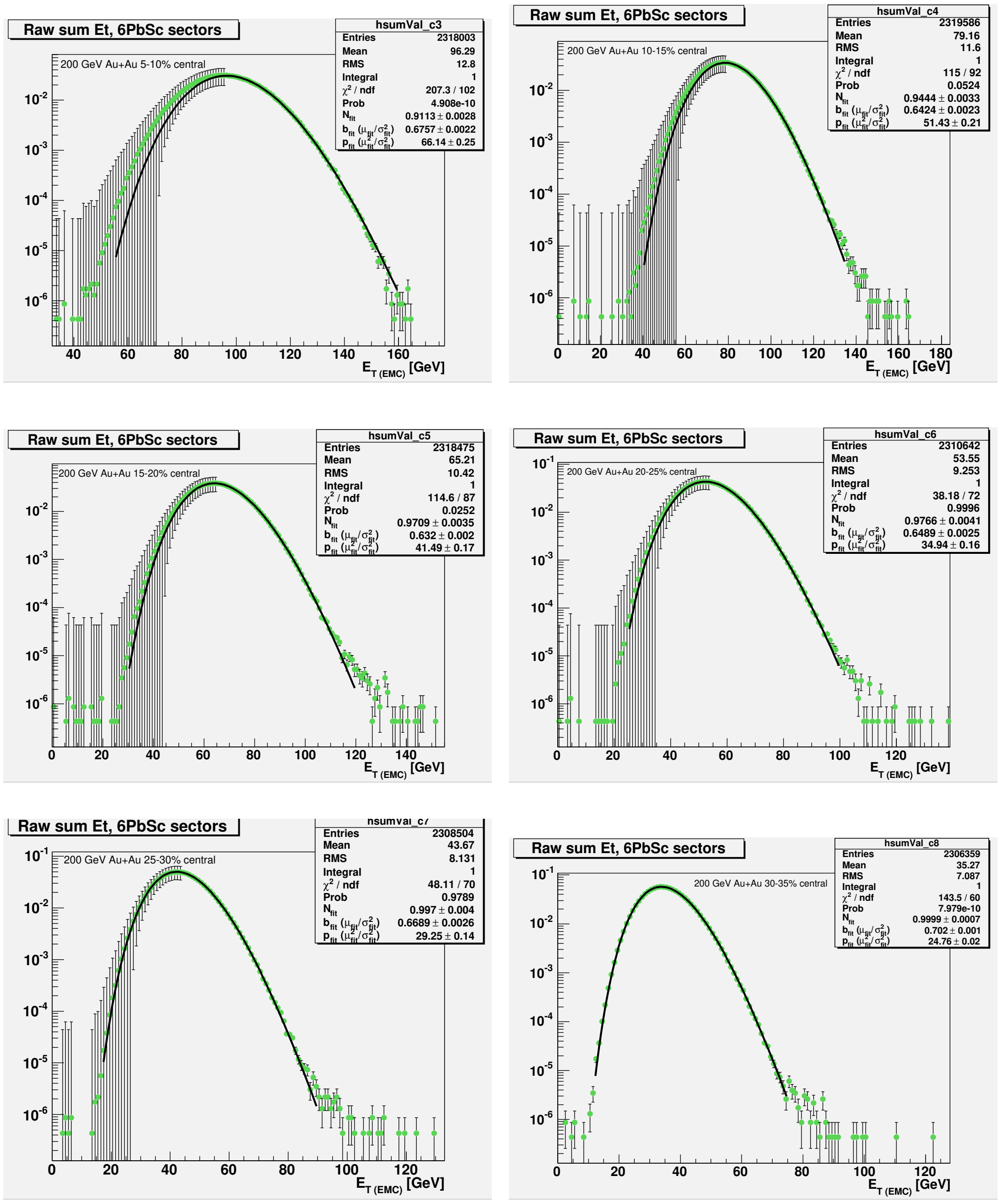

Figure 92: 200 GeV Au+Au 5% wide centrality $E_{T\ (\mathrm{EMC})}$ distributions fitted to gamma distribution; measured in 5.5 equivalent sectors. The errors were increased in the low E_T bins as necessary to get a lower χ^2/dof, and fit to the upper tail (as the imperfect centrality definition may corrupt the low $E_{T\ (\mathrm{EMC})}$ part of the semi-inclusive distribution as explained in the text). Made in centrality-by-clock. Figure referenced in Chapter 5.

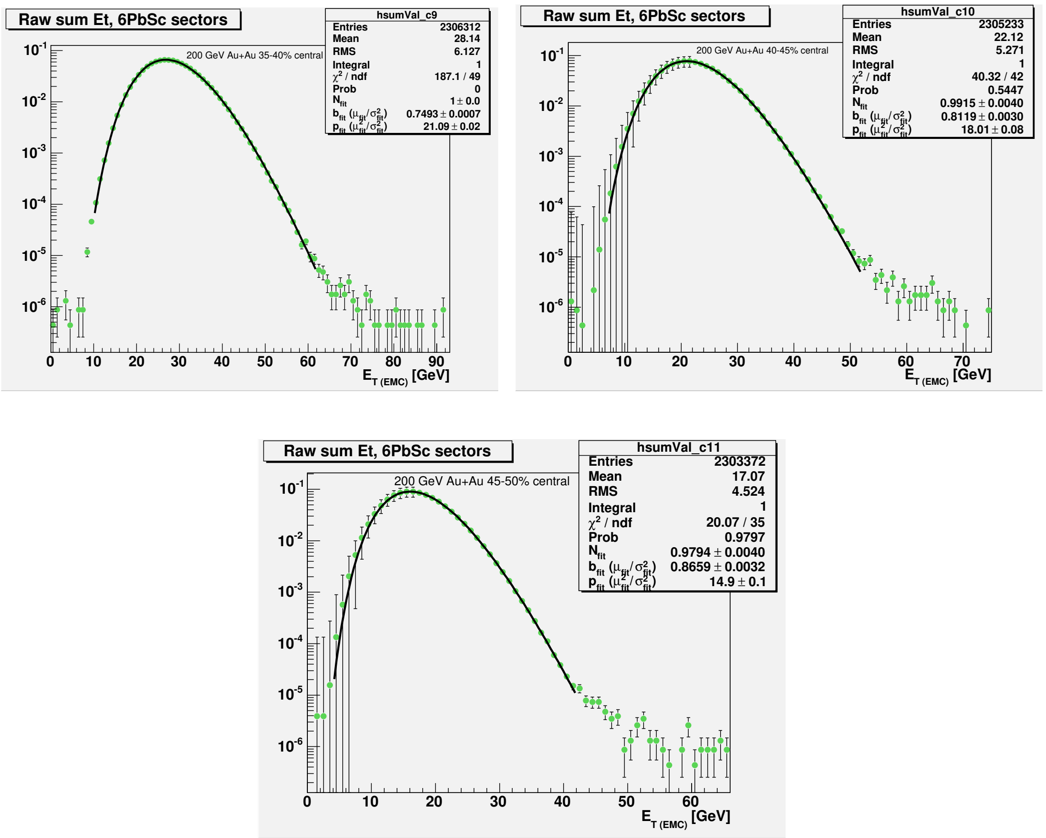

Figure 93: 200 GeV Au+Au 5% wide centrality peripheral $E_{T\ (\mathrm{EMC})}$ distributions fitted to a gamma distribution; measured in 5.5 equivalent sectors. The errors were increased in the low $E_{T\ (\mathrm{EMC})}$ bins as necessary to get a lower χ^2/dof, and fit to the upper tail; as the imperfect centrality definition may corrupt the low E_T part of the semi-inclusive distribution as explained in the text. Made in centrality-by-clock. Figure referenced in Chapter 5.

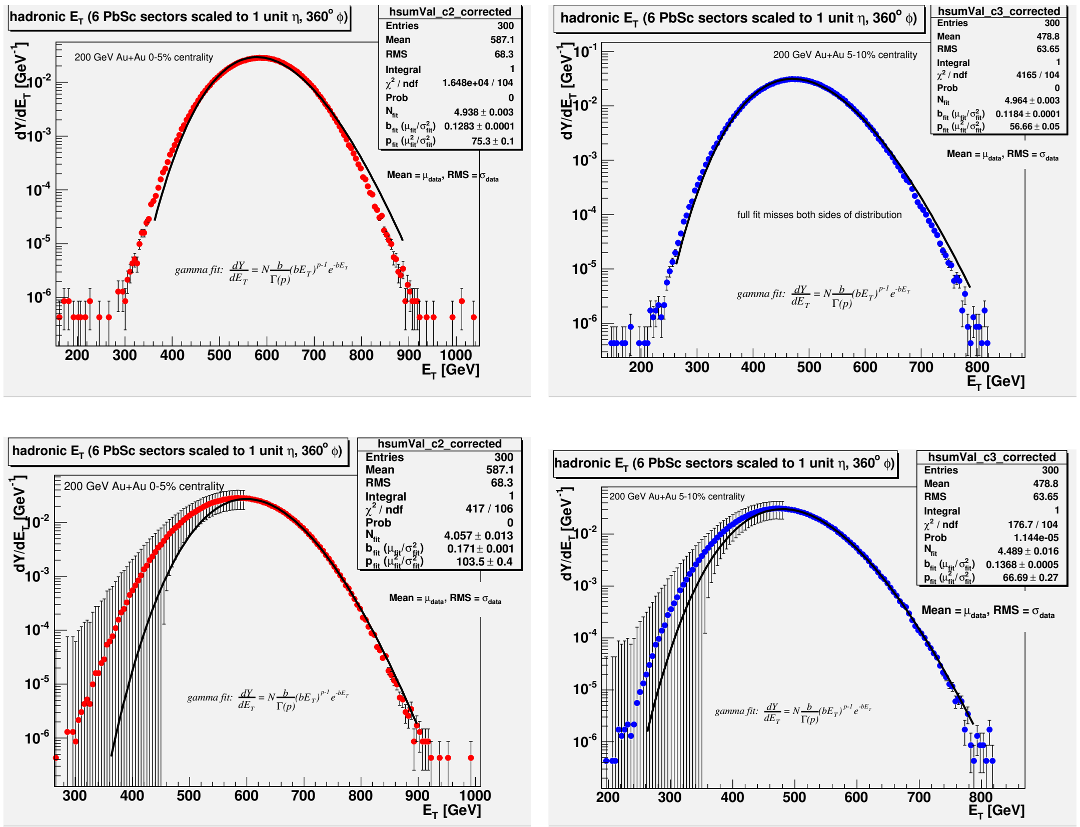

Figure 94: 200 GeV Au+Au E_T distributions for (left plots) 0-5% centrality, and (right plots) 5-10% centrality fitted to gamma distributions. The top plots show the fits fail. The bottom plots have the errors enlarged on the low E_T bins to get a lower χ^2/dof, and fit to the upper tail (as the imperfect centrality definition may corrupt the low E_T part of the semi-inclusive distribution as explained in the text). Made in centrality-by-clock. Measured in 5.5 equivalent sectors and scaled to the reference acceptance. Figure referenced in Chapter 5.

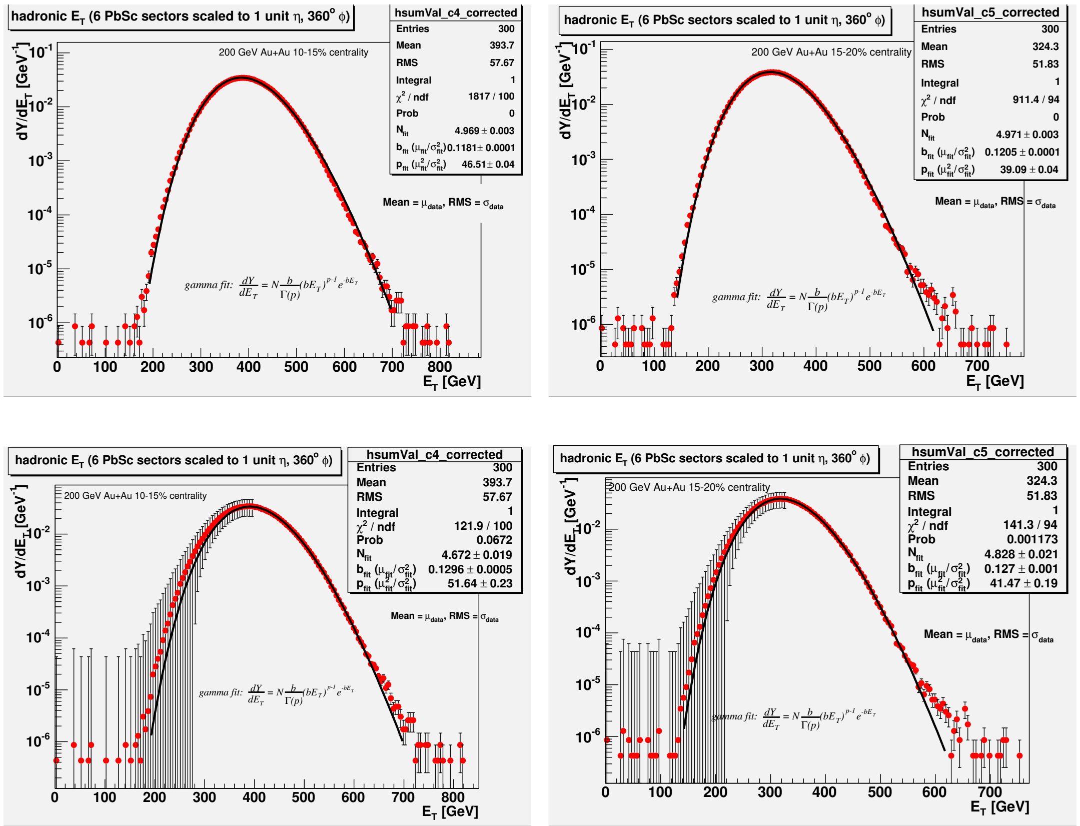

Figure 95: 200 GeV Au+Au E_T distributions for (left plots) 10-15% centrality, and (right plots) 15-20% centrality fitted to gamma distributions. The top plots show the fits appear by eye to be reasonable on both sides in these high statistics distributions, but the χ^2/dof are large. The bottom plots have the low E_T bin errors enlarged to get a lower χ^2/dof, and fit the upper tail (as the imperfect centrality definition may corrupt the low E_T part of the semi-inclusive distribution as explained in the text). Made in centrality-by-clock. Measured in 5.5 equivalent sectors and scaled to the reference acceptance. Figure referenced in Chapter 5.

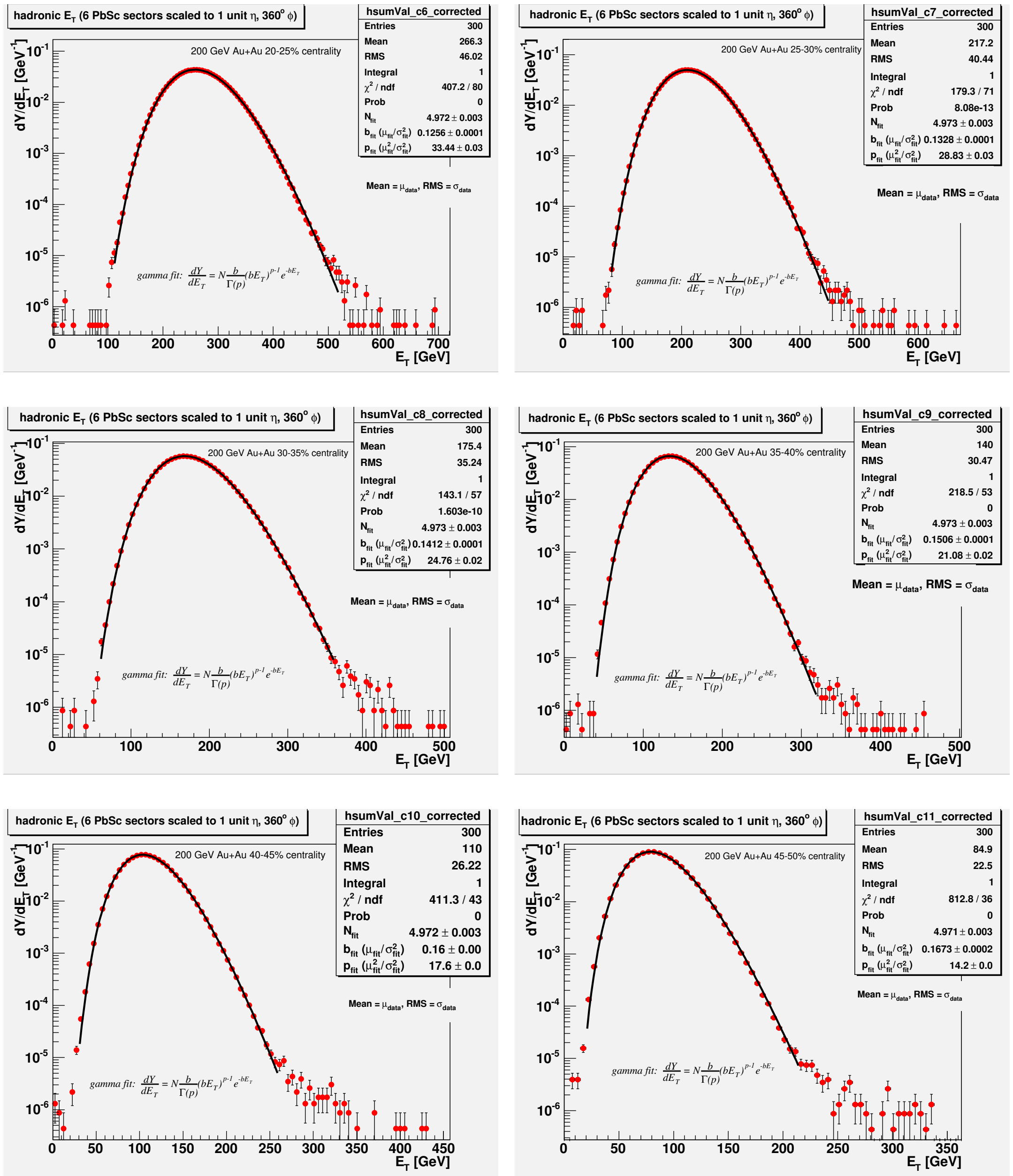

Figure 96: 200 GeV Au+Au 5% wide centrality E_T distributions, fitted to gamma distribution. The fits work a bit better for these mid-central distributions made in centrality-by-clock. Measured in 5.5 equivalent sectors and scaled to the reference acceptance. Figure referenced in Chapter 5.

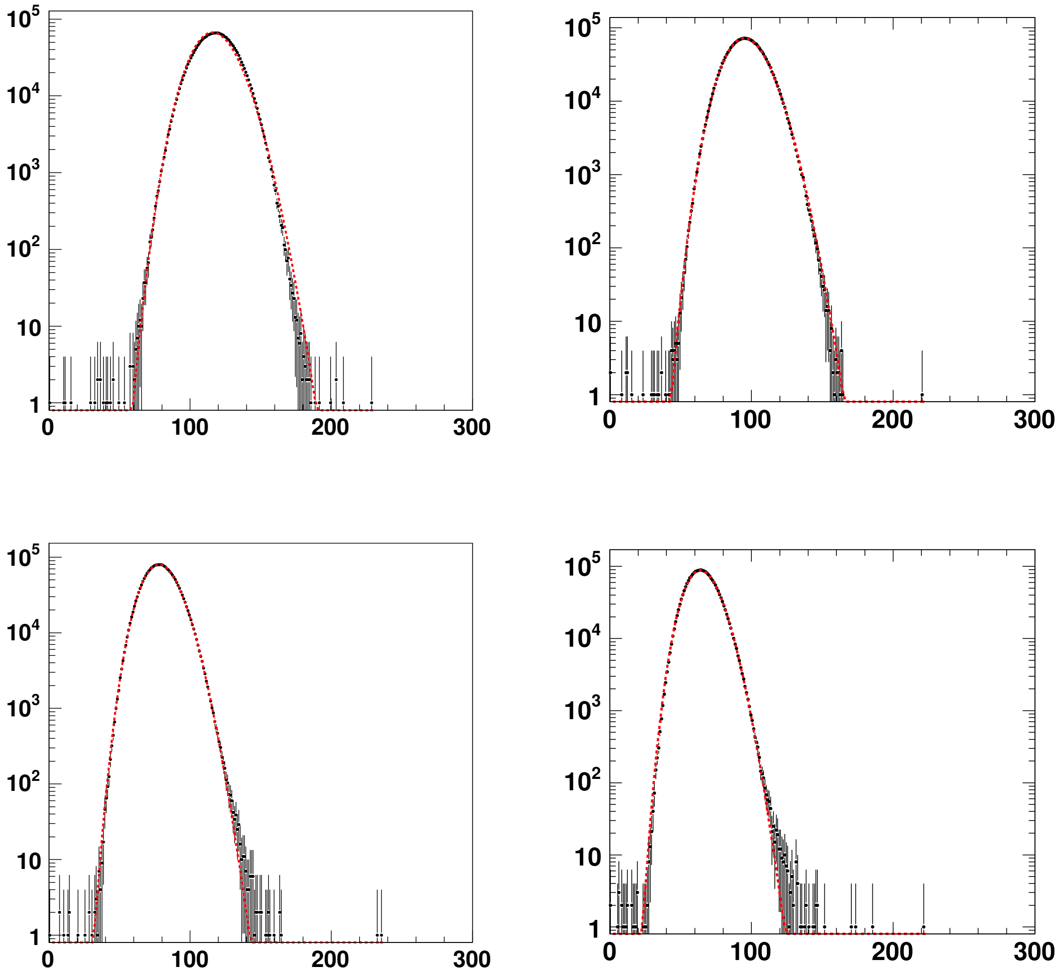

Figure 97: 200 GeV Au+Au $E_{T\ (\mathrm{EMC})}$ distributions fitted to negative binomial distribution where the fit parameters were obtained by manually minimizing (the horizontal scale is GeV). Top left 0-5%, top right 5-10%, bottom left 10-15%, bottom right 15-20% centrality. 5.5 equivalent sectors measured in centrality-by-clock. Figure referenced in Chapter 5. The fit results are in Table 5 (courtesy J. Mitchell (BNL)).

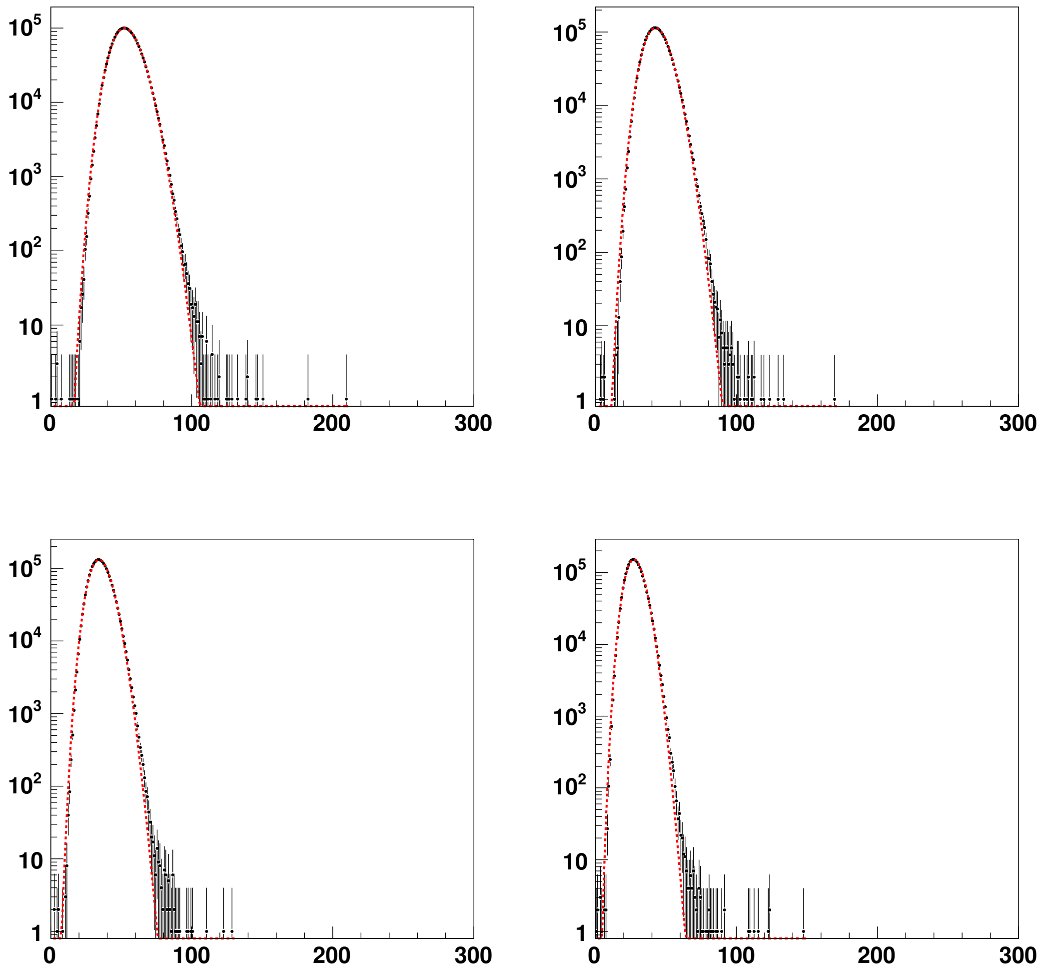

Figure 98: 200 GeV Au+Au $E_{T\ (\mathrm{EMC})}$ distributions fitted to negative binomial distribution where the fit parameters were obtained by manually minimizing (the horizontal scale is GeV). The top left 20-25%, top right 25-30%, bottom left 30-35%, bottom right 35-40% centrality. 5.5 equivalent sectors measured in centrality-by-clock. Figure referenced in Chapter 5. The fit results are in Table 5. (courtesy J. Mitchell (BNL))

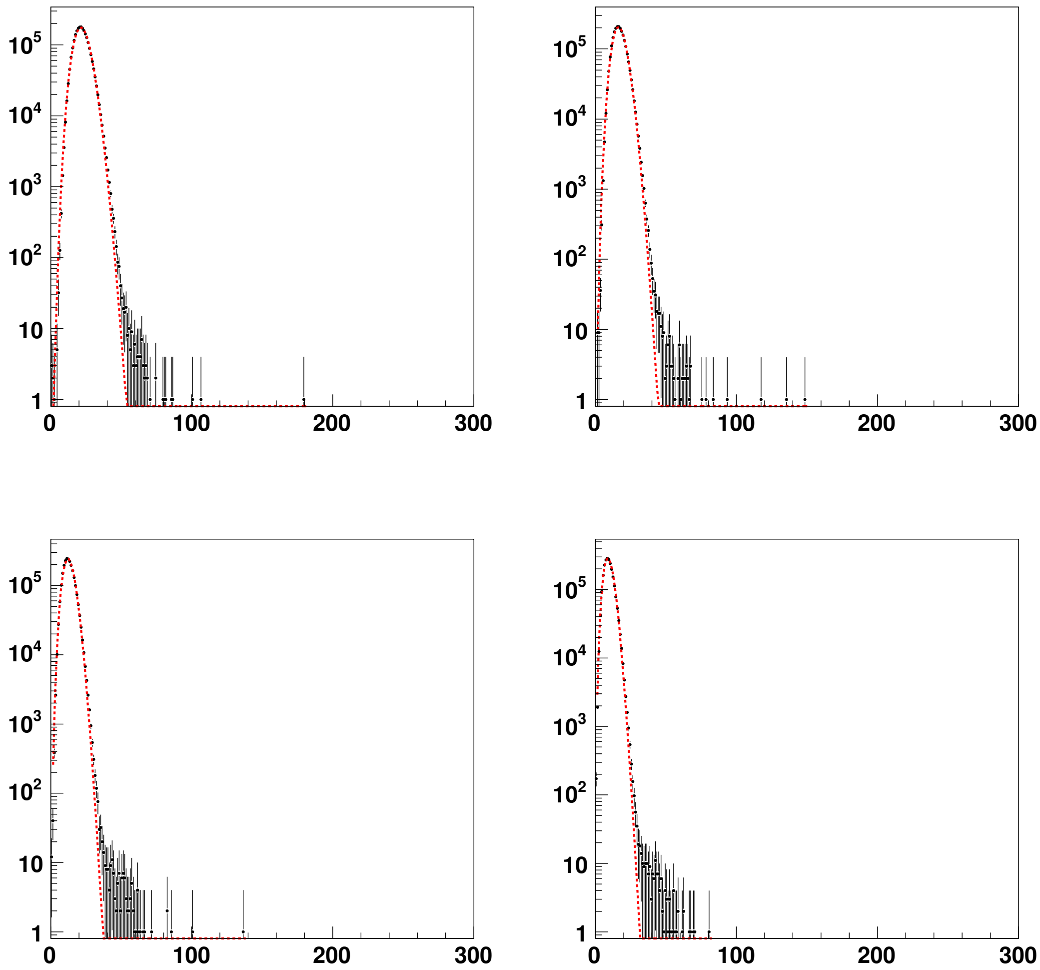

Figure 99: 200 GeV Au+Au $E_{T\ (\mathrm{EMC})}$ distributions fitted to negative binomial distribution where the fit parameters were obtained by manually minimizing (the horizontal scale is GeV). The top left 40-45%, top right 45-50%, bottom left 50-55%, bottom right 55-60% centrality. 5.5 equivalent sectors measured in centrality-by-clock. Figure referenced in Chapter 5. The fit results are in Table 5 (courtesy J. Mitchell (BNL))

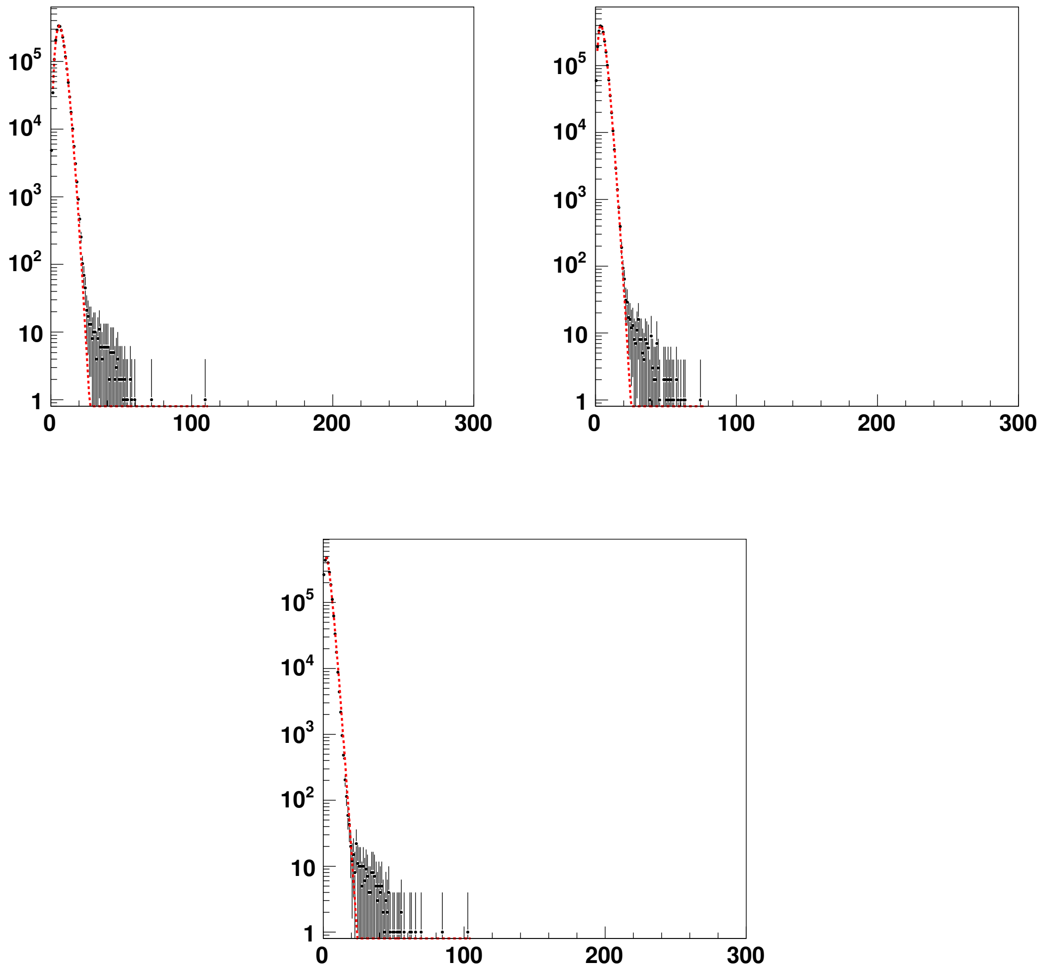

Figure 100: 200 GeV Au+Au peripheral $E_{T\ (\mathrm{EMC})}$ distributions fitted to negative binomial distribution where the fit parameters were obtained by manually minimizing (the horizontal scale is GeV). The top left 60-65%, top right 65-70%, bottom 70-75% centrality. 5.5 equivalent sectors measured in centrality-by-clock. Figure referenced in Chapter 5. The fit results are in Table 5 (courtesy J. Mitchell (BNL)).

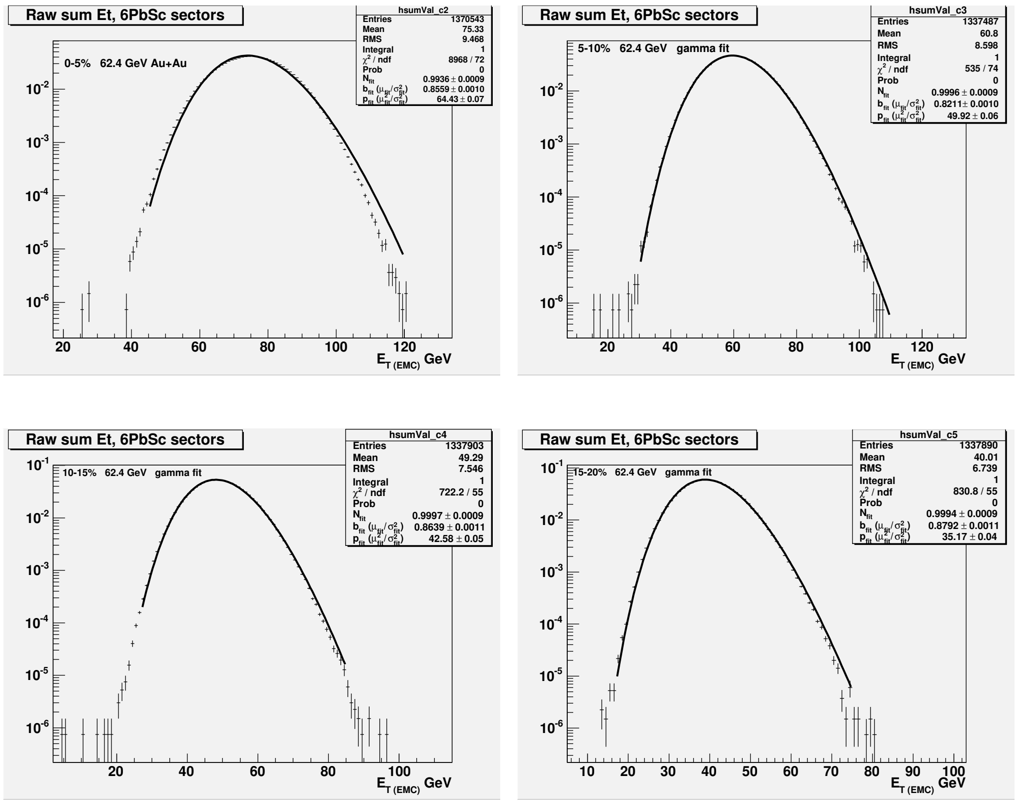

Figure 101: 62.4 GeV Au+Au 5% wide centrality $E_{T\ (\mathrm{EMC})}$ distributions fitted to gamma distribution. Measured in 5.5 equivalent sectors. Shown are 0-5%, 5-10%, 10-15%, and 15-20% centrality. Made in centrality-by-BBC. Figure referenced in Chapter 5.

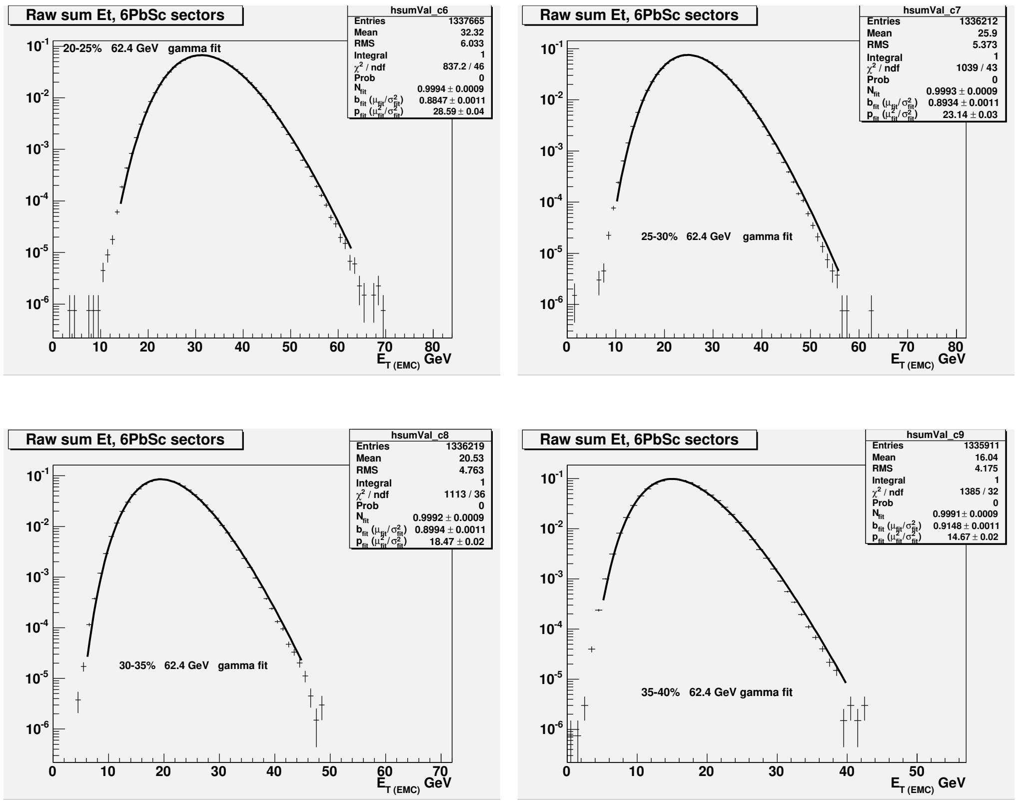

Figure 102: 62.4 GeV Au+Au 5% wide centrality $E_{T\ (\mathrm{EMC})}$ distributions fitted to gamma distribution. Measured in 5.5 equivalent sectors. Shown are 20-25%, 25-30%, 30-35%, and 35-40% centrality. Made in centrality-by-BBC. Figure referenced in Chapter 5.

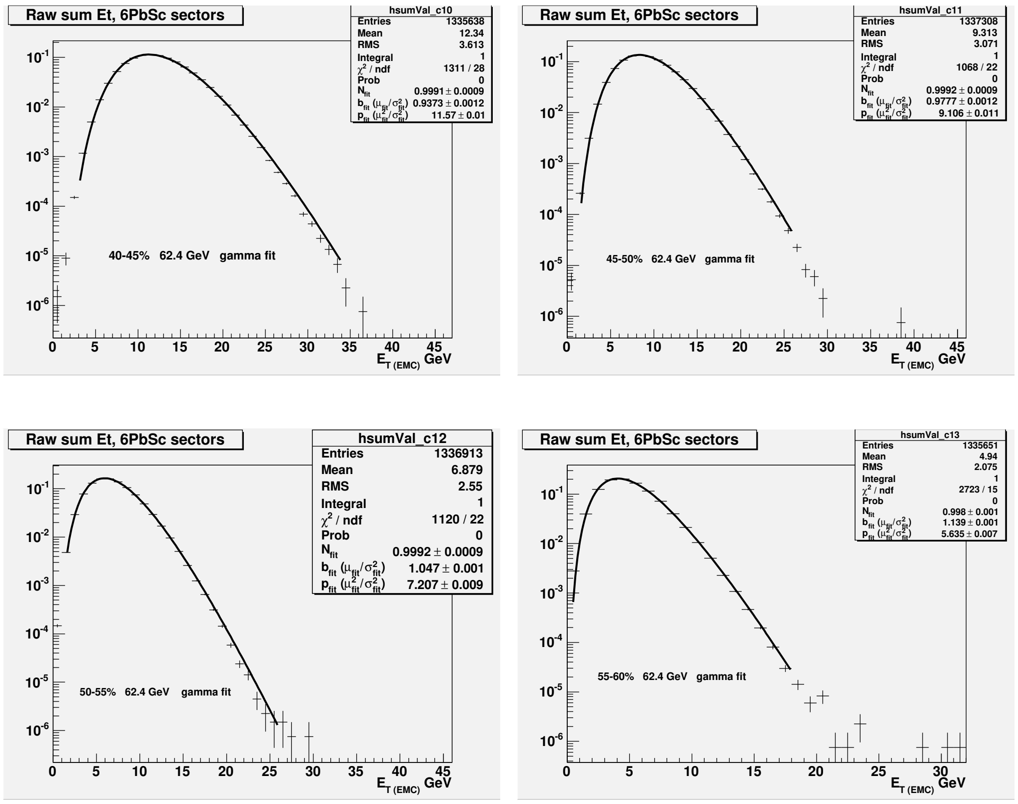

Figure 103: 62.4 GeV Au+Au 5% wide centrality $E_{T\ (\mathrm{EMC})}$ distributions fitted to gamma distribution. Measured in 5.5 equivalent sectors. Shown are 40-45%, 45-50%, 50-55%, and 55-60% centrality. Made in centrality-by-BBC. Figure referenced in Chapter 5.

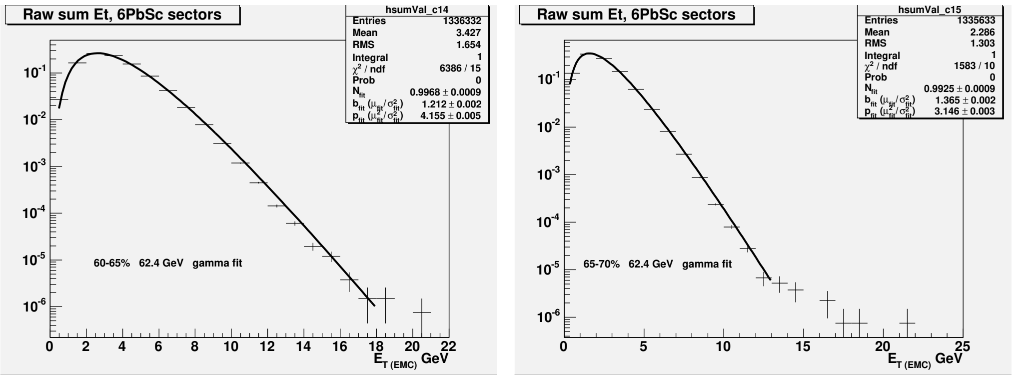

Figure 104: 62.4 GeV Au+Au 5% wide centrality $E_{T\ (\mathrm{EMC})}$ distributions fitted to gamma distribution. Measured in 5.5 equivalent sectors. Shown are 60-65% and 65-70% centrality. Made in centrality-by-BBC. Figure referenced in Chapter 5.

B.5.2 Figures of $\langle E_T \rangle$ in centrality

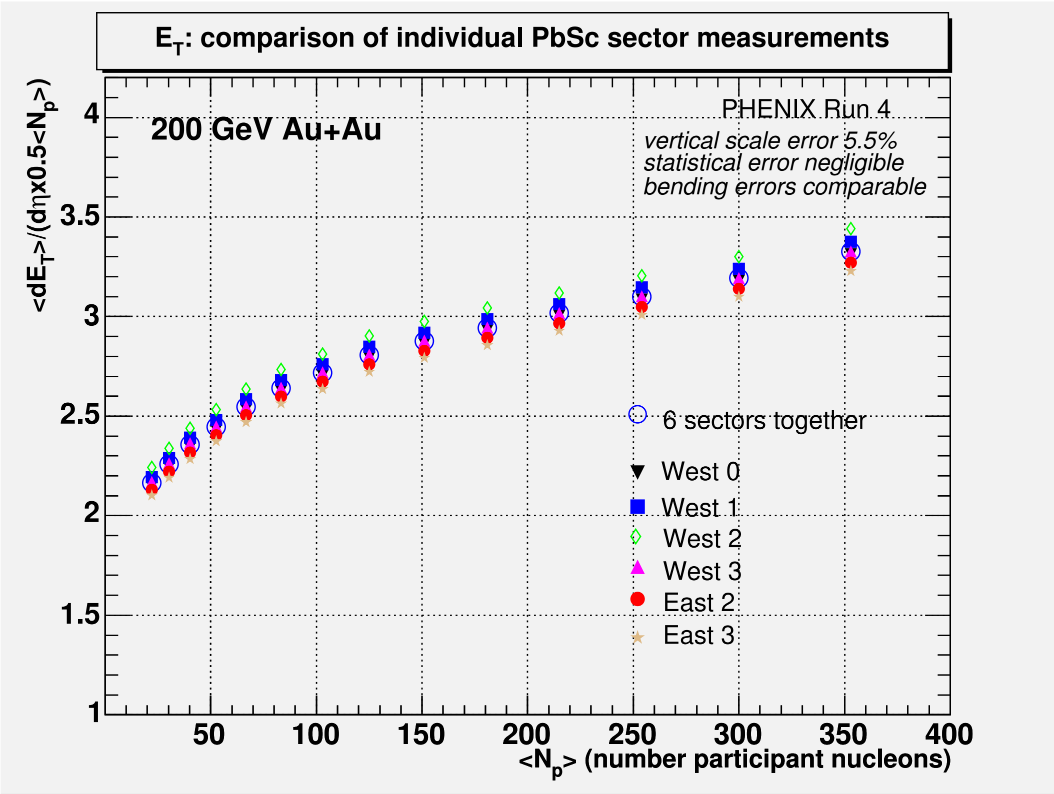

Figure 105: 200 GeV Au+Au $\langle E_T \rangle / \langle N_{\mathrm{nuc-part}} \rangle$ measured in the individual PbSc EMC sectors and in the 6-sector combination. The $\sim \pm 4 - 5\%$ energy difference across the sectors is due in part to different observed multiplicities in the different sectors (3.6%), which may be related to sector location on the PHENIX Arm, and in part to the different responses at the sector edges (1.5%). Figure referenced in Chapter 5.

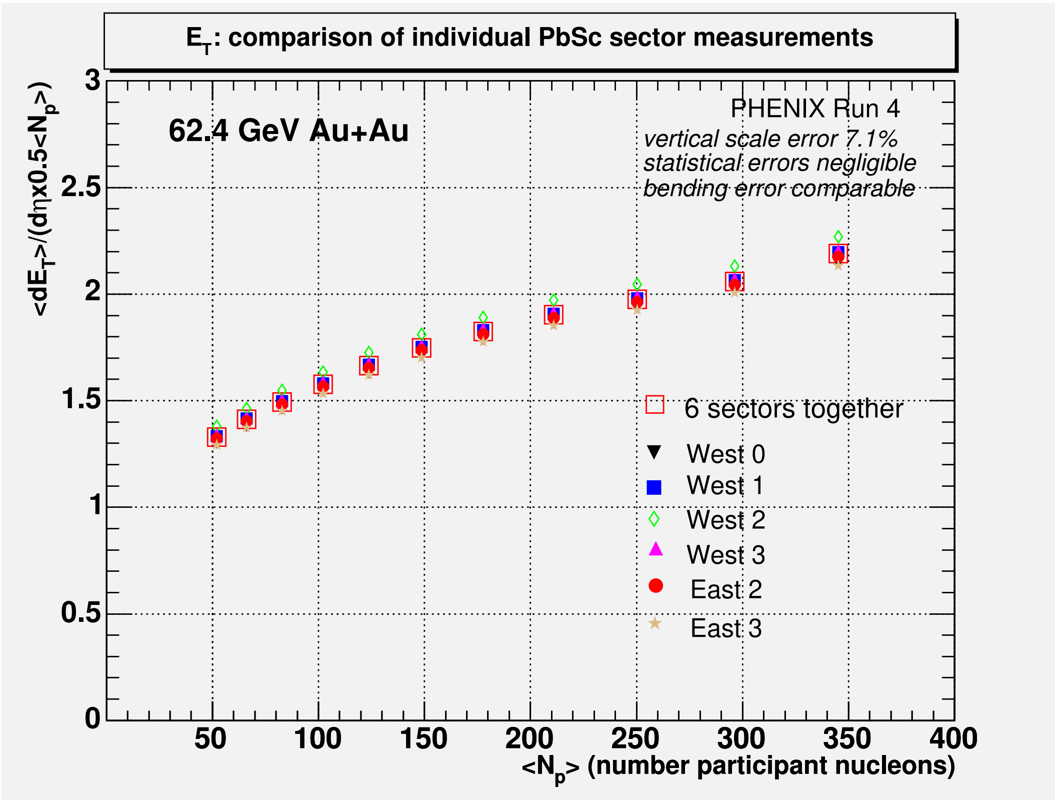

Figure 106: 62.4 GeV Au+Au $\langle E_T \rangle / \langle N_{\mathrm{nuc-part}} \rangle$ measured in the individual PbSc EMC sectors and in the 6-sector combination. The $\sim \pm 4 - 5\%$ energy difference across the sectors is due in part to different observed multiplicities in the different sectors (3.6%), which may be related to sector location on the PHENIX Arm, and in part to the different responses at the sector edges (1.5%). Figure referenced in Chapter 5.

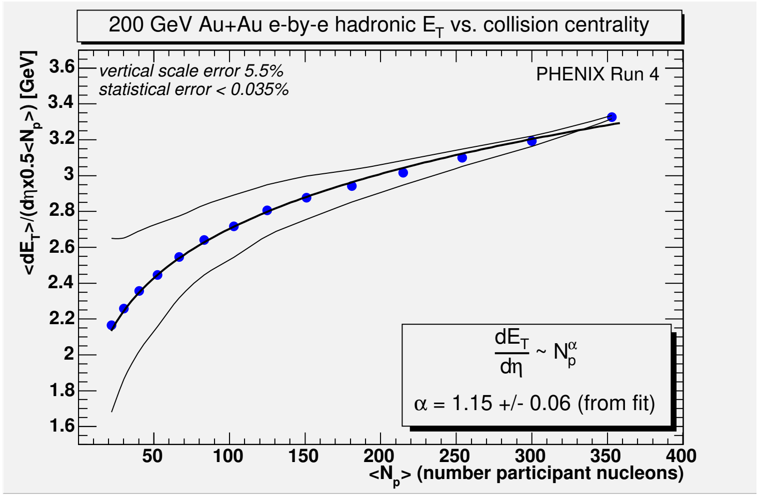

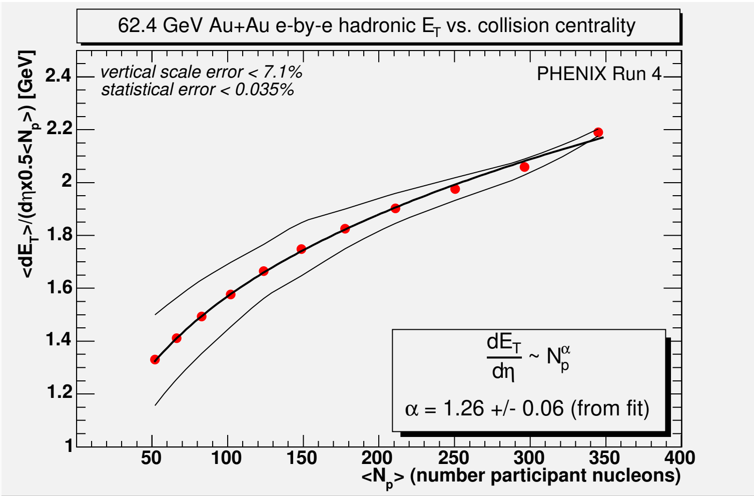

Figure 107: (top plot) 62.4 and (bottom plot) 200 GeV Au+Au $\langle E_T \rangle / \langle N_{\mathrm{nuc-part}} \rangle$ plotted versus centrality. The E_T normalized in the participant nucleon model is not flat over centrality suggesting the model does not describe E_T production. Note that the most central point turns upward and away from the fit line; this is possibly an artifact of the centrality definition due to the fact that the most central class of events does not have a cut on the high E_T side of that distribution. Figure referenced in Chapter 5.

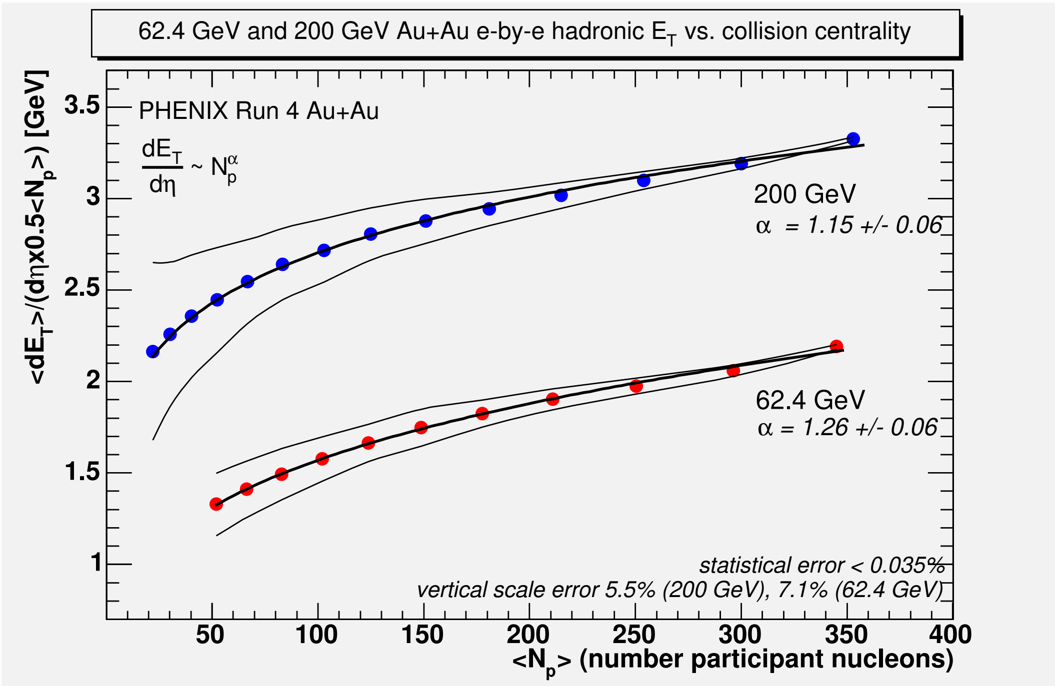

Figure 108: Comparison of 62.4 GeV and 200 GeV Au+Au $\langle E_T\rangle/\langle N_{\mathrm{nuc-part}}\rangle$ in centrality. E_T is proportional to the energy density of the collision zone; expected QGP producing energy densities of some 1-3 GeV/fm^3 are achieved in both the 62.4 and 200 GeV interactions, and at 200 GeV these densities occur at about 20 participant nucleons and 150 participant nucleons respectively. Figure referenced in Chapter 5.

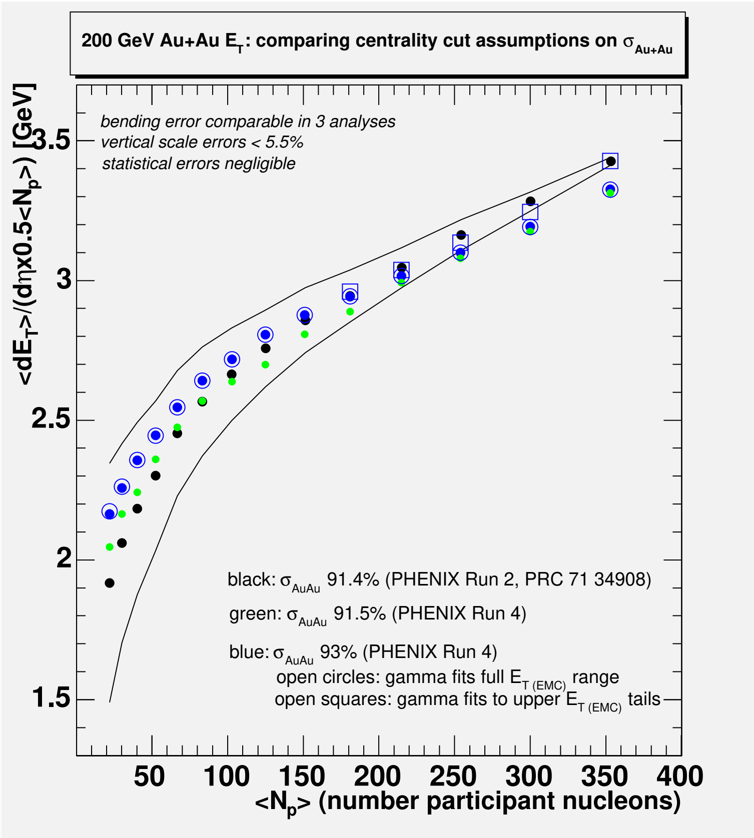

Figure 109: 200 GeV Au+Au $\langle E_T \rangle / \langle N_{\text{nuc-part}} \rangle$ measurements compared. The black points are RHIC Run 2 previous published results which assumed a cross section of $\sigma_{\text{Au+Au}} = 91.4\%$. The green, blue, and open points are RHIC Run 4 measured in this thesis analysis and using different estimates for $\sigma_{\text{Au+Au}}$: the solid points are from data, open points from gamma fits; open blue circles are from fits to the full $E_{T\ (\text{EMC})}$ distributions, open squares from fitting with enlarged errors on the low $E_{T\ (\text{EMC})}$ sides of the distributions (equivalent to fitting only the upper tail regions). The choice of $\sigma_{\text{Au+Au}}$ used to bin the data affects the bending slope in the peripheral region. Regarding the $\sim 4\%$ discrepancy in the position of the most central point it's likely that half of this is due to background which was removed, but the reason for the other half of the discrepancy remains unclear, possibly related to included towers. Figure referenced in Chapter 5.

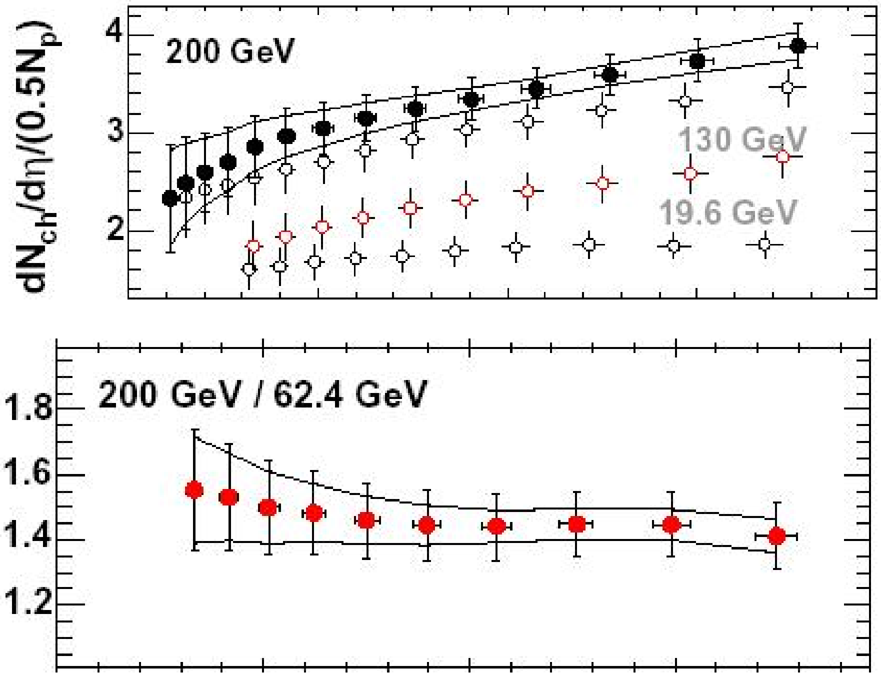

Figure 110: PHENIX previous results (2004): 62.4 GeV Au+Au $\langle N_{\mathrm{ch\ tracks}}\rangle/\langle N_{\mathrm{nuc-part}}\rangle$ versus centrality, compared to other collision energies. For both plots the horizontal axis is $N_{\mathrm{nuc-part}}$ ranging over 0 to 400. The top plot shows $\langle N_{\mathrm{ch\ tracks}}\rangle/\langle N_{\mathrm{nuc-part}}\rangle$ versus centrality, and the hallow red colored points (the middle points) are the 62.4 GeV measurements. The bottom plot shows the ratio $\langle N_{\mathrm{ch\ tracks\ 200GeV}}\rangle/\langle N_{\mathrm{ch\ tracks\ 62.4GeV}}\rangle$ – note the trend of the points curves downward illustrating that the power α in $N_{\mathrm{ch\ tracks}} \sim N^{\alpha}_{\mathrm{nuc-part}}$ is measured larger in the 62.4 GeV data than in the 200 GeV data. Figure referenced in Chapter 5. (courtesy A. Milov from PHENIX AN304 [31]).

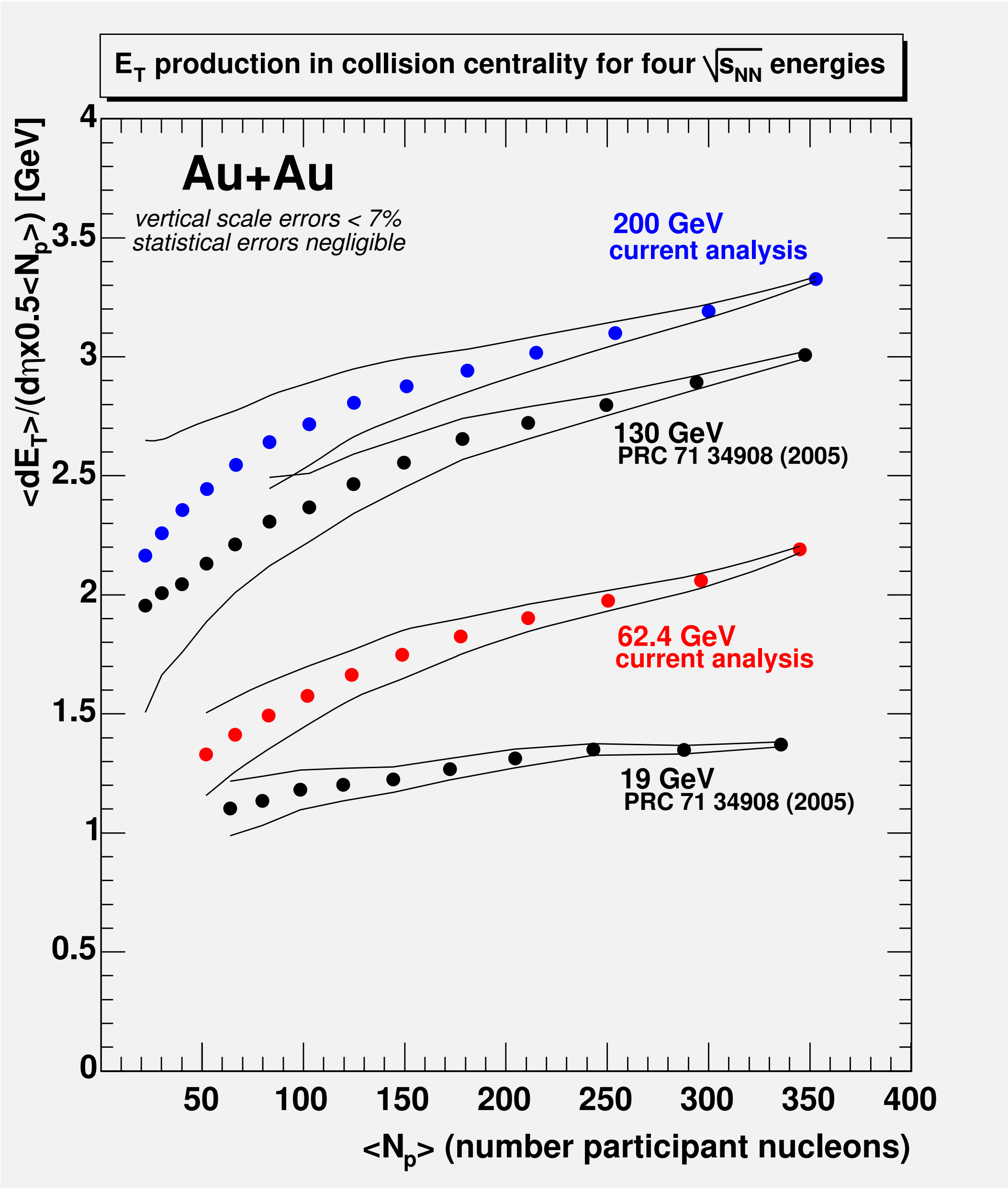

Figure 111: 19.6, 62.4, 130, and 200 GeV Au+Au $\langle E_T \rangle / \langle N_{\text{nuc-part}} \rangle$ plotted versus centrality. Only the 19.6 GeV is close to flat within its systematic error bars suggesting that E_T production at 19.6 GeV may scale with participant nucleons, but not at higher energies. Figure referenced in Chapter 5 (19.6 GeV, and 130 GeV (black points) courtesy A. Milov (BNL) [4]).

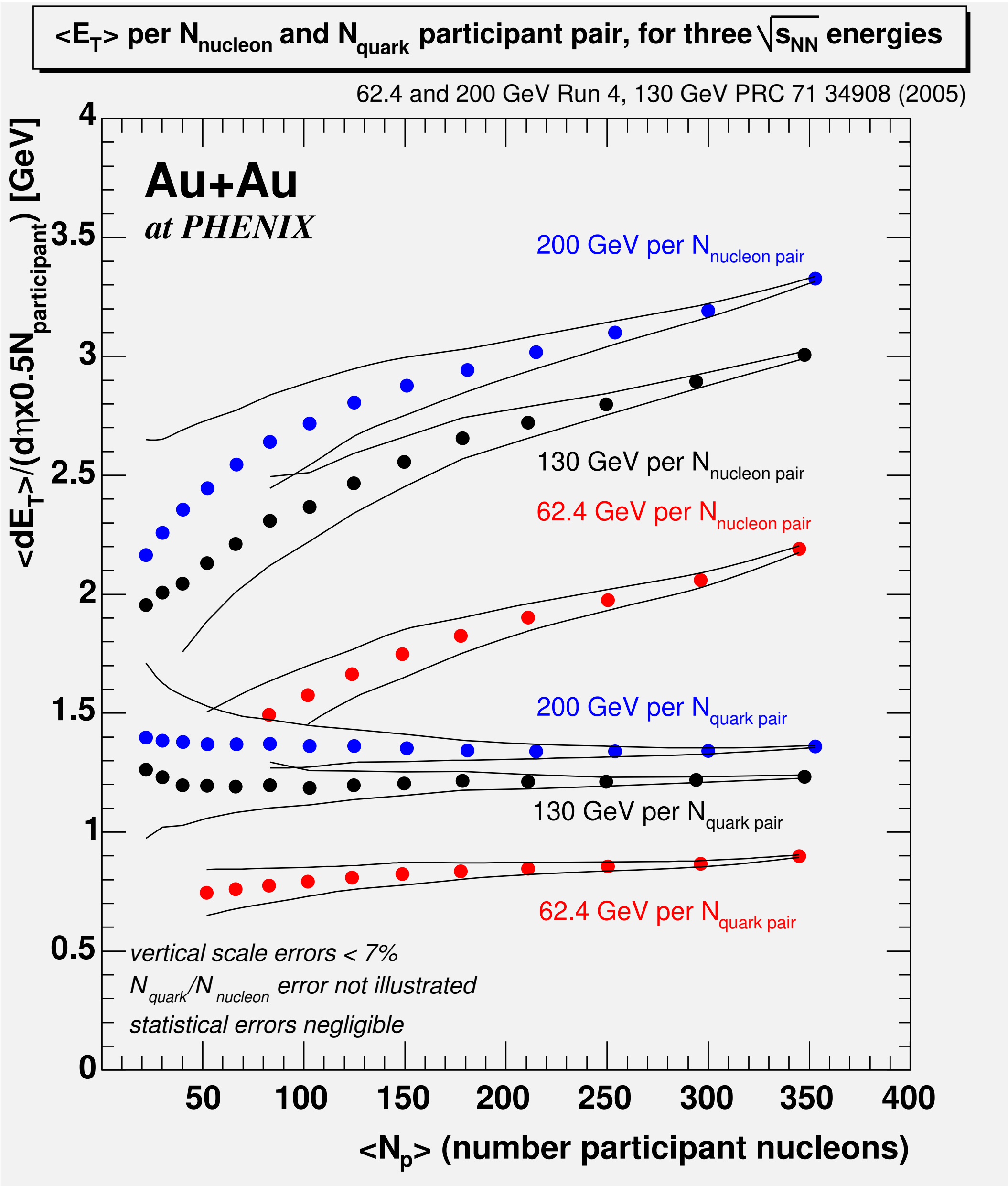

Figure 112: 62.4, 130, and 200 GeV Au+Au $\langle E_T\rangle/\langle N_{\mathrm{nuc-part}}\rangle$ and $\langle E_T\rangle/\langle N_{\mathrm{quark-part}}\rangle$ over centrality compared. $\langle E_T\rangle$ per quark participant is flat suggesting the quark participant normalization [21] explains the data. The 130 GeV measurements were taken from reference [4] and renormalized here in the quark framework. Figure referenced in Chapter 5 .

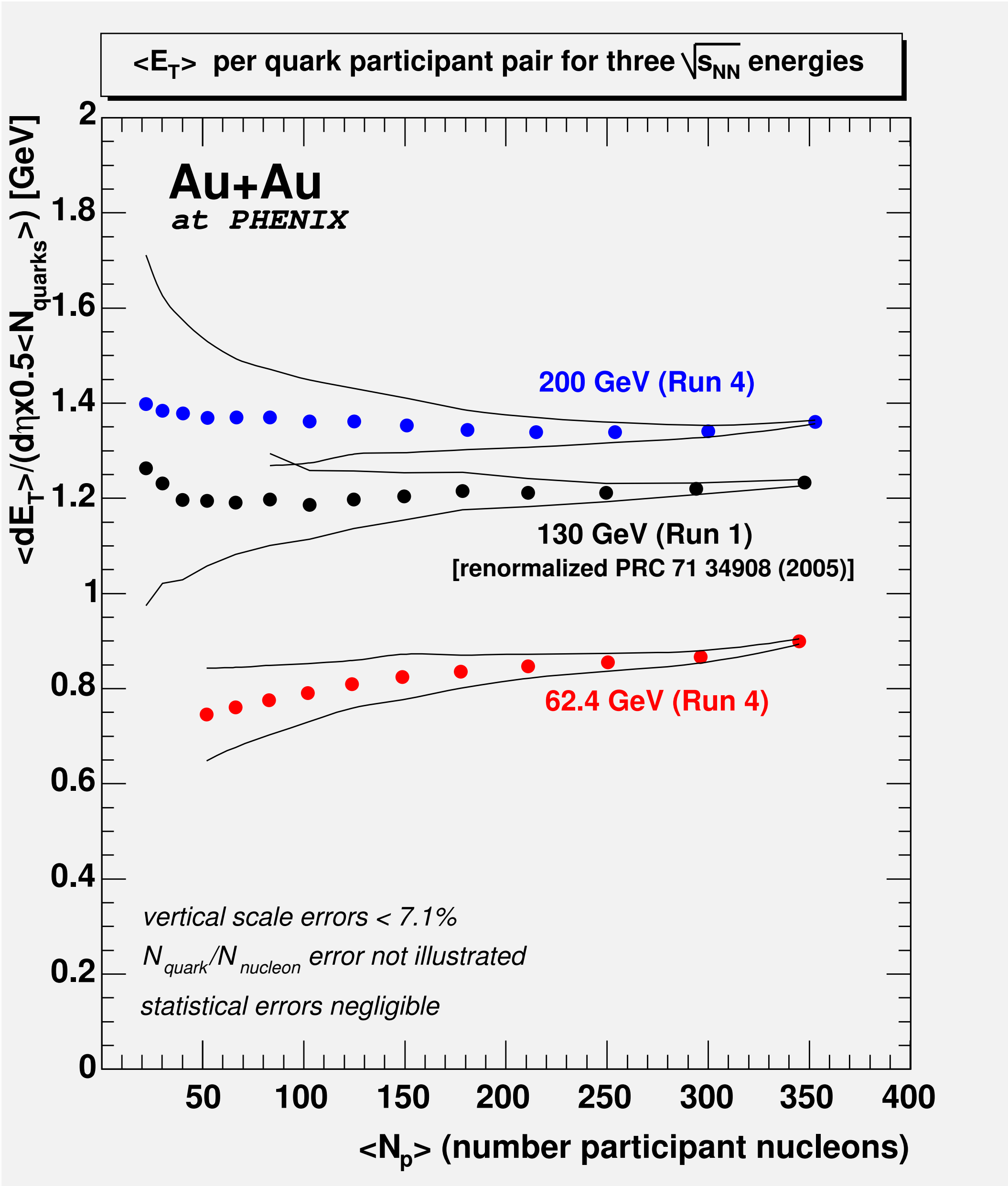

Figure 113: 62.4, 130, and 200 GeV Au+Au $\langle E_T \rangle / \langle N_{\mathrm{quark-part}} \rangle$ plotted versus centrality and viewed up close. The quark participant estimation utilized is that located in [21]. The 130 GeV measurements from reference [4], and renormalized in this thesis in the quark framework. Figure referenced in Chapter 5.

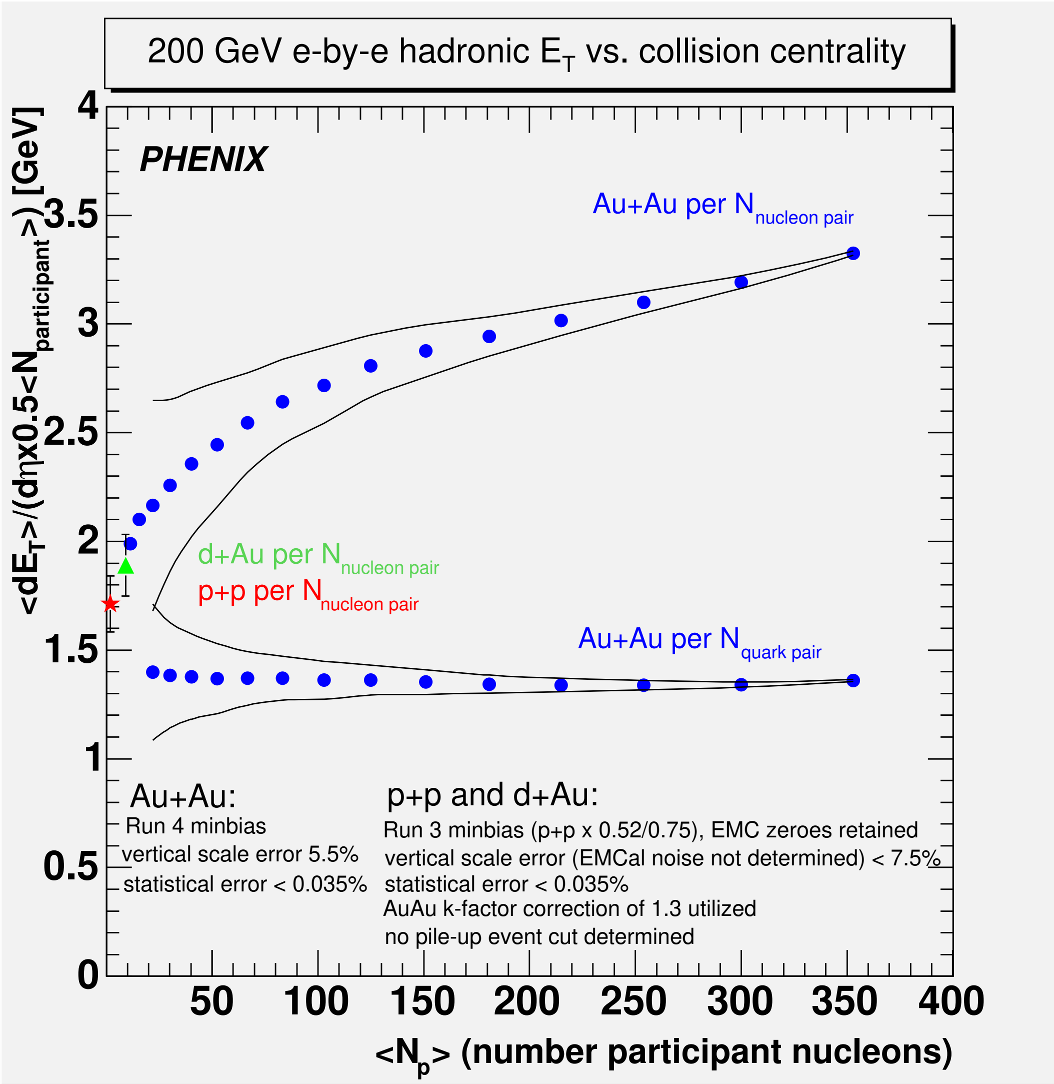

Figure 114: 200 GeV $p+p$ and d+Au $\langle E_T\rangle/\langle N_{\text{nuc}-\text{part}}\rangle$ measurements compared to 200 GeV Au+Au $\langle E_T\rangle/\langle N_{\text{nuc}-\text{part}}\rangle$ and $\langle E_T\rangle/\langle N_{\text{quark}-\text{part}}\rangle$. The quark participants used in the normalization are from [21]. Regarding the ordinates of the $p+p$ and d+Au points: corrections were used of 6.03 (p+p) and 6.07 (d+Au) (which corrects for faulty towers, geometric acceptance, a k-correction of 1.3 borrowed from Au+Au simulations); the minbias triggers of zero EMC energy were re-included via factors 0.813 ($p+p$) and 0.94 (d+Au); for $p+p$ an additional correction applied for interactions which did not trigger the BBC of $\frac{\sigma_{\text{BBC}}/\sigma_{p+p}}{\epsilon_{\text{EMC}}} = \frac{21.8 \text{ mb}/41 \text{ mb}}{0.75} = 0.52/0.75 = 0.69$. Thus for $p+p$: $\frac{dE_T}{d\eta} = 6.03 \times 0.813 \times 0.69 \times \langle E_{T\ (\text{EMC})}\rangle$, and for d+Au: $\frac{dE_T}{d\eta} = 6.07 \times 0.94 \times \langle E_{T\ (\text{EMC})}\rangle$. Error was not determined on $p+p$ and d+Au for PbSc sector electronic noise. Figure referenced in Chapter 5.

B.5.3 Figures of E_T fluctuations in centrality

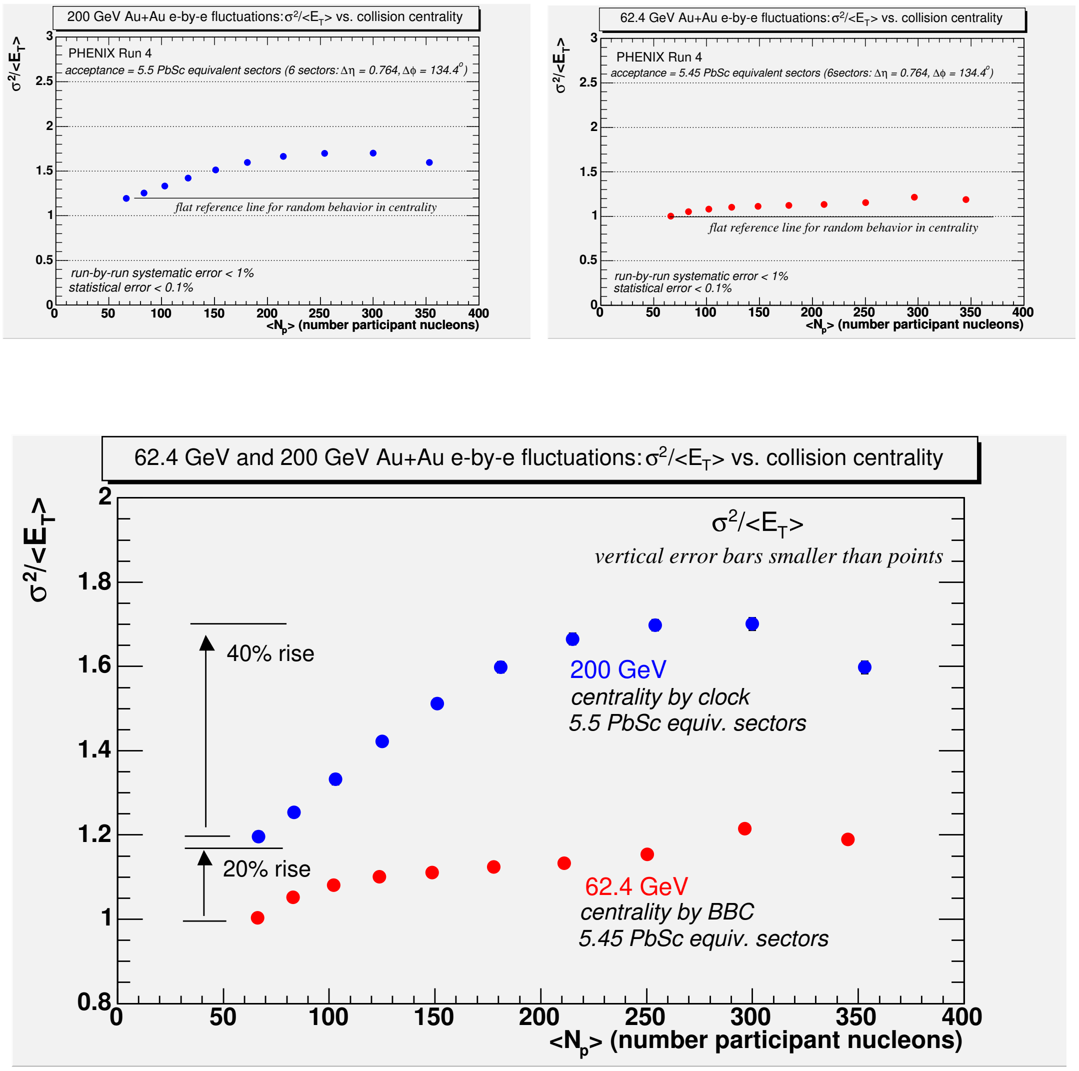

Figure 115: (Top left) 200 GeV and (top right) 62.4 GeV Au+Au scaled variance fluctuations $\sigma^2/\langle E_{T\ (\mathrm{EMC})}\rangle$. The 200 GeV was measured in the centrality-by-clock and shows a 40% rise in fluctuations which are larger than the 62.4 GeV 20% rise measured in the centrality-by-BBC. These shapes are compared in the bottom plot and were determined to be due to the centrality definitions. Figure referenced in Chapter 5.

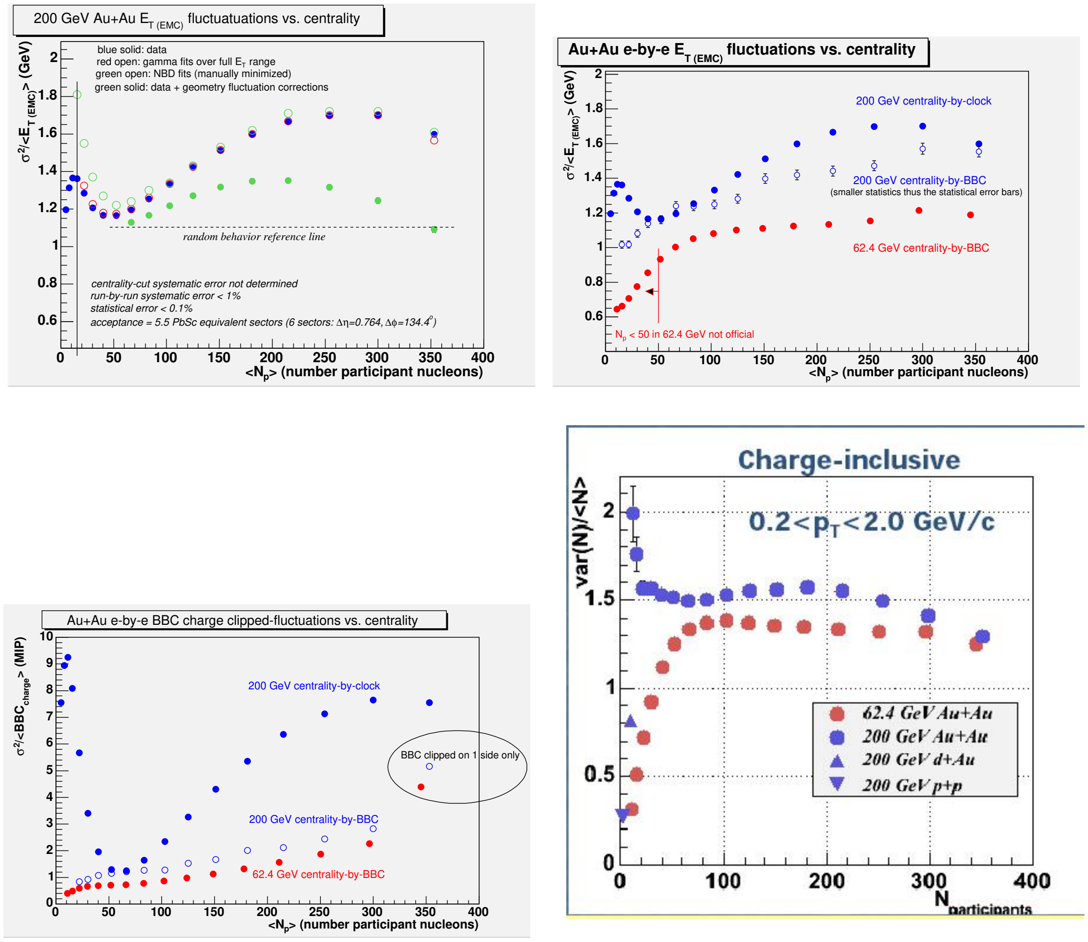

Figure 116: Au+Au scaled variance fluctuations σ^2/μ. The bottom left plot is 200 GeV and 62.4 GeV BBC charge σ^2/μ using different centrality cuts; these are not a measure of fluctuations as the tails of the distributions are purposefully cut. Obviously the choice of the centrality cut determines these "fluctuations." The top plots are E_T fluctuations – top left 200 GeV comparison of data, data + geometry fluctuation corrections, and results from fitting attempts; top right compares 62.4 and 200 GeV fluctuations for different centrality definitions, note choice of centrality cut determines trend of the points. The bottom right are multiplicity $\sigma^2/\langle N_{\rm ch\ tracks}\rangle$ for 200 GeV Au+Au (made in centrality-by-clock), and 62.4 GeV (with centrality-by-BBC), without geometry-fluctuation corrections. Note same general shape as in E_T. E_T and multiplicity fluctuations follow the BBC "fluctuations." Note (bottom left plot) in centrality-by-BBC the most-central σ^2/μ is large, due to the fact that the upper tail of that distribution is not cut. Figure referenced in Chapter 5. (multiplicity, NBD fits, geometry fluc. corrections courtesy J. Mitchell (BNL)).

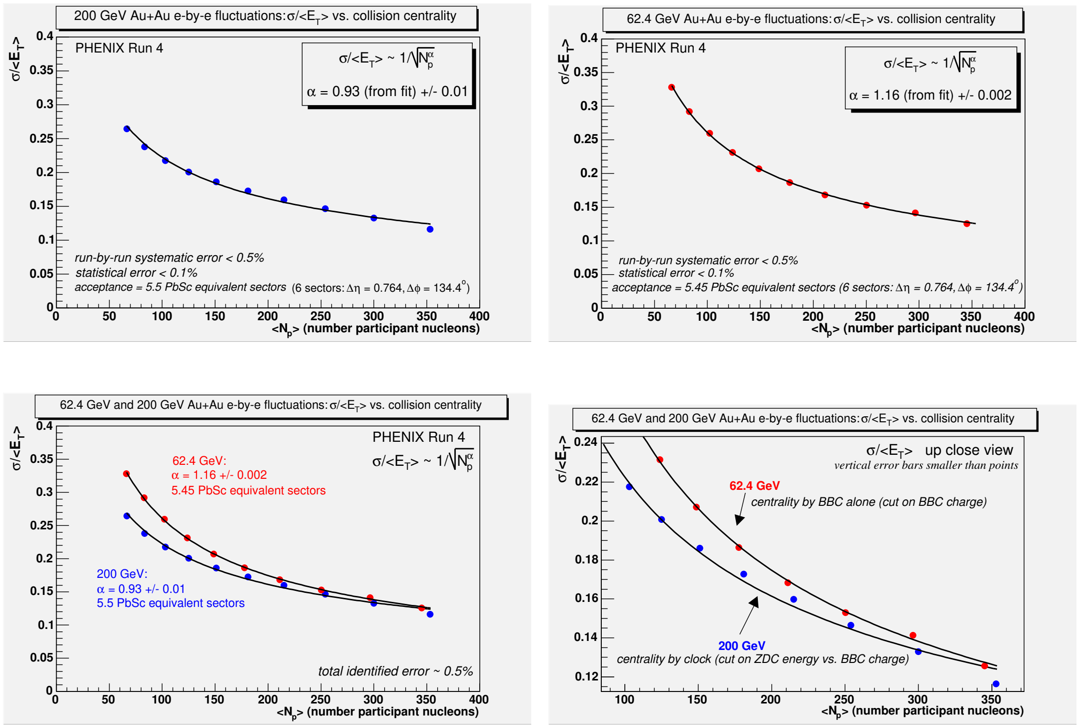

Figure 117: 200 and 62.4 GeV Au+Au $E_{T\ (\mathrm{EMC})}$ relative width measurements $\sigma/\langle E_{T\ (\mathrm{EMC})}\rangle$. The plots are fit to a power law function, and the top plots show that the distribution width σ has a comparable dependency on $N^{\alpha}_{\mathrm{nuc-part}}$ as does the distribution means. The bottom left plot shows the relative width in 62.4 GeV are larger than in 200 GeV. The bottom right plot is a close up view showing that the points for 200 GeV data which uses the centrality-by-clock definition do not fit to the power law as well as the 62.4 GeV which uses centrality-by-BBC. Figure referenced in Chapter 5.

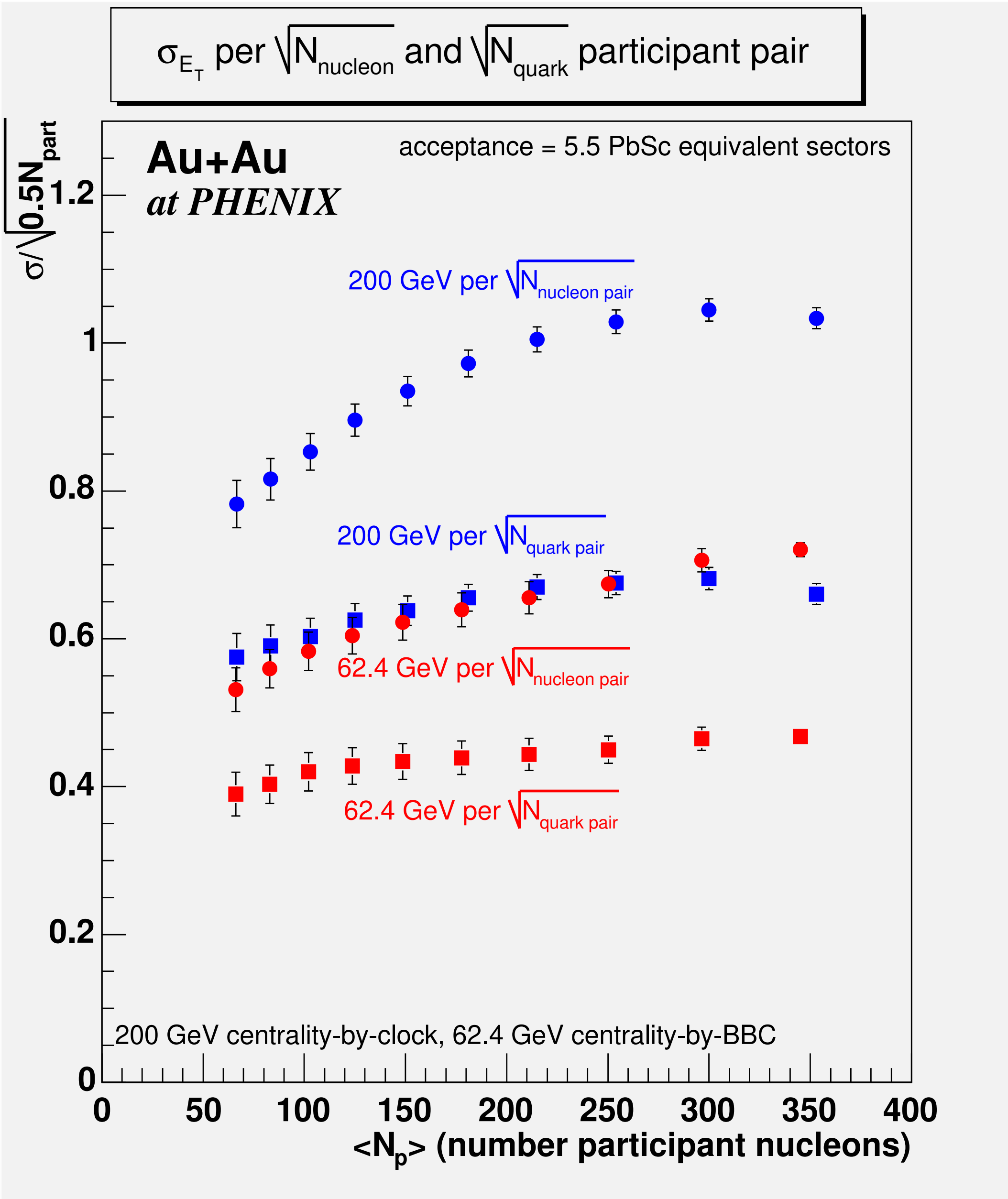

Figure 118: 62.4 and 200 GeV Au+Au 5.5 equivalent sector $E_{T\ (\mathrm{EMC})}$ distribution width measurements $\sigma/\langle\sqrt{N_{\mathrm{nuc-part}}}\rangle$ and $\sigma/\langle\sqrt{N_{\mathrm{quark-part}}}\rangle$ compared. The dominant identified error on the ordinate axis is the centrality cut, followed by the N_{part} estimation; error related to cross section estimates were not considered. The imperfect centrality cuts create the shapes. Figure referenced in Chapter 5.

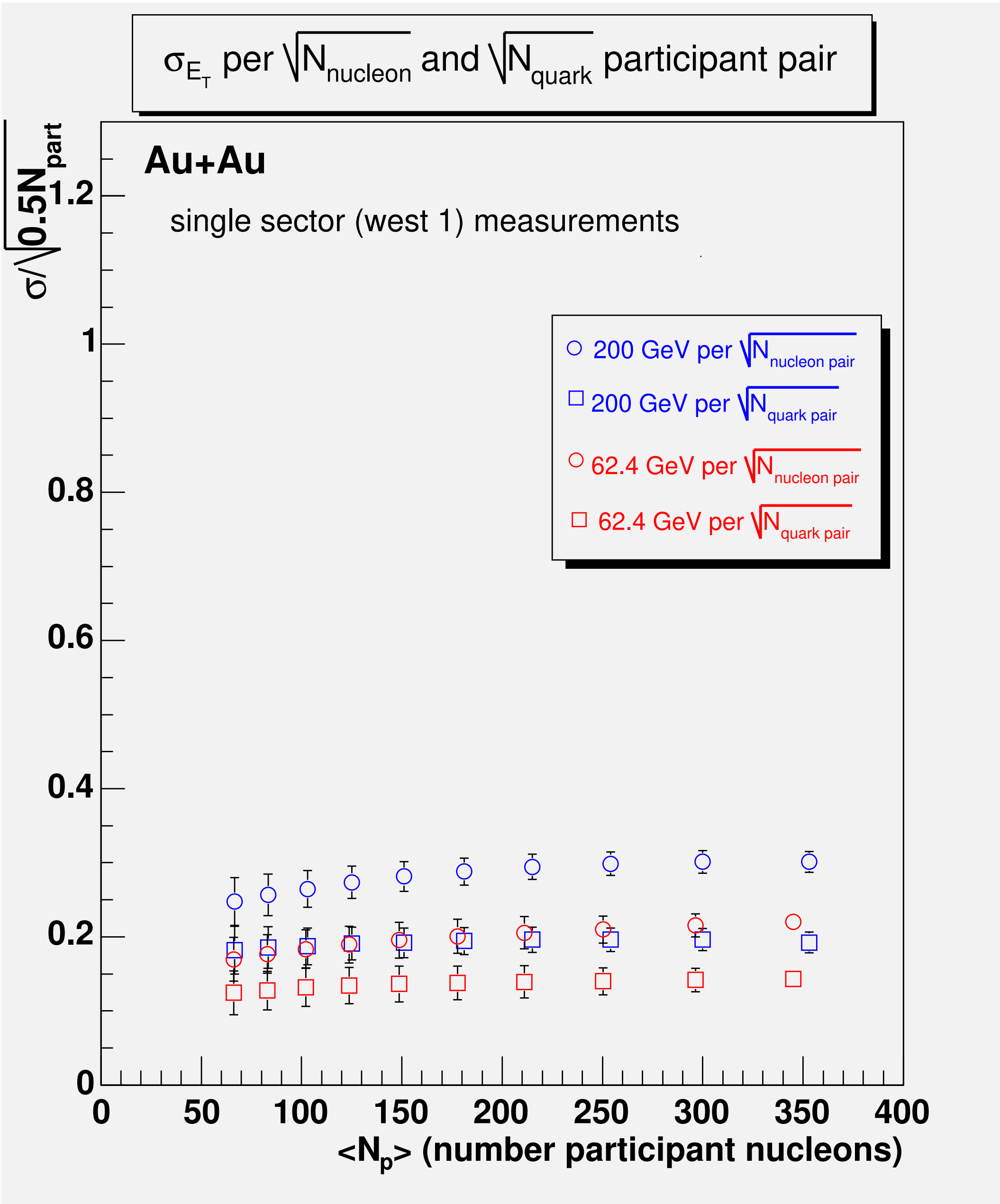

Figure 119: 62.4 and 200 GeV Au+Au 0.9 equivalent sector $E_{T\ (\mathrm{EMC})}$ distribution width measurements $\sigma/\langle\sqrt{N_{\mathrm{nuc-part}}}\rangle$ and $\sigma/\langle\sqrt{N_{\mathrm{quark-part}}}\rangle$ compared. The dominant error on the ordinate axis is the centrality cut, followed by the N_{part} estimation; error related to cross section estimates were not considered. Figure referenced in Chapter 5.

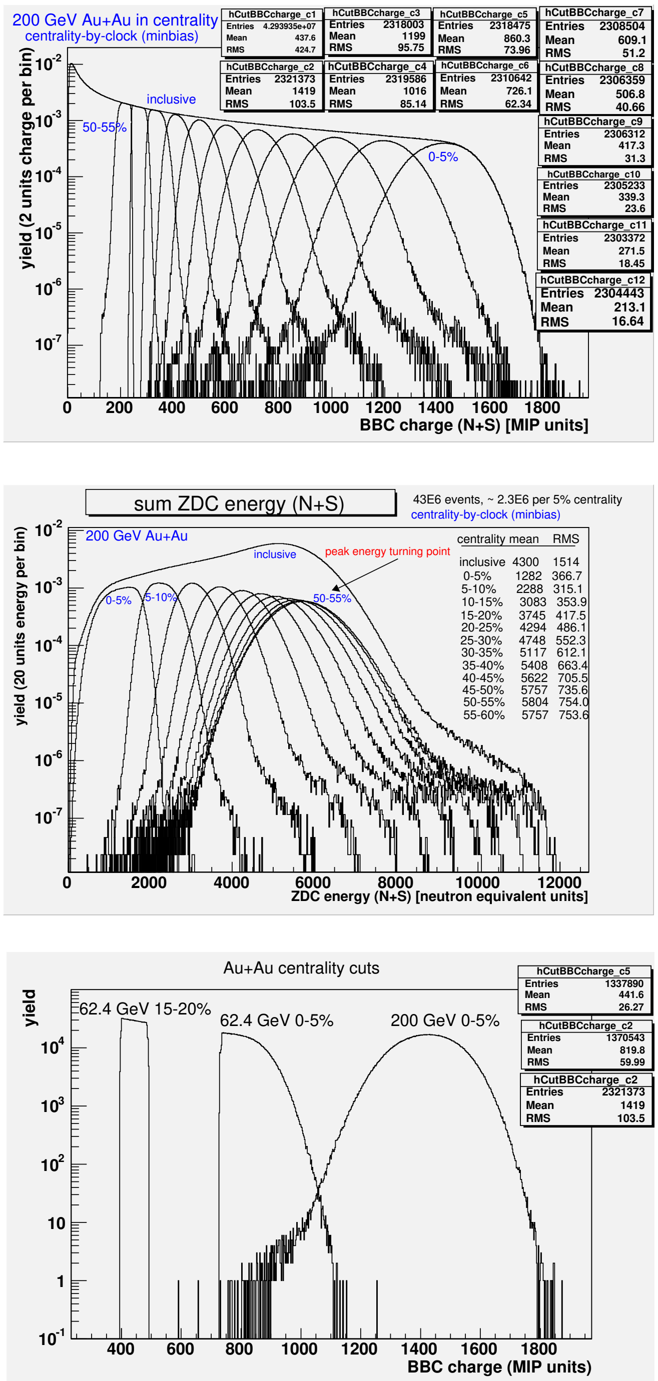

Figure 120: Au+Au inclusive and semi-inclusive BBC charge and ZDC energy clipped-distributions used for centrality definitions. The top plot contains the 200 GeV BBC distributions, the middle plot contains the 200 GeV ZDC distributions, both in centrality-by-clock. The bottom plot compares the central distribution for 62.4 GeV in centrality-by-BBC, to 200 GeV in centrality-by-clock, showing the different types of cuts used on the BBC charge in the definitions. Figure referenced in Chapter 5.

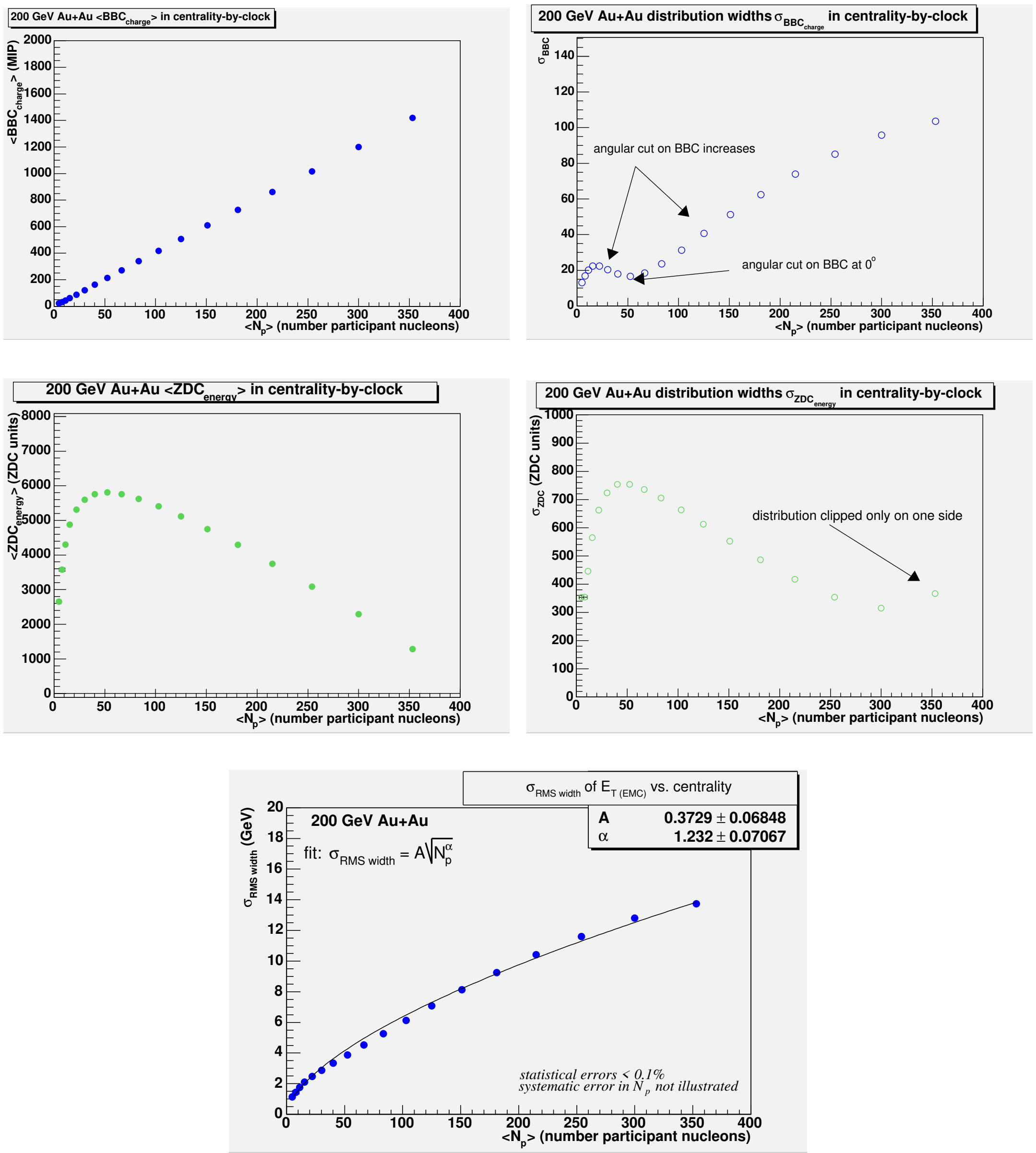

Figure 121: 200 GeV Au+Au BBC, ZDC, and E_T semi-inclusive distribution widths and means which result from clipped trigger distributions in centrality-by-clock. The top plots are (left) mean BBC charge, and (right) RMS widths showing the widths fluctuate around 50 participants which is where the centrality cut is roughly at zero degrees and close to a vertical cut on the BBC, allowing maximal BBC freedom. The middle plots are (left) mean ZDC energy, and (right) RMS widths showing the most central width is relatively large; this is likely due to that distribution only being clipped on one side. The bottom plot are the $E_{T(\text{ EMC})}$ distribution widths; notice the kinks where the points deviate from the power-law fit are exactly where the BBC and ZDC widths deviate. Figure referenced in Chapter 5.

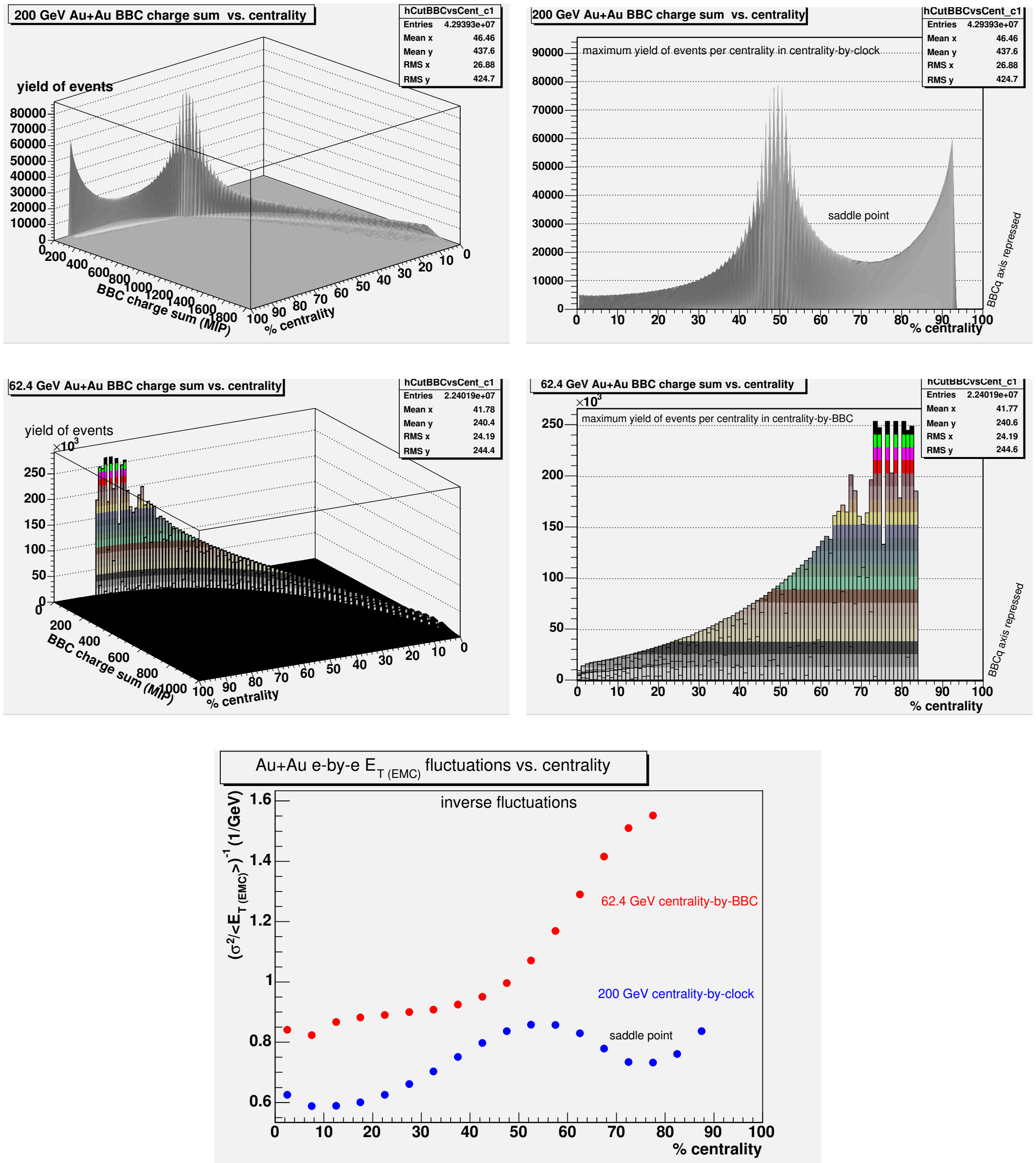

Figure 122: Au+Au: top plots are 200 GeV yield of events plotted over centrality vs. BBC charge plane in centrality-by-clock method; top right plot is cross-sectional view; the peaks correspond to where the BBC is allowed less range whether that be due to the angle at which it's cut, or the bin size which shrinks towards the peripheral region. Middle plots are 62.4 GeV yield of events plotted over centrality vs. BBC charge for centrality-by-BBC method, the middle right plot is cross-sectional view; here again the rising peak corresponds to the peripheral region where BBC is allowed less range. Bottom plot is 62.4 and 200 GeV Au+Au $E_{T\ (\mathrm{EMC})}$ scaled variance fluctuations $\sigma^2/\langle E_{T(\ \mathrm{EMC})}\rangle$, inverted, and plotted as a function of centrality bin rather than the usual $N_{\mathrm{nuc-part}}$ – notice the different centrality cut shapes drive the fluctuations. Figure referenced in Chapter 5.

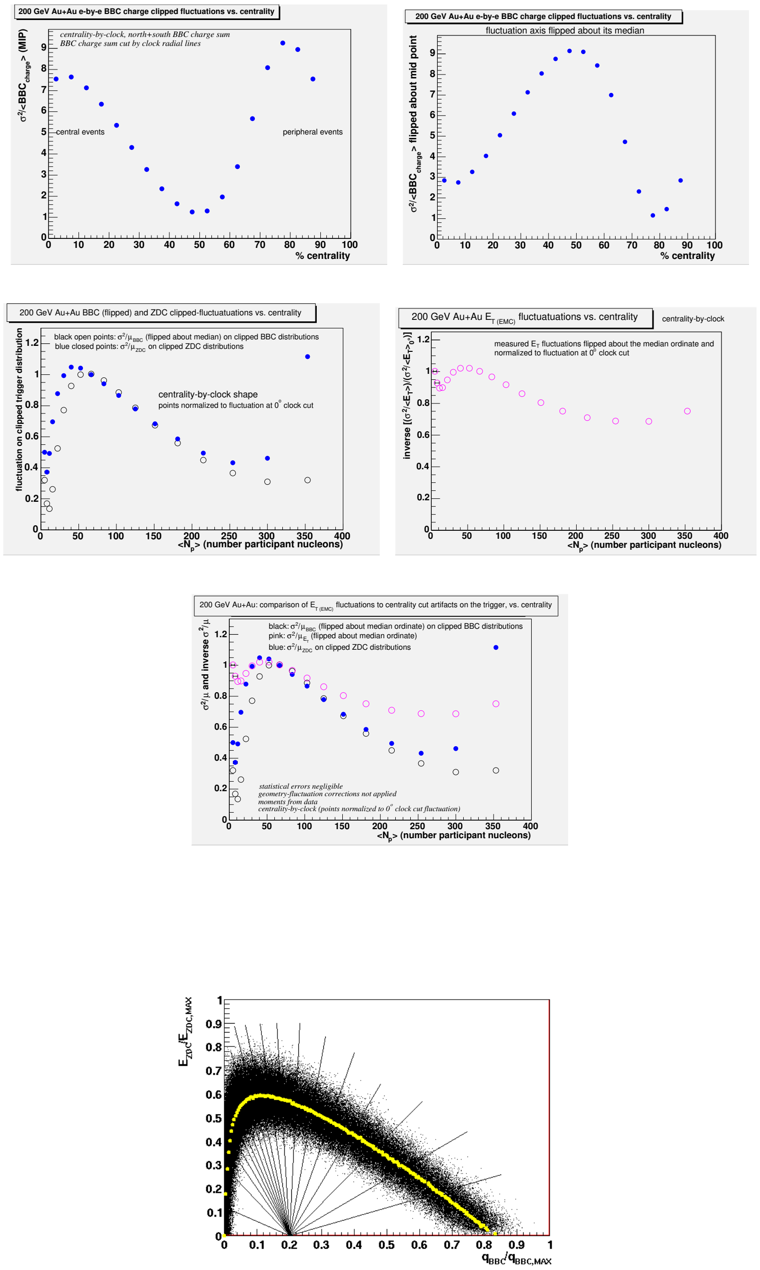

Figure 123: 200 GeV Au+Au fluctuations σ^2/μ made from centrality-by-clock. Top left plot are BBC fluctuations, and top right plot BBC fluctuations flipped about median ordinate. Middle left plot compares flipped BBC fluctuations to ZDC fluctuations. Middle right plot are the $E_{T\ (\mathrm{EMC})}$ fluctuations flipped about median ordinate. Plot 3rd from the top is a comparison of the fluctuations in $E_{T\ (\mathrm{EMC})}$ (flipped), BBC (flipped), and ZDC. This illustrates very clearly that the fluctuations in the central arm are merely following the artificial fluctuations in the clipped distributions of the trigger detectors. Bottom plot is the BBC vs. ZDC scatter plot used in centrality-by-clock, notice the dominant features are simply a recreation of the clock shape. Figure referenced in Chapter 5.

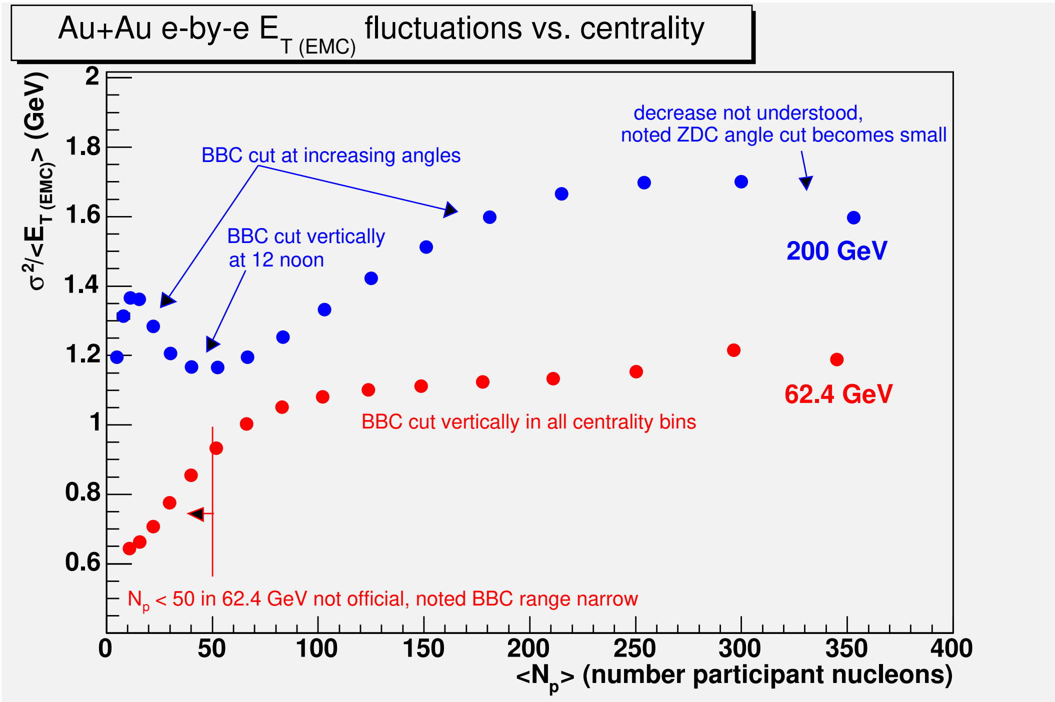

Figure 124: Au+Au: $E_{T\ (\mathrm{EMC})}$ scaled variance fluctuations $\frac{\sigma^2}{\langle E_{T\ (\mathrm{EMC})}\rangle}$ in centrality – the variation in the fluctuations is due to error in the centrality cuts; in 200 GeV the drop in fluctuations in the most central points is likely due to the fact that the width of ZDC-BBC clock becomes narrow in the most central region of that scatter plot. The drop in fluctuations in the 62.4 GeV peripheral is identified to be due to the BBC bin width becoming very small. Measured in 5.5 equivalent sectors. Figure referenced in Chapter 5.

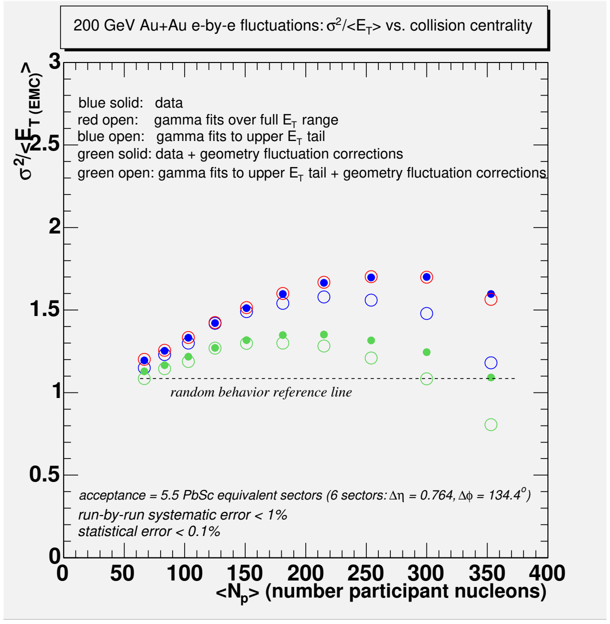

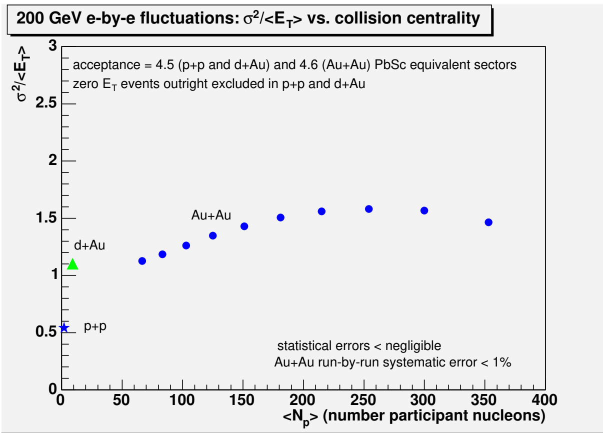

Figure 125: 200 GeV $p+p$, d+Au, and Au+Au scaled variance $\sigma^2/\langle E_{T\ (\mathrm{EMC})}\rangle$. Top plot: Au+Au fluctuations measured in the 5.5 equivalent PbSc sectors, comparison of data, gamma fits, and gamma fits with expanded errors at low E_T to better approximate the upper $E_{T\ (\mathrm{EMC})}$ tails. Also compared are the affect of applying geometry fluctuation corrections. It was not concluded why fitting only to the upper tails follows the affect of the geometry fluctuation corrections. Bottom plot: 200 GeV $p+p$, d+Au, and Au+Au $E_{T\ (\mathrm{EMC})}$ fluctuations measured in 4.5 equivalent sectors. For $p+p$ and d+Au the minbias triggers with zero E_T were excluded (zeros comprised 19% of $p+p$ and 6% of d+Au events); although not shown when the zero E_T minbias triggers are retained the $p+p$ point moves up about 19%; this raises speculation about where the $p+p$ point would be if the additional 31% of missed interactions due to the trigger bias (seen by the EMC) were included. Only statistical errors were considered for $p+p$, d+Au. Figure referenced in Chapter 5.

B.5.4 Figures of E_T fluctuations in acceptance

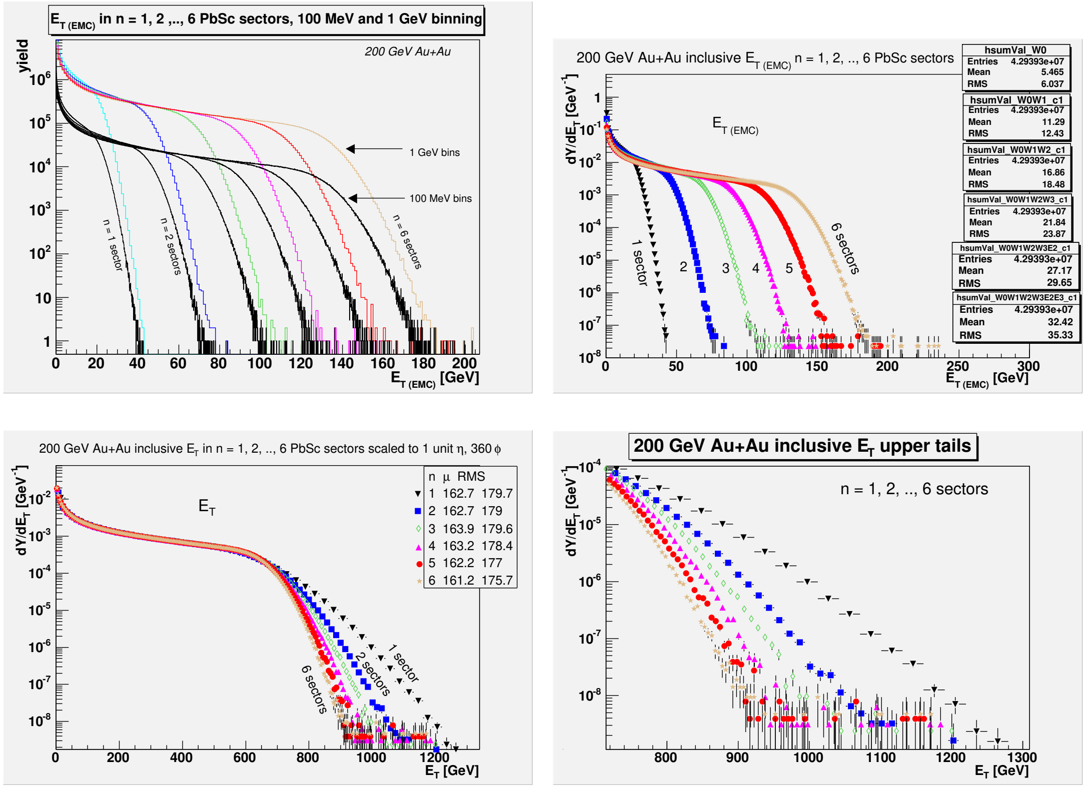

Figure 126: 200 GeV Au+Au $E_{T\ (\mathrm{EMC})}$ correlations: inclusive distributions in acceptance. The top plots are the 6 $E_{T\ (\mathrm{EMC})}$ inclusive distributions made in increasing acceptance, (top left) for different binning resolutions of 100 MeV and 1 GeV, and (top right) using markers to represent the acceptance measurements. The bottom plots are the same 6 measurements in acceptance (1 GeV per bin) where now the energy of each histogram bin has been scaled to the same $E_{T\ (\mathrm{EMC})} \rightarrow E_T$ reference, essentially using the scale factors 1, 2, .., 6. The number of events in each bin is also normalized by the same scale factor to maintain an “affective” binning resolution of 1 GeV. Note that the smaller the acceptance of the initial measurement the larger the overshoot of the scale-corrected tail, this was investigated. In the bottom left plot the RMS, σ, of the scaled distributions are essentially the same regardless of the dramatic differences in how far out the tails shoot, indicating the different sizes of the tails are compensated for by low E_T events. The bottom right is a close up view. Figure referenced in Chapter 5.

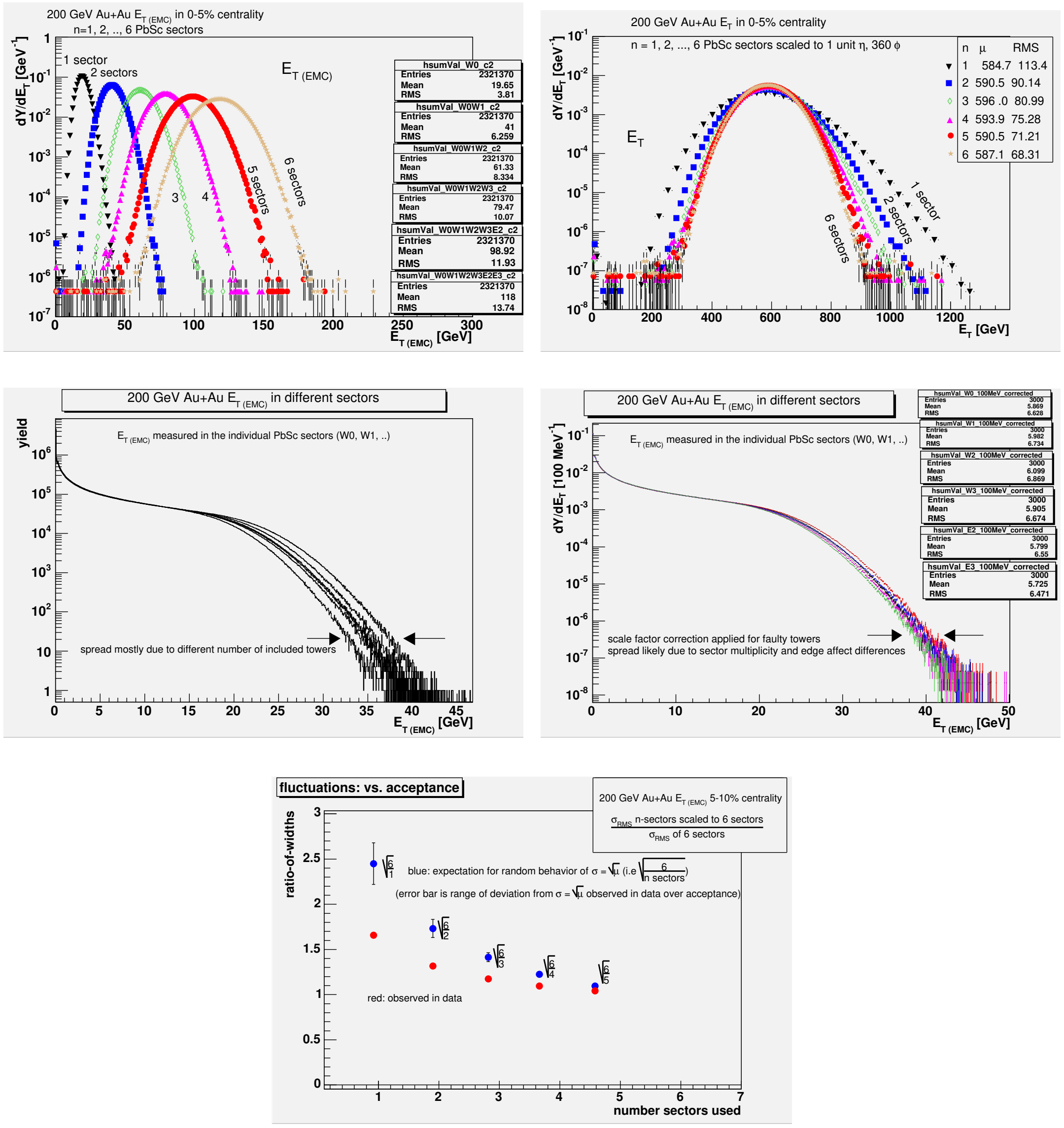

Figure 127: 200 GeV Au+Au $E_{T\ (\mathrm{EMC})}$ correlations: top left plot are 0-5% centrality 6 measurements in increasing acceptance; top right plot are the histograms corrected to the reference acceptance resulting in overshooting upper tails. Middle plots are the 6 inclusive individual sector measurements where (left plot) differences due to different quantities of missing PbSc towers, and (right plot) after scale-correcting to account for missing PbSc towers. It was determined the $\sim$ 15% difference in numbers of included towers does not explain overshooting tails (nor observed rise in fluctuations with acceptance). Bottom plot compares RMS widths of scale-corrected distributions to a value the scale shift is expected to change the RMS widths to in the case of purely random distributions: the fact that the widths with overshooting tails are smaller than that expected when scale-correcting illustrates the overshoot is possibly non-physical and simply a result of scale shifting. Figure referenced in Chapter 5.

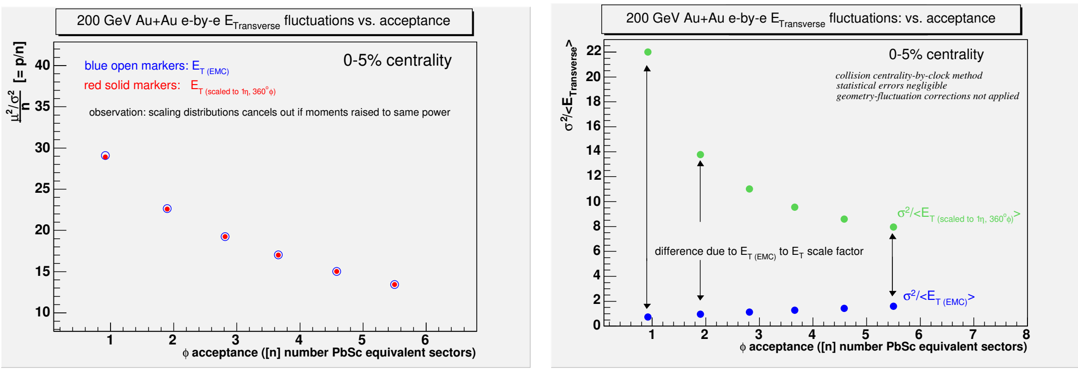

Figure 128: 200 GeV Au+Au 0-5% centrality: $E_{T\ (\mathrm{EMC})}$ versus E_T correlations. Left plot compares the affect on the fluctuation $\frac{\mu^2}{\sigma^2 n}$ when using measured $E_{T\ (\mathrm{EMC})}$ distributions versus scale corrected E_T distributions, no difference. The reason there is no difference is because the two distribution moments are raised to the same power. The right plot is the same comparison but for $\frac{\sigma^2}{\mu}$ where now the moments are not raised to the same power. Notice the very large difference. The conclusion is that it appears incorrect to use the RMS width, σ to represent fluctuations after a scale shift is applied to the events in a distribution, as the natural behavior of the "fluctuation" has been changed to something artificial. Figure referenced in Chapter 5.

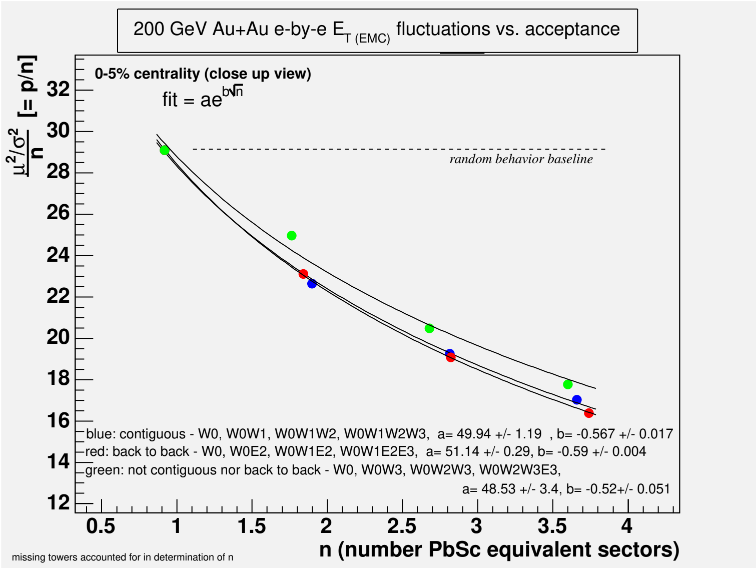

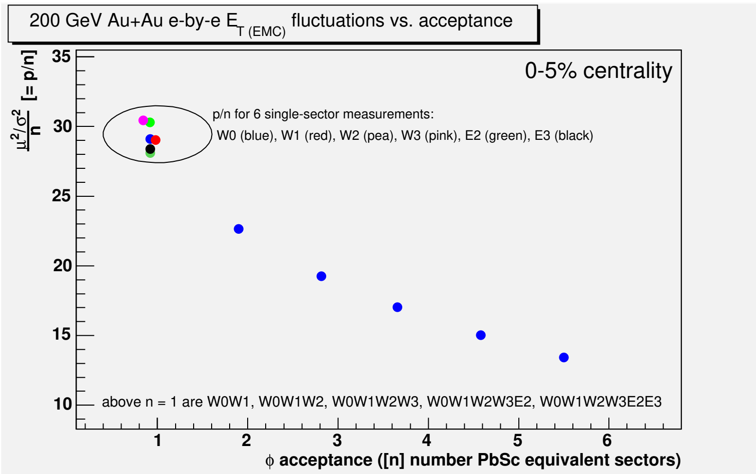

Figure 129: 200 GeV Au+Au $E_{T\ (\mathrm{EMC})}$ correlations: 0-5% centrality $\mu^2/\sigma^2 n$ vs. acceptance. The curves in the top plot were made using different choices of sector combinations illustrating the large drop in fluctuations have little to do with the separation distance between the sectors, or if the energy is added from opposite sides transverse to the beam (back-to-back). In the bottom plot the single sector measurement was compared using the different sectors which established the dominant systematic error. Figure referenced in Chapter 5.

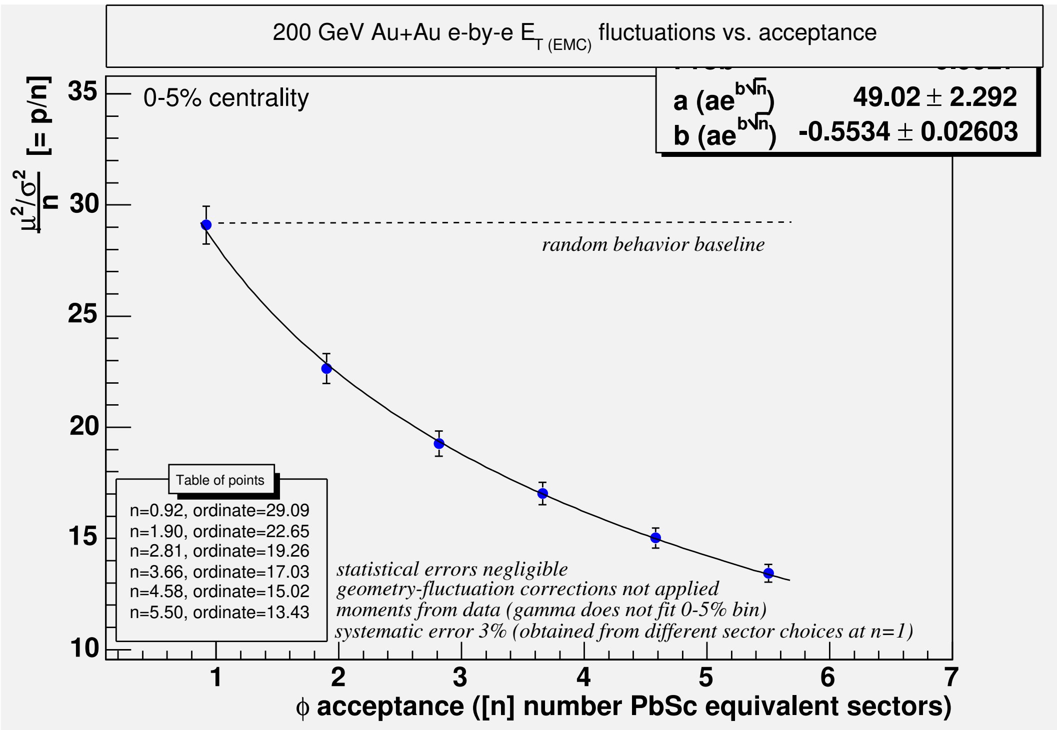

Figure 130: 200 GeV Au+Au correlations $E_{T\ (\mathrm{EMC})}$: 0-5% centrality $\mu^2/\sigma^2 n$ vs. acceptance. The final result fitted to a power function to quantify the fluctuation. Figure referenced in Chapter 5.

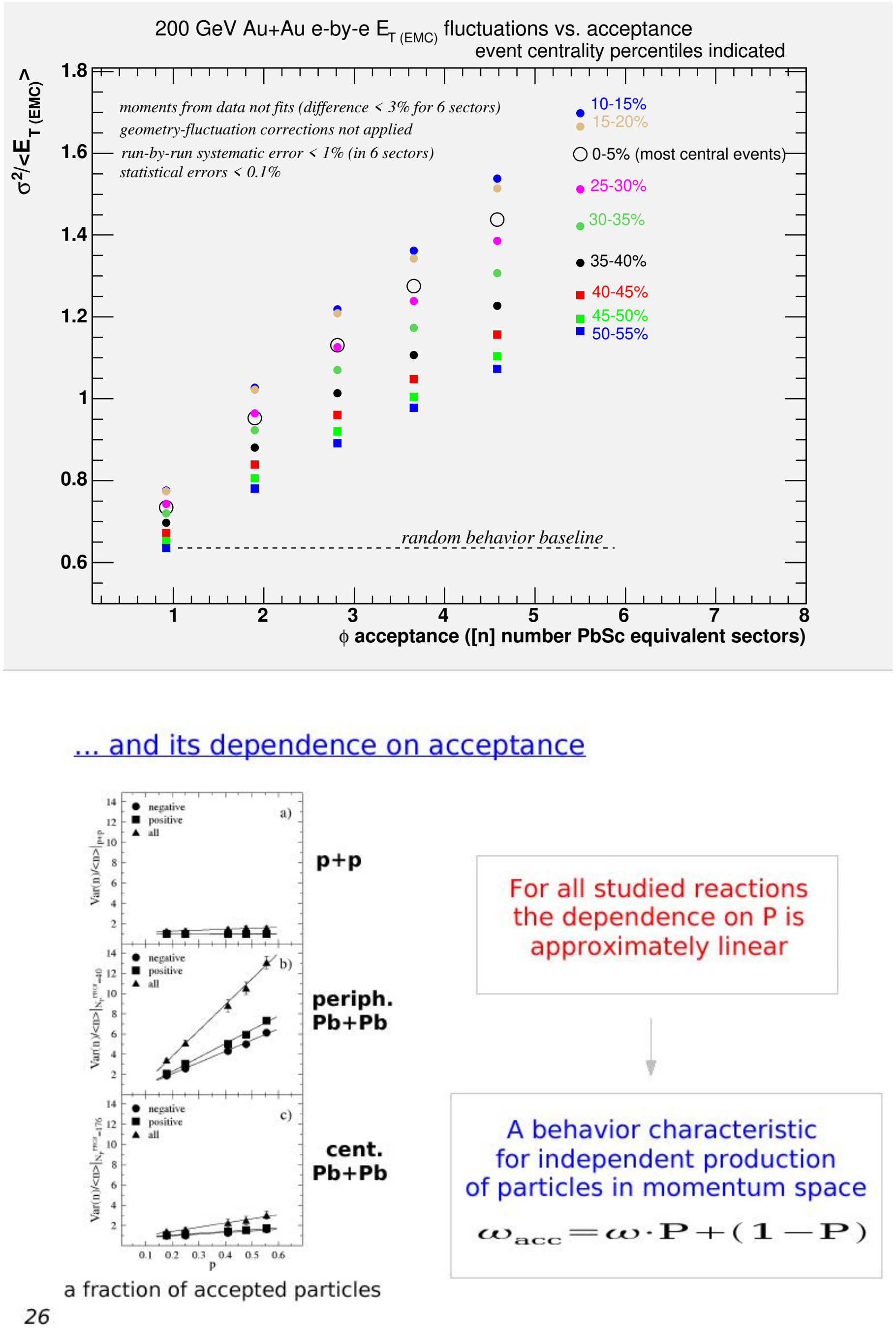

Figure 131: Scaled variance fluctuation $\frac{\sigma^2}{\mu}$ vs. acceptance. Top plot shows PHENIX 200 GeV Au+Au $\frac{\sigma^2}{\langle E_{T\ (\mathrm{EMC})}\rangle}$ made for the different centrality bins (recall the different fluctuations over centrality were demonstrated to be artificial). Bottom plot CERN fixed target ($\sim \sqrt{s_{NN}}$ =17 GeV) fluctuations for $p+p$ and Pb+Pb multiplicity where the increasing acceptance is of accepted particles. The CERN fluctuations appear centrality dependent. Figure referenced in Chapter 5. (bottom plot courtesy M. Gazdzicki of NA49, Correlations Workshop, M.I.T., 2005).

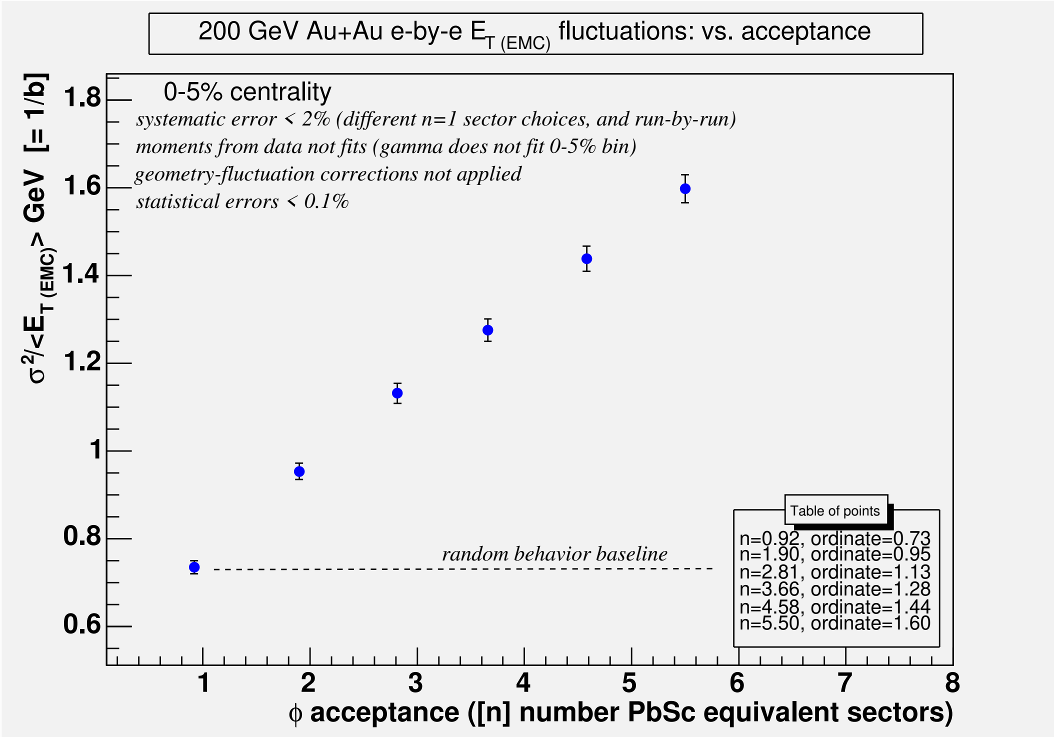

Figure 132: 200 GeV Au+Au $E_{T\ (\mathrm{EMC})}$ correlations: 0-5% centrality fluctuation σ^2/μ vs. acceptance. The plot is the final result illustrating a 115% rise in the scaled variance fluctuation σ^2/μ with a 6-fold increase in $\Delta\phi$ acceptance. Figure referenced in Chapter 5.

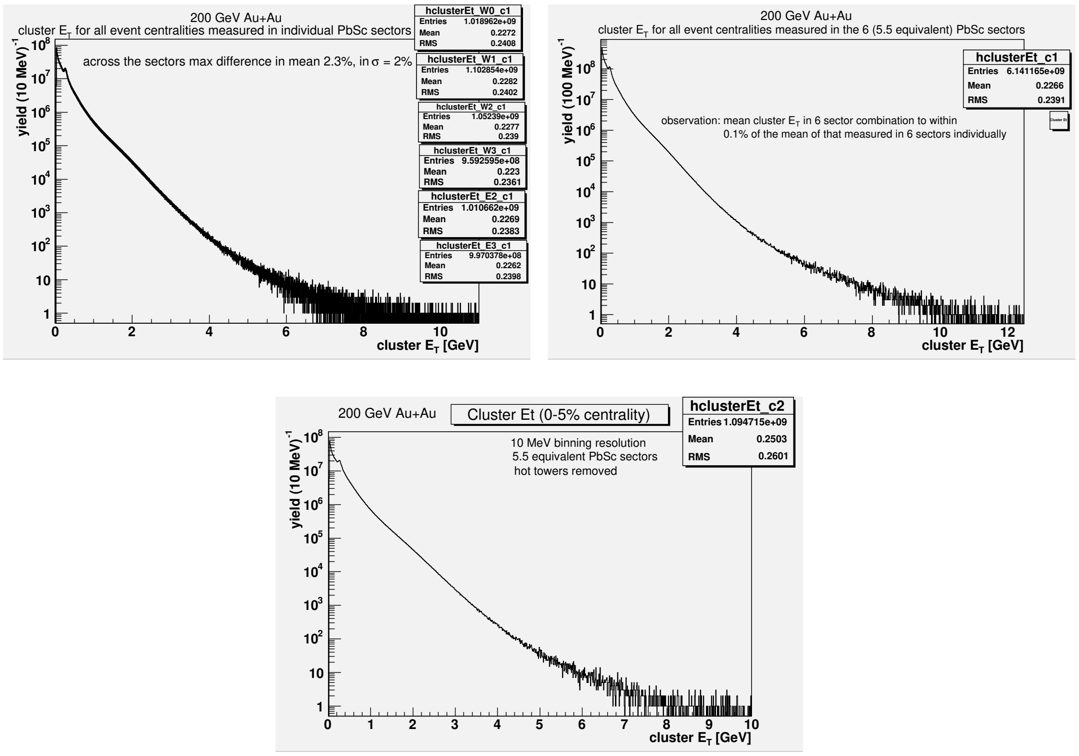

Figure 133: 200 GeV Au+Au: transverse energy per cluster, e_T, measurements. The $\langle e_T \rangle$ per cluster is used with the fluctuation in acceptance measurement of the distribution cumulant to extract a correlation length. The top left plot is the inclusive e_T per cluster determined using the six sectors individually illustrating consistency – the six distributions are lying on top of one another. The top right plot is the inclusive e_T per cluster measured in the 6 sector combination illustrating the $\langle e_T \rangle$ per cluster is not a function of acceptance. The bottom plot is the 0-5% centrality e_T per cluster distribution measured in the 6 sector combination - which has a slightly larger $\langle e_T \rangle$ than the inclusive distribution illustrating a small rise in the $\langle e_T \rangle$ with centrality, this is not understood and was not considered further. Figure referenced in Chapter 5.

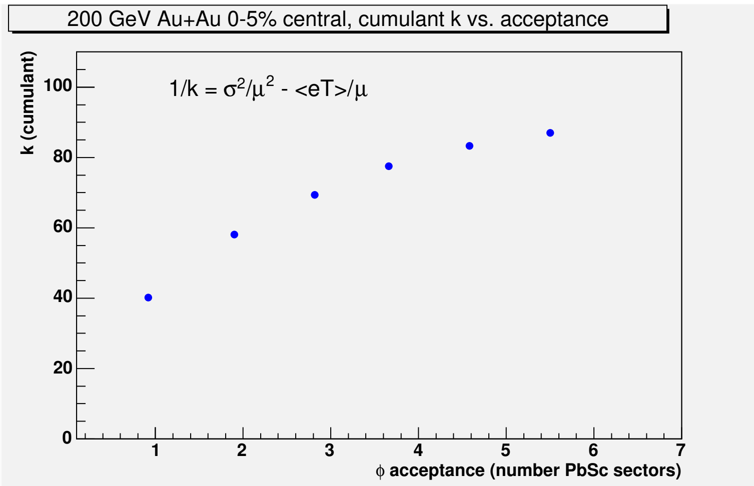

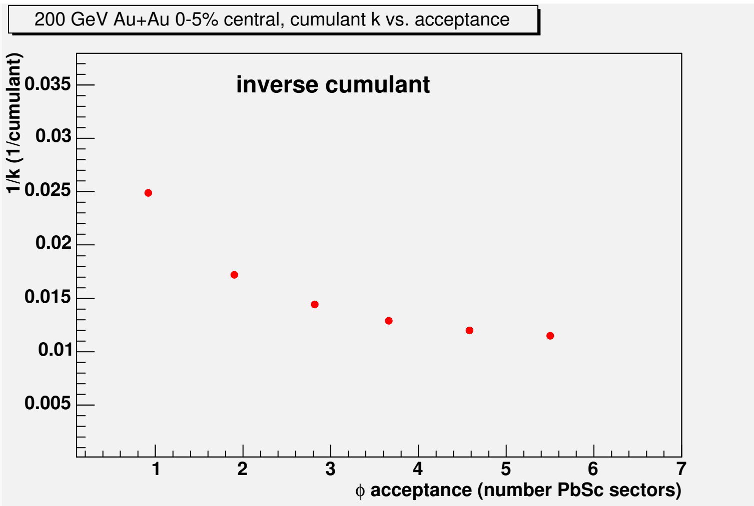

Figure 134: 200 GeV Au+Au 0-5% centrality $E_{T\ (\mathrm{EMC})}$ correlations: (top plot) k cumulant vs. $\Delta\phi$ acceptance, and (bottom plot) $1/k$ vs. $\Delta\phi$ acceptance. k was fit to a particle correlation function and a correlation length of 0.14 PbSc sector ($\sim$ 28 cm), which corresponds to 3.1° was extracted from the fit. Figure referenced in Chapter 5.

B.5.5 Figures approved PHENIX Preliminary for publication

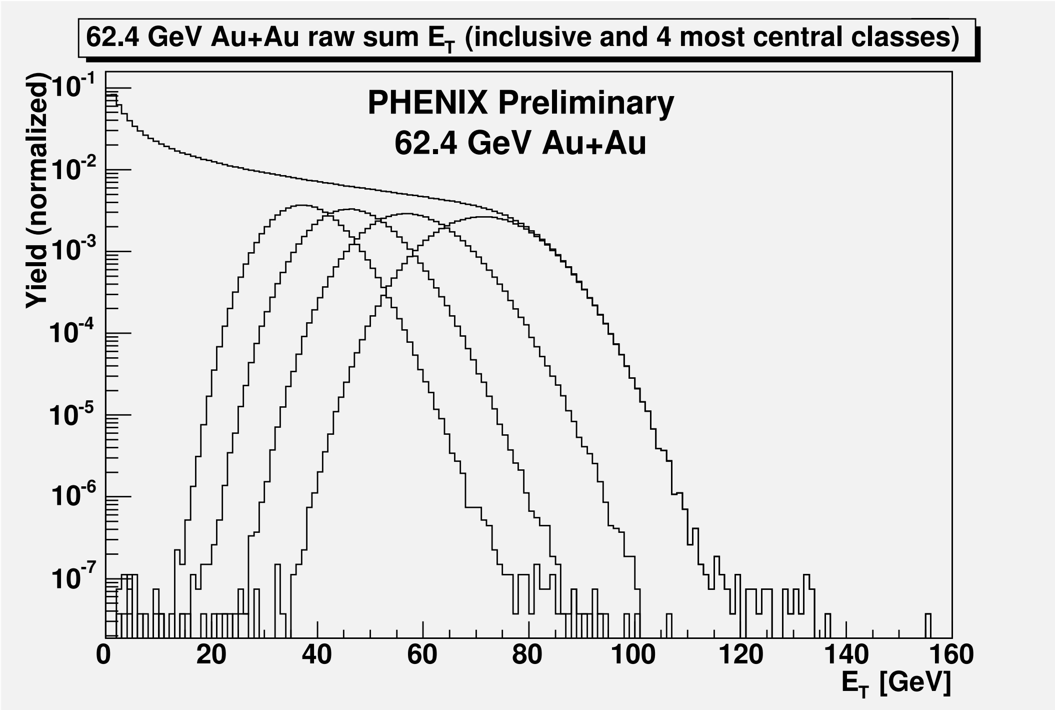

Figure 135: 62.4 GeV Au+Au inclusive $E_{T\ (\mathrm{EMC})}$ distribution and four most central 5% wide semi-inclusive distributions. Figure referenced in Chapter 6.

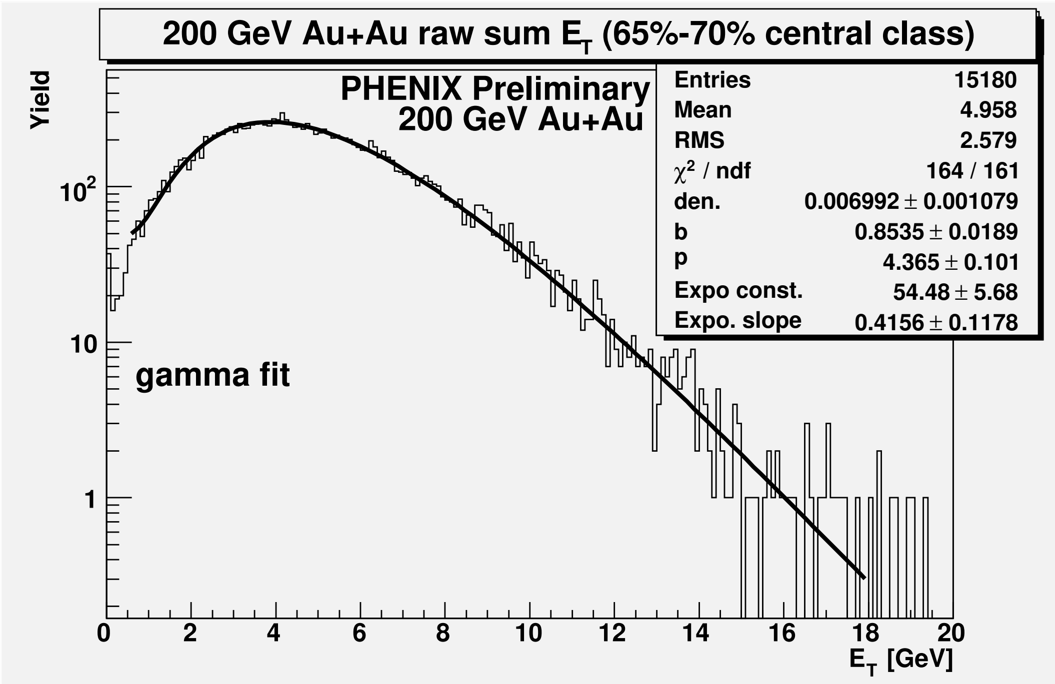

Figure 136: 200 GeV Au+Au $E_{T\ (\mathrm{EMC})}$ distribution, in 5% wide centrality, fit to a gamma distribution. Figure referenced in Chapter 6.

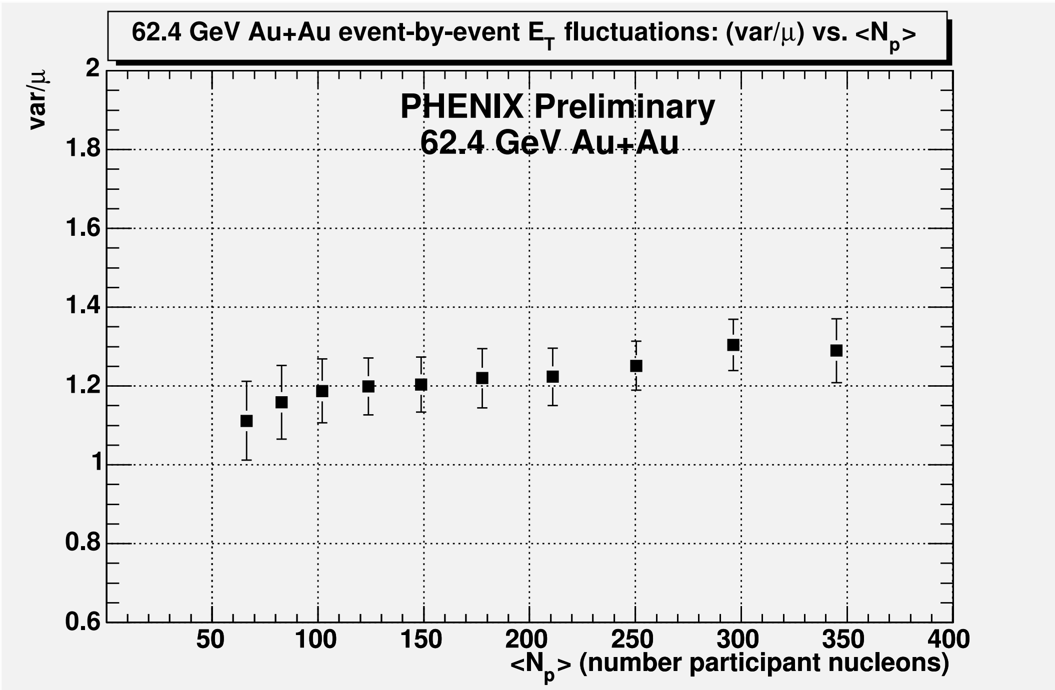

Figure 137: 62.4 GeV Au+Au E_T fluctuations σ^2/μ. Figure referenced in Chapter 6.

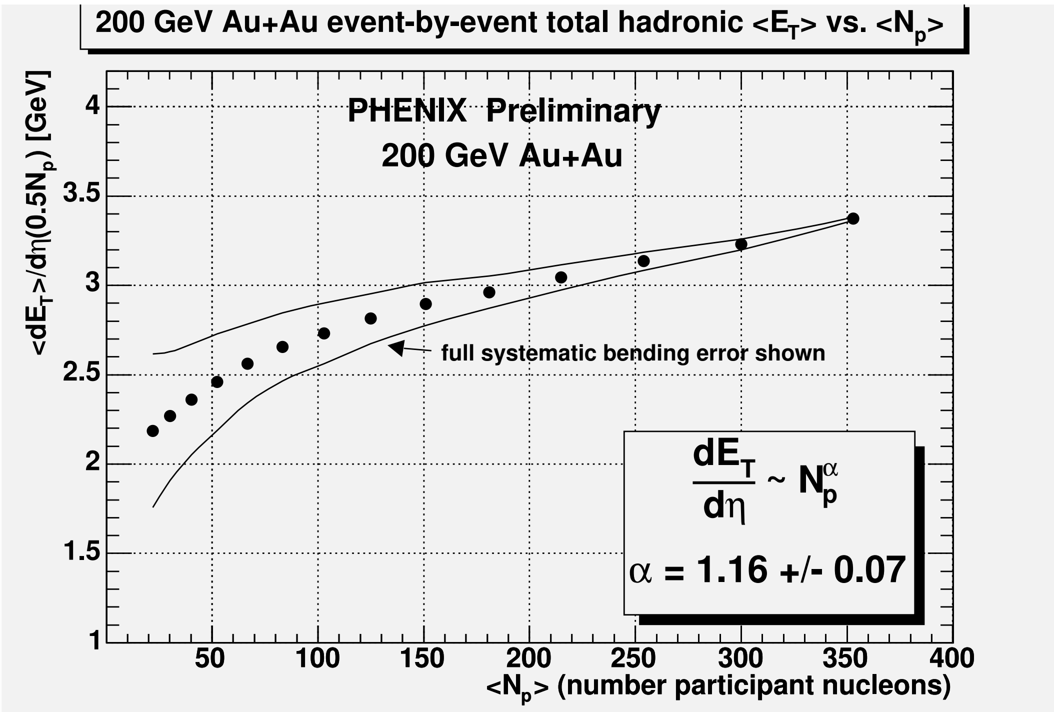

Figure 138: 200 GeV Au+Au mean E_T per participant nucleon; α is from the fit to a power law function. Figure referenced in Chapter 6.

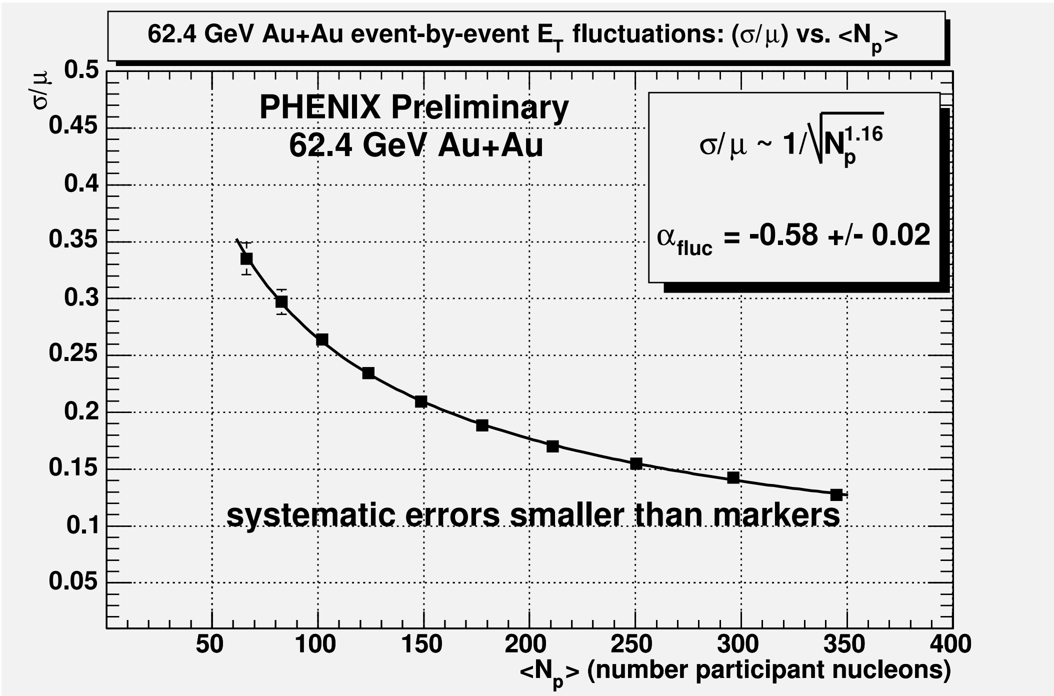

Figure 139: 62.4 GeV Au+Au E_T fluctuations σ/μ. Figure referenced in Chapter 6.

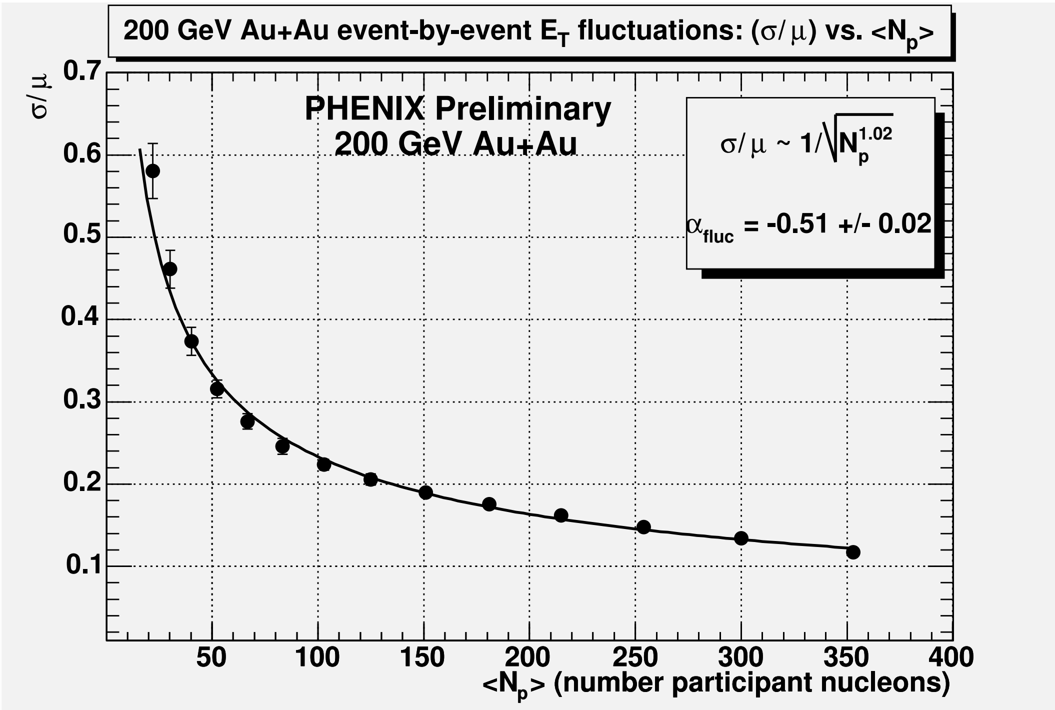

Figure 140: 200 GeV Au+Au E_T fluctuations σ/μ. Figure referenced in Chapter 6.

REFERENCES

[1] T. Abbott et al. Measurement of energy emission from O+Au and p+Au collisions at 14.5 GeV/c per nucleon with a lead-glass array. *Physics Letters B*, 197(1, 2):285, October 1987.

[2] K. Adcox et al. Centrality dependence of charged particle multiplicity in Au+Au collisions at $\sqrt{s_{NN}} = 130$ gev. *Phys. Rev. Lett.*, 86(16):3500, April 2001.

[3] K. Adcox et al. Measurement of the midrapidity transverse energy distribution from $\sqrt{s_{NN}} = 130$ GeV Au+Au collisions at RHIC. *Phys. Rev. Lett.*, 87(5):052301, July 2001.

[4] S. Adler et al. Systematic studies of the centrality and $\sqrt{s_{NN}}$ dependence of $\frac{dE_T}{d\eta}$ and $\frac{dN_{ch}}{d\eta}$ in heavy ion collisions at mid-rapidity. *Phys. Rev. C*, 71:034908, 2005.

[5] A. Angelis et al. Observation of jet structure in high transverse energy events at the CERN intersecting storage rings. *Physics Letters*, 126B(1, 2):132, 1983.

[6] L. Aphecetche et al. Neutral pion spectra measured with the EMCal in $\sqrt{s_{NN}} = 62.4$ GeV Au+Au collisions. PHENIX Internal Report AN292, Brookhaven National Laboratory, May 2004.

[7] R. Armendariz. Incorrect pad chamber minbias data and subsequent corruption to the $\sqrt{s_{NN}} = 62.4$ GeV Au+Au Run 4 centrality prescription presented in analysis note 290. PHENIX Internal Report AN452, Brookhaven National Laboratory, September 2005.

[8] R. Armendariz. $\sqrt{s_{NN}} = 200$ GeV Au+Au and $\sqrt{s_{NN}} = 62.4$ GeV Au+Au event-by-event distribution mean E_T and E_T width fluctuation measurements over collision centrality in RHIC Run 4. PHENIX Internal Report AN465, Brookhaven National Laboratory, November 2005.

[9] R. Armendariz. Evolution of event-by-event E_T fluctuations over collision centrality in RHIC interactions; 17th Particles and Nuclei International Conference (PANIC) 2005. *AIP Conf. Proc.*, 842:68–70, July 2006.

[10] A. Bamberger et al. Multiplicity and transverse energy flux in ^{16}O+Pb at 200 GeV per nucleon. *Physics Letters B*, 184(2, 3):271, January 1987.

[11] M. Banner et al. Observation of very large transverse momentum jets at the CERN $\vec{p} + p$ collider. *Physics Letters*, 118(1, 2, 3):203, 1982.

[12] Barletta et al. The relativistic heavy ion collider project: RHIC and its detectors. *Nuc. Instrum. Methods Phys. Res. A*, 499(2-3), March 2003.

[13] R. Barlow. *Statistics*. John Wiley and Sons, 1989.

[14] A. Bazilevsky et al. Measurement of the mid-rapidity transverse energy distribution from $\sqrt{s_{NN}} = 130$ GeV Au+Au collisions at RHIC. PHENIX Internal Report AN41, Brookhaven National Laboratory, January 2001.

[15] A. Bazilevsky et al. E_T distributions in Au+Au and $p+p$ collisions at $\sqrt{s_{NN}} = 200$ GeV. PHENIX Internal Report AN220, Brookhaven National Laboratory, September 2003.

[16] A. Bialas et al. Multiplicity distributions in nucleus-nucleus collisions at high energies. *Nuclear Physics B*, 111:461, 1976.

[17] A. Bialas et al. Additive quark model of multi-particle production and nucleus-nucleus collisions at high energies. *Physical Review D*, 25(9):2328, May 1982.

[18] M. Chiu et al. Determining the number of participants using a hybrid Glauber model approach. PHENIX Internal Report AN18, Brookhaven National Laboratory, September 2000.

[19] B. De et al. Rapidity spectra of the secondaries produced in heavy ion collisions and the constituent picture of the particles. *Physical Review C*, 71:024903–1, 2005.

[20] A. Drees et al. Centrality determination and p_T centrality dependence in d+Au collisions. PHENIX Internal Report AN210, Brookhaven National Laboratory, June 2003.

[21] S. Eremin et al. Nucleon participants or quark participants? *Physical Review C*, 67:064905, 2003.

[22] R Fernow. *Introduction to Experimental Particle Physics*. Cambridge University Press, 1990.

[23] M. Gazdzicki. Fluctuations and NA49. Invited talk, Correlations and Fluctuations 2005, MIT, CERN, 2005.

[24] H. Heiselberg et al. Anomalous multiplicity fluctuations from phase transitions in heavy ion collisions. *arXiv:nucl-th/0006021*, v3, April 2001.

[25] A. Hoover. The PHENIX muon spectrometer and J/psi production in $\sqrt{s_{NN}}$ = 200 GeV proton-proton collisions at RHIC. PhD Thesis, New Mexico State University, 2003.

[26] S. Jeon et al. Charged particle ratio fluctuations as a signal for QGP. *arXiv:hep-ph/0003168*, 3, July 2000.

[27] S. Kelly et al. Calculation of the number of participating nucleons for centrality classes defined with the ZDC and the BBC. PHENIX Internal Report AN33, Brookhaven National Laboratory, November 2000.

[28] P. Kumar et al. Quark participants and global variables. *Physical Review C*, 70:027901, 2004.

[29] G. Martinez et al. Glauber calculation of N_{coll} and N_p in d+Au collisions at $\sqrt{s}$ =200 GeV. PHENIX Internal Report AN295, Brookhaven National Laboratory, 2004.

[30] C. Marzo et al. A study of deep inelastic hadron-hadron collisions with a large acceptance calorimeter trigger. *Physics Letters*, 112B(2):173, 1982.

[31] M. Mendenhall et al. Charged particle multiplicity analysis for $\sqrt{s_{NN}} = 62.4$ GeV run. PHENIX Internal Report AN304, Brookhaven National Laboratory, June 2004.

[32] D. Morrison et al. Centrality determination for 62.4 GeV Au+Au. PHENIX Internal Report AN290, Brookhaven National Lab, 2004.

[33] S. Mrowczynski et al. Transverse momentum versus multiplicity fluctuations in high energy nuclear collisions. *arXiv:nucl-th/0407012v2*, 2, September 2004.

[34] R. Nouicer. Multi-particle production from Au+Au, Cu+Cu, d+Au, and p+p collisions. Invited presentation, International Symposium on Multi-particle Dynamics, Czech Republic, Brookhaven National Laboratory, 2005.

[35] R. Nouicer. Charged particle multiplicities in A+A and p+p collisions in the constituent quarks framework. *arXiv:nucl-th*, 0608038v1, 2006.

[36] D. H. Perkins. *Introduction to High Energy Physics.* Cambridge University Press, 4th edition, 2000.

[37] K. Reygers. Glauber Monte-Carlo calculation for Au+Au collisions at $\sqrt{s_{NN}}$ =200 GeV. PHENIX Internal Report AN169, Brookhaven National Laboratory, February 2003.

[38] H. Satz. The search for the QGP: A critical appraisal. *Invited Talk at Lattice 2000: 18th Int. Symposium on Lattice Field Theory*, August 2000.

[39] M. Tannenbaum. Further comments on fits to $k(\delta\eta)$ in Analysis Note 432. PHENIX Internal Report, Brookhaven National Laboratory, February 2006.

[40] M.J. Tannenbaum. Transverse energy production in light and heavy ion interactions. *International Journal of Modern Physics A*, 4(14):3377, 1989.

[41] M.J. Tannenbaum. E_T and other event-by-event distributions from AGS to RHIC energies. *Progress in Particle and Nuclear Physics*, 53:239, 2004.

[42] H. Tydesjo. Net charge fluctuations in ultra-relativistic nucleus-nucleus collisions. Licentiate (PhD) Thesis, Lund University, February 2003.